

DESIGNING MULTIFUNCTIONAL MATERIAL SYSTEMS FOR SOFT
ROBOTIC COMPONENTS

A Dissertation

Submitted to the Faculty

of

Purdue University

by

R. Adam Bilodeau

In Partial Fulfillment of the

Requirements for the Degree

of

Doctor of Philosophy

May 2020

Purdue University

West Lafayette, Indiana

THE PURDUE UNIVERSITY GRADUATE SCHOOL
STATEMENT OF DISSERTATION APPROVAL

Prof. Rebecca Kramer-Bottiglio, Co-Chair

School of Mechanical Engineering

Prof. Andres F. Arrieta, Co-Chair

School of Mechanical Engineering

Prof. Kendra A. Erk

School of Materials Engineering

Prof. Rodney W. Trice

School of Materials Engineering

Approved by:

Nicole L. Key

Associate Head for Graduate Studies

This is dedicated to my wonderful wife, Miranda Bilodeau. She chose to marry me knowing that within the week I would whisk her across the country to begin my Ph.D. From day one till today she has been an unflagging support to me and my goals, and without her this would have never happened.

ACKNOWLEDGMENTS

I would like to acknowledge the mentorship of Prof. Rebecca Kramer-Bottiglio throughout the past six years. Her vision for what can be done with soft robotic technologies has helped push me to discover and make what I have done over these past years.

I would also like to acknowledge the advise, suggestions, and help from my colleagues, especially Dr. Michelle C. Yuen. Not only an excellent collaborator, Michelle has been an ever present sounding board of ideas and a source of inspiring encouragement through the challenges of research. I would like to acknowledge my other coauthors, Dr. Edward White, who was a huge support during my early Ph.D., Trevor L. Buckner who spearheaded the Robotic Fabrics project, and Amir M. Nasab for his incredible energy with which he tackled the challenges in the final paper that comprises this thesis.

I would like to acknowledge financial support from the National Aeronautics and Space Administration Early Career Faculty program, the Air Force Office of Scientific Research Young Investigator Program, and the National Science Foundation Emerging Frontiers in Research and Innovation program.

Finally, I must acknowledge my family and their support. Having a second child born to our family in the same month that I'm writing this has been challenging, in a word. Throughout this and every other challenge, my wife and our first child have supported me.

TABLE OF CONTENTS

LIST OF TABLES	9
LIST OF FIGURES	10
ABSTRACT	24
1. INTRODUCTION	25
1.1 Soft Robotics	25
1.2 Summary Outline of Thesis	26
1.3 Contributions	28
2. MONOLITHIC FABRICATION OF SENSORS AND ACTUATORS IN A SOFT ROBOTIC GRIPPER	33
2.1 Introduction	33
2.2 Previous Work	35
2.3 Experimental	37
2.3.1 Fabrication	37
2.3.2 Sensor Design	39
2.3.3 Sensor Characterization	41
2.3.4 Sensor-Actuator Interaction	42
2.4 Results and Discussion	44
2.5 Conclusion	45
2.6 Future Work	47
3. DESIGN FOR CONTROL OF A SOFT BIDIRECTIONAL BENDING AC- TUATOR	48
3.1 Introduction	48
3.2 Physical Embodiment	51
3.2.1 Fabrication	53
3.3 Design	54
3.3.1 FEA modeling of cross-section	57
3.3.2 Sensor Characterization & Model Verification	60
3.3.3 Design Exploration	62
3.4 Closed Loop Control	64
3.4.1 SCAPA Design Selection	64
3.4.2 Empirical Model	64
3.4.3 Controllers	64
3.4.4 System Response	68
3.5 Conclusion and Future Work	69

4. ACTIVE VARIABLE STIFFNESS FIBERS FOR MULTIFUNCTIONAL ROBOTIC FABRICS	73
4.1 Introduction	73
4.2 Previous Work	76
4.3 Materials	77
4.4 Manufacturing Methods	78
4.4.1 Variable stiffness fibers	78
4.4.2 SMA actuator	79
4.4.3 Integration into AVS fiber	80
4.5 Characterization	80
4.5.1 Stiffness Characterization	80
4.5.2 Force and Load Characterization	85
4.6 Applications	88
4.6.1 Single-fiber active lifting and passive holding	88
4.6.2 AVS fabric for conformable robotic skins	92
4.7 Conclusion and Future Work	93
5. A METHOD FOR ROBOTICIZING FABRIC BY INTEGRATING FUNC- TIONAL FIBERS	95
5.1 Introduction	95
5.2 Results	98
5.2.1 Actuation	98
5.2.2 Variable-Stiffness Support Structure	101
5.2.3 Sensing	105
5.3 Applications	106
5.4 Discussion	108
6. ADDRESSABLE, STRETCHABLE HEATING SILICONE SHEETS . . .	113
6.1 Introduction	113
6.2 Manufacturing and Characterization of Heater Silicone sheets	115
6.2.1 Conductive Composite Electrical Characterization	115
6.2.2 Liquid Metal Interfacing and Localized Heating	119
6.2.3 Stretchable Heating	121
6.3 Implementation in Silicone-based Material Devices	123
6.3.1 Stretch-and-Hold Operations	123
6.3.2 Robust, Addressed Spot Heating	127
6.4 On-Demand Shape Change	128
6.4.1 Reversible Shape Change	128
6.4.2 Reversible Hinges	130
6.4.3 2D On-Demand Hinges	132
6.5 Conclusion	134
6.6 Experimental Section	136
7. UNIFORM CONDUCTIVITY IN STRETCHABLE SILICONES VIA MUL- TIPHASE INCLUSIONS	138

7.1	Introduction	138
7.2	Principles of Operation	142
7.3	Material Characterization	146
7.3.1	Electrical and Mechanical Properties	148
7.3.2	Thermal Characteristics and Cyclic Robustness	152
7.4	Applications	153
7.4.1	High Deformation Sensing	153
7.4.2	Solid State, Damage Resilient Actuation	156
7.4.3	Multi-directional single-channel pneumatic soft actuators	159
7.4.4	Pneumatic bladder trajectory change with sensor feedback	161
7.5	Conclusions	164
7.6	Addendum about Generalizability	164
7.7	Materials and Methods	166
7.7.1	Materials and Material Preparation	166
7.7.2	Mechanical and Electrical Characterization	169
7.7.3	Electrodes and Interfaces	170
7.7.4	Capacitive Strain Sensors	170
8.	SUMMARY	172
	REFERENCES	176
	VITA	199
A.	LIQUID METAL SWITCHES FOR ENVIRONMENTALLY RESPONSIVE ELECTRONICS	202
A.1	Introduction	202
A.2	Experimental	205
A.2.1	Depinning Droplets through Oxide Removal	205
A.2.2	Repinning Droplets through Oxide Regrowth	212
A.2.3	Applications	218
A.3	Conclusion	222
A.4	Methods & Materials	223
A.4.1	Contact Angles	223
A.4.2	Goniometry	224
A.4.3	XPS and Sample Preparation	224
B.	ALL-SOFT MATERIAL SYSTEM FOR STRONG SOFT ACTUATORS	227
B.1	Introduction	227
B.2	Background	229
B.3	Manufacturing	231
B.3.1	Silicone Actuator Manufacturing	231
B.3.2	Muscle Assembly and Electrode Contacts	233
B.4	Characterization	234
B.4.1	Manufacturing Implementation	234
B.4.2	Heating and Energy Distribution	237

B.4.3	Force Output	240
B.5	Results and Discussion	243
B.6	Conclusion and Future Work	244

LIST OF TABLES

3.1	Naming convention for the three controllers implementing the control loops in Figure 3.6 and state machines in Figure 3.7.	65
4.1	Bending modulus of ABS- and PLA-based AVS fibers with the stiffening thermoplastic heated ($> T_g$) and cooled (25°C).	82
4.2	Force produced by the SMA actuator portion of ABS-and PLA-based AVS fibers in the softened and stiffened state.	86
A.1	Contact angles of galinstan droplets on various substrates, immersed in either 1M HCl or 1M NaOH.	205
A.2	Surface tension on galinstan droplets in various environments.	211

LIST OF FIGURES

2.1	Pneumatic robot with liquid metal sensors embedded into the body. Above: the robot in its relaxed state. Below: the robot after pneumatic actuation. Scale bars are 1 cm.	34
2.2	3D modeling representations of the molds that were printed to cast the robot. (a) The primary mold, initially filled with liquid elastomer, with an inset showing the embossed channels that create the sensor channels. (b) The channel mold that is placed in the primary mold to create the pneumatic channels in the robot.	36
2.3	(a) The bottom half of the mold is printed and (b) filled with liquid elastomer. (c) The channel mold (previously printed) is embedded inside the liquid elastomer to create the pneumatic channels. When the elastomer has cured (d) the mold can be removed from around it. To finish the sensors, (e) the eGaIn channels are filled with liquid metal and (f) sealed with liquid elastomer. Finally, (g) the pneumatic channels are sealed by bonding the body to a thin layer of Silgard 184.	38
2.4	A preliminary design with the liquid metal sensors directly over the pneumatic channels. The image on the left is the top of the channels before the arm is inflated (the surface is flat), and the image on the right is the same surface, at the same scale, after it is inflated. The liquid metal channels undergo a large increase in both length and width causing an extreme collapse in the channel's third dimension. The box in both photos is surrounding the same section of the sensor. The inset is a magnification of the inflated channel with an outlined area that experienced eGaIn withdrawal due to the channel collapse. The scale bars on both images are 2mm, and the inset has 2.5x magnification.	40
2.5	The pneumatic robot gripping a cylindrical container. The serpentine liquid-metal sensor channels are clearly visible around the outside edges of the pneumatic channels (dark against the white background).	41

- 2.6 A comparison of the strain gauge's percent increase in resistance for one of the robot arms experiencing two modes of strain. The linear extension tests were an application of unidirectional strain to the arm. The error bars are a 90% confidence interval, and the red dotted line is a fit of the data. The other four tests were performed by pneumatically actuating the robot and recording the resistance change, with the solid magenta line representing a linear fit and the blue dashed line representing a curved fit of all the tests. 43
- 2.6 The resistance change in three of the robot's strain sensors during the 5s actuation tests. Each graph (a,b,c) represents a different arm on the robot. The test setup only permitted gathering simultaneous data from 3 arms, though the sensors on all 4 arms were fully functional. The solid red line is the average of the baseline tests (the robot inflating in empty air). The dashed blue line is the average of the tests with the robot gripping the test cylinder at approximately 3 seconds. The shaded area surrounding each line represents a 90% confidence interval. The percent change was calculated using the initial and final resistances of the tests with the robot gripping an object. 46
- 3.1 Sensor-controlled antagonistic pneumatic actuator (SCAPA). (a) Overhead view of a SCAPA sweeping across its full range of achievable curvatures, κ . (b) Due to its fully soft construction, the SCAPA can be rolled up, compressed, and still return to full functionality. (c) Optical microscope image of the interface between the actuator, embedded sensor, and conductive fabric. (d) A cross-section schematic of a SCAPA, including an indicator for the location of the optical image in (c). 49
- 3.2 (a-c) Manufacturing the SCAPA. (a) The capacitive sensors were first fabricated in large films and then laser cut into the desired patterns. (b) The casting process created the pneu-net actuators while simultaneously embedding a sensor in the actuator body. (c) Conductive fabric was glued between two actuators to create the antagonistic bending system and the electronics controlling actuation and measure the sensors were attached to the SCAPA. (d) Photos showing two of the designs explored. The actuator body, sensors, and conductive fabric are clearly visible in the cross-sectional images. (e) For all experiments performed, each SCAPA was fixed vertically such that the tip would sweep horizontally. A camera was situated above the SCAPA to record truth data on its curvature. . . . 52

3.3	Design study to determine the effects of sensor width and placement on the quality of the sensor output. (a) Schematic of the loading conditions for the FEA (left) and cross-section geometry (right), with only the boxed section being modeled. (b) Sketches of the initial modeled geometry and the FEA results. Design 1 shows the base case for the system. Design 2 reduces the width of the sensor and Design 3 moves sensor to the top of the actuator. (c) Experimental verification plots showing the sensor responses to curvature. The circles indicate experimental data and the line is a quadratic fit with the shaded region being a 95% confidence bound about the regression.	55
3.3	Con't from Previous Page	56
3.4	Design exploration of various geometries that should limit the effect of actuator inflation on sensor response. (a) Schematic of the the loading conditions for the FEA (left) and the cross-section geometry (right), with only the boxed section being modeled. (b) Sketches of the initial modeled geometry and the FEA results. Design 4 and 5 introduce a notch along the outer edge of the actuator with the sensor embedded near the fabric layer and on top of the notch respectively. Design 6 increases the distance between the sensor and the pneu-nets by increasing the width of the actuator wall. (c) Experimental verification plots showing the sensor responses to curvature. Design 6 began to twist while actuating resulting in unpredictable sensor responses. The circles indicate experimental data and the line is a quadratic fit with the shaded region being a 95% confidence bound about the regression.	58
3.4	Con't from Previous Page	59
3.5	Sensor calibration results for Design 4 (see Figure 3.4) comparing the actual curvature to state reconstructed curvature. The shaded region represents the 95% confidence interval. The inset shows an inflated SCAPA with a fitted circle used to measure the actual curvature. r is the radius of the circle and κ is the curvature.	63
3.6	Control loops used to follow the input signal.	65
3.7	State machines used in the logic controllers.	66
3.8	Closed-loop curvature control using the Simultaneous, Fixed Rate Quasi-Static, and Varying Rate Quasi-Static controllers, with two different proportional gains in the VRQS controller. Each plot shows the reference signal (black) and the reconstructed curvature (blue - both mean and 95% confidence bounds), and indicates the mean deviation (error) of the system response from the desired curvature for the whole test.	68

- 4.1 Active variable stiffness fabric composed of active variable stiffness fibers sewn onto inextensible muslin fabric. (a) Unactuated, stiff AVS fabric with a hanging 200 g mass. (b) Actuated then stiffened AVS fabric holding a 200 g mass. (c) Unactuated, stiff AVS fabric acting as a bridge supporting a 200 g mass on a small plate. (d) Unactuated, softened AVS fabric sinking under the weight of a 200g mass. Scale bars are 2 cm. 75
- 4.2 Active variable stiffness fibers. (a) Diagram of the composition of an AVS fiber. (b) PLA-based AVS fiber (the PLA core and the SEBS coating are both transparent). (c) ABS-based AVS fiber. Scale bars are 1 cm. 77
- 4.3 Manufacturing ABS-based active variable stiffness fibers. (a) Coating ABS solution onto a heating NiTi wire for variable stiffness fiber. (b) Programming active SMA wire into a helical coil in a 390°C oven. (c) Twisting the programmed SMA wire onto the variable stiffness fiber. (d) Encapsulating the twisted wires with SEBS. (e) Completed AVS fiber. 79
- 4.4 Setup for characterization of AVS fibers. (a) Stiffness characterization using a 3-point bending setup. (b) Force and load characterization setup. Scale bars are 2 cm. 81
- 4.5 Stress-strain plot for two AVS fibers in a 3-point bending setup. A PLA-based and an ABS-based AVS fiber were tested repeatedly in stiff (cold) and softened (hot) states. The shaded area around each average line represents a 95% confidence interval. 82
- 4.6 Stiffness characterization plot for a single ABS-based AVS fiber softened with various currents. At high currents, the SMA actuator begins to activate during the stiffness test resulting in an increased modulus. 84
- 4.7 Plot of force produced by an ABS-based AVS fiber. Hot: VS fiber was softened before SMA actuation. Cold: VS fiber was not softened before SMA actuation. Cold-to-Hot: VS fiber was softened 30 s after the SMA was actuated. The shaded area around each average line represents a 95% confidence interval. 86
- 4.8 Plot of force produced by an ABS-based AVS fiber as a function of applied current. The VS fiber was softened prior to the start of each run. The currents applied ranged from 0.5 A to 1.75 A in increments of 0.25 A. The shaded area around each average line represents a 95% confidence interval. 87

- 4.9 Comparison of an actuation cycle of (a) an SMA wire, (b) a PLA-based AVS fiber, and (c) an ABS-based AVS fiber. The top of the fiber is fixed and a 47 g mass is attached to the hanging end of the fiber. The mass acts as an electrode, with a small copper wire attached to it. From top to bottom: (I) the fiber is not actuated, (II) the fiber is softened and fully actuated, (III) all power is turned off to the fiber, and it is allowed to cool for 15 s, (IV) the fiber is completely cooled. For scale, each square is 1 cm². 89
- 4.10 AVS fabric attached to a cantilevered foam block to create a soft robotic lifting arm structure. One end of the foam block is fixed; the other end is free and supports a 50 g mass. (a) AVS fabric is stiff, (b) AVS fabric is softened and fully actuated, (c) AVS fabric is stiff and cooling, and (d) Robotic arm structure sustaining mass for extended period of time with no additional power input. Scale bars are 2 cm. 91
- 5.1 Robotic fabrics. (A) Rendering of a potential robotic fabric capable of locomotion. (B) Actualized robotic fabric demonstration. (C) Current robotic fabric vs rendering of potential fully-woven robot. (D) Fiber-form robotic components (from the left: sensors, actuators, and structural supports) can be combined in a variety of ways to create thin fabric-based machines. 97
- 5.2 Shape memory alloy actuator ribbons. (A) SMA ribbon programmed to exhibit bending motion. (B) Sewn SMA ribbon used to actuate fabric body. (C) Couching method to affix SMA ribbon to a fabric substrate. (D) Initial round SMA wire. (E) Flattened SMA ribbon. (F) Bending an SMA against its programmed direction induces higher flexural stress and encourages the wire to twist instead. Error cloud is 95% confidence interval. (G) Round and flattened wires were subjected to forces at increasing out-of-plane angles to determine bending response. (H) A flattened ribbon will tend to bend and buckle in plane (green), and a round wire will tend to twist and bend out of plane (red). (I) Round SMA actuators tend to generate higher bending force than flattened actuators of comparable cross section. Error bars are one standard deviation. 99

5.3	Variable stiffness fibers. (A) A shaped VS fiber supports a 20 g load. (B) VS fiber sewn onto a fabric substrate. (C) Added support from fabric allows VS fiber to support up to 50 g before legs begin slipping. (D) Neat epoxy VS fiber. (E) Neat epoxy cross-section. (F) FM composite cross-section. (G) FM composite VS fiber. (H) Hot and cold flexural modulus for both the neat epoxy and FM composite (46 vol% FM), with and without stainless steel yarn core used for Joule heating. Error bars are standard deviation. (I) Ultimate flexural strength of the VS fibers. (J) Measured thermal conductivity of the composite vs. vol% of Field's metal, compared with Bruggeman effective medium theory. Error bars are 95% confidence interval. (K) Free convection cooling of VS fibers. Experimental data is for neat epoxy specimens. Numerical simulations for both neat epoxy and FM composite had negligible difference. Inset shows computed cross-sectional thermal gradient for both 0 and 50 vol% FM fibers after 7 s of cooling from 65°C. (L) Numerical simulation results for 'worst case' heating scenario, with the heating core center offset to 2/3 of the VS fiber diameter. Inset shows computed cross-sectional thermal gradient after 6 s of heating at 13W/m.	103
5.3	Con't from Previous Page	104
5.4	Conductive ink sensors. (A) The carbon-black/PDMS/ethanol emulsion is printed directly onto the fabric. The surface conductivity is sufficient such that printed sensor blocks can be electrically connected by sewing over them with conductive thread. (B) A microscope image of ink-coated knitted spandex fabric. (C) Porosity measurement of neat, unstrained fabric. (D) Porosity of inked fabric. (E) Porosity of inked fabric after stretching. (F) A simple actuator-sensor device curls up and down, generating a sensor signal dependent on device curvature. (G) The curling device follows the control signal by modulating the power output to the SMA actuators. Each sensor is actively used only when the corresponding fabric face is in extension.	107

- 5.5 Robotic fabric demonstrations. (A) Robotic fabric tourniquet. (B) Tourniquet is buttoned about a foam body. It reacts to a damaged circuit by contracting and holding a tightened pose. (C) Thermal image of the tourniquet as VS fibers soften. (D) Thermal image of activated SMA actuators constricting. (E) Robotic fabric “popup” table. (F) From an initial flat state, the table is able to stand up, stiffen into a load-bearing platform, and then collapse under a load as it softens and actuates back into its initial flat configuration. (G) Fabric “popup” table is approximately 2 mm thick. (H) Activation and softening of table “leg” VS fibers. (I) Activation of SMA actuator wire, causing table to stand up. (J) Robotic fabric wing in self-stowed position. (K) Robotic fabric wing curls and uncurls from deployed, open state into a compacted, stowed state. (L) Robotic fabric wing in deployed position. (M) Activation and softening of wing VS fibers. (N) Activation of curling SMA wires. 109
- 6.1 Manufacturing steps and electrical characterization data from the strain tests performed on high aspect ratio samples of the heater silicone. a) Multiple layers of EIG composite silicone are deposited onto a neat silicone backbone to create the heater silicone sheet, and samples are cut out of the sheet with a laser cutter for electrical testing. b,i) An example of a cyclic test dataset (sample design parameters: 10 cm x 1 cm, 35 wt% EIG, $n = 2$ layers). b,ii-b,iii) cyclic tests focusing on 10% and 15% strain (10 cm x 1 cm, 15 wt% EIG, $n = 2$ layers) with the same y-scale and color distinguishing test cycles (1st cycle always omitted). c,i) Representative resistance-strain curves from heater silicone samples (10 cm x 1 cm, $n = 3$ layers) with different concentrations of EIG. Curves show the final 10 repetitions of a 50-cycle test (steady-state response). c,ii) Sheet resistance of unstrained heater silicone with different concentrations of filler and increasing numbers of layers. 117
- 6.2 Two different liquid metal channels cast into the heating silicone, and their corresponding effect on the way the material heats up. a) Top: Two parallel line electrodes create a heat ‘patch’ over an area. Middle: Liquid metal channels ending at point create a point of heat. Bottom: photographs showing the copper wires cast into the silicone to create the channels. b) The left column has a semi-transparent IR image overlaid on a visible light image of the heater silicone/liquid metal line pattern. The right column is a zoomed in view of the IR image. 120

- 6.3 Results from cyclic strain tests while Joule heating samples of heater silicone. a) The normalized, average resistance of the sample in each cycle, as well as the average power required to Joule heat the sample, presented against the cycle number. The plateau in the resistance curve and the flat power consumption indicate good sample health throughout the tests. b) IR images of one of the samples tested, at 0% strain and then at the maximum strain (40% strain) over the 1000 cycle period, showing little-to-no degradation in the sample's ability to evenly heat. Sample heating area is approximately 3 cm x 1 cm at 0% strain. 122
- 6.4 'Stretch and hold' shape change. a) Manufacture of the temperature-sensitive wax-silicone composite which leverages the low temperature phase change of wax to hold a new length when cooled while stretched. b,i) a sample of heater silicone bonded to wax silicone used for this demonstration, with inextensible tabs to allow for an even straining of the heater silicone while reinforcing the liquid metal electrical contacts. b,ii-viii) the sequential steps as the system starts from cooled state, is heated to melt the wax silicone, stretched, cooled to solidify the wax silicone, allowed to relax (with the wax silicone holding its extension), and then reheated to re-melt the wax silicone and restore it to its unstrained state. 124
- 6.5 a) A visible light image of our fully soft 2D addressable heater composed of a heater silicone square with liquid metal electrodes. b) Manufacturing the 2D addressable heater pixel interfaces by adding a droplet of heater silicone at the location of interest on the wire molds. The liquid silicone seeps under the wire separating the rest of the liquid metal channel from the conductive composite. c,i) The 2D addressable heater with a temperature-responsive silicone laid on top (visible and IR images). c,ii) The addressable heater functions even when warped/flexed during operation (visible and IR images). c,iii) a higher-density board with 36 pixels (6x6) in the same form-factor as the 4x5 board, showing several letters. c,iv) The 6x6 board remains active while experiencing a large deformation stress. d) Visible light images of the automated system printing out the letters "HELLOWORLD" consecutively, and IR images of other letters captured, and organized to spell "FABORATORY". 126

- 6.6 Reversible shape change. a) Manufacturing the heater silicone sheets with bonded variable stiffness elements (PLA). b) Heater silicone bonded to PLA is Joule heated enabling shape changing and holding operations in the PLA. b,i) The bond keeps the silicone connected to the PLA even when compressed and stretched. b,ii) A 90° fold in the variable stiffness sheet. Inset shows the shape-memory recovery of the material when Joule heated again. b,iii) The bonded system is given a permanent twist, with IR images of the sample as it is heated and cooled into the twisted shape. c) A second sample of the material undergoing a much tighter twist & hold (360°). After reheating, the PLA showed permanent warping. The heated system was then was crumpled to produce additional folds, twists, and bends, demonstrating the continued functionality of the heater silicone. 129
- 6.7 1D pixelized addressable variable stiffness system. a) Schematic of the system demonstrating the various components allowing for addressable variable stiffness. b) IR images of the PLA side of the functional system with each pixel heated above the glass transition temperature ($\sim 62^\circ\text{C}$), showing the capability of a digitally controlled system to heat various pixels simultaneously. c) Visible light photo of the addressable system. d) The system undergoing shape-changes into two load-bearing forms (see ii. and iv.) through heating of individual pixels. Insets in ii. and iii. show that the addressed pixel is the only heated point, allowing the system to be folded by a single finger. e) All pixels activated allowing the system to relax and be flattened into its original shape. f) The system, once cool, is again load bearing. 131
- 6.8 a-b) An unprogrammed variable stiffness sheet is heated using the 4x5 pixel heater to create artificial folds. a,i) The sheet laying on the heater. a,ii-iv) Top-down IR images showing the heated folds on the sheet. b) Images of the sheet in i) its initial state, ii-iii) intermediate states, and iv) final airplane-like shape after being cooled. c,i) PLA sheet bonded to a 6x6 pixel heater silicone sheet. c,ii-iv) The PLA sheet is bent (and flattened) along lines not previously defined in the polymer block, simply by heating a selection of pixels that make up a line with the heater silicone sheet. In both ii) and iii) the top view and a side-profile view of two successive bends are presented, along with an IR photo just before the bend occurred with the PLA sheet outlined. iv) An isometric view showing multiple bends in the same sheet, as well as an isometric view of the initial straight-line bend on the bottom (with its associated IR image). All IR images show temperatures up to 90°C. All PLA sheets are 4 cm x 5.5 cm. 133
- 7.1 An activated 4×16 cm sample of MPC being simultaneously twisted and stretched, while maintaining a consistent, uniform Joule heating profile. The sample is fully encapsulated in silicone. 141

7.2	Principles of operation of the MPC. a) Schematic compares pre- and post-stretch structures of three composite materials of LM-SE [192, 204], SE-EIG [128], and LM-SE-EIG (left to right). In the left column, although some microcracks appear on the surface of the LM-SE composite while being stretched, a conductive pathway through the whole structure does not form. In the middle column, the majority of conductive pathways in the SE-EIG composite are lost due to macroscopic cracks forming in the material. In the right column, the EIG facilitates microcracks in the LM-SE-EIG composite during stretching, which creates conductive pathways throughout the structure (activation). b) mm- and μm -scale images show the surface features of the three composites as cast, while stretched, and relaxed post-stretch. Light reflections from the microscope are visible on the LM beads expelled from the LM-SE-EIG surface. c) Optical and thermal images of samples of the three aforementioned composites Joule heated with electrical current at rest and stretched states, after a one-time ‘activation’ event. Temperature variance is used to view the resistance uniformity, as higher resistance areas generate more heat when a current is passed through the system.	143
7.2	Con’t from Previous Page	144
7.3	Electrical and mechanical characterization of MPC silicone. a) Electrical resistivity of the MPC after stretch as a function of LM and EIG volume fractions. Truncated pyramids show the compositions with electrical conductivity and full pyramids show the non-conductive compositions. b-c) Electrical resistivity of MPC silicone pre- and post-activation. b) LM 60%-SE 40% composition, varying the EIG volume fraction. c) EIG 1% composition, varying the LM-SE volume fraction. d) Mechanical testing of unactivated MPC (LM 60%-SE 40%, no backing layer), with 0.5%, 1.0%, and 2.0% volume fractions of EIG showing the elongation at break. e) Cyclic loading of MPC silicone (LM 60%-SE 40%) with 1.0% volume fraction of EIG. The material displays a Mullins effect at the first loading cycle at each strain. The stress is significantly smaller in the next cycles at the same strain level. f) Activation process of the MPC at two strain rates of 5%/s and 25.0%/s. Five samples at each speed are stretched up to 250% strain for the first time and the resistivity change is recorded. The material begins activating at lower strains when stretched with a higher strain rate. A representative plot of resistance drop for a sample is shown in Figure S3. Error bars in b and c, and shaded regions in d and f represent ± 1 standard deviation.	147

- 7.4 Thermal characteristics and cyclic robustness. a) Temperature of a $40 \times 10 \times 0.4$ mm activated MPC silicone sample supported with a 1 mm thick backing layer while being Joule heated with 0.5 A, 1.5 A, and 2.5 A for four minutes at 0% strain. The sample was then allowed to cool for six minutes at room temperature. Additionally overlaid is the same sample heated with 2.5 A at 100% and 200% strain. b) Resistance change of a MPC silicone sample ($30 \times 10 \times 0.4$ mm) cycled 10,000 times to 200% strain. Inset shows 30 s of cycling. c) IR images of the sample heating up with electrical current of 2.2 A before and after the cyclic test, showing no visible decrease in uniformity inside the main body. 151
- 7.5 Response of MPC strain sensors. a) Comparison to SE-EIG capacitive sensors [59], as measured using our charge-integration capacitance measuring circuit over 10 cycles. Normalized response is highly stable across all eight MPC sensors, while each of the three graphite sensors behaved similar over strains lower than $\sim 60\%$ but had large inter- and intra- specimen variation at high strains. b) MPC sensors stretched to 200% for 1000 cycles. Three sensors are plotted individually, showing high linearity and that they mainly differ in their intercept and slope. Dashed lines represent the mean over 10 cycles. Shaded regions in both plots represent ± 1 standard deviation. 155
- 7.6 MPC silicone damage resilience. a) MPC silicone shown to be conductive before and after being cut into pieces. b) Cross-sectional diagram of the actuator system, with photograph inset of the same. c) Joule heating the MPC boils the ethanol trapped in the silicone core. The resulting expansion is controlled by the fiber reinforced silicone wrap, resulting in a 46% maximum elongation of the actuator. (Inset) The solid-state nature of the system allows for easy electrode creation by piercing the system with a pin. d) Both the actuator and the MPC silicone heater are agnostic to being cut in half, and, once the electrodes are restored, the system can continue to produce a 25% elongation. 158
- 7.7 MPC silicone applied as a heater on a stretchability-changing pneumatic bladder. a) Front view of the pneumatic bladder, along with an IR image showing the MPC increasing the temperature sufficiently to melt the metal particles inside the Field's metal silicone (FMSi) bladder wall. b) Cross-sectional diagram of the actuator. c) Still frames (both IR and visible light) of the trajectory-changing pneumatic bladder cycling through different trajectories enabled by selectively heating the bladder's walls. 160

7.8	MPC silicone applied as a heater and a sensor on a stiffness-changing pneumatic bladder. a) Schematics and photographs of the cross section of the pneumatic bladder. Inset scalebar is 1 mm. Silicone glue layers are not shown in the schematic unless they serve an additional functional purpose b) Visible light and IR photographs of the sensorized bladder at various times, along with graphs of the raw sensor response as the system undergoes both temperature and pressure changes.	162
A.1	The evolution of the contact angle and droplet profile for a galinstan droplet placed on a flat PDMS in either a 1M HCL or a 1M NaOH bath. It should be noted that the last frame of the NaOH shows the droplet completely depinned (it has begun rolling).	206
A.2	Experimental method for comparing galinstan oxide removal rates by HCl and NaOH. Large droplets of galinstan are placed on a PDMS substrate (a), and allowed to sit for 24 hours. The liquid metal inside of the droplet is then removed (b), causing the solid oxide layer to develop a visible texture (c). When the textured oxide is immersed into a chemical etchant bath (d), the exterior of the oxide begins to dissolve until the original, reflective surface is restored (e-f). The time it takes to move from (d) to (e) depends on the chemical etchant used, and the insets for (c) and (f) show examples of textured droplets treated by either HCl or NaOH, along with the time required to remove the visible oxide. We tested the removal rate of the oxide at several concentrations, and present the data in logarithmically scaled plots (g-h). The data gathered by Xu et al. using rheometry (in HCl) [247] is presented alongside ours, as validation of our method. Scale bar is 4mm.	209
A.3	In 4d/Ga 3d/Sn 4d XPS spectra obtained from the two samples that were treated with NaOH (top panel) and HCL (bottom panel). Two spectra in each panel obtained following short rinsing (bottom spectrum) and soaking for 24 hours (top spectrum).	215
A.4	Changing contact area between a galinstan droplet and a glass substrate in water. The droplet was initially removed from the substrate using a 1M NaOH solution. The NaOH was replaced with clean water, and the droplet collapse was observed for 4 hours. The inset shows the droplet's initial and final states in the water.	218
A.5	Controlling the location and fixity of a liquid metal droplet. a) The droplet is pinned to the substrate in air. b) Submerging the droplet in 1M NaOH causes the droplet to depin. c) The depinned droplet moves under gravitational force. d) The droplet is repinned to the substrate through an H ₂ O bath. e-h) shows photographs of the active test, matching the diagrams in a-d). Inset boxes are approximately 3mm x 3mm.	219

A.6	Opening and closing a circuit via chemical manipulation of a liquid metal droplet. a-d) Schematic representation of the side profile of the droplet during one Air-NaOH-Water-Air treatment cycle: a) initial state, b) submersion in 1M NaOH disconnecting the circuit, c) replacing the NaOH with water encourages the droplet to collapse, d) the droplet is dried re-connecting the circuit. e) A photograph of the environmental chamber and LED used for this test (for scale, the LED is 3mm dia). h) A series of photographs of the LED with power supplied to the circuit during two consecutive cycles. i) Close up views of the droplets in the chamber when power was supplied, along with f) the chamber environment and g) a measurement of the resistance across the chamber's leads, during the two consecutive cycles. A video of the droplet profile during a third cycle is available in the Supporting Information.	221
B.1	All-soft heater/actuator being used as a McKibben-like muscle. The actuator is lifting its DC power supply, whose mass is greater than 200x that of the actuator.	228
B.2	All-soft actuator operation. Heating the core causes the external silicone to expand as the ethanol droplets trapped inside boil.	230
B.3	Manufacturing the all-soft silicone based actuator. (a) A silicone-ethanol mixture is poured into a mold to cure, creating a cylindrical actuator with a hollow core. (b) To make the heater core, part B is mixed with an EIG-ethanol mixture, set under an airflow until nearly dry, and then part A is mixed in. Before it cures, the silicone-EIG composite is injected into the hollow core of the actuator. (c) The ends of the actuator are sealed with silicone and liquid metal is injected into the joint at the end of the heater composite. Finally, a pin (or copper wire) is inserted into the liquid metal bead to create an electrical connection to the heater core.	232
B.4	Macro- and microstructure images of the all-soft material system for actuators. (a) SEM image of the soft heater composite. (b) SEM image of a silicone/heater interface cross-section. (c)-(f) macrostructure of actuator composites after preparation with different mixing modes and rates: (c) hand mixing for 4 min, (d) mixer machine mixing for 0.5 min, (e) mixer machine mixing for 1 min, (f) mixer machine mixing for 3 min (scale bars are 500 μm). All-soft actuator composite before (g) and during (h) hand-stretching, showing 50% linear strain extension in the core.	235
B.5	CAD diagrams and photographs of the various heater core geometries. (a) A cut-away of the CAD rendering of the three-part mold. (b) Models of the four different cores used in the mold. (c) Cross-sectional photographs of three of the resultant heater core/actuator combinations.	237

- B.6 IR images of several Joule heating experiments using 9 W of input power. (a)-(b) Two silicone heater composite cores are compared with a Ni-Cr wire heater via encapsulation in pure silicone. (a) At 2 min, the X-shaped core is distributing its heat better to the exterior of the silicone, when compared to the other two systems. (b) The same cross section achieves an external temperature of $\sim 78^{\circ}\text{C}$ two minutes faster than the other systems. (c) The Ni-Cr wire heater compared with (d) the X-shape core, encapsulated in the actuator composite in their initial (cool) and final (heated) states. Scale bars are 1 cm. 239
- B.7 Blocked force setup and test. (a) A Ni-Cr wire heated actuator. (b) The same actuator inside a mesh sleeve for use as a McKibben-like muscle. (c) The actuator installed in a blocked force test. Insets show the Joule heated actuator at its maximum force and then after complete failure (due to melting the external mesh). 240
- B.8 Blocked force test results for the McKibben-like muscles. (a) The measured results of the force output of several all-soft muscle designs, compared with a Ni-Cr wire heater. Error bars represent 95% confidence. (b) Characteristic curves from the build up of force in the actuator muscle over time for three examples of different heater types. The 9 mm core and Ni-Cr wire, with nearly identical resistances, heat up at nearly the same rate, whereas the 7 mm core (with a higher resistance) takes longer to heat up. 241

ABSTRACT

Bilodeau, R. Adam Ph.D., Purdue University, May 2020. Designing Multifunctional Material Systems for Soft Robotic Components. Major Professor: Rebecca Kramer-Bottiglio, School of Mechanical Engineering.

By using flexible and stretchable materials in place of fixed components, soft robots can materially adapt or change to their environment, providing built-in safeties for robotic operation around humans or fragile, delicate objects. And yet, building a robot out of only soft and flexible materials can be a significant challenge depending on the tasks that the robot needs to perform, for example if the robot were to need to exert higher forces (even temporarily) or self-report its current state (as it deforms unexpectedly around external objects). Thus, the appeal of multifunctional materials for soft robots, wherein the materials used to build the body of the robot also provide actuation, sensing, or even simply electrical connections, all while maintaining the original vision of environmental adaptability or safe interactions. Multifunctional material systems are explored throughout the body of this dissertation in three ways: (1) Sensor integration into high strain actuators for state estimation and closed-loop control. (2) Simplified control of multifunctional material systems by enabling multiple functions through a single input stimulus (*i.e.*, only requiring one source of input power). (3) Presenting a solution for the open challenge of controlling both well established and newly developed thermally-responsive soft robotic materials through an on-body, high strain, uniform, Joule-heating energy source. Notably, these explorations are not isolated from each other as, for example, work towards creating a new material for thermal control also facilitated embedded sensory feedback. The work presented in this dissertation paves a way forward for multifunctional material integration, towards the end-goal of full-functioning soft robots, as well as (more broadly) design methodologies for other safety-forward or adaptability-forward technologies.

1. INTRODUCTION

1.1 Soft Robotics

We can see, in the natural world around us, many highly deformable materials that enable biological organisms to adapt, change, and perform delicate tasks in a way that few of our rigid machines can. So, taking inspiration from natural systems that can materially adapt or change to their environment, a new path to robotics design is opening with the aim of applying deformable materials in a new array of ‘soft robotic’ systems. By using flexible and stretchable materials in place of fixed components, soft robots can have built-in safety mechanisms for robotic operations around humans and other delicate objects, as well as natural adaptability when operating in unstructured environments. To fully capture this end goal, today’s soft robotics design, development, and manufacture requires its own, unique, materials-focused paradigm. This is because soft materials are usually given the ability to perform a function during material casting either via a prescribed, path-controlling shape, or via gradients in material properties throughout the body.

It is relatively easy to define a separate robotic component to perform different functions, and then combine those components together to create the final robot. In the more common field of rigid robotics, this is seen as having a motor for actuation, an inertial measurement unit (IMU) to provide 3D acceleration tracking, and a chassis that holds the components together. In soft robotics, this same trend can be observed as novel soft actuators, sensors, or load bearing materials are created and then frequently demonstrated in a void, *i.e.*, with only a single functional capacity. Though this design philosophy (manufacture each component separately, then integrate them) seems so easy for rigid robotics, it would be the downfall of feature-complete soft robots. Since each structural component is made of soft materials,

adding additional mass via tacked-on actuators or sensor often results in a system that cannot lift its own weight, let alone perform a task. Thus there is a new drive to hybridize materials into a multifunctional composite that enables actuation, sensing, structure, trajectory control, heating, and/or electrical transmission in a single composite. Reduced materials translates to a savings in space, power, and, if the materials can have built-in logic, even a reduced load on the soft robotic controller.

My objective has been to build materials with a system of functions, all interconnected, reducing component count for final soft robotic technologies. To meet this objective, I have studied, created, and improved different ways to design composite functional materials for soft robotics. Often, as will be presented throughout this dissertation, I have made them through additive manufacturing of materials into a bulk system. Finding a way to use a common composite matrix, or a strong material binder, has been crucial to creating robust multifunctional materials that integrate together. This reduces the potential of material failures at the composite's interfaces, a common problem in anisotropic composites. A second key has been the development and integration of multiphase (solid-liquid or liquid-gas) composites into soft robotic components. All this has allowed for complex material segments with tailored, adaptable function and form, creating soft robotic components out of multifunctional materials.

1.2 Summary Outline of Thesis

This document is composed of chapters, which are each, individually, a published paper. The chapters are laid out in blocks that encapsulate a particular theme or objective, often as the papers built upon each other. Each block is introduced with a small summary before the next chapter begins. What follows is a holistic summary of the blocks and their overarching focus.

The first block comprises chapters 2 and 3, and focuses on the heavy coupling of manufacturing and design in soft robotic technologies. These chapters shine a light

on the importance of design decisions when choosing to integrate sensor systems into an as-cast manufactured actuator. In both chapters, a system is developed so that sensors can be directly integrated into the body of a soft robotic actuator, and provide feedback on the actuator’s position (and not just stimulus). The work in chapter 3 builds on the work of chapter 2 in many ways, most importantly by demonstrating closed-loop control of the actuator using the embedded sensing.

The second block comprises chapters 4 and 5, and focuses on multifunctional textiles for use as potential soft robotic components. Since fabrics are soft, conformable, and very common, an overarching goal in this block was to interconnect this common material into the soft robotic multifunctional material ‘toolbox.’ This goal starts in chapter 4, which details the design of a single, multifunctional fiber that contains both actuation and stiffness control, and integrates this fiber into a fabric substrate. Chapter 5 separates out these two components into different fibers, in order to simplify additional customization of each fiber’s material and design. This allows for a significant enhancement of both the actuation and stiffness switching in the textile, while also facilitating the addition of sensing and feedback control to the now-functionalized textile.

The third block comprises chapters 6 and 7, and focuses on thin, multi-layer material composites that allow for thermally controlled multifunctionality in solid-body material systems. Chapter 6 introduces the idea of planar sheets of stretchable silicone that can be electrically addressed for selective thermal control of nearby materials. Chapter 7 then expands further on this conductive silicone sheet, enhancing the stretchability such that it is capable of advanced performance as both a heater, conductor, and sensor, in a sub-millimeter thick sheet.

Note on Appendix A: A eutectic alloy of gallium and indium (sometimes with tin included) is a room-temperature liquid metal used in much of the work performed herein (as either eutectic gallium-indium [eGaIn] or as eutectic gallium-indium-tin [galinstan]). This alloy is a particularly powerful tool in soft robotics, as it allows for metal-like electrical conductivity in a fluidic body. This material has many unique

properties, including a near instantaneous oxidation of the gallium to create an inert shell around the liquid. Appendix A is an additional published paper where this material is studied in greater depth, particularly with regards to manipulation of this external oxide layer.

Note on Appendix B: The uniform joule-heating composites created in chapters 6 and 7 have potential applications beyond solely planar, skin-like heating. This appendix is an additional published paper where the conductive composite (specifically the composition discussed in chapter 6) is used as a heating core inside of a cylindrical expansion actuator. Since the heater is a bulk material, it was formed into various shapes and sizes in order to facilitate the transfer of the thermal energy into the actuator for improved actuator responsiveness.

Note on ‘Supporting Information’: Since the bulk of this dissertation is previously-published, peer-reviewed material, the text often refers to images, data, and videos that are contained in “supporting” or “supplemental” information. This supporting information is available online, for free, from the respective publishers of each paper.

1.3 Contributions

This dissertation presents a number of intellectual contributions to the field of soft robotics. These include multifunctional material design guidelines for both enhancing sensory feedback and reducing input requirements, and synthesizing novel materials with greatly enhanced material properties for thermally responsive soft robotic applications. In detail, I have contributed the following:

- A series of guidelines for embedding sensors in soft actuating robots. My work demonstrates the value of embedded sensing and provides a design framework so that the actuator’s input stimulus has a greatly reduced impact on the sensor. I show that following these guidelines improves the ability to track the actuator’s

output response to its input stimulus, facilitating closed-loop control of the actuator's output response.

- Control over materials with multiple functions via a single input stimulus. This idea is initially embodied in a fiber-form that is tangentially integrated onto a textile. Then, this idea is broadened to encompass manipulation of an active-fiber fabric system as a whole.
- A new mechanism that enables uniform liquid networks embedded in a soft silicone elastomer. The mechanism involves adding solid and liquid inclusions directly into the silicone during casting, and then straining the whole material. The solids act like stress concentrators, nucleating internal failures that are then filled in by the encapsulated liquid, resulting in a continuous liquid network throughout the material. The uniformity of the liquid networks are demonstrated by use of a room temperature liquid metal that creates an elastomer with uniform electrical conductivity, which is then employed as stretchable electrodes and Joule heaters.

Introduction to Block 1:

This is the first block of work, comprising chapters 2 and 3. This block focuses on presenting a series of three guidelines on embedding sensors into soft actuators. The first guideline tackles the question of value: is embedding sensing into actuators worth the increased manufacturing complexity required to do so? The process of integrated sensing, demonstrated through two different projects, will help designers do a mental cost-benefit check to see if embedded sensing is worth the effort for their specific product goal. The second guideline covers the design principles that will help with sensor placement in the actuator body, providing a framework and examples of how to analyze the actuator’s construction and body to find ideal locations for embedded sensors. The third and final guideline is an overarching demonstration that multiple types of strain sensors can be embedded in soft bodies (examples shown are resistive and capacitive), and that the choice of sensor can reduce the complexity of disentangling the sensor’s response to output and input.

I demonstrate the value of this type of sensor-actuator integration by incorporating sensing directly into silicone actuator bodies. I show that this multifunctionality reduces some of the manufacturing steps required to build a responsive actuator (while increasing others – a potentially net-neutral benefit), but that doing this also adds more value through reduced part counts, improved internal material boundaries (no glue/adhesive required between sensor and actuator as a potential source of failure) while fixing the sensor’s position relative to the actuator, reduced assembly steps, and a sensor response that is highly intertwined with the actuator’s state. Another potential benefit, though not directly demonstrated but can be inferred from the work done herein, is that embedded sensing can also reduce impact on actuator performance. Additionally, in both of these works I show that following the traditional design choice of “add the sensor where the strain is highest” may result in non-ideal sensor feedback. Instead, the sensors need to be carefully placed in the actuator body in such a way as to isolate them from the actuator’s input stimulus. This often means placing the sensors in the location where the strain is significantly lower, but is

more responsive to the actuator’s output shape deformation than its input stimulus. The interconnection of the actuator and sensor response can be observed using FEA modeling, enabling iteration through many geometric design possibilities. Finally, specifically through the second project, I demonstrate that careful selection of the type of sensor (using a capacitive sensor rather than a resistive sensor) can greatly improve the feedback decoupling just discussed, and also potentially simplify the FEA model requirements (so more designs can be iterated on faster). Understanding these design guidelines, demonstrated through two different case-studies, will greatly facilitate the success of multifunctional actuators with baked-in sensory feedback. What follows are two abstracts for the chapters, summarizing the work therein.

In chapter 2, I present a fluidically functionalized soft-bodied robot that integrates both sensing and actuation. Rather than combining these functions as an afterthought, I designed sensors and actuators into the robot at the onset, both reducing fabrication complexity and optimizing component interactions. I utilize liquid metal strain sensors and pneumatic actuators embedded into a silicone robotic gripper. The robot’s body is formed by curing the silicone in complex 3D printed molds. I show that the liquid metal strain gauges provide a repeatable resistance response during robotic actuation. I further show that it is possible to determine when the robot begins gripping an object during actuation.

In chapter 3, I build on the work done in chapter 2 by designing sensor-controlled antagonistic pneumatic actuators (SCAPAs) that integrate soft robotic actuators and sensors into a simplified, controllable design. The antagonistic actuators together compose a bidirectional bending actuator with embedded capacitive strain sensors. By designing the SCAPAs from the ground up for closed-loop control, I was able to minimize both the number of constituent components and the types of materials used, and further streamline the manufacturing processes. These improvements are embodied in the multipurpose use of a single conductive fabric sheet for both actuation and sensing, integrated into an otherwise all-silicone device. Such reduced material complexity allows us to use simple finite element analysis (FEA) models to predict the

performance of a given design. After converging on a final design, I demonstrate that this design enables the use of simple control strategies to achieve closed-loop position control over the actuator. This ends the two-chapter set of work that demonstrates the true power of soft, material-based solutions to complex problems (*i.e.*, actuation and positional feedback in a single body for closed-loop control). These two works show that it is possible to design the materials to have multiple functions, by integrating various soft material components into a single, unified system. And, by so doing, reduce either manufacturing or design complexity.

2. MONOLITHIC FABRICATION OF SENSORS AND ACTUATORS IN A SOFT ROBOTIC GRIPPER

The following chapter is based on work previously published as [1] R. A. Bilodeau, E. L. White, and R. K. Kramer, “Monolithic fabrication of sensors and actuators in a soft robotic gripper,” in 2015 IEEE/RSJ International Conference on Intelligent Robots and Systems (IROS), 2015, pp. 2324–2329.

Copyright ©2015 IEEE, reproduced with permission.

2.1 Introduction

Researchers in robotics are beginning to diverge from the traditional rigid robots that are so prominent in manufacturing. Engineers in the emerging field of soft robotics are working on solving problems that cannot be solved easily with rigid robots, including improving human-robot interactions, developing formable robots that can adapt to varying geometric constraints, and robots that can absorb impacts/shocks by deforming their main body. Silicone-bodied pneumatic robots have helped to shape the idea of a truly “soft” robot, since most of the body is formed out of a soft, elastomeric material with an extremely low stiffness [2]. Many of the silicone elastomers used in soft robotics are capable of sustaining strains anywhere from 100-500% [3]. Since these elastomers are highly deformable, engineers can inflate internal pneumatic channels to provide rigidity and stability to the robot. With the proper configuration, such robots can use their pneumatically actuated components to gain form, function, and even locomotion [2–4].

One of the challenges associated with soft robotic design is adding sensors that can close the robotic control loop. Researchers are actively working on soft-bodied control methods [5–7], but lack general proprioceptive feedback sensors for soft robots. Since soft robots undergo extremely high strains during actuation, traditional feedback

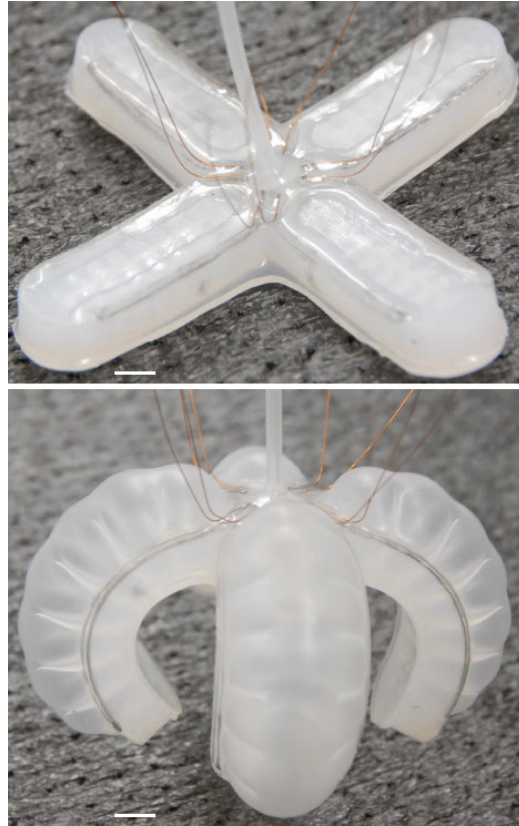


Figure 2.1. Pneumatic robot with liquid metal sensors embedded into the body. Above: the robot in its relaxed state. Below: the robot after pneumatic actuation. Scale bars are 1 cm.

systems either break or are difficult to attach to the robot. One solution to high deformation strain sensing has been to create a strain gauge made out of a room-temperature liquid metal embedded in an elastomeric matrix [8, 9]. These strain gauges can be an effective way of gathering data in some robots [10], but the issue of attaching the gauges to the robot remains an open problem.

In this paper, we present a manufacturing process that incorporates liquid metal strain sensors directly into the body of a 4-arm, pneumatically-actuated, soft robotic gripper (see Figure 2.1). This is in contrast to previous work where the sensors and actuators are built separately and integrated afterwards. In the robot, each strain sensor is independent of the others and capable of providing real-time feedback about the actuation of the arm of the robot. The feedback from the sensors can be characterized in a way that distinguishes activated states of the robotic gripper and, given control over other actuation parameters, makes it possible to determine if the robot is gripping an object or not.

2.2 Previous Work

A pneumatically-actuated soft robot was described in detail by Shepherd, et al. [2]. This robot was actuated through pressurization of internal cavities called “pneunets” formed within a highly elastic polymer body. This work has been extended by researchers who have all primarily focused on improving actuation. Great strides have been made in improving the speed of pneumatic actuation [3, 11] and in untethering pneumatic robots from an external compressed air source [4, 5]. Other researchers have created soft-hard hybrids that take advantage of the strengths associated with both rigid robots and soft pneumatically-actuated robots to perform tasks that neither can do alone [12].

Sensors for soft robotic systems have also been an area of recent research, as they provide state reconstruction that allows for control feedback. One approach to sensing in soft-bodied systems is with eutectic gallium indium alloy (eGaIn) encased in

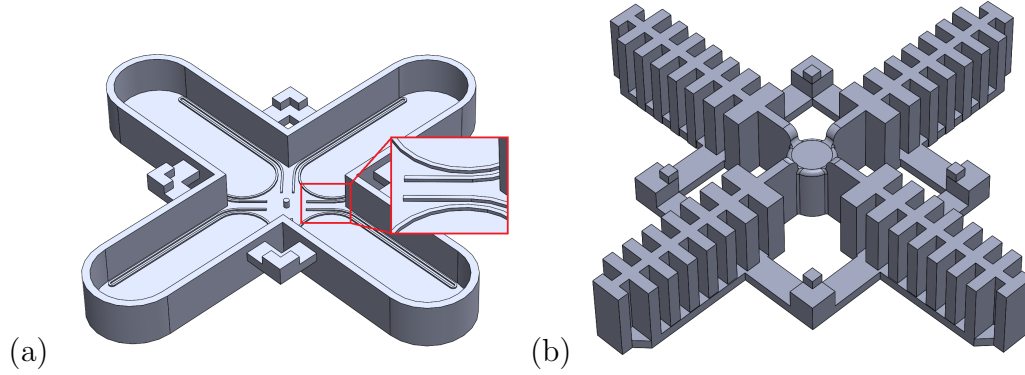


Figure 2.2. 3D modeling representations of the molds that were printed to cast the robot. (a) The primary mold, initially filled with liquid elastomer, with an inset showing the embossed channels that create the sensor channels. (b) The channel mold that is placed in the primary mold to create the pneumatic channels in the robot.

microchannels within a highly elastic substrate. Gallium indium alloy is a room-temperature liquid metal that is non-toxic and highly conductive [13, 14]. The basic principle behind these high displacement strain gauges is simple: as the elastomer is stretched, the length of the channel increases and the cross-sectional area is reduced. Changing the geometry of the channel alters the resistance across the channel (following basic resistance laws), providing sensory feedback on the physical deformation. Since the conductor inside of the channel is liquid, and the matrix surrounding it is highly elastic, the gauges are ideal for large strain applications. Park, et al. investigated the sensitivity of this class of devices to variations in channel geometry [15].

Gallium indium alloy has been used in a number of different soft robotic applications. Examples of sensing elements fabricated from eGaIn-filled microchannels include curvature sensors [16, 17], stress sensors [18, 19], and strain sensors [20, 21]. The sensors we have fabricated into our robot rely on the same mechanism as those previously discussed. What is unique about our approach is that the sensor is fabricated directly into the robot instead of as a separate structure.

2.3 Experimental

2.3.1 Fabrication

The initial pattern for the pneumatic robot is a derivative of a simplified pneumatic robot designed by Finio et al. [22]. We started with this concept because it is extremely simple, and allowed us to focus on adding sensory elements to the robot instead of focusing on the pneumatic robot body design. The robot is a composite of two silicones: Ecoflex 00-30 (Smooth-On, with hardness below the Shore A scale) to form the pneumatic channels and the main body, and Silgard 184 (PDMS, Dow-Corning, Shore A hardness of 50) to seal the channels. The design has a single air input port and is formed with a 3D printed mold. We kept the single fill port design as it allowed us to simultaneously activate and control all arms of the robot from the same air source, but we modified the fabrication method so that we could incorporate sensory channels into the robot. Because the molds were simple and easy to form in a 3D printer, we were able to quickly iterate through different methods to integrate the sensors.

Our modified process includes a 2-step mold (Figure 2.2) for the main body that embeds the pneumatic channels and the sensory channels into the Ecoflex body. As demonstrated in Figure 2.3a-2.3d, we first filled the primary mold (depicted in Figure 2.2a) with uncured Ecoflex. This section of the mold has embossed features to create channels for the liquid metal sensors. The mold for the pneumatic channels (depicted in Figure 2.2b) was then lowered into the Ecoflex, creating hollows on the opposite side of the robot body from the liquid metal sensor channels. The Ecoflex was allowed to cure completely and was removed from the mold.

Figures 2.3e-2.3f show the next two steps of the process. We filled the open serpentine channels with room temperature liquid metal (eGaIn, Sigma-Aldrich). Once the channels were filled, a small amount of liquid Ecoflex was placed over the channels to seal them. Most soft strain sensors are sealed before being filled with liquid metal [20], but in our case we found that it was easier to seal them afterward. When

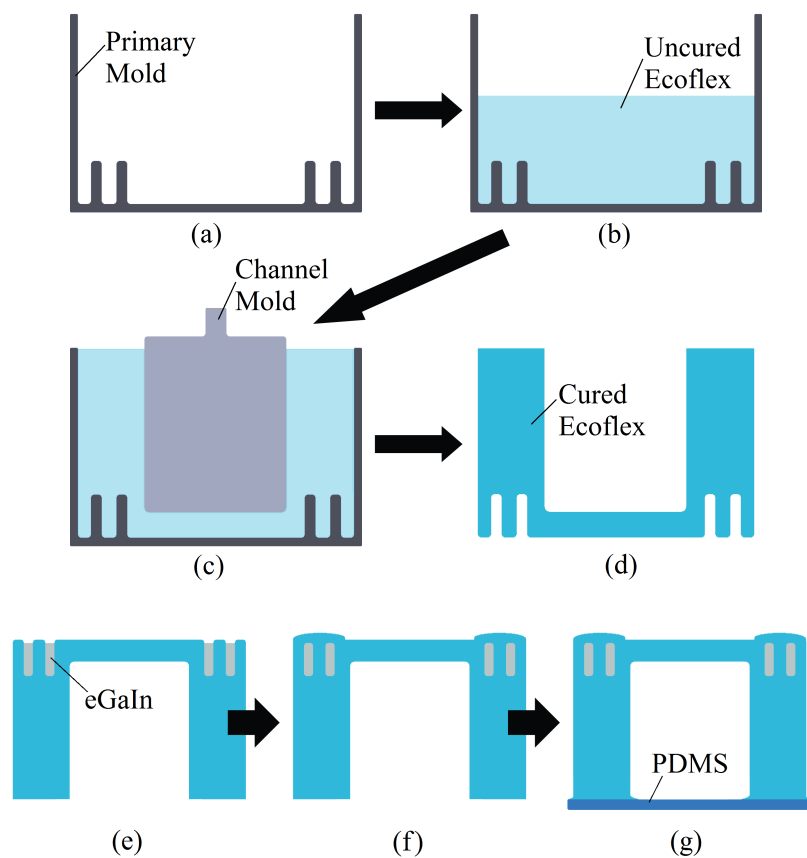


Figure 2.3. (a) The bottom half of the mold is printed and (b) filled with liquid elastomer. (c) The channel mold (previously printed) is embedded inside the liquid elastomer to create the pneumatic channels. When the elastomer has cured (d) the mold can be removed from around it. To finish the sensors, (e) the eGaIn channels are filled with liquid metal and (f) sealed with liquid elastomer. Finally, (g) the pneumatic channels are sealed by bonding the body to a thin layer of Silgard 184.

sealing the channels, we took care to prevent the liquid elastomer from running across the top of the robot and building up a thick layer of polymer. Because the curling actuation motion is a result of the stiffness difference between the bottom and the top of the robot, both material properties and geometric design can change the stiffness and therefore change the actuation motion. A thicker layer of Ecoflex on top of the robot would increase stiffness and result in less curl in the robotic arm. Once the silicone cured, we punctured the thin layer with the electrical wiring, making a contact with the liquid metal. The wires were then folded down and sealed onto the robot with a few more drops of liquid elastomer, preventing the wires from pulling out while the robot is undergoing large deflections. The pneumatic tube was also punctured into the robot through a central hollow (created in the mold) and sealed in the same manner. To finish building the pneu-nets, we prepared and cured a thin, flat layer of Silgard 184. We then sealed the two layers together by adding a small amount of liquid elastomer on top of the Silgard 184 and placing the body of the robot down onto the layer. When the liquid elastomer cured, it bonded the two halves of the robot together (Figure 2.3g).

2.3.2 Sensor Design

Our initial, unsuccessful, sensor design placed the sensors down the center of the pneumatic arm, the area that experiences the greatest strain during actuation. Although we did this to maximize the response from the gauges, the strain gauges would either lose conductivity or break completely. Loss of conductivity occurred during inflation, when the outside of the pneu-nets experienced biaxial strains (along the length and width of the robotic arm). These strains induced channel collapse, forcing the eGaIn to withdraw from sections of the channel and breaking conductivity (see Figure 2.4). After actuation, the channel would need to be massaged to push the eGaIn back into the pinched area, removing any potential automation from this design. Furthermore, the channels did not have a high fatigue life. Previous demon-

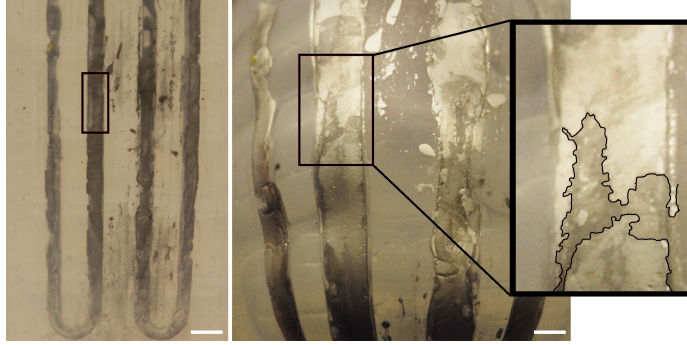


Figure 2.4. A preliminary design with the liquid metal sensors directly over the pneumatic channels. The image on the left is the top of the channels before the arm is inflated (the surface is flat), and the image on the right is the same surface, at the same scale, after it is inflated. The liquid metal channels undergo a large increase in both length and width causing an extreme collapse in the channel’s third dimension. The box in both photos is surrounding the same section of the sensor. The inset is a magnification of the inflated channel with an outlined area that experienced eGaIn withdrawal due to the channel collapse. The scale bars on both images are 2mm, and the inset has 2.5x magnification.

strations have shown the silicone in these types of pneumatic robots will endure many cycles of actuation without failure [2, 11]. However, when we placed the sensors over the areas of highest strain, the silicone (Ecoflex) sealing the liquid-metal channels was unable to sustain the repeated strains and the sensors would burst after 5-10 cycles. Adding a thicker layer of elastomer mitigated this issue, but it did so by significantly impacting the actuation dynamics of the robot.

We studied the robot during actuation to find a location for the sensors that could result in appropriate dynamic response without failure. Pneumatic channels are typically designed with regions that have a thicker cross section than other locations (see Figure 2.3). This helps create a specific motion in the arm during pneumatic actuation [3]. Although these sections deform, they are not subjected to the same magnitude of strains as the original location we selected for the sensors. In the final design of our robot, we embedded the serpentine liquid metal pattern into these



Figure 2.5. The pneumatic robot gripping a cylindrical container. The serpentine liquid-metal sensor channels are clearly visible around the outside edges of the pneumatic channels (dark against the white background).

sections (see Figures 2.3 and 2.5), preventing many of the problems associated with previous design locations. Furthermore, finite element analysis by Mosadegh et al. suggests that our selected location still experiences moderate strains and stresses during actuation [11]. Though we do not claim that this location is perfectly optimized, identifying a location that experiences strain, but is not excessively stressed, is key to successfully integrating feedback strain sensors directly into the bodies of soft robots.

2.3.3 Sensor Characterization

Our sensor characterization tests were designed to provide evidence of the success of our proof-of-concept robot. We performed a simple test on one of the robot's arms to ensure that the strain gauge location provides a measurable response during actuation. We measured the sensor's response to two different modes of strain: linear extension and pneumatic actuation (Figure 2.6). For the linear extension tests, we pulled the tip of the robot arm linearly away from the body of the robot, duplicating a load similar to that of a normal strain gauge [23]. We then used a hand pump to

pneumatically actuate the robot in steps while taking profile photographs of the arm, which we analyzed to measure the length change of the liquid metal sensors.

2.3.4 Sensor-Actuator Interaction

To test the robot’s potential for automated control, we measured the resistance of the strain sensors in each arm in real time while actuating the robot using a constant air flow. To measure the resistance in the gauges, we wired each sensor as a resistor in a voltage dividing circuit. Because of the low resistivity of eGaIn ($\sim 29.4 \times 10^{-6} \Omega\text{-cm}$ [24]), a small 2 Ohm resistor was added as the second resistor in each circuit. Using a KORAD KA3005D DC power supply we limited the voltage across the whole system to 0.7V to prevent excessive current draw through the low resistance devices. To activate the robot, we attached it to a compressed air source with a flow-valve control system that limited the gauge pressure to between 5 and 6 KPa during the tests. We chose a low air pressure for the input line to limit the air flow velocity and slow the actuation of the robot to the timescale of the test. During actuation, we measured the voltage across the strain gauges using a Tektronics TDS 2014C 4-channel input oscilloscope limited to a 50 Hz measuring frequency. Although the oscilloscope had 4 channels for input, one of the channels was dedicated to measuring the voltage across an electronic gauge-pressure sensor (Honeywell 001PDAA5, DigiKey), which provided a digital marker that was used to synchronize the different tests. This limited us to characterizing only three of the four arms, which were picked at random from the robot.

At the beginning of each test we recorded the initial resistance for several seconds with the robot in its resting state. Each characterization test then consisted of filling the robot with air for 5 seconds while measuring the voltage drop across the arms, and releasing the air in the robot. After the robot returned to its resting state, we recorded another brief dwell period before actuating the robot again. We tested the robot actuating under two test conditions: the robot actuating in empty air (see

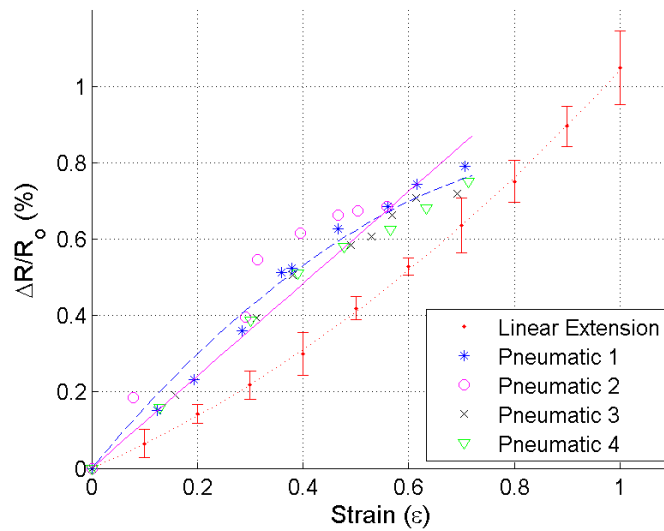


Figure 2.6. A comparison of the strain gauge's percent increase in resistance for one of the robot arms experiencing two modes of strain. The linear extension tests were an application of unidirectional strain to the arm. The error bars are a 90% confidence interval, and the red dotted line is a fit of the data. The other four tests were performed by pneumatically actuating the robot and recording the resistance change, with the solid magenta line representing a linear fit and the blue dashed line representing a curved fit of all the tests.

Figure 2.1) and the robot clamping a cylindrical object (see Figure 2.5) with a radius of about 4.5cm. We filmed each test so that we could compare the recorded data to events that the robot was experiencing.

The pressure sensor was connected to the robot's input valve, and indicated when the pressure in the infill tube changed. There was a nearly instantaneous change after the valve was opened, and the pressure remained constant during the tests. The recorded initial pressure spike acted as a time marker, enabling us to overlay all the tests we ran on the robot under both testing conditions.

2.4 Results and Discussion

Change in resistance as a function of strain for two loading conditions is shown in Figure 2.6. Engineering strain was calculated from the extended length of the strain gauge. In the case of the linear extension tests, this was measured during the test. The extended length of the strain gauge during pneumatic actuation was considered to be the arc-length of the gauge, as seen from a profile view. The percent change in resistance was calculated by dividing the actuated resistance by the initial resistance.

These tests demonstrate our success in integrating the sensors into the robot’s body. Figure 2.6 shows that the strain gauges are appropriately placed and return results that correlate strain to a resistance change. There is a high degree of repeatability in the results from both the uniaxial tests and the pneumatic actuation tests. The curve fit to the linear extension data is characteristic of uniaxial strain gauges and agrees with the literature [21, 25–27]. The pneumatic actuation data also increases monotonically, however, it does not display the quadratic response typical of uniaxial strain loading. For clarity, we have included two possible fits to the data: a linear fit and an inverse quadratic fit. We note that a more in-depth model and expanded data range would be needed to verify either trend. Nonetheless, the pneumatic actuation data has sufficient contrast from the linear extension data to indicate that the strain gauges undergo a complex strain state that is not purely uniaxial during actuation.

To analyze the data gathered during the gripping actuation tests, we first applied a 20 point moving average filter to remove the noise. We then used basic electrical circuit theory to calculate the resistance in each strain gauge based on the measured voltage. We noticed that each of the robot’s arms had a different initial resistance and electrical response to actuation. To permit easy comparison between the three different arms, we calculated the percentage rise of resistance based off of the total overall change that the sensor underwent when gripping the cylinder. We present the results of our 3 tests with a 90% confidence interval in Figure 2.6. Though a 50 Hz signal with a 20 point filter slows down the response time of a control system,

the inherently high compliance in the soft robot tolerates imprecision in the control while preventing damage to the robot or the object being gripped, ideally simplifying feedback control.

Each arm’s strain gauge demonstrates a similar response during the tests. When gripping air, there is a consistent increase in resistance throughout the whole test. During the object gripping tests, each sensor initially experiences the same increase as the control, with a sudden departure from the trend when the robot begins to contact and grip the object. The videos of the tests validate that at about 3s the robot begins to contact and grip the object, matching the recorded data (Figure 2.6). By keeping the inflow pressure controlled, the strain gauges provide feedback in a predictably linear manner until boundary conditions change (an object is encountered). Since the slopes of each section of the data are constant, it is possible to distinguish the time that the robot begins to grip an object. This performance is consistent with the observations performed by Kramer et al. with their liquid metal curvature sensors. By changing the boundary conditions of their curvature sensors (from air to a rigid joint), they experienced a magnification of the resistance change by over an order of magnitude [17]. This means that the integrated strain gauges can be used to mark events (such as gripping or other boundary changes) during the actuation of the robot.

2.5 Conclusion

We prototyped a pneumatically actuated soft robot with liquid metal strain gauges built into the soft robot’s body that provide real-time feedback during actuation of the robotic system. Two simple tests on the robot provided strong evidence of the validity of this integrated sensor design. Under controlled conditions, the resistance in the strain gauges changes in a predictable manner relating directly to both the strain in the robot’s arms and the rate of actuation. We also show that, under a constant input air pressure, we can sense if and when the robot is gripping an object.

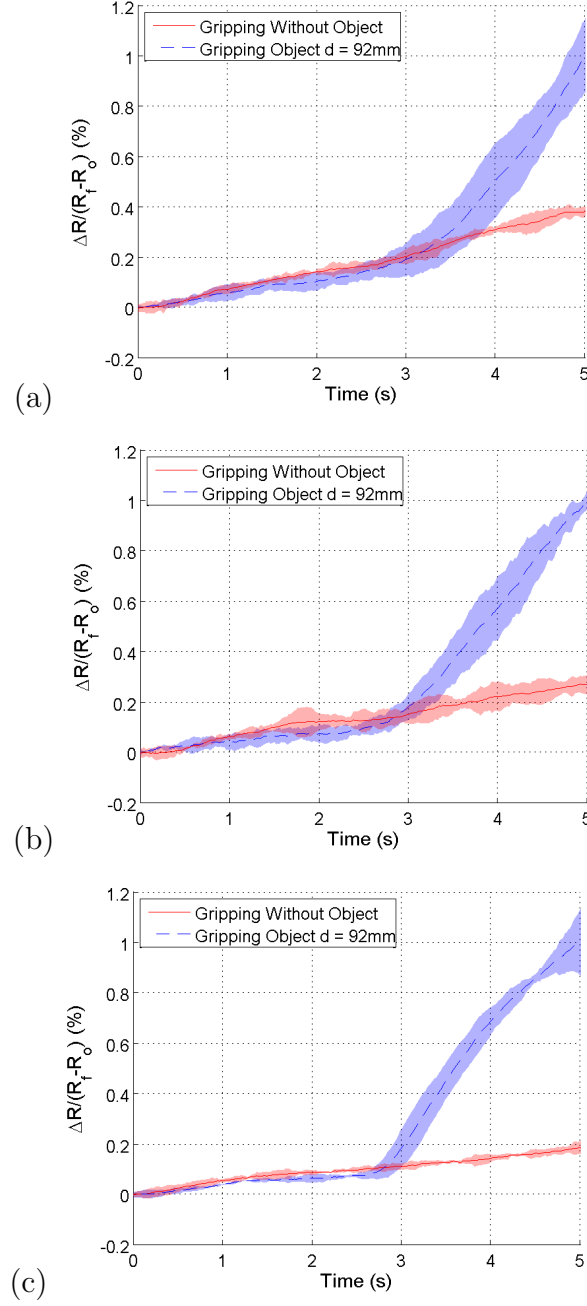


Figure 2.6. The resistance change in three of the robot's strain sensors during the 5s actuation tests. Each graph (a,b,c) represents a different arm on the robot. The test setup only permitted gathering simultaneous data from 3 arms, though the sensors on all 4 arms were fully functional. The solid red line is the average of the baseline tests (the robot inflating in empty air). The dashed blue line is the average of the tests with the robot gripping the test cylinder at approximately 3 seconds. The shaded area surrounding each line represents a 90% confidence interval. The percent change was calculated using the initial and final resistances of the tests with the robot gripping an object.

The modified fabrication method of these robots is outlined so that this work can be easily expanded on in the future.

2.6 Future Work

This proof of concept robot demonstrates significant potential for many future projects that integrate sensors into the body of a pneumatically actuated robot. It has the possibility of finally closing the control loop and opens up a greater potential to automate soft robots. Each sensors' response to actuation can be characterized independently, eventually allowing for computer control to optimize the actuation in each arm. Furthermore, since each arm provides actuation and gripping feedback independently of the other arms, there is redundancy in the gripping information provided to the robotic controller. Regardless of the complexity of the eventual model, the repeatability of our simple tests demonstrate the potential to use the resistance response in the gauge to generate a state reconstruction model for control of a pneumatic robot.

We also believe that there are more possibilities for sensor locations and types on a pneumatic robot like that presented in this paper. In the future, we would like to integrate pressure sensors into the Silgard 184 bottom layer of the robot (which is the side that grips objects). This will provide a secondary sensory system that a computer controller can use to determine if an object is being gripped and potentially how much force is being applied to grip an object. These sensors may also be able to provide a faster feedback response to a control system than our currently heavily filtered system. This would free up the strain sensors to be primarily used for arm position and location control.

3. DESIGN FOR CONTROL OF A SOFT BIDIRECTIONAL BENDING ACTUATOR

The following chapter is based on work previously published as [28] R. A. Bilodeau*, M. C. Yuen*, J. C. Case, T. L. Buckner, and R. Kramer-Bottiglio, “Design for Control of a Soft Bidirectional Bending Actuator,” in 2018 IEEE/RSJ International Conference on Intelligent Robots and Systems (IROS), 2018, pp. 1–8. Copyright ©2018 IEEE, reproduced with permission.

* indicates co-first-authorship

Contributions: This chapter was worked on primarily by two individuals: myself and Dr. Michelle Yuen, in a tight collaboration. We both contributed equally to the development of the overall design of the actuator system (including materials selection), and to the development of the reduced-step manufacturing technique for the actuator. We made sure that, through careful analysis and testing of the design, we could get sensory feedback on the actuator’s position. In this, Michelle focused more on the mass manufacture and design parameters of the final product, whereas I ensured that our hardware and software combined to enable closed-loop control on the soft bodied actuator. Finite element analysis was executed by Trevor Buckner, although I provided oversight and suggestions on how to model the geometry and forces in a way that enabled convergence.

3.1 Introduction

Elastomer-based pneumatic actuators have been demonstrated as highly adaptable functional systems [3]. Initial work presenting inflatable “pneu-nets” in an elastomeric body demonstrated that the silicone structures could grip objects or slowly walk when given simple, open-loop commands [2, 12]. Since then, they have seen significant forward progress in their fabrication, adaptability, and control [29]. However, this forward progress has come coupled with both a rise in the manufacturing complexity of casting the pneumatic chambers [1, 11], and in the design complexity as additional sensory systems are embedded [29–32]. It has also increased the need for on-demand high-pressures and vacuums [4, 33, 34] and their corresponding,

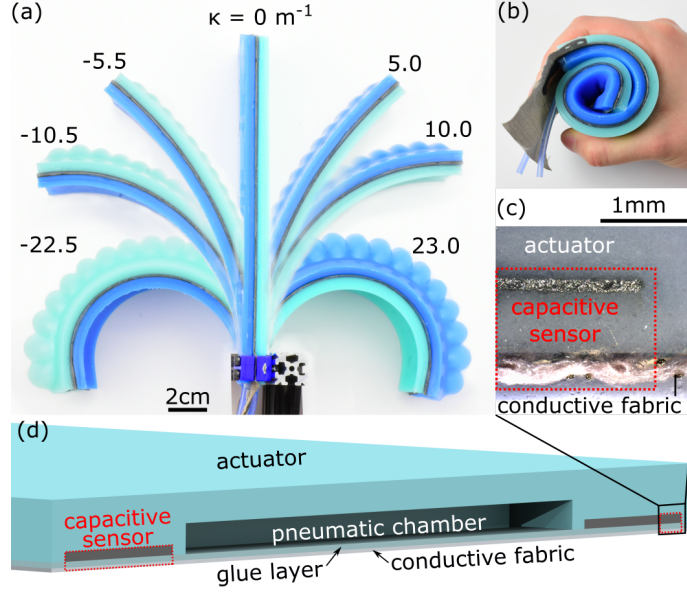


Figure 3.1. Sensor-controlled antagonistic pneumatic actuator (SCAPA). (a) Overhead view of a SCAPA sweeping across its full range of achievable curvatures, κ . (b) Due to its fully soft construction, the SCAPA can be rolled up, compressed, and still return to full functionality. (c) Optical microscope image of the interface between the actuator, embedded sensor, and conductive fabric. (d) A cross-section schematic of a SCAPA, including an indicator for the location of the optical image in (c).

often bulky, equipment. This trend of increased complexity will likely only rise as researchers strive to derive additional functionality, logic, or adaptability out of otherwise inert soft materials.

One of the challenges of soft robotic systems is in creating reliable controls [35]. Since inflatable soft technologies experience large deformations during operation, and are constructed with viscoelastic materials, closed-loop control is not a trivial task [36]. Though pneumatic actuators were demonstrated early on, development of soft sensors capable of matching the physical response of these systems lagged behind. As such, much of the state-of-the-art in soft robotic controls has focused on predictive models and feed-forward controls [37–41] or on actuator (pressure) feedback rather than true state reconstruction and closed-loop control via sensors [42,43].

Recently, there has been an increase in the use of finite element analysis (FEA) to better understand and predict the response of a soft system [11, 44–46], but due to material non-linearity and large system deformation, these FEA models are complex and difficult to implement. Forays into sensor-enabled closed-loop control have used commercially available flexible sensors to demonstrate state reconstruction and control [47–49]. These sensors also provide a strain-limiting layer while providing the state-reconstruction feedback.

Recent advances in silicone-based all-soft sensors are beginning to allow for more advanced demonstrations of closed-loop control in soft actuators. Early soft sensors used conductive liquid metals embedded in elastomer as high-deformation resistive sensors [17, 50]. These have been used both as embedded sensors for state reconstruction and as external sensors for closed-loop control [1, 18, 31, 51]. More recently, soft conductive silicone composites have been demonstrated as reliable, repeatable, high-deflection capacitive sensors that can be placed externally on soft joints for 2D and 3D state reconstruction [52–56] or as integrated resistive sensors providing both proprioception and tactile feedback in closed-loop controlled pneumatic grippers [57]. As an alternative, stretchable optics have been demonstrated as embedded sensors in pneumatic actuators, providing state reconstruction, curvature control, and tactile feedback [30, 58]. With all this available research into soft sensors and controllable soft systems, we see an opportunity to synthesize simpler robotic constructs without losing functionality or utility.

In this paper, we present sensor-controlled antagonistic pneumatic actuators (SCAPAs, Figure 3.1) which integrate proven soft robotic actuation and sensing technologies in a simplified design targeting controllability of the system state (*i.e.* design for control). Specifically, we embed silicone-based capacitive strain sensors [59] into pneumatic bending actuators [3], which we then assemble as antagonistic pairs to achieve bi-directional, controllable actuation. Compared to previous work, we make two key improvements to the system: 1) utilizing inextensible conductive fabric as both the strain-limiting layer for the actuators and the ground plane for the capacitive

sensors, and 2) utilizing the same silicone material in both the actuators and sensors. These improvements result in fewer constituent components, fewer interfaces between dissimilar materials, and fewer manufacturing steps. This reduction in physical complexity allows us to use a simple FEA model to predict the quality of a given design, which we experimentally verify. We compare various candidate designs using the FEA model and subsequent experimental tests to determine which design can provide strong state reconstruction. Finally, we select a SCAPA design and use it to demonstrate closed-loop curvature control using various basic feedback control strategies.

3.2 Physical Embodiment

A SCAPA consists of an antagonistic pair of thin bending pneumatic actuators, each with an embedded capacitive sensor for differential measurement of curvature (Figure 3.1). At the core of each SCAPA is conductive fabric, which serves dual purposes as both the strain-limiting layer for the actuators and as the grounding electrode for the sensors. The system’s reduced profile allows us to roll a SCAPA into a compact cylinder without damaging any of the constituent components (Figure 3.1(b)). Previous work used conductive fabric as both the strain-limiting layer of a one-sided pneumatic actuator and an electrode for capacitive contact detection [60]. Here, we expand on their work by using the fabric in a state feedback sensor for closed-loop control, rather than object detection.

The sensors are constructed as a parallel-plate capacitor using an expanded graphite silicone composite for the active conductive layer and unmodified silicone elastomer for the dielectric layer. As the sensor geometry changes due to applied strain or pressure, the capacitance changes measurably. White, *et al.* previously conducted a study of the materials and manufacturing of these strain sensors, as well as their response to many cycles of strain [59]. We made the sensors out of the same elastomer as was used in the actuator body, resulting in a nearly invisible, fully bonded interface

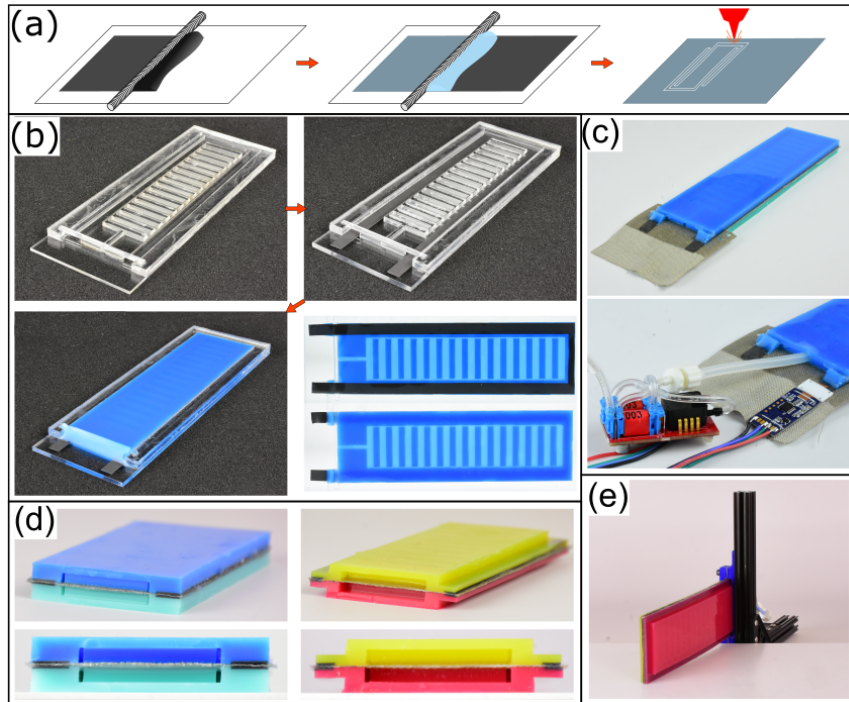


Figure 3.2. (a-c) Manufacturing the SCAPA. (a) The capacitive sensors were first fabricated in large films and then laser cut into the desired patterns. (b) The casting process created the pneu-net actuators while simultaneously embedding a sensor in the actuator body. (c) Conductive fabric was glued between two actuators to create the antagonistic bending system and the electronics controlling actuation and measure the sensors were attached to the SCAPA. (d) Photos showing two of the designs explored. The actuator body, sensors, and conductive fabric are clearly visible in the cross-sectional images. (e) For all experiments performed, each SCAPA was fixed vertically such that the tip would sweep horizontally. A camera was situated above the SCAPA to record truth data on its curvature.

between the sensor and actuator (Figure 3.1(c)). This material continuity reduces risk of delamination failure that can occur at interfaces between dissimilar materials. We also leverage the single material construction to simplify analysis of strain fields in the device’s silicone walls.

To bend a SCAPA, one of the actuators is inflated while the other is vented to atmosphere. This bend causes the capacitance of the embedded sensors to change. The actuator inflation is controlled by “pneumatic servos” which serve effectively as 3-port, digital pressure regulators [61]. To read the capacitance change, we use custom signal conditioning boards that charge the sensor for a fixed length of time and record the time it takes to discharge to ground voltage (based on [59] with modified software). The entire system is controlled using an Arduino Mega communicating with the pneumatic servos and the sensor signal conditioning boards via I2C protocol.

3.2.1 Fabrication

The SCAPAs were manufactured in three phases: 1) sensor fabrication, 2) actuator casting, and 3) assembly (Figure 3.2(a-c)). As stated previously, the conductive fabric acted as a shared ground layer for both capacitive sensors. To make the rest of the sensor, we cast the remaining two layers in a sheet by rod-coating first the silicone-graphite composite (DragonSkin 10 Slow, Smooth-On; Expandable graphite, Sigma-Aldrich) for the active electrode layer [59], followed by the pure silicone for the dielectric layer (DragonSkin 10 Slow) (Figure 3.2(a)). Upon curing, we used a laser to cut out two U shapes that fit along the outside edges of the actuators. We cleaned the cut shapes with ethanol and laid them in the bottom of the actuator molds. The molds were fabricated from laser-cut acrylic sheets (Figure 3.2(b)). We poured silicone into the molds (DragonSkin10 Slow; SilcPig silicone dye, Smooth-On), degassed the cast material in a vacuum chamber, and clamped a lid on top to ensure uniform thickness across all actuators. After the actuators cured, we glued one to each side of inextensible conductive fabric (Technicot, LessEMF) using additional uncured

silicone, completing both the actuators and the sensors. The tubing for the actuators was inserted and epoxied to the actuator body (Sil-Poxy, Smooth-On), and connected to the pneumatic servos (Figure 3.2(c)). The capacitance signal conditioning boards were sewn directly to the grounding fabric to improve the electrical contact between the two. Flexible copper-clad polyimide strip electrodes extending from the signal conditioning boards were sandwiched against the active silicone sensor layer by two polystyrene plates that were also sewn to the fabric. These strip electrodes allowed for a larger contact area between the interfacing surfaces, giving the signal conditioning board a strong electrical connection to the active layer.

3.3 Design

In order to properly characterize and study a symmetric actuator sensor pair, we defined a simple, perspective-based nomenclature to differentiate the sensors and the curvature of the SCAPA. From the top-down perspective shown in Figure 3.1(a), when the right-side actuator is inflated, the SCAPA body will bend to the left, which we define as a negative curvature. Conversely, when the left actuator is inflated, the SCAPA body bends to the right, which we define as a positive curvature. The sensors located in the left and right actuators are referred to as the left and right sensors, respectively.

In theory, when the curvature is positive, the capacitance of the left sensor should increase due to stretching and Poisson thinning of the dielectric layer. Similarly, the right sensor should increase in capacitance as the sensor length is compressed. By convolving the two sensor signals it should be possible to determine the curvature of the SCAPA for state feedback to the controller [51].

In practice, with a highly deformable sensor embedded in the actuator, we must consider how the sensor response is coupled to all deformations in the soft body, from those we want to measure (curvature proprioception) and those we do not want to measure (inflation expansion). To address this coupled response, we performed a

Figure 3.3. Design study to determine the effects of sensor width and placement on the quality of the sensor output. (a) Schematic of the loading conditions for the FEA (left) and cross-section geometry (right), with only the boxed section being modeled. (b) Sketches of the initial modeled geometry and the FEA results. Design 1 shows the base case for the system. Design 2 reduces the width of the sensor and Design 3 moves sensor to the top of the actuator. (c) Experimental verification plots showing the sensor responses to curvature. The circles indicate experimental data and the line is a quadratic fit with the shaded region being a 95% confidence bound about the regression.

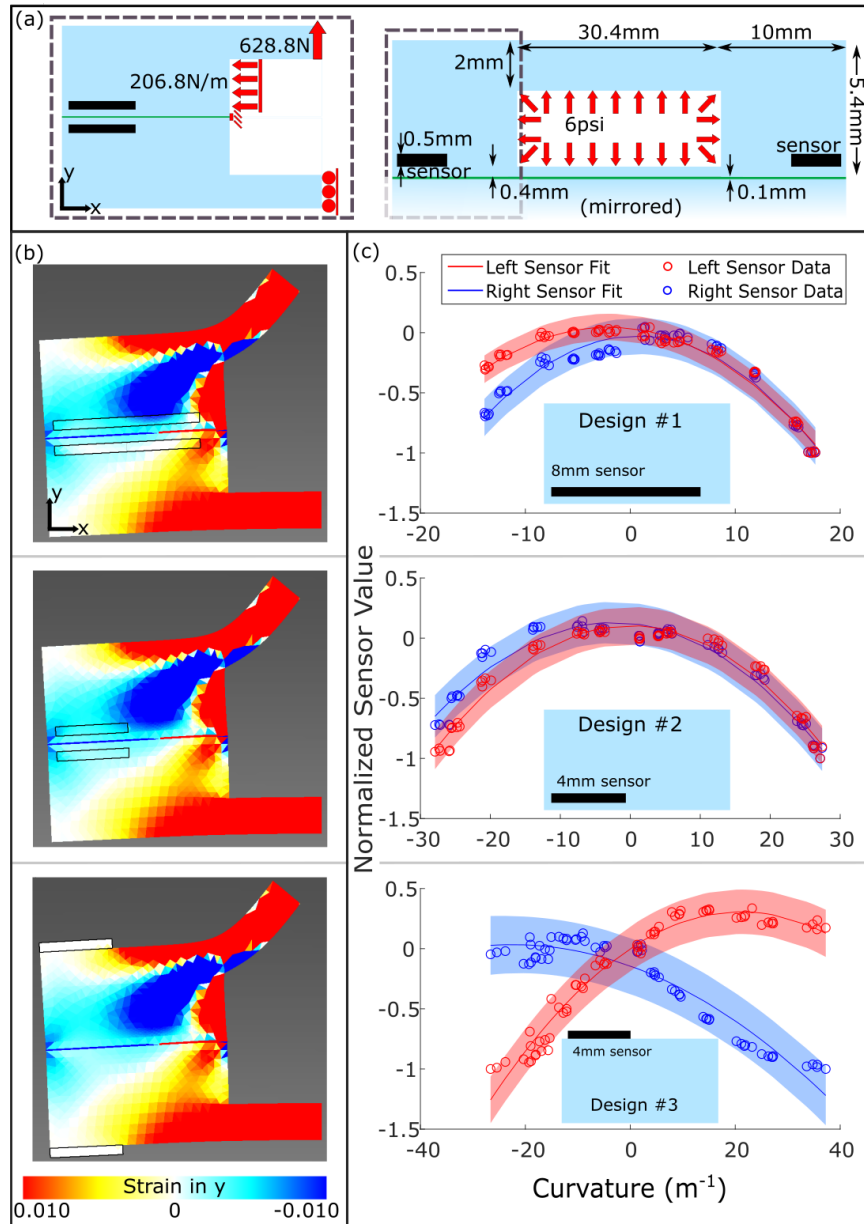


Figure 3.3.

design study of the cross-sectional geometry to develop designs in which the sensors would be minimally affected by actuator pressure. This design study consisted of two parts: 1) FEA modeling to predict deformation fields in the actuator cross-section due to inflation expansion, and 2) empirical verification of the design’s effect on sensor response.

3.3.1 FEA modeling of cross-section

A series of FEA simulations were run in SolidWorks to assess the deformation in the sensor region due to inflation (Figure 3.3). The analyses were set up using a 2D cross-section of the SCAPA, with reduced geometry to encourage faster solution times. Expecting large deformations in the wall, the simulations were run using a nonlinear solver. Our model includes three assumptions:

1. A fixed fabric layer that is completely inextensible, perfectly flexible, and perfectly bonded to the silicone. We are confident with this assumption due to the orders-of-magnitude difference in tensile elasticity between the silicone and fibers in the fabric, and because we chose a fabric with an open weave that allowed the pre-cured silicone to fully permeate between all the fibers.
2. Uniform material throughout the elastomer, since both the sensor and the actuator are silicone, the active composite layer is very thin, and there is little conductive filler in the composite itself.
3. Linear elastic behavior of the silicone, where $E = 0.12$ MPa, obtained via a linear extension test on dogbone shaped silicone samples using an Instron 3345 materials testing system, with samples tested to 50% strain at 100% strain per minute.

Previous work showing detailed 3D analysis of an inflating elastic chamber indicate that the thick outer walls experience stresses that are 2-3 orders of magnitude less than the thin, expanding ‘roof’ of the chamber [44]. Since our soft sensors are placed

Figure 3.4. Design exploration of various geometries that should limit the effect of actuator inflation on sensor response. (a) Schematic of the the loading conditions for the FEA (left) and the cross-section geometry (right), with only the boxed section being modeled. (b) Sketches of the initial modeled geometry and the FEA results. Design 4 and 5 introduce a notch along the outer edge of the actuator with the sensor embedded near the fabric layer and on top of the notch respectively. Design 6 increases the distance between the sensor and the pneu-nets by increasing the width of the actuator wall. (c) Experimental verification plots showing the sensor responses to curvature. Design 6 began to twist while actuating resulting in unpredictable sensor responses. The circles indicate experimental data and the line is a quadratic fit with the shaded region being a 95% confidence bound about the regression.

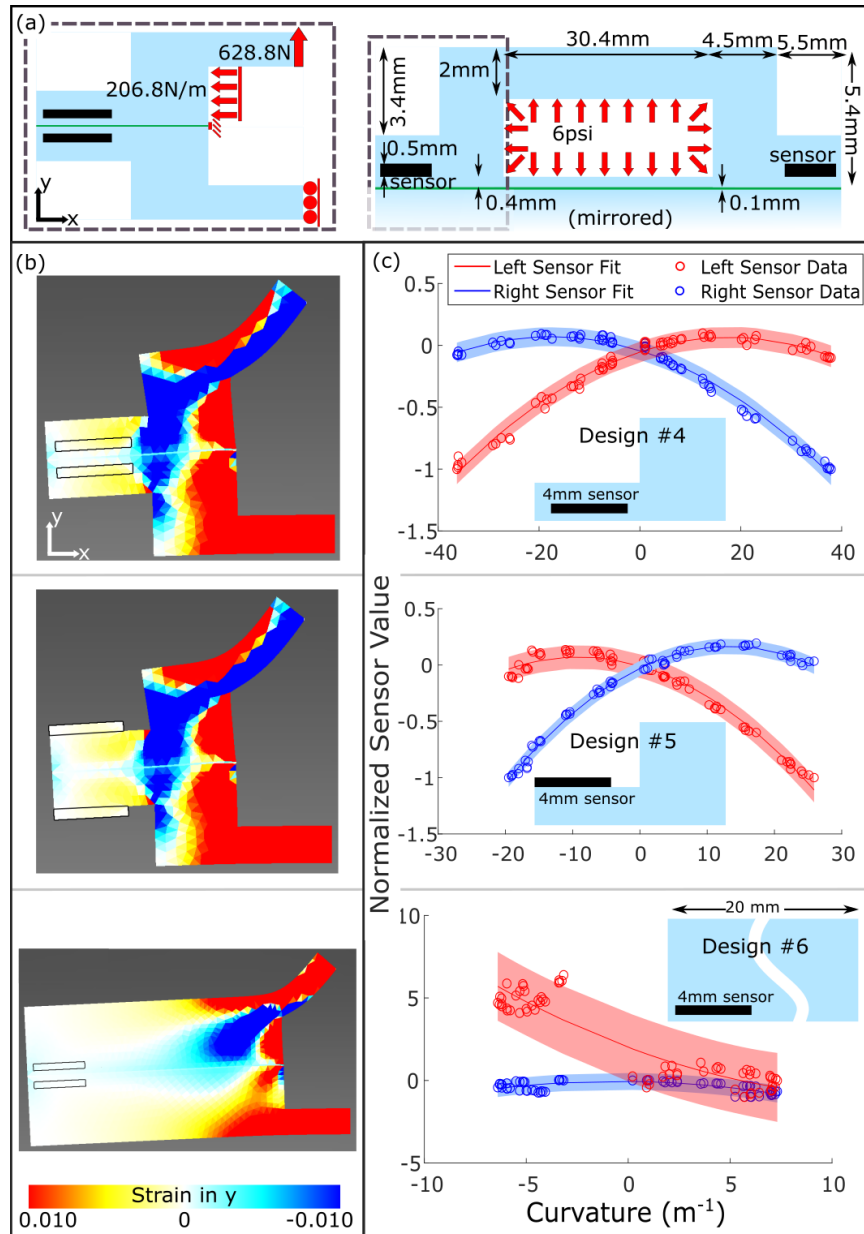


Figure 3.4.

along the outer wall of the device, we considered only this section as our area of interest, and simplify our model accordingly. This simplification is further supported by inspecting additional modeling work that has recently been performed [11, 45]. Instead of applying pressure to a geometric reconstruction of the whole cross section, we applied an upward force equivalent to the pressure lifting the pneumatic pocket, acting along a moment arm. This accounted for both a lifting motion and bending moment experienced at the juncture between the pneumatic pocket and the actuator wall (Figure 3.3(a)). We then applied the remaining internal pressure directly to the wall's edge. Due to symmetry, it was only necessary to analyze one side of the structure.

In this analysis, we were primarily interested in sensor strain in the y-direction (normal to the fabric), as defined by the axes in Figure 3.3(a). Since one half of the parallel-plate capacitor is a wide fabric sheet, sensor displacement in the x-direction should not affect the sensor output. However, y-strain will have a significant impact on the sensor, as it reflects changes in the distance between the electrodes, while discounting bulk motion of the entire system in the y-direction. Any y-strain in and under the sensor induces a sensory response that is not reflective of the SCAPA's bending motion. By marking out the area of the sensor in our FEA model, and plotting the strain in the y-direction, we clearly see the effects of actuator inflation on compression and tension in the sensor (Figure 3.3(b)).

3.3.2 Sensor Characterization & Model Verification

To verify the FEA modeling, we initially modeled three designs with different sensor sizes (8mm or 4mm wide) and locations (embedded or on top of actuator) and then built these designs to experimentally evaluate their viability for curvature state reconstruction (Designs 1, 2 and 3, shown in Figure 3.3(b-c)). Using the experimental setup shown in Figure 3.2(e), we mounted the SCAPAs onto a stand such that both actuators were perpendicular to the benchtop. We sewed a thin strip of Teflon to

the tip of the actuator to minimize friction during motion. A webcam was mounted overhead to record the curvature truth data of each SCAPA during actuation. In each experiment, we actuated both actuators individually through a range of inflation pressures between 6-11 psi (at 1 psi increments and five repetitions at each pressure), in a randomized order. This range of pressures correspond to the range of curvatures shown in Figure 3.1. Once inflated to the desired pressure, we allowed the actuator to settle into a steady state for 5 s. We then sampled and recorded the sensors 100 times over a period of 10 s and averaged the data to obtain a representative sensor reading. Finally, we took a photo of the actuator from which we measured the curvature of the actuator (truth data) using a three-point fitting algorithm that assumes constant curvature in the system.

We plotted the sensor values against the curvature to evaluate the design's performance (Figure 3.3(c)). We first normalized the sensor data to the data range between 0 curvature (x_0) and the minimum measured sensor value (x_{min}): $x_{norm} = (x - x_0)/(x_0 - x_{min})$. In an ideal bending beam, negative curvatures would correspond to the right sensor's capacitance increasing and the left sensor's capacitance decreasing, with the converse expected when bending to the right. Instead, we observed that both sensors have a parabolic response. In Designs 1 and 2, this response is centered near a curvature of 0 m^{-1} , while the response in Design 3 shows a significant offset. Because of this, the positive and negative curvatures for Designs 1 and 2 cannot be well-distinguished, even when convolving the two sensor signals. We hypothesize that this is due to the sensor response being coupled with inflation pressures. As suggested by the FEA models for these two designs, there is a field of y-strain (marked in blue) cutting through the location of the sensors. Design 3's asymmetric response corroborates the conclusions from the FEA, which suggests that only a portion of the area under the sensor is undergoing strain, and so the sensor is only marginally affected by actuator inflation. This initial design study showed us that our FEA model is able to predict the impact of sensor placement in a cross-section, even with our embedded modeling assumptions.

3.3.3 Design Exploration

Having experimentally verified our FEA model, we used it to qualitatively examine multiple cross-section designs without the need for building physical prototypes. After testing many designs that varied in geometric parameters, we removed those that performed poorly in the FEA models and converged on three designs (Designs 4, 5, and 6, shown in Figure 3.4(b)). These designs minimized the impact of the actuation pressure on the sensor, and we fabricated each design to confirm the results of the FEA. Designs 4 and 5 introduce a stress-relieving notch in the actuator wall above the sensor; Design 6 widens the wall of the actuator and moves the sensors further away from the pneu-nets.

Our results show that the notched designs isolated the sensors from a significant portion of the actuator inflation deformation. The sensors' responses in Designs 4 and 5 show unique pairings of left and right sensor values across the entire range of curvatures tested. Compared to Design 3, the confidence bounds on Design 4 and 5 are greatly reduced, indicating a stronger and more repeatable response to curvature change. Additionally, we observed that the sensor values rise above 0, indicating that the sensors' capacitances increase as expected, albeit slightly, when it is on the outside of the curve.

The results of the experimental characterization of Design 6 indicate a breakdown in our simplified FEA model. The increased wall width changed the deformation dynamics of the actuator. Rather than simply bending, the SCAPA twisted and/or curled into a bowl-like shape, which resulted in highly unusual, asymmetric sensory response (Figure 3.4). This sort of dynamic 3D response was not accounted for in our simplified 2D FEA, indicating a model limitation.

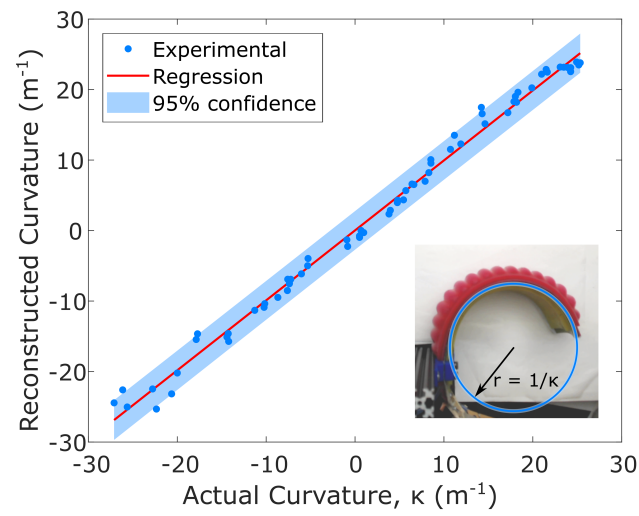


Figure 3.5. Sensor calibration results for Design 4 (see Figure 3.4) comparing the actual curvature to state reconstructed curvature. The shaded region represents the 95% confidence interval. The inset shows an inflated SCAPA with a fitted circle used to measure the actual curvature. r is the radius of the circle and κ is the curvature.

3.4 Closed Loop Control

3.4.1 SCAPA Design Selection

We chose to use Design 4 to demonstrate closed loop control. This particular design (demonstrated in Figure 3.2(d)) met all of the goals we sought to achieve for improved state estimation: simplified manufacturing with embedded sensing cast into the actuator in a single-step, a sensory response to actuator strain in which both actuators produced distinct responses to the actuator's shape change, and low variation in the sensory response with respect to curvature. After choosing this design, we then remounted the system in our testing setup, we and collected a new set of calibration data using a higher refinement in pressure steps (incrementing by 0.5 psi) to get a better resolution in curvatures.

3.4.2 Empirical Model

Once the sensor data was correlated with the measured curvature of the system, a generalized least squares regression was used to determine the coefficients for the following equation:

$$\kappa = a_0 + a_1 S_1 + a_2 S_2$$

where κ is the curvature of the SCAPA, S_i are the raw sensor output values from the sensor boards, and the constants a_i are the coefficients of the fit. Using the regression model, we reconstructed the curvature for each set of sensor values gathered during calibration, and plotted it against the measured curvature values (see Figure 3.5). The fit has a 95% confidence interval of 5.549 m^{-1} or 10.58% of the full scale.

3.4.3 Controllers

We tested the system response of our SCAPA using three different controllers (Table 3.1). These controllers are composed of two different control loops (a logic

Table 3.1. Naming convention for the three controllers implementing the control loops in Figure 3.6 and state machines in Figure 3.7.

Controller Name	Control Loop	State Machine
Simultaneous	Logic	Dynamic
Fixed Rate Quasi-Static (FRQS)	Logic	Quasi-Static
Varying Rate Quasi-Static (VRQS)	Logic + Proportional	Quasi-Static

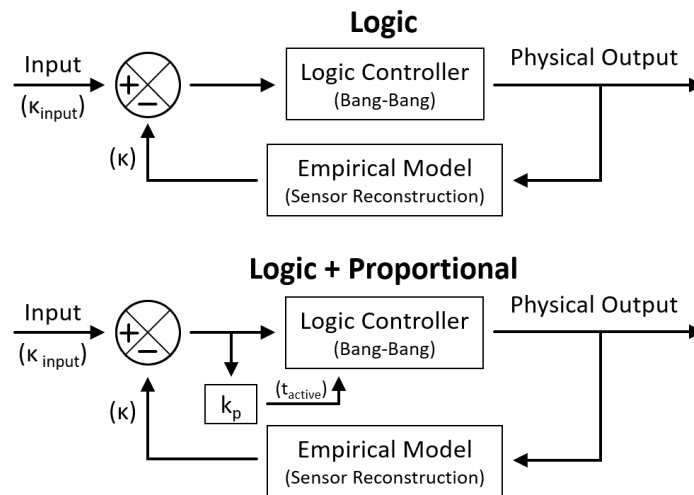


Figure 3.6. Control loops used to follow the input signal.

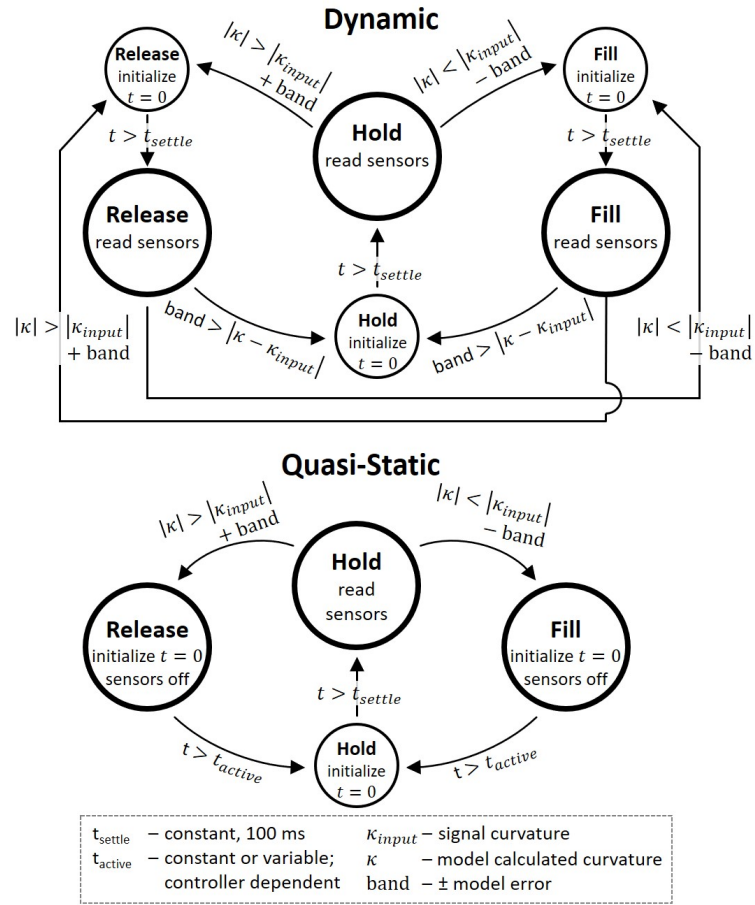


Figure 3.7. State machines used in the logic controllers.

loop and a proportional-logic loop, diagrammed in Figure 3.6) with two different internal logic controllers (whose state machines are sketched in Figure 3.7). We used a target curvature (κ_{input}) as the input signal for all three controllers. This signal could be either positive or negative, and all three logical controllers had a built-in filter to switch between which of the two actuators was active, based on the sign of the desired curve.

The physical design of the SCAPA instilled some common requirements for each controller. First, since the inactive actuator was compressed during actuation, it was always held in the ‘deflate’ state to ensure that its internal pressure was equal to atmosphere. Second, the capacitive sensors are sensitive to the activation of the solenoids in the pneumatic servos [61]. To compensate, we added intermediary ‘settling time’ states with a fixed delay ($t_{settle} = 100$ ms) in which sensor-reading was locked out (all smaller circles in Figure 3.7). Finally, the hold response of all three controllers would trigger if the sensory response was within a band around the signal curvature, derived from the model error (see Figure 3.5).

As outlined in Table 3.1, we named each controller based on the operation goal. The simultaneous controller, the most basic controller we could implement, is a logic controller that increases, holds, or releases pressure in the pneumatic actuator, while sampling the sensors simultaneously. The quasi-static logic state machine removes the dynamic response of the physical system from the sensor data by locking out the sensor reading when the actuator is inflating or deflating. The inflation or deflation time was either fixed (fixed rate quasi-static controller, FRQS) or could vary proportionally to the curvature error (varying rate quasi-static controller, VRQS). The FRQS controller used only fixed values for all of the timings, coded directly into the logic controller. It operated on a 250 ms cycle frequency, actuating for 50 ms, settling for 150 ms, and then reading the sensors 10 times during the last 100 ms (and averaging the data). In contrast, the VRQS controller used proportional control to determine the timing that the actuator should be allowed to inflate/deflate (between 0-450 ms). Since the proportional timings allowed for much larger inflate/deflate times during large jumps

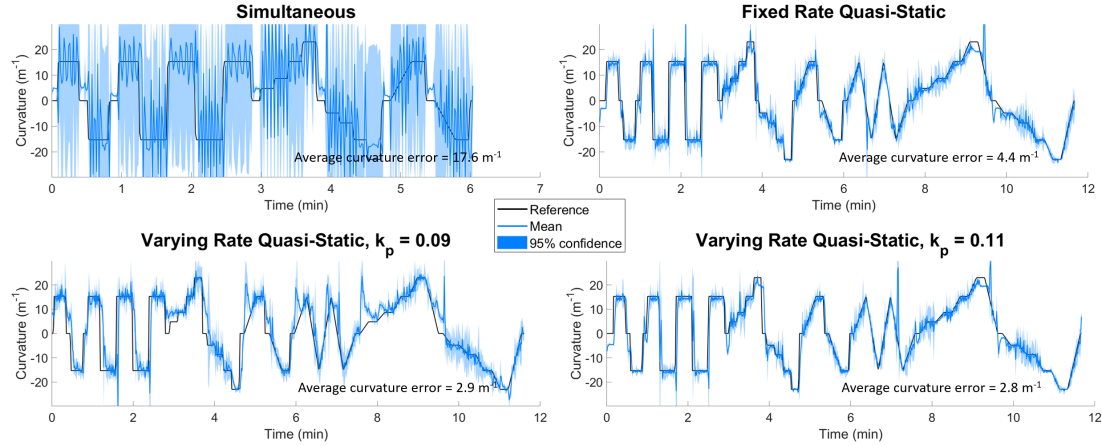


Figure 3.8. Closed-loop curvature control using the Simultaneous, Fixed Rate Quasi-Static, and Varying Rate Quasi-Static controllers, with two different proportional gains in the VRQS controller. Each plot shows the reference signal (black) and the reconstructed curvature (blue - both mean and 95% confidence bounds), and indicates the mean deviation (error) of the system response from the desired curvature for the whole test.

in the input signal, we were able to allow the system to settle for longer (350 ms) without slowing down the overall performance, and thus improve the sensor data retrieved and therefore the accuracy of the controller.

3.4.4 System Response

The responses of the three controllers are shown in Figure 3.8. The input signal is shown as a solid black line, with the mean system response shown as a solid blue line and 95% confidence error bound shaded. For each controller, we also calculated the mean error in curvature of the experimental response from the signal (the average absolute difference between the signal curvature and the SCAPA's curvature at any given moment in time) in order to quantitatively judge the three different controllers.

As is evident in Figure 3.8, the simultaneous controller performed poorly, with the system having an average curvature error of 17.6 m⁻¹. The immediate, continuous feedback caused the controller to whip the actuator back and forth so wildly

that we discontinued the test before completion to prevent damage to the actuator. We hypothesize that the (potentially internal oscillatory) dynamic response of the physically inflating system was coupled into the sensor response in a way that was unpredicted in our quasi-static empirical model, causing the measured curvature to vary.

Switching to the FRQS controller, the SCAPA’s performance improved, with an average curvature error of only 4.4 m^{-1} . This immediate improvement further reinforced our conclusion about the simultaneous controller: that the internal dynamics of the physical silicone, combined with the sensitivity of our sensors, resulted in sensor responses that gave inaccurate feedback to the logic control loop. In order to improve the error further, we allowed the fill time to vary with a proportional controller. We tested two different gains (0.09 and 0.11) and the average error reduced to 2.9 m^{-1} and 2.8 m^{-1} , respectively. This exercise demonstrates that soft-bodied control is achievable using a just simple proportional control loop.

3.5 Conclusion and Future Work

In this paper, we presented sensor-controlled antagonistic pneumatic actuators (SCAPAs), designed for simplified fabrication and control. Towards streamlined and efficient fabrication, we utilized conductive fabric to serve as both the inextensible layer for the actuators enabling bending, and as the ground layer of the embedded capacitive sensors. In order to achieve curvature control, we designed the SCAPAs so that the embedded sensors would respond to curvature, rather than actuator inflation. We used FEA modeling and experimental characterization of the sensor response to curvature to evaluate various SCAPA geometries and determine an appropriate design. After selecting an appropriate design, we demonstrated that the chosen SCAPA design could be controlled with a simple quasi-static control strategy with only minimal error. With both functional antagonistic actuators and feedback sensors, the SCAPA we presented is a fully autonomous, soft pneumatic robot.

Future efforts will explore the dynamic behavior of the SCAPAs and expand from a single SCAPA to multiple units connected in series to form a fully controllable soft continuum manipulator. Future work will also focus on exploration of the FEA, quantitatively comparing run-time and model complexity with the physical response. By changing the assumptions, material properties, modeled regions and including out-of-plane stresses, which can result in additional unexpected warping and buckling, we will be able to optimize the model for both speed and result quality. Additionally, a quantitative comparison of presented control strategies and additional controllers (for example, PID), each with optimized timings and gains, should be studied through automated empirical testing. Finally, coupled sensor responses could be used to determine when an external force is acting on the SCAPA.

Introduction to Block 2:

Chapter 4 begins the second block of work that continues into chapter 5, focusing on fiber-like material systems that can be integrated into textiles, creating fabric-based soft robots. I propose that the robotic platforms used for soft robots be broadened past silicone or polymer matrix composites, and be extended to include fabrics, which are known for their extreme deformability, versatility, and customizability. Specifically, chapter 4 shows how integrating multiple materials into a single fiber allows for a control of a multifunctional system that operates off of a single stimulus. Also, chapter 4 explores how the choice of polymer material allows for coupling and decoupling of the functional mechanisms, providing flexibility on the control scheme while implementing these single-stimulus fibers in soft robotic components. Chapter 5 shows that it is possible to integrate a conductive material into fabric to provide a feedback-control mechanism for integrated fiber actuators. This imbues the passive fabric structure with functionality, while only requiring the addition of an electrode to connect to the sensor via a sewn-in conductive thread. What follows are the two (modified) abstracts for the chapters, summarizing the work therein.

In chapter 4, I introduce active variable stiffness fibers that are made from shape memory alloy and thermally responsive polymers. This combines the actuation of shape memory alloy with the variable stiffness of a thermoplastic using electric current as the stimulus. By combining both actuation and variable stiffness functions, the multifunctional fibers can move to a new position then hold that position without requiring additional power. I explore the possibility of tuning the fibers to meet varying structural and performance demands by selecting different thermoplastics with different glass transition temperatures. Finally, I integrate the active variable stiffness fibers into a fabric to demonstrate multifunctional robotic fabrics that can control the motion of soft, compliant bodies from their surface.

In chapter 5, partnered with the primary author of the study, I build on the work presented in chapter 4, separating out the action and stiffness fibers, but adding in sensing improving each component for use in a fabric-based robot. I explore the use

of thin, fiber-like systems for integration into fabric I explore the use of a flattened shape-memory-alloy wire as a possible thin-body actuator, and demonstrate its effectiveness at pure-bending motion. This contrasts with typical fiber actuators which rely on axial contraction alone, such as those presented in chapter 4. I also present a stiffness-changing fiber based on a glass-transition polymer epoxy with low-melting-point metallic alloys inclusions that is capable of a stiffness change of two orders of magnitude using Joule heating. Finally, by embedding sensors within the fabric substrate, the fabric itself becomes multifunctional as both the linking structure and the source of proprioception for the whole system, I show the utility of this pairing by demonstrating closed-loop control over antagonistically paired actuation fibers sewn into the fabric substrate. Additionally, by integrating actuation and stiffness change into fabric, applications of damage-responsive tourniquets, self-deploying structures, and collapsible airplane wings become possible.

4. ACTIVE VARIABLE STIFFNESS FIBERS FOR MULTIFUNCTIONAL ROBOTIC FABRICS

The following chapter is based on work previously published as [62] M. C. Yuen*, R. A. Bilodeau*, and R. K. Kramer, “Active Variable Stiffness Fibers for Multifunctional Robotic Fabrics,” IEEE Robotics and Automation Letters, vol. 1, no. 2, pp. 708–715, Jul. 2016. Copyright ©2016 IEEE, reproduced with permission.

* indicates co-first-authorship

Contributions: This chapter was worked on primarily by two individuals: myself and Dr. Michelle Yuen, in a tight collaboration. We both contributed equally to the development of the manufacturing techniques for the multifunctional fibers. Michelle did the bulk of the stiffness characterization with me acting as support, and I did the bulk of the force characterization with her acting as support. We contributed equally to creation of the demonstrations showing the utility of the fibers, as well as to the text of the final manuscript.

4.1 Introduction

The emerging field of soft robotics aims to bring highly deformable electromechanical systems for applications in wearables, search-and-rescue, medical devices, exploratory robots, and more. This field actively pushes forward non-conventional actuators, sensors, and structures while removing the frames, motors, and linkages associated with traditional robots. To achieve versatility in soft robotic design, we envision robotic fabrics bringing actuation, sensing, and stiffness control to the exterior of integrated systems. Robotic fabrics are 2D fabrics that can wrap around any highly deformable 3D object (e.g. an inflatable balloon or foam) to create a soft robot. These fabrics are currently expanding the possibilities of wearable and conformable robotics by adding function to textiles and manipulating soft-bodied objects [10, 63, 64]. With no fixed shape of their own, robotic fabrics can exist on the

surface of deformable objects and in spaces that do not have a pre-defined geometry or volume.

In this paper, we introduce active variable stiffness fibers (AVS fibers) made from a combination of shape memory alloy and thermally responsive polymers (e.g. thermoplastics). This combination couples the actuation of shape memory alloy with the passive softening/holding capabilities (variable stiffness) of a thermally responsive material using only a single input: electric current. We have previously demonstrated variable stiffness using a thermoplastic in a fabric-based system [65] and the integration of shape memory alloy (SMA) into fabric to form compliant and actuating planar structures [10]. This paper combines these two bodies of work into an integrated, active, variable stiffness material that demonstrates performance as a multifunctional active variable stiffness fabric (AVS fabric). By combining both actuation and variable stiffness functions, the AVS fabric can change the position of a soft structure and hold the new position without requiring additional power. Figure 4.1 shows the AVS fiber sewn into muslin fabric (an inextensible cotton textile) to form an AVS fabric.

This paper contributes the following innovations: (1) integrated actuation and variable stiffness functions in a single fiber, enabled by a novel room-temperature manufacturing technique that avoids activation of the thermally responsive materials during processing, (2) coupled and un-coupled actuation and variable stiffness, achieved by tuning the thermoplastic's glass-transition temperature either higher or lower than the activation temperature of the SMA actuator, and (3) multifunctional fabrics with integrated active variable stiffness fibers. The integrated fabric demonstrates both actuation and variable stiffness on-demand. The fabric acts as a connecting medium where multiple fibers can be integrated and activated in parallel, thereby increasing overall lifting and holding capacity. Figure 4.1(a-b) demonstrates the AVS fabric lifting a 200 g mass and holding it suspended even after power has been shut off to the system. The serpentine pattern of the stiffness element enables the fabric to support the 200g mass suspended between two blocks when not activated

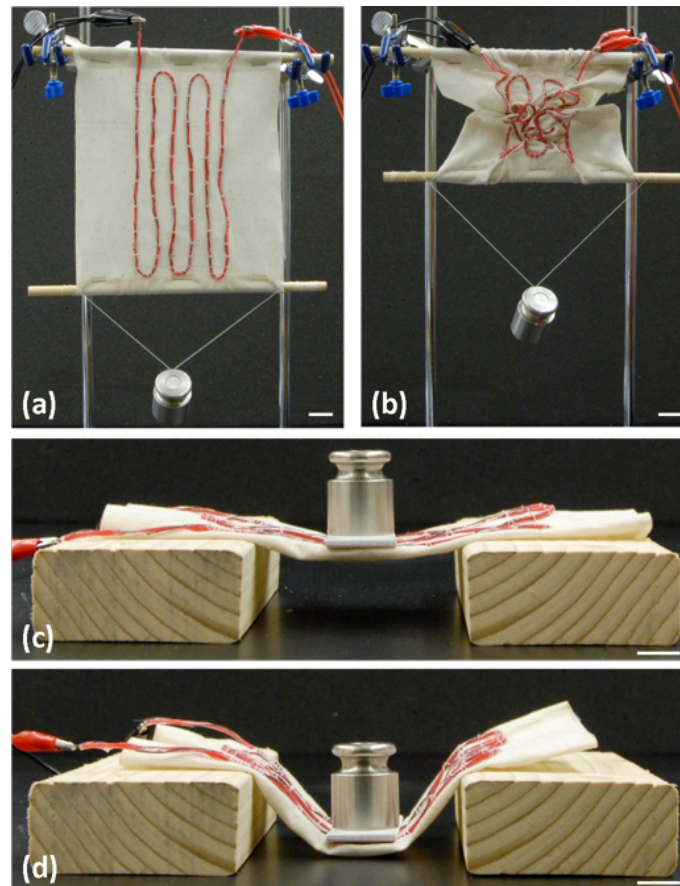


Figure 4.1. Active variable stiffness fabric composed of active variable stiffness fibers sewn onto inextensible muslin fabric. (a) Unactuated, stiff AVS fabric with a hanging 200 g mass. (b) Actuated then stiffened AVS fabric holding a 200 g mass. (c) Unactuated, stiff AVS fabric acting as a bridge supporting a 200 g mass on a small plate. (d) Unactuated, softened AVS fabric sinking under the weight of a 200g mass. Scale bars are 2 cm.

(Figure 4.1(c)). After being softened, the fabric is then allowed to deform under the weight (Figure 4.1(d)).

4.2 Previous Work

Variable stiffness actuators for soft machines have taken two approaches: system-level and material-level. System-level variable stiffness actuators contain elastic and/or damping elements or employ control algorithms to tune the stiffness and impedance of the device [66–72]. Variable stiffness actuators may also derive their stiffness control at the material level. For example, the McKibben actuator is a widely-used soft pneumatic actuator, consisting of a braided mesh that shortens in length and increases in stiffness as it is inflated with air (the stiffness and actuation are coupled) [73, 74]. Similarly, changes in both volume and rigidity have been demonstrated by swelling of polymer gels [75]. Wang, et al. developed a composite system using SMA wire actuators and a low-melting point fusible alloy as a variable stiffness component, then encapsulated both in a silicone elastomer [76].

Multifunctional fibers have been developed by researchers to duplicate the tensile strength and actuation capabilities of natural muscle fibers. Approaches include the use of carbon nanotubes to create a conductive, strong fiber [77–79], with a disadvantage of small displacements (less than 5%), micron sizing, and an inability to maintain a structural shape. Other recent work created fibers using polymer structures [80], but these fibers also only provide actuation and tensile strength without structural rigidity.

In the broader community of robotic fabrics, shape memory alloy wires are a common actuator choice due to ease of integration by stitching [10], felting [63], weaving [81, 82], and other fixture methods [64]. Previously demonstrated active fabrics have been used in robotic applications [10], kinetic and technical garments [63, 83], and self-deploying structures [81, 84]. Our previous work demonstrated variable stiffness fibers integrated into fabrics to distribute stiffness control over a surface [65].

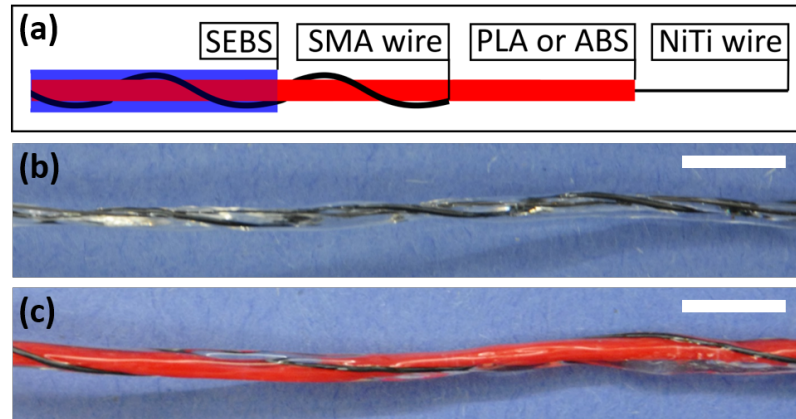


Figure 4.2. Active variable stiffness fibers. (a) Diagram of the composition of an AVS fiber. (b) PLA-based AVS fiber (the PLA core and the SEBS coating are both transparent). (c) ABS-based AVS fiber. Scale bars are 1 cm.

These fibers leveraged the glassy-rubbery transition in thermoplastics for variable stiffness function.

4.3 Materials

The active variable stiffness (AVS) fibers were composed of an actuating shape-memory alloy (SMA) wire and a variable stiffness (VS) fiber, bound together with a polymer rubber as seen in Figure 4.2. The SMA wire actuator, composed of a nickel-titanium (NiTi) alloy (Dynalloy, 0.508 mm dia.), changes shape to return to a programmed helical coil when heated above its activation temperature (70°C - 75°C). The VS fibers were composed of a heating element coated with a film of thermoplastic that changes stiffness in response to temperature. Our previous work utilized unprogrammed NiTi wire (Dynalloy, 0.254 mm dia.) encased in a thin coating of polylactic acid (PLA) (Open Source Printing, LLC) [65]. Here, we built on this work and also introduced acrylonitrile butadiene styrene (ABS) (MakerBot Industries, LLC) as a variable stiffness coating. Both types of VS fibers reduced in stiffness when the thermoplastic was heated above its glass-transition temperature (T_g): 55°C - 65°C for

the PLA [65], and 105°C for the ABS (manufacturer specified). Though ABS has a lower stiffness than PLA, we included it in this study because it has a higher T_g than the SMA transition temperature. This allows us to couple and decouple the variable stiffness effect from the SMA actuation, using the PLA and ABS as the stiffening material, respectively. The SMA actuator and VS fibers were bound together by encapsulating them with polystyrene-*block*-poly(ethylene-*ran*-butylene)-*block*-polystyrene (SEBS) (Sigma-Aldrich, $M_w = 89,000$), a polymer rubber that withstands the operating temperatures of the fibers and remains rubbery even below room temperature.

We note here that although the NiTi heating wire used in the VS fibers can also exhibit the shape-memory effect if properly programmed, in our work it was used purely for its efficacy as a Joule heater. In the following discussions, the heating wire in the VS fibers will be referred to as NiTi wire; the SMA actuator will be referred to as SMA wire.

4.4 Manufacturing Methods

4.4.1 Variable stiffness fibers

In this work, we manufactured two varieties of AVS fibers: ABS-based and PLA-based. Drawing upon our previous work, PLA-based variable stiffness fibers are manufactured by drawing 0.254 mm diameter NiTi wire through melted PLA thermoplastic as described by Chenal, et al. [65]. Our resulting fiber diameter was 1.50 ± 0.28 mm (95% confidence).

In order to process the ABS, an amorphous polymer with no true melting point, we developed a solvent-based approach to manufacture the VS fibers at room temperature (25°C). ABS filament (1.75 mm dia.) was cut into approximately 1 cm long pellets and then placed in a solvent (2-butanone, Sigma-Aldrich) at a 50% polymer (by weight) concentration. The mixture homogenized over a 12hr period, and was then transferred into a syringe tipped with a T-junction (4mm inner dia.). The solution was allowed to degas for 4hrs. To coat the wire, the NiTi wire was fed through the

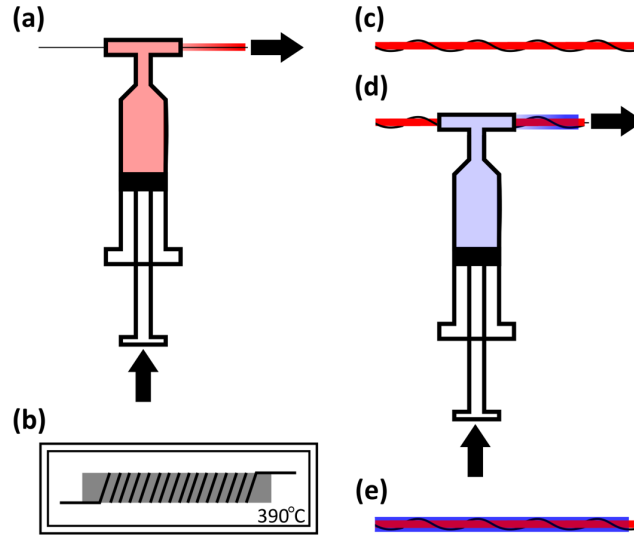


Figure 4.3. Manufacturing ABS-based active variable stiffness fibers. (a) Coating ABS solution onto a heating NiTi wire for variable stiffness fiber. (b) Programming active SMA wire into a helical coil in a 390°C oven. (c) Twisting the programmed SMA wire onto the variable stiffness fiber. (d) Encapsulating the twisted wires with SEBS. (e) Completed AVS fiber.

T-junction, as shown in Figure 4.3(a), at a constant rate of approximately 30 cm/min. Simultaneously, pressure was applied to the syringe to ensure the T-junction was full of the ABS mixture. At this rate of pull, the resulting thickness of the variable stiffness fiber was 2.08 ± 0.80 mm (95% confidence).

4.4.2 SMA actuator

The SMA actuator was programmed through the following series of steps. The wire was coiling tightly onto a 9.525 mm diameter shaft (Figure 4.3(b)) as tension was applied to the wire. The wire was then secured onto the shaft using two collars. The shaft was then placed in an oven at 390°C for 10 min and then quenched and dried [85]. This cycle was repeated 10 times to ensure shape fixity.

4.4.3 Integration into AVS fiber

After the coating on the VS fiber solidified either by cooling or solvent evaporation, the SMA wire and VS fiber were twisted around each other in the same direction as the SMA's programming coil to prevent internal torsion, as demonstrated in Figure 4.3(c). This twist had a pitch of approximately 0.25 (ABS) and 0.4 (PLA) rotations per cm, influenced by the diameter of the VS fiber. The low-pitch twist bound the SMA wire and the VS fiber with a slight mechanical connection in anticipation of the next processing step. The twisted pair was then passed through a T-junction filled with a polymer solution (Figure 4.3(d)) composed of SEBS polymer and toluene (30% polymer, by weight), prepared in a manner similar to the ABS 2-butanone solution, to bond the two components together. After the toluene evaporated from the SEBS coating, the AVS fiber was complete (Figure 4.3(e)). The final diameter of the ABS-based AVS fiber was 2.78 ± 0.20 mm (95% confidence); the final diameter of the PLA-based AVS fiber was 2.04 ± 0.18 mm (95% confidence). Because of the VS fibers' small diameter, the twisted SMA can be approximated as linear along the length of the VS fiber, allowing the SMA to deform without interference when activated.

4.5 Characterization

4.5.1 Stiffness Characterization

We characterized the AVS fibers with the thermoplastic in the inactive (stiff, glassy) state and active (soft, rubbery) state. We did this with a 3-point bending test using an Instron 3345 as seen in Figure 4.4(a). The distance between supports was 5 cm and the nose radius was 5 mm. In our tests, strain was applied at a rate of 0.01 (mm/mm)/min. The glassy state tests were performed at room temperature (25°C). To achieve the rubbery state, the VS fibers, contained within the AVS fibers, were activated for 5 s at $I=0.75$ A before the start of the test to transition the

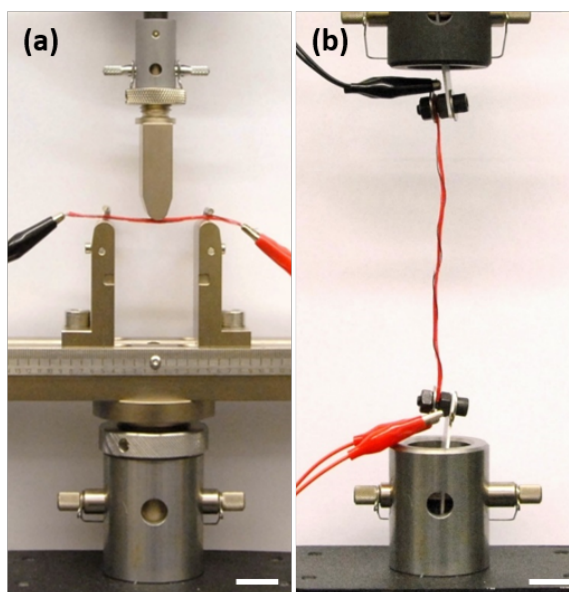


Figure 4.4. Setup for characterization of AVS fibers. (a) Stiffness characterization using a 3-point bending setup. (b) Force and load characterization setup. Scale bars are 2 cm.

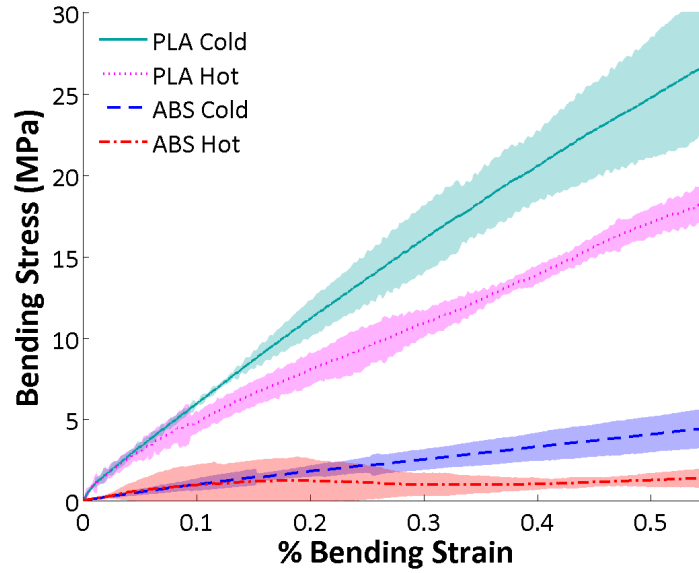


Figure 4.5. Stress-strain plot for two AVS fibers in a 3-point bending setup. A PLA-based and an ABS-based AVS fiber were tested repeatedly in stiff (cold) and softened (hot) states. The shaded area around each average line represents a 95% confidence interval.

Table 4.1. Bending modulus of ABS- and PLA-based AVS fibers with the stiffening thermoplastic heated ($> T_g$) and cooled (25°C). \pm value is 95% confidence on mean.

		Bending modulus (GPa)	
		Cold VS fiber	Hot VS fiber
ABS	Specimen 1	0.89 ± 0.12	0.34 ± 0.24
	Specimen 2	0.72 ± 0.18	0.17 ± 0.25
	Specimen 3	0.57 ± 0.16	0.17 ± 0.20
	Average Modulus	0.73 ± 0.15	0.23 ± 0.23
PLA	Specimen 1	3.91 ± 2.60	0.42 ± 1.31
	Specimen 2	4.73 ± 3.09	0.82 ± 0.26
	Specimen 3	5.12 ± 3.70	2.52 ± 1.09
	Average Modulus	4.59 ± 3.13	1.25 ± 0.89

thermoplastic into the rubbery state. Each fiber specimen was tested three times in both glassy and rubbery states.

The bending modulus, calculated as the ratio of the bending stress to the bending strain, was determined for three specimens of each type of AVS fiber. The 3-point bending test provided a set of stress-strain data points that follow a linear trend in the elastic range of the material (Figure 4.5). We fit a straight line to each data set to obtain the bending modulus from the slope of fitted line, given in Table 4.1. This table shows the bending modulus fluctuated from one specimen to another. We attributed the variation between the values from each specimen to two sources: manufacturing inconsistency and geometric anisotropy. Manufacturing inconsistency refers to variation in the thermoplastic and SEBS coating thicknesses, which resulted in variance in the cross-sectional geometry of both the VS fibers and the AVS fibers. The geometric anisotropy of the AVS fibers arises from the change in position of the SMA wire relative to the loading direction as the fiber is rotated during the 3-point bending test. The maximum stiffness configuration occurs when the loading direction is aligned with the axis passing through the center of both the VS fiber and SMA, and the minimum stiffness configuration occurs when the loading direction is orthogonal to this axis. To ensure that the measured values are within reason, we performed a stiffness analysis of the cross-section by integrating the second moment of area and elastic modulus to determine the overall bending modulus of the AVS fibers in their stiffened state. By considering the upper and lower extremes for both coating thicknesses and geometric anisotropy, we calculated possible modulus ranges as 0.453-4.80 GPa and 2.11-7.70 GPa for the ABS-based and PLA-based fibers, respectively. These ranges include the values that we measured (Table 4.1), confirming that the spread of the experimental values is within reason.

The bending modulus was also determined as a function of current for a single representative ABS-based AVS fiber specimen (Figure 4.6). We varied the current from 0 A to 1 A, focusing on the currents near the transition from the stiff to soft state. A sigmoidal curve fit to the experimental data follows the trend expected of a thermoplastic's modulus going through its T_g [86]. However, the trend breaks at the higher currents (represented by the 1A data point) when the heated VS fiber is hot

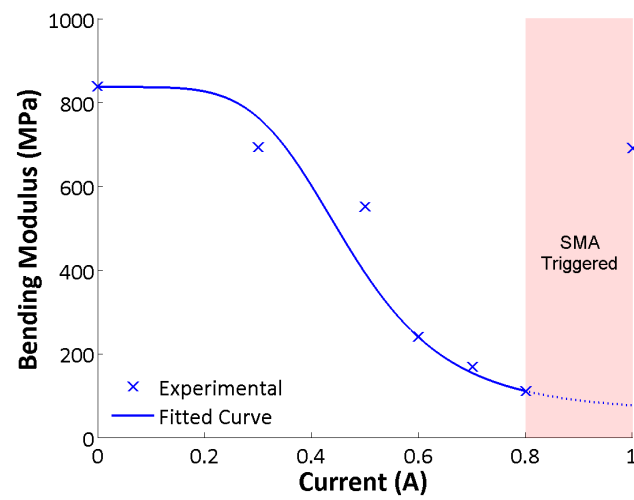


Figure 4.6. Stiffness characterization plot for a single ABS-based AVS fiber softened with various currents. At high currents, the SMA actuator begins to activate during the stiffness test resulting in an increased modulus.

enough to trigger activation of the adjacent SMA actuator, transitioning the SMA from its flexible martensite phase into a stiff austenite phase, thereby increasing the general bending modulus of the AVS fiber. This curve provided us with a range of currents to use that would soften the ABS-based AVS fiber. The PLA-based AVS fibers were not characterized in this work, as a similar analysis appears in previous work done by Chenal, et al. [65].

The average modulus values presented in Table 4.1 shows that the ABS-based fibers are softer than the PLA fibers both when stiffened and softened. To determine how the stiffnesses of the fibers affect actuation, we subsequently performed force tests on the fibers.

4.5.2 Force and Load Characterization

To characterize the force produced by the AVS fibers, 10 cm long AVS fiber segments were clamped in an Instron 3345 fitted with a 50 N load cell (Figure 4.4(b)). Throughout the test, the specimens were held in tension at a fixed length to measure the force produced by the isometrically actuating SMA when the VS fiber was both stiff and softened.

In contrast to the stiffness tests, only the ABS-based AVS fibers were tested for force in both their stiffened and soft state. The PLA-based fibers were tested only in their soft state, because the PLA stiffness cannot be decoupled from the SMA actuation. Since the T_g of PLA is below the activation temperature of SMA, when the SMA is powered the PLA will soften regardless of whether or not the VS fiber is powered. This effect does not occur in the ABS-based fibers because the T_g of ABS is above the activation temperature of SMA—only overheating the SMA will cause the ABS to transition into the rubbery state.

We averaged the tests from multiple segments of the ABS-based AVS fiber (Table 4.2). When the ABS was softened, the SMA was able to produce 2.25 ± 0.17 N of actuation force. In contrast, when the ABS was stiff, the testing apparatus was unable

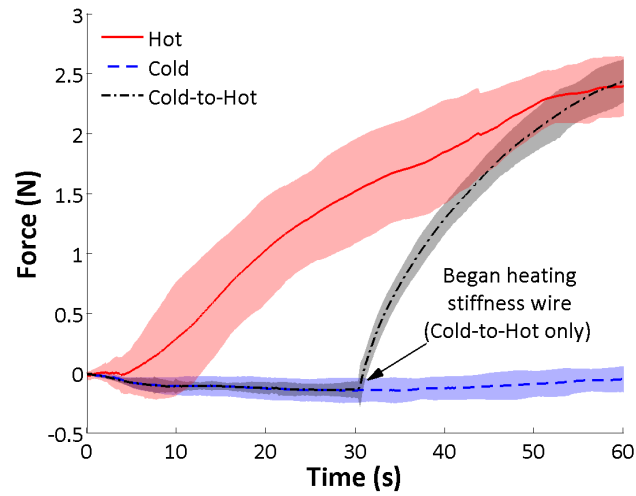


Figure 4.7. Plot of force produced by an ABS-based AVS fiber. Hot: VS fiber was softened before SMA actuation. Cold: VS fiber was not softened before SMA actuation. Cold-to-Hot: VS fiber was softened 30 s after the SMA was actuated. The shaded area around each average line represents a 95% confidence interval.

Table 4.2. Force produced by the SMA actuator portion of ABS-and PLA-based AVS fibers in the softened and stiffened state. \pm value is 95% confidence on mean.

		Force (N)
ABS-based fiber	Soft state	2.25 ± 0.17
	Stiff state	-0.09 ± 0.22
PLA-based fiber	Soft state	1.04 ± 0.30
	Stiff state	N/A

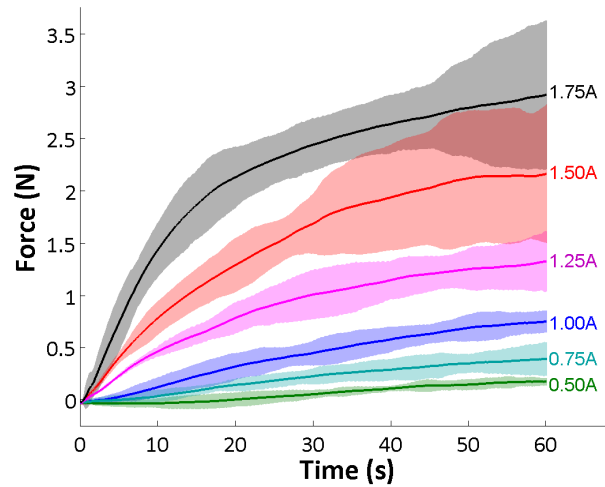


Figure 4.8. Plot of force produced by an ABS-based AVS fiber as a function of applied current. The VS fiber was softened prior to the start of each run. The currents applied ranged from 0.5 A to 1.75 A in increments of 0.25 A. The shaded area around each average line represents a 95% confidence interval.

to detect any pulling forces from the SMA wire. The negative force values result from the hot SMA reducing the whole fiber's modulus slightly. This test demonstrates that the ABS-based AVS fiber will maintain its position when the VS fiber is inactive, even when the SMA is powered. The results also show that the ABS-based AVS fibers produce higher forces compared to the PLA-based AVS fibers. This is likely due to both the PLA having a higher bending modulus than ABS in its soft state (Table 4.1) and the soft ABS adding heat to the SMA wire.

In Figure 4.7, we plotted the data from a single ABS-based AVS fiber showing the force being generated from the active SMA wire over time for 60 s. The fiber was subjected to 3 operating conditions: 1) actuation of the SMA without softening the ABS, 2) actuation of the SMA after softening the ABS, and 3) actuation of the SMA for 30 s prior to softening the ABS. These conditions are shown in Figure 4.7 as “Hot”, “Cold” and “Cold-to-Hot”, respectively. The plot clearly shows that the fiber follows the zero-force trend when the fiber is stiff, but once the fiber is softened,

the actuating SMA is able to produce force. This demonstrates complete decoupling of the actuation and stiffening components in the ABS-based AVS fibers.

We further characterized a single ABS-based AVS fiber for the force produced as a function of current applied (Figure 4.8). For all of these experiments, the VS fiber was softened prior to actuating the SMA, identical to the “Hot” tests shown in Figure 4.7. We measured the amount of force produced by the fiber over 60 s of applied current across a range from 0.5 A to 1.75 A. As expected, increasing the input current results in increased output force, showing that the incorporation of the SMA actuator in an AVS fiber does not change the SMA actuation behavior [85].

In addition to the force generation experiments, we also characterized the load capacity of the fibers and SMA wire in their stiffened, coiled shape. The fibers and wire were first actuated (without load) then cooled into a fully contracted coil. This stiffened coil was then placed in the same Instron setup shown in Figure 4.4(b). We applied a constant linear displacement of 10 mm/min to the coil and measured the resulting load. The resulting load-extension curve indicated that the coils behaved as linear springs with spring constants of 3.85 ± 2.91 N/m for the SMA wire, 22.2 ± 6.28 N/m for the PLA-based AVS fibers, and 51.8 ± 14.8 N/m for the ABS-based AVS fibers (95% confidence).

4.6 Applications

4.6.1 Single-fiber active lifting and passive holding

To demonstrate the “move and hold” potential of AVS fiber, we lifted a 47 g mass with the AVS fiber and then removed power to the system, allowing the fiber to passively hold the weight. As shown in Figure 4.9, we compared a programmed SMA actuation wire with the PLA-based and ABS-based AVS fibers. The bare SMA actuator wire is identical to the actuation wire in the AVS fibers. To set up the test, we clamped a 15 cm segment of the fiber to a support, then hung a mass from the free end of the fiber, applying a downward force. The bottom leads of the fiber were

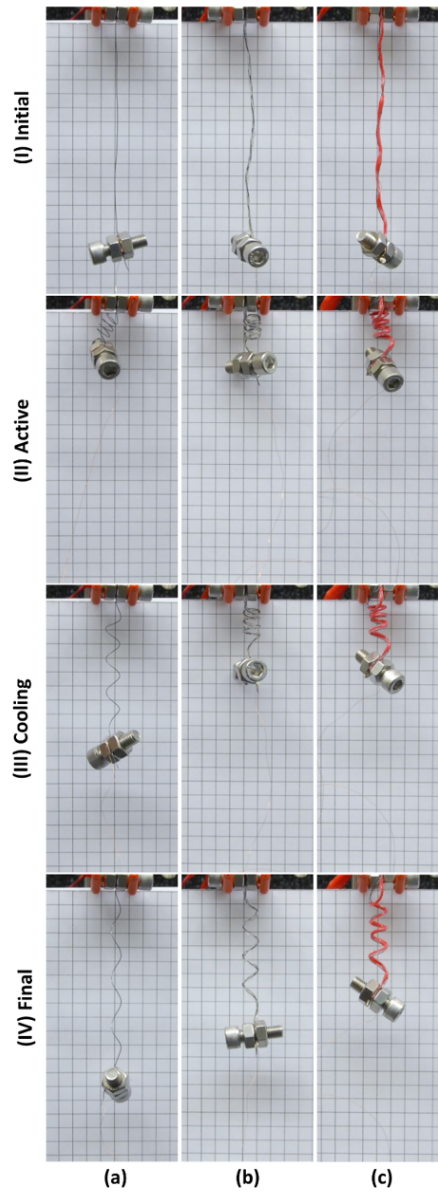


Figure 4.9. Comparison of an actuation cycle of (a) an SMA wire, (b) a PLA-based AVS fiber, and (c) an ABS-based AVS fiber. The top of the fiber is fixed and a 47 g mass is attached to the hanging end of the fiber. The mass acts as an electrode, with a small copper wire attached to it. From top to bottom: (I) the fiber is not actuated, (II) the fiber is softened and fully actuated, (III) all power is turned off to the fiber, and it is allowed to cool for 15 s, (IV) the fiber is completely cooled. For scale, each square is 1 cm².

attached to the weight making it a common ground for the fiber. A small copper wire of negligible mass (0.2 g) was attached to the weight and traveled with the weight to maintain electrical contact.

For each test, after hanging the fiber, the NiTi wire was heated briefly to soften the variable stiffness thermoplastic (Figure 4.9(I)). Current was then applied to the SMA actuator to lift the weight. Both the VS fiber and SMA wire were powered until the SMA actuator achieved maximal displacement (Figure 4.9(II)). At this point, all power to the fibers was shut off, and the entire AVS fiber was allowed to cool. The AVS fiber relaxation was recorded 15 seconds after the power was shut off (Figure 4.9(III)) and 5 minutes later (Figure 4.9(IV)) when the fibers had completely cooled. The SMA wire was tested using this same procedure, without the initial step of heating up a variable stiffness fiber prior to actuation.

Figure 4.9 presents the results of this test. The bare SMA wire lifted the bolt higher than the AVS fibers by 1 cm, but once the power was disconnected the weight dropped 11 cm (85%) (Figure 4.9(a)). The PLA-coated AVS fiber lifted the bolt 12 cm, but lost 7 cm (58%) of this initial displacement during cooling (Figure 4.9(b)). In comparison, the ABS-based fiber lifted the bolt up 12 cm and then, upon cooling, only lost 4 cm (33%) of its actuation height (Figure 4.9(c)).

According to the previously calculated spring constants, the displacement (the distance between actuation height and final height) for each fiber type was predicted as 11 cm, 2.08 cm and 0.89 cm for the SMA wire, PLA-based, and ABS-based fibers, respectively. While the actual displacement of the SMA wire was consistent with the predicted displacement, the actual displacement of the AVS fibers was greater than predicted. We attribute this discrepancy to the cooling and re-stiffening period of the thermoplastic. As the AVS fibers cool down (Figure 4.9(III)), the ABS is able to drop below its T_g and stiffen even while the SMA is still at its activation temperature. In contrast, the PLA remains soft while the SMA cools below its activation temperature. With no lifting force, the weight can stretch out the PLA-based fiber more than the ABS-based fiber. This explains why both fibers dropped more than their spring

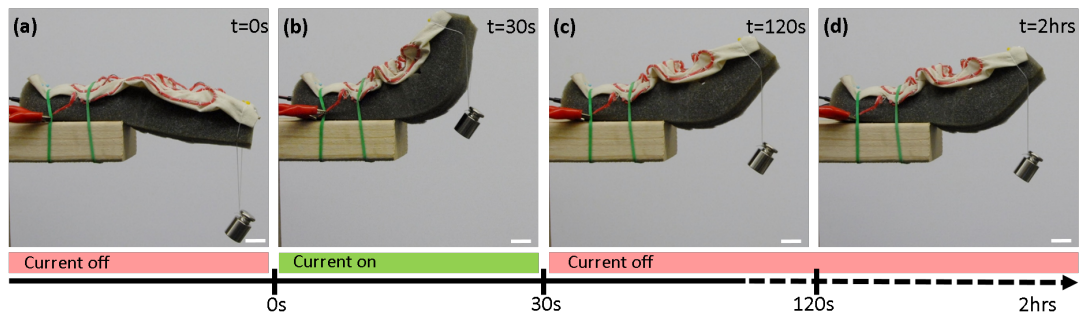


Figure 4.10. AVS fabric attached to a cantilevered foam block to create a soft robotic lifting arm structure. One end of the foam block is fixed; the other end is free and supports a 50 g mass. (a) AVS fabric is stiff, (b) AVS fabric is softened and fully actuated, (c) AVS fabric is stiff and cooling, and (d) Robotic arm structure sustaining mass for extended period of time with no additional power input. Scale bars are 2 cm.

constants predicted, as well as why the PLA-based fiber dropped an additional 5 cm when the ABS-based fiber dropped only an additional 3 cm.

It is important to note that the bare SMA wire actuated significantly faster than the other two AVS fibers. Though we did not record the data precisely, the overall activation time for the SMA wire was 20-30 s shorter than the tests for the AVS fibers (about 60-70 s).

4.6.2 AVS fabric for conformable robotic skins

The second test demonstrates the potential of these AVS fibers to be used in robotic fabric. We sewed a long ABS-based AVS fiber to a strip of cotton fabric, creating a fabric capable of manipulating objects from their surface. The AVS fiber adds both structure and function to the fabric, giving the fabric the ability to mechanically manipulate objects (Figure 4.10). Figure 4.1(a-b) shows the AVS fabric used in this demonstration in both a flattened and actuated state. The holding capability of the ABS-based fibers from the first demonstration encouraged us to choose these fibers over the PLA-based fibers in our final demonstration. We stitched the AVS fiber at 2 cm intervals in a serpentine pattern consisting of six lines. This stitch length adequately secured the AVS fibers to the fabric without constricting the AVS fiber deformation during actuation.

We attached the AVS fabric to the top of a foam block as shown in Figure 4.10(a) to simulate a soft robotic arm. The foam block was fixed in a cantilever position with a 50 g mass suspended from the free end. In Figure 4.10(a), the fabric is stiff with the mass causing the foam block to sag. After softening the VS fiber with 0.75 A of current and actuating the programmed SMA for 30 s at 1.5 A, the fully actuated state of the AVS fabric is attained (Figure 4.10(b)), lifting the mass 10 cm. Immediately after full actuation, power was disconnected to the fiber and the AVS fabric was left to cool. While the AVS fabric was cooling to a glassy, stiffened state, the spring-force of the curled foam block and the weight of the 50 g mass pulled the foam arm

partially down from the fully actuated position (Figure 4.10(c)). The soft robotic arm structure then sustained the weight 5.75 cm higher than its original position with no additional energy input, for 2 hours. Figure 4.10(d) shows the structure holding the weight, with the weight only dropping an additional 0.75 cm from the 2 minute mark in Figure 4.10(c). This small drop in position can be attributed both to creep in the polymer and the AVS fabric not having fully cooled at the 2 minute mark.

4.7 Conclusion and Future Work

In this work, we have demonstrated active variable stiffness fibers for use in conformable robotic applications. The active variable stiffness fibers are comprised of two functional elements intertwined: a variable stiffness fiber and an actuating shape memory alloy wire. Both fibers are activated by thermal energy generated by Joule heating. The active variable stiffness fibers can actuate and sustain displacements even after power has been disconnected from the system.

We introduced active variable stiffness fibers using two different thermoplastics: PLA and ABS. Because the T_g of PLA is below the SMA activation temperature, the variable stiffness effect is coupled to SMA actuation. In contrast, the T_g of ABS is higher than the SMA activation temperature, and thus the variable stiffness and actuation are decoupled. The fibers were characterized for their change in stiffness and for force production. We studied the behavior of individual AVS fibers in performing a “move-and-hold” operation, demonstrating an improved holding capacity in the ABS-based due to the decoupled stiffening and actuation. The ABS-based AVS fibers were used to manufacture an active variable stiffness fabric by stitching the fibers onto cotton fabric. By attaching the planar AVS fabric to a soft foam block, motion and stiffness control was imparted upon the foam. Actuation of the fabric caused the foam block to bend and lift a mass, then proceed to hold the deformation without continuous actuation via stiffening of the fabric. This demonstrated that

the 1D capabilities of multifunctional fibers can be extended to 2D surfaces and 3D structures.

Future work will focus on optimization of the manufacturing process and further characterization of the fibers. An improved manufacturing framework would increase control over the cross-sectional geometry of the fibers, allowing for greater customizability and uniformity of the fibers' function. Full characterization of the stiffness and force production would enable a better understanding of the behaviors and functional coupling of the fibers. Additionally, future work may explore the use of other materials, such as alternatives to the stiffening agent and encapsulation polymer, as it is possible to tune the fibers precisely to structural and/or performance requirements. Additionally, a parametric study to determine the effect of different diameters of wire, thickness of polymer coatings, and twisting pitch may contribute to future design optimization. Future work will also explore the effect of different or more complex sewing patterns on the performance of AVS fabrics, as well as the addition of sensing elements for proprioceptive feedback, enabling closed-loop control of a robotic fabric.

5. A METHOD FOR ROBOTICIZING FABRIC BY INTEGRATING FUNCTIONAL FIBERS

The following chapter is based on work currently under review as T. L. Buckner, R. A. Bilodeau, S. Y. Kim, and R. Kramer-Bottiglio, “A Method for Roboticizing Fabric by Integrating Functional Fibers,” Pending Publication, 2020.

Reproduced with permission from senior author.

Contributions: This chapter was worked on primarily by two individuals: Trevor Buckner and myself. I am not a first author on this paper, although I did significant work on the materials characterization, modeling, and executed feedback control on the sensor-actuator fabric, as well contributing technical expertise that lead to the final design of each material component. I did not deserve first author credit as the bulk of the text was written by the first author. I contributed significantly to all of the main figures (the figures with multiple parts), including almost all of the images taken of the materials and the fabric system. The final composition of all of the figures was left to the first author to complete. Any figures the published work in which I had no contributions appear exclusively as supporting information in the original text, and are not included in this dissertation. Worth additional note is that some of the supporting figures are comprised of my work exclusively. Although I did not write the original manuscript, I performed a significant edit and rewrites of large sections of the text of the paper to get it to this current written format.

5.1 Introduction

From natural plant fibers and animal wool to modern glass filaments and synthetic polymer thread, fabrics are among the most ubiquitous and adaptable materials in history. By nature of their interlaced fiber structure, fabrics are breathable, conformable, and highly compactible. Further, their general resiliency to crushing, tearing, and bending positions fabrics as the perfect class of material for wearables and other conformable applications, including specialized products such as extreme weather protective garments, rugged ripstop nylon in parachutes, and bullet-resistant vests. Given these versatile characteristics and unique application design space, the

possibility of roboticizing fabrics could lead to smart adaptive clothing, self-deploying shelters, and lightweight shape-changing machines.

Preliminary work in this area introduced the terms “smart textiles” and “e-textiles” [87–89] to designate fabrics enhanced with electrical circuitry via the development of flexible [90–92] or miniaturized [93, 94] versions of traditional electrical components. In particular, flexible sensors [87, 95, 96], electrically-conductive threads [89, 95], and energy collection devices [97–99] have come forth as potential building blocks for robotic fabrics. There have even been rare demonstrations of wearable fabric devices that use responsive materials for embedded actuation, including self-rolling temperature-sensitive sleeves [100], an orthotic limb support [101], and dynamic compression stockings [102]. While the vast majority of these works showcase the success of individual robotic components, they are generally passive or uncontrolled, and the actuators rely on external actors to “reset” them after a single use or actuation cycle. As many of these concepts rely upon the presence of a host structure, such as the user of a wearable device, the notion of independently functioning fabric machines has also been little-explored [103].

We demonstrate an expanded scope of fabric functionalization, allowing fabric to become a complete standalone robotic platform (Figure 5.1A). Our work addresses several gaps in the literature by introducing a set of functional fibers that unify actuation, structural control, and sensing functions into a cohesive robotic fabric unit (Figure 5.1B, C). By using fiber-like components as the active elements (Figure 5.1D), we retain the desirable qualities of fabric, which opens the way for machines that are not only thin, lightweight, and breathable, but which harness complex curvature and limitless surface configurations as key functions.

Below, we detail the design and optimization of functional fibers as actuators, variable stiffness components, and sensors. We then describe the integration of these functional fibers into robotic fabrics that enable new capabilities, such as reactive wearables and deployable fabric structures.

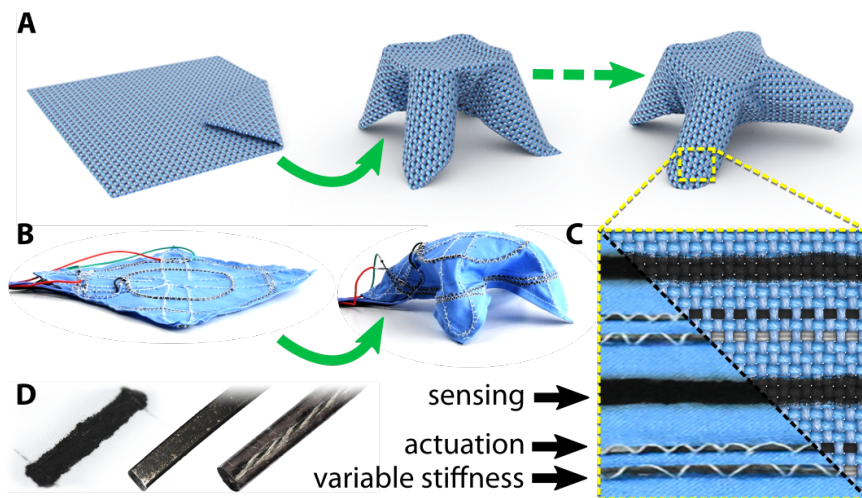


Figure 5.1. Robotic fabrics. (A) Rendering of a potential robotic fabric capable of locomotion. (B) Actualized robotic fabric demonstration. (C) Current robotic fabric vs rendering of potential fully-woven robot. (D) Fiber-form robotic components (from the left: sensors, actuators, and structural supports) can be combined in a variety of ways to create thin fabric-based machines.

5.2 Results

5.2.1 Actuation

As of this writing, motion-generating fabrics have made only rare appearances in end-user products [63]. However, as efforts are made to mimic the stranded muscular tissue in living animals, several different fiber-like actuators of varying utility have come to light [103, 104]. Some of the more promising examples include shape-memory polymers [105], shape-memory alloys [106], electromechanical twisted carbon nanotube yarns [107], and supercoiled nylon strands [108].

We selected Nitinol shape-memory alloy (SMA) wire as our actuating fiber. SMA is electrically conductive and, when programmed to remember a shape, activates with heat. These two traits make electrical control via Joule heating a simple process. SMA wire is usually shaped into a coil or mesh to allow for high-strain linear contraction [106, 109, 110]. We instead utilize SMA wire to generate bending motion (Figure 5.2A), which has typically only been demonstrated using large SMA panels bent into “hinges” [111, 112]. Bending allows the SMA wire to actuate “in-plane” with the fabric substrate (Figure 5.2B), and facilitates reversible antagonistic motion when paired with an actuator on the opposite side of the fabric. Bending wire actuators can also be easily anchored to fabric by couching (Figure 5.2C) – a well-established sewing technique.

One challenge when integrating antagonistic wire bending actuators into a highly flexible fabric is that any off-center forces encourage the wire to twist the fabric rather than purely bend. This contortion can introduce chaotic actuation or even bending opposite the intended direction if the wire turns over within its couching. We overcame this challenge by flattening the round SMA wires (Figure 5.2D) into ribbons (Figure 5.2E), modifying the area moment of inertia such that bending is favored over twisting. Additionally, the couching is able to hold a flattened ribbon tighter to a fabric base, preventing the actuator from overturning.

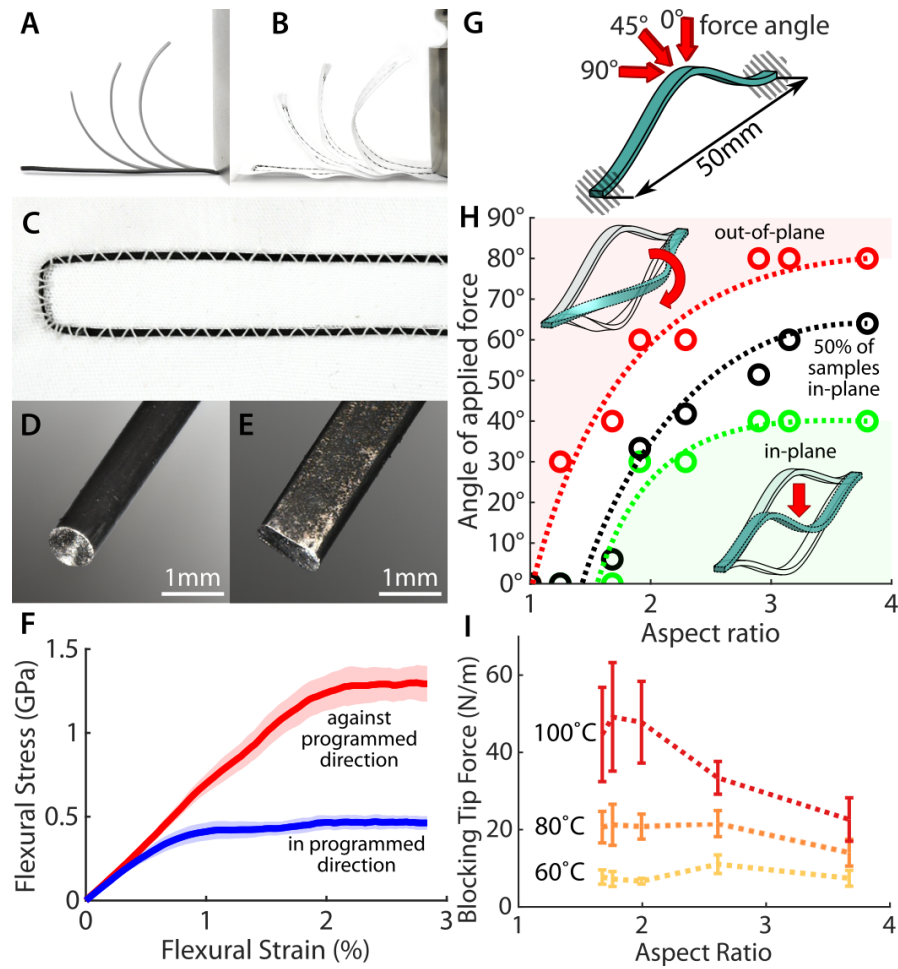


Figure 5.2. Shape memory alloy actuator ribbons. (A) SMA ribbon programmed to exhibit bending motion. (B) Sewn SMA ribbon used to actuate fabric body. (C) Couching method to affix SMA ribbon to a fabric substrate. (D) Initial round SMA wire. (E) Flattened SMA ribbon. (F) Bending an SMA against its programmed direction induces higher flexural stress and encourages the wire to twist instead. Error cloud is 95% confidence interval. (G) Round and flattened wires were subjected to forces at increasing out-of-plane angles to determine bending response. (H) A flattened ribbon will tend to bend and buckle in plane (green), and a round wire will tend to twist and bend out of plane (red). (I) Round SMA actuators tend to generate higher bending force than flattened actuators of comparable cross section. Error bars are one standard deviation.

To elucidate the cause of twisting we studied bi-directional actuation of fabric, where SMA ribbons are used in antagonistic pairs. When its opposing actuator is active, an SMA ribbon is forced to bend backward against its programmed actuation trajectory, building up a spring response within the ribbon. Three-point bending tests revealed that the flexural modulus of our SMA ribbons is consistent regardless of bending direction ($E \approx 66$ GPa), however, plastic deformation occurs at different stresses depending on the bending direction (Figure 5.2F). We surmise that it is this difference in maximum stress that often encourages a wire to twist such that it is again bending “forward”, avoiding excessive buildup of elastic energy.

We characterized the effectiveness of the flattening treatment by measuring the tendency for SMA wires and ribbons of various aspect ratios to remain in the desired bending plane in response to an external force. We clamped the SMA specimens in a pre-buckled configuration and applied a force to the centerpoint at different incoming angles (Figure 5.2G). At an applied force angle of 0° , the wire is expected to experience a snap-through, remaining fully in-plane as it deflects. Conversely, at an angle of 90° , the wire should twist out of plane about the fixed-fixed axis. After recording the dominant behavior (in-plane or out-of-plane motion) for intermediate force angles, the results confirm that by increasing the wire aspect ratio (flattening the wires), they become more resistant to out-of-plane forces and favor in-plane deflection (Figure 5.2H).

‘Activated’ (heated) SMA generates force by building up internal material stresses as its crystalline structure transitions from martensite to austenite [106]. Given that stresses in bending are greatest on the outer surface, we would expect that regions farthest from the neutral axis contribute most to the bending force. That is, thicker wires generally provide larger output forces than a thin ribbon of similar cross-sectional area (Figure 5.2I). Indeed, we see that for flattened wires, the output force is linearly proportional to the area moment of inertia (Supplemental Figure S1). However, round wires underperform, reaching a force-output plateau due to actuation forces being directed out of plane.

As mentioned, when bending in the direction of programmed actuation, plastic deformation occurs at a relatively low stress, which is mostly a result of reversible detwinning of the martensitic crystal lattice [106]. In the reverse direction, it is possible to introduce permanent dislocations and microcracks into the ribbon that interfere with the austenite-martensite transition and adversely affect the programmed actuation [113, 114]. The point at which this damage occurs is determined by the material flexural strength (Supplemental Figure S2A), although measured strength seems to be influenced by the processing steps and was not constant across SMA aspect ratios (Supplemental Figure S2B). We maximize the lifetime of our actuators by avoiding this overstrained regime except for the initial unwrapping and straightening of the ribbon in preparation for the sewing step. By also avoiding excessive temperatures, we have continuously used our antagonistic actuators for upwards of 1,000 cycles with no noticeable degradation.

Given this characterization, we selected an SMA ribbon aspect ratio of 2.5 for all further demonstrations, as it provided a reasonable balance of output bending force, system stiffness, and stable in-plane motion.

5.2.2 Variable-Stiffness Support Structure

Although a fabric might be equipped with locally-reliable actuators, its inherent lack of a supportive structure limits control of the overall robot configuration. By actively softening and stiffening our variable-stiffness (VS) fibers, we can regulate the direction and degree of actuation with higher repeatability and fewer total actuators. In addition, an on-demand support structure allows a robotic fabric to perform move-and-hold operations to sustain loads which would otherwise collapse a typical fabric. VS is possible using many different techniques [115, 116], but expressions of this concept in fiber-like morphologies are limited. The most successful examples include silicone tubes filled with a low-melting-point material [117, 118], strands of glass-

transition polymer [62, 65], and segment jamming via tension in an axial wire [119, 120].

Our VS fibers (Figure 5.3A, B, C) are based upon a thermally-responsive epoxy that softens significantly as it undergoes a glass transition at approximately 60°C [121] (Figure 5.3D, E). We also incorporate a low-melting-point metallic alloy particulate filler (Field's Metal; FM) [122] at a volume ratio of approximately 100:85 (46 vol% FM), which increases the rigidity of the VS fibers when cold, yet melts at 62°C to further soften the material when heated (Figure 5.3F,G). The fibers are Joule heated via an internal conductive stainless-steel thread (Figure 5.3E, F).

We measured the flexural moduli of fibers made from both the neat epoxy matrix and the FM composite over a range of temperatures (Figure 5.3H). The addition of FM raises the maximum rigid modulus while lowering the heated (i.e. soft) modulus [122]. Even with the addition of the flexible stainless-steel core in the fiber, the lower stiffness bound remains below 25 MPa, which is slightly less flexible than latex rubber, and, when in fiber form, well matched to the output force capabilities of our SMA actuators. While the addition of FM enables an increased modulus range, the FM composite has a lower ultimate flexural strength than neat epoxy, which may be due to poor bonding at the interfaces between epoxy and FM particles (Figure 5.3I, Supplemental Figure S3).

Because the response of a thermally responsive fiber is time-dependent, characterizing the time to completely transition between rigid and soft states is crucial for effective control sequencing in robotic fabrics. We measured the thermal conductivity of the VS composite fiber, and as expected when compared to analytical models, the increased volume fractions of FM lead to increased thermal conductivity (Figure 5.3J). We then developed a numeric heating and cooling simulation of the VS fibers under a wide range of material conditions and compared it to experimental data (Supplemental Figures S4 - S8). Fully cooling from a uniform 65°C in free convection takes approximately 70 seconds regardless of FM content (Figure 5.3K). On the other hand, heating times varied slightly depending on the material composition and whether the

Figure 5.3. Variable stiffness fibers. (A) A shaped VS fiber supports a 20 g load. (B) VS fiber sewn onto a fabric substrate. (C) Added support from fabric allows VS fiber to support up to 50 g before legs begin slipping. (D) Neat epoxy VS fiber. (E) Neat epoxy cross-section. (F) FM composite cross-section. (G) FM composite VS fiber. (H) Hot and cold flexural modulus for both the neat epoxy and FM composite (46 vol% FM), with and without stainless steel yarn core used for Joule heating. Error bars are standard deviation. (I) Ultimate flexural strength of the VS fibers. (J) Measured thermal conductivity of the composite vs. vol% of Field's metal, compared with Bruggeman effective medium theory. Error bars are 95% confidence interval. (K) Free convection cooling of VS fibers. Experimental data is for neat epoxy specimens. Numerical simulations for both neat epoxy and FM composite had negligible difference. Inset shows computed cross-sectional thermal gradient for both 0 and 50 vol% FM fibers after 7 s of cooling from 65°C. (L) Numerical simulation results for 'worst case' heating scenario, with the heating core center offset to 2/3 of the VS fiber diameter. Inset shows computed cross-sectional thermal gradient after 6 s of heating at 13W/m.

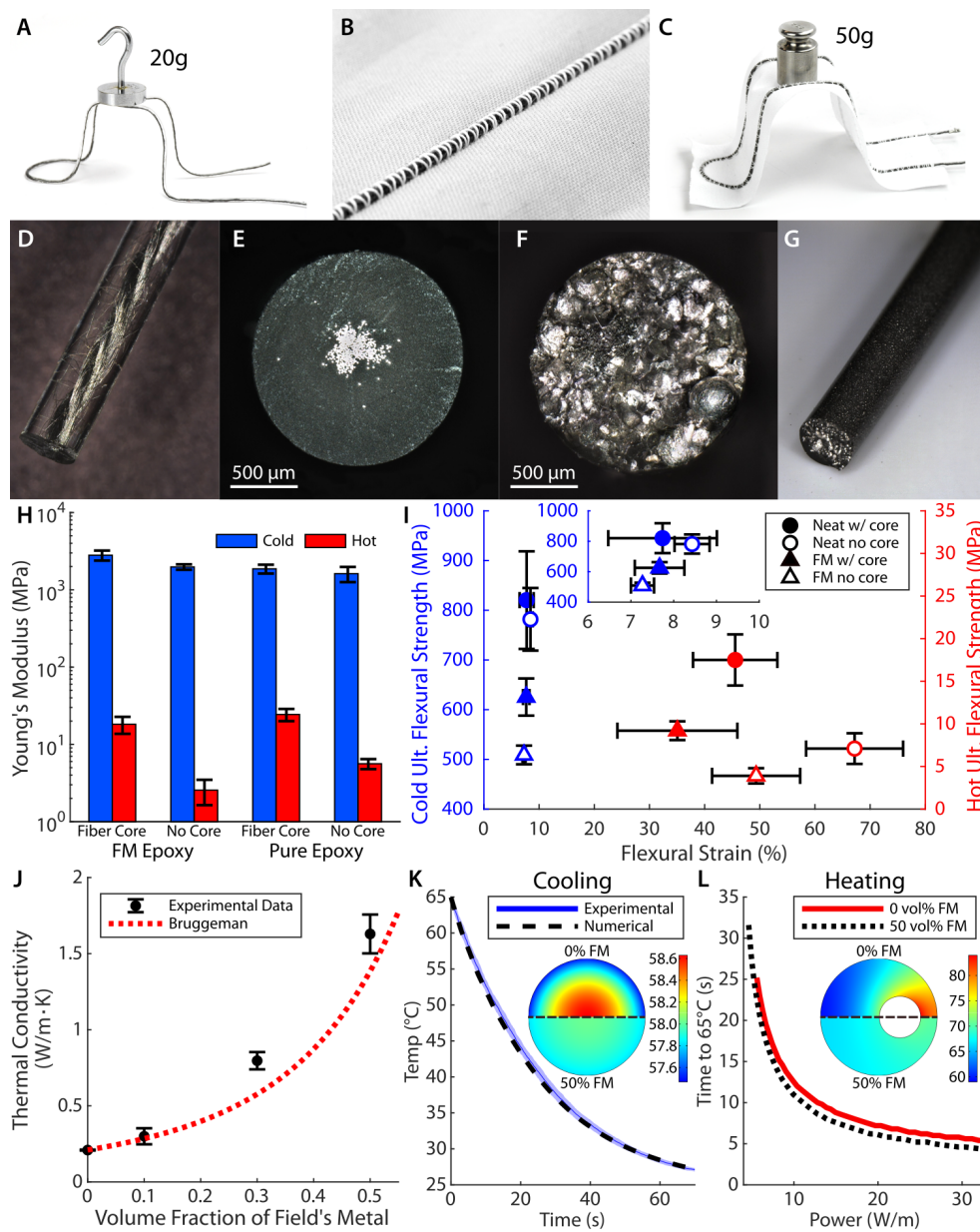


Figure 5.3.

steel heating yarn was properly centered in the fiber (Figure 5.3L). Notably, the increased thermal conductivity from the FM inclusions smooths the thermal gradient in the fiber, reducing hotspots which could result in premature material degradation and cold spots with incomplete phase transitions (Figure 5.3K, L).

With these results, we selectively use both the neat and composite VS fiber formulations depending on the use case, favoring higher stiffness with the FM composite or higher strength with the neat epoxy.

5.2.3 Sensing

An important part of any robot is the ability to sense internal or environmental changes and respond appropriately. To create sensors, we used a self-coagulating, paintable conductive ink, which allows a region of fabric to become highly sensitive to small changes in strain while adding negligible stiffness to the fabric [123]. Composed of a polydimethyl-siloxane (PDMS) precursor emulsified in a carbon black nanoparticle/ethanol suspension, this ink can easily permeate and bond to individual filaments of a fabric (Figure 5.4A, B). Penetration into the fiber weave itself maintains much of the porosity of the fabric (Figure 5.4C, D) and creates an electrically conductive pathway that changes in resistance as the fabric weave is stretched and the gaps present between fibers are enlarged (Figure 5.4E).

By printing this ink on opposite faces of a fabric, sensors can be used to detect structural bending. Despite some permeation through the cloth, the printed face will have a higher density of conductive material, and this small offset from the neutral axis is enough to bias the sensor toward a compression response in one bending direction and extension in the other. The sensor signal is most consistent in extension, so querying the corresponding sensor depending on bend direction leads to repeatable sensor values.

In Figure 5.4F, we show a section of fabric with these printed sensors and two antagonistic bending SMA ribbon actuators attached via couching. The sensor feed-

back made it possible to control the fabric actuation and hold different curvatures (represented as target sensor signals, Figure 5.4G, Supplemental Movie S1). Without VS elements, the device naturally relaxes into a neutral center position when neither actuator is active due to a balance in opposing spring forces in the SMA ribbons.

5.3 Applications

We present a series of demonstrations that utilize the SMA ribbon actuators, VS fibers, and in-fabric strain sensors, suggesting a range of possible applications for robotic fabric.

First, we showcase a robotic fabric tourniquet (Figure 5.5A; Supplemental Movie S2). This device comprises a breathable fabric sleeve with embedded rows of parallel ribbon actuators, VS fibers, and conductive carbon ink traces. When the fabric is severed along one of the conductive carbon ink traces, the damage is detected as a broken circuit and an emergency response is triggered at the damage site. The fabric will compress and then hold that position without further power expenditure (Figure 5.5B, C, D). Each SMA ribbon was measured to contribute $\approx 1.6 \pm 0.1$ kPa, which approaches the recommended arm cuff pressure of ≈ 2 kPa to combat orthostatic hypotension [124]. We expect that further developments and an increased actuator count may achieve the higher pressure of ≈ 26.6 kPa that is recommended to properly cut off blood flow [125]. This type of responsive sleeve could potentially be used as a smart garment in military or exploratory environments, where automatic emergency measures could counteract life-threatening situations if medical aid is not immediately available. By altering the arrangement of actuators, sensors, and VS fibers, it is conceivable that other types of assistive wear could also be created, such as clothing that augments muscular motion, provides dynamic orthostatic pressure, or even simply changes shape to fit different climate conditions.

Second, we demonstrate a shape-changing robotic fabric sheet that functions independently from any host body (Figure 5.5E, F; Supplemental Movie S3). The initial

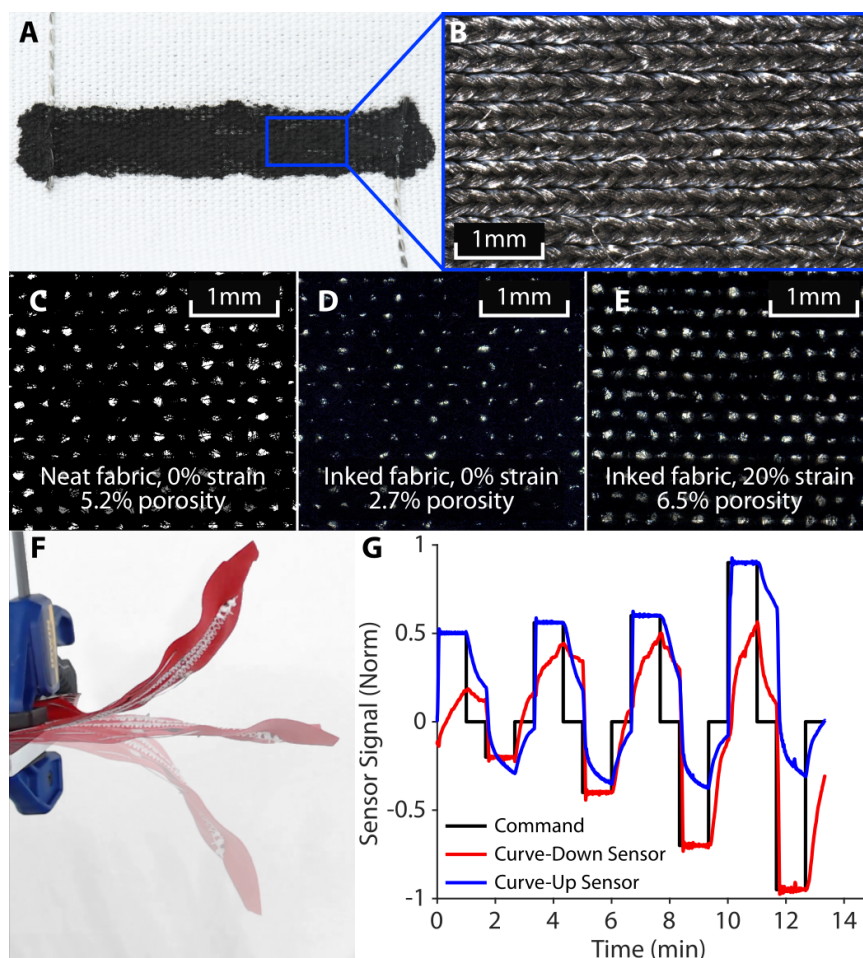


Figure 5.4. Conductive ink sensors. (A) The carbon-black/PDMS/ethanol emulsion is printed directly onto the fabric. The surface conductivity is sufficient such that printed sensor blocks can be electrically connected by sewing over them with conductive thread. (B) A microscope image of ink-coated knitted spandex fabric. (C) Porosity measurement of neat, unstrained fabric. (D) Porosity of inked fabric. (E) Porosity of inked fabric after stretching. (F) A simple actuator-sensor device curls up and down, generating a sensor signal dependent on device curvature. (G) The curling device follows the control signal by modulating the power output to the SMA actuators. Each sensor is actively used only when the corresponding fabric face is in extension.

form of this device is a flat, square section of cloth (Figure 5.5G). Upon activation, the device softens its VS frame and lifts itself up into a table-like platform structure. This new shape becomes rigid and load-bearing, as demonstrated by placing weights on the platform. The shape is then returned to its initial configuration via an antagonistic ribbon actuator, which flattens the device again (Figure 5.5F). By choosing not to soften certain VS fibers, such as the central VS ring (Figure 5.5H, I), the actuation motion and subsequent shape is influenced. This signifies that even complex transformations may be possible with reduced component counts by leveraging actuators and VS components in concert. Further, the continuous curvature displayed by this machine sets robotic fabrics apart from origami-inspired machines [126], as the range of transformation and conformability is not limited by discrete folds. The shape change ability demonstrated is an early indication of the potential for extremely adaptable, independent machines with on-demand tool generation.

Last, taking inspiration from the fabric wings of the 1903 Wright Flyer, we demonstrate a self-deploying airplane wing in a fully untethered system (Supplemental Movie S4). The robotic fabric wings are seated into small slits in the side of the fuselage, wherein all additional circuitry, microcontrollers, and batteries are enclosed. The fabric wings curl to wrap around the fuselage for compact storage (Figure 5.5J), and uncurl into a deployed, rigid state with wings extended (Figure 5.5K, L, M, N). This demonstration shows the potential for robotic fabrics as an adaptable component in a larger machine, and shows how a particular robotic fabric segment or tool might self-stow or move out of the way when not in use. This is a key functionality for use cases when light weight and low storage volumes are highly desired, as in transportation to and from remote locations or in space exploration.

5.4 Discussion

By treating fabric as the foundation of a robot, it can be enhanced from a passive material to smart adaptive clothing, self-deploying structures, or lightweight shape-

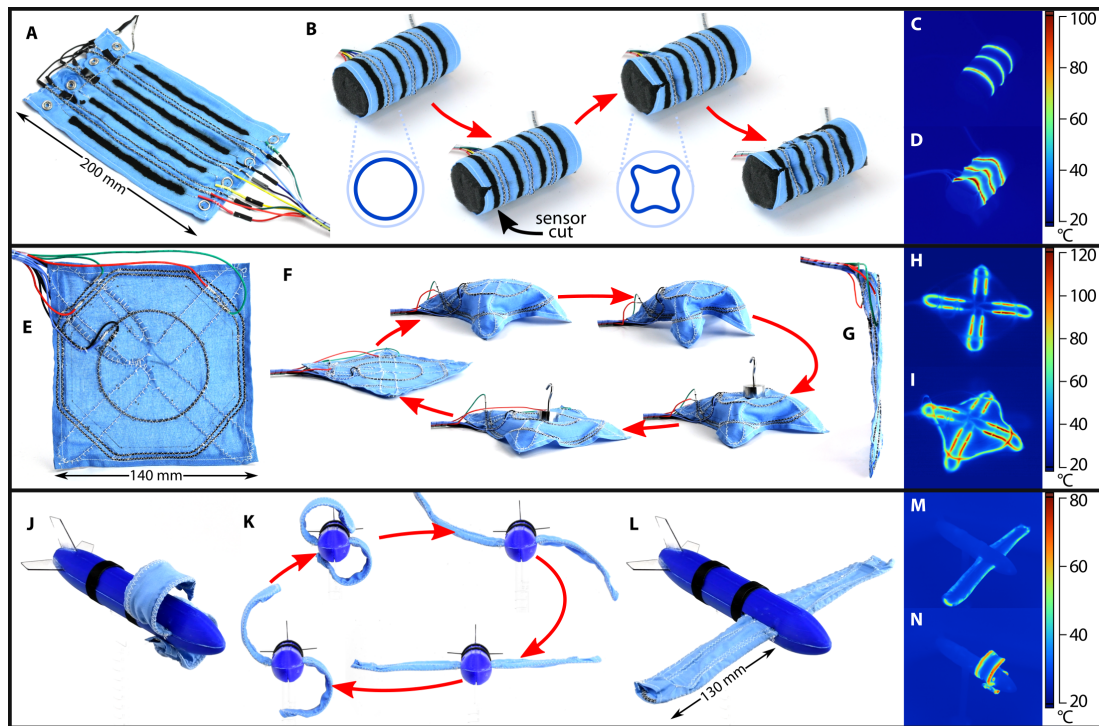


Figure 5.5. Robotic fabric demonstrations. (A) Robotic fabric tourniquet. (B) Tourniquet is buttoned about a foam body. It reacts to a damaged circuit by contracting and holding a tightened pose. (C) Thermal image of the tourniquet as VS fibers soften. (D) Thermal image of activated SMA actuators constricting. (E) Robotic fabric “popup” table. (F) From an initial flat state, the table is able to stand up, stiffen into a load-bearing platform, and then collapse under a load as it softens and actuates back into its initial flat configuration. (G) Fabric “popup” table is approximately 2 mm thick. (H) Activation and softening of table “leg” VS fibers. (I) Activation of SMA actuator wire, causing table to stand up. (J) Robotic fabric wing in self-stowed position. (K) Robotic fabric wing curls and uncurls from deployed, open state into a compacted, stowed state. (L) Robotic fabric wing in deployed position. (M) Activation and softening of wing VS fibers. (N) Activation of curling SMA wires.

changing machinery. There are still many hurdles to overcome before robotic fabrics reach their full potential. We expect that with time, scientific advances will unveil improved actuation, variable-stiffness, and sensory technologies that are ideal for future robotic fabric developments. By leveraging well-established textile manufacturing process, we envision that the future will bring mass-produced rolls of robotic fabric, available for purchase, and programmable as-required to fit varied tasks. Self-reconfiguring machinery made from this material could bend and twist into new and complex shapes as needed, and then collapse for compact storage. Such visions will require advancements in other areas, such as the development of practical simulation and design tools, robust thin-body controls, and even lightweight embedded power supplies. We hope that our early step toward robotic fabrics can inspire many more future advances in a field with so much potential.

Introduction to Block 3:

Chapter 6 and 7 comprise the final block of this dissertation. Together, they show two material compositions that enable stretchable, conductive bulk material composites with uniform Joule heating. Many soft robotic components require highly stretchable, electrically conductive materials for proper operation. However, there is a scarcity of stretchable materials that can withstand the high strains typically experienced by soft robots, while maintaining sufficiently uniform, high conductivity to be used as a Joule heater. Chapter 6 is the initial work that aims to fill this material void (although with low strain capacities). It contains many of the potential applications for creating stretchable, digitally addressed heating skins. These include thermochromatic displays, shape-on-demand control over rigid materials that enable rapid forming of weight-bearing structures, and even minor control over thermally responsive silicones. Chapter 7 is the follow-on work which, assuming that the possibilities shown in chapter 6 are understood, demonstrates a significant leap forward in the capacity of the bulk heating material to sustain high strains over many cycles.

In Chapter 7, I show a new activation mechanism that allows us to enhance previously observed functions (stretchable, conductive silicone composites using internal conductive liquid inclusions) with softer, more stretchable silicones than was formerly possible. In previous works, stiffer silicones were composited with conductive liquid inclusions and activated through an application of pressure. This caused the silicone walls separating the conductive liquid to crack allowing the microcapsules of conductive liquid to “burst” and coalesce into a conductive network [127]. With softer (and inherently more stretchable) silicones, this does not work; a problem since these same softer silicones enable the very-high strain in many soft robotic systems. By including a small amount of solid particles in the final composite, the rigid inclusions act as strain concentrators (and thus crack nucleation sites) embedded into the material, causing a multitude of microscopic internal failures that results in the coalescence of the internal conductive liquid. Thus, the composite material can be activated via strain-induced internal microcracking. It’s from this simple activation method that

the true leap forward in stretchable conductivity emerges. What follows are the two (modified) abstracts for the chapters, summarizing the work therein.

In chapter 6, I present stretchable, addressable heating silicone sheets that can control soft, thermally responsive materials. The sheets are created using layer-by-layer deposition of a bulk conductive elastomer that can be Joule heated, with embedded liquid-metal microchannels used as electrodes. This combination allows the bulk, addressed material to be stretched and twisted while in operation. I demonstrate local, addressable heating in a silicone-based composite that is capable of cyclic strains of up to 40%, while still capable of self-heating to over 100°C. I also demonstrate the utility of these sheets to become a thermal control platform in both color changing and stretch-and-hold operations using all silicone-based composites. Finally, I bond the platform to a variable-stiffness polymer that, with the heating sheet's selective heating capability, enables folding at targeted locations.

In chapter 7, I build upon the work done in chapter 6, improving the overall functionality of the heating silicone sheets. In the chapter, I present a silicone composite containing both liquid and solid inclusions that can maintain a uniform conductivity while experiencing 200% linear strains. This composite can be cast in thin sheets and wrapped around thermally responsive soft materials that increase in volume or stretchability when heated. I show how this material opens up possibilities for electrically controllable shape changing soft robotic actuators, as well as all-silicone actuation systems powered only by electrical stimulus. Additionally, I show that this stretchable composite can be used as an electrode material in other applications than those of chapter 7, including a strain sensor which attains a linear response up to 200% strain with near-zero signal noise.

6. ADDRESSABLE, STRETCHABLE HEATING SILICONE SHEETS

The following chapter is based on work previously published as [128] R. A. Bilodeau, M. C. Yuen, and R. Kramer-Bottiglio, “Addressable, Stretchable Heating Silicone Sheets,” *Advanced Materials Technologies*, vol. 4, no. 9, p. 1900276, Sep. 2019. Copyright 2019, John Wiley and Sons, reproduced with permission.

6.1 Introduction

Soft robotic systems are of great interest due to their robustness to impacts and vibrations, conformability to surfaces and objects, and potential to undergo large deformations due to low material stiffnesses. These advantages allow soft robots to fulfill functions such as grasping diverse and delicate objects, maneuvering around obstacles, or traveling over difficult terrain [3, 129–132]. Research into new active materials for soft, highly deformable systems has yielded promising new branches of study, such as thermally responsive variable stiffness materials [65, 115, 116] and actuators [126, 133]. Yet, these new thermally responsive materials require a form of thermal control that is compatible with the host materials. In this work, we present a stretchable, addressable silicone sheet that enables thermal control, and demonstrate its utility through integration with thermally responsive soft materials.

Many thermally responsive materials are utilized by the soft robotics community. Thermally-softening polymers (such as thermoplastics and thermosets) are passively-stiff, actively-soft variable stiffness materials [115, 134] that have been used in robotic systems for move-and-hold operations [62, 121] as well as in conformable and on-demand structural systems [65, 135]. Additionally, thermally responsive shape memory polymers and alloys have been employed as both stiffening agents and actuators [115, 116]. Finally, thermally responsive silicone-based actuators have been

recently developed, which undergo bulk expansion when trapped solvent is vaporized [133]. All of these previous examples required some thermal control, and so researchers have sought out ways to embed a close-contact heater where the compliance of the heater was properly matched with its thermally responsive material pair [62, 121, 136, 137].

In an effort to fill the need for compliance-matched thermal control, flexible and stretchable heaters are an active area of research, as are addressable heating structures and systems. Stretchable heating composite materials have been successfully developed with either conductive fillers or microstructures [138–142] and have demonstrated linear strains of up to 100% [143, 144]. Proposed applications have included wearable technology and active therapy [143, 145–150], surface-based temperature control of non-planar objects [151], and thermo-chromatic flexible, active microdisplays [152–154]. These examples, however, require high-complexity patterning techniques (*e.g.* lithographic masking) and often only heat up moderately. To facilitate thermal controllability across a 2D plane, researchers have begun to implement thermal addressability onto stretchable or flexible surfaces, in which only localized regions of the surface are heated [155–159]. These pioneering works have successfully implemented the concept, but have also required lithographic masking, complex assembly processes, high operational voltages (>100 V), or a fixed framework around only a few small pockets of thermally responsive material. Prior work has demonstrated stretchability and addressability in geometrically soft material systems, (*i.e.*, silicon-based electronics made stretchable through patterning crystalline materials onto prestretched silicone) [145, 146], but to our knowledge, there has not yet been a combination of these two functions in a system which uses intrinsically soft materials (*i.e.*, silicones and liquids). With our work, we combine the manufacturing simplicity gained from using a bulk silicone composite with the utility of a thermally addressed heating platform to gain the strengths from both sets of prior research.

Here we present a planar, stretchable, silicone-based Joule heating composite material strengthened by a pure-silicone support structure, with fluidic electrical in-

interfaces, creating a robust ‘heater silicone’ capable of stretching up to 40% while maintaining heater functionality. The support structure can be embedded with liquid metal wiring to enable an addressable electrical connection for localized Joule heating, which we use to demonstrate a mechanically robust, 2D thermal ‘pixel’ display. This addressable heater sheet can be coupled with thermally responsive materials, such as variable stiffness and phase changing materials. In this work we show coupling of the heating composite to a variable-stiffness thermoplastic (polylactic acid, or PLA) or a thermally triggered, stiffness-changing silicone (wax-silicone composite), ensuring uniform heating of the adjacent material and enabling both reversible shape changes and stretch-and-hold operations. Finally, we demonstrate example systems comprising the addressable, stretchable heating sheet coupled to a uniform PLA sheet (with no pre-set mechanical hinges) reshaping in both two and three dimensions, showing how this platform opens up possibilities of on-demand origami folding in the future.

6.2 Manufacturing and Characterization of Heater Silicone sheets

We first studied the effect of various manufacturing parameters of the bulk heater silicone material on its performance (*i.e.*, electrical resistance as a function of applied strain). We then developed a compliant interfacing technique that enables heating while undergoing large deformations and demonstrate its utility and robustness by performing heating tasks while undergoing significant deformation.

6.2.1 Conductive Composite Electrical Characterization

The heater silicone is an electrically conductive composite made from expanded intercalated graphite (EIG) conductive filler dispersed in a silicone matrix, supported by a pure-silicone backbone, creating a monolithic, electrically conductive material sheet. EIG is an inexpensive filler formed by bulk exfoliation of graphene sheets from graphite flakes [160, 161], and has been used to create conductive composites in rigid-polymer composites [162, 163], including self-heating variable stiffness compos-

ites [121]. It has been used as a low loading (<15 wt% EIG) filler for stretchable, conductive elastomer composites and sensors [59,164,165], and for our heater silicone we simply increased the loading (> 15 wt% EIG) to improve material conductivity. We adapted the rod-coating technique demonstrated by White, *et al.* [59] to manufacture our composite (see Figure 6.1a), but coated multiple layers of conductive silicone on top of each other to increase the thickness of our conductive layer, reducing the overall sheet resistance in our samples. To create the heater silicone in a stretchable, sheet form, we encased the initial conductive composite in a pure silicone backbone (a strengthening support that bonds through the composite), increasing the cyclic stretchability of the composite (embrittled from the high filler loading) with minimal impact on conductivity (see Supporting Information S1).

We performed a detailed characterization of the electrical resistance of the heater silicone under cyclic strain, while varying several manufacturing and design parameters. In Figure 6.1, we highlight some of the results from varying two key manufacturing parameters: the weight percent of the expanded intercalated graphite (EIG) filler (15, 25, and 35 wt%), and the number of layers of the heater silicone ($n = 1, 2$, or 3, based on the number of times we rod coated the heater silicone onto the sheet). The thickness of the conductive layer varied between $52\text{ }\mu\text{m}$ and $300\text{ }\mu\text{m}$ and was dependent on both the filler ratio and the number of layers (Supporting Information S1) . We also varied the design of the heater silicone sheets by including a silicone backbone reinforcement on one-side or both sides of the conductive composite, and those results and comparisons can be found in Supporting Information S1. We tested three samples at each level of each design parameter, for a total of 54 samples tested. Figure 6.1b,i is an example of a dataset collected for a single sample with the following parameters: 35 wt% EIG heater silicone concentration, two layers of heater silicone coated onto the sample, and a backbone on both sides of the material.

Each sample was mounted in a materials tester (Instron 3345) and clamped using an electrically conductive clamp to measure the resistance of the sample *in situ* . Samples were cyclically strained 200 times to 10% strain and then strained 50 times

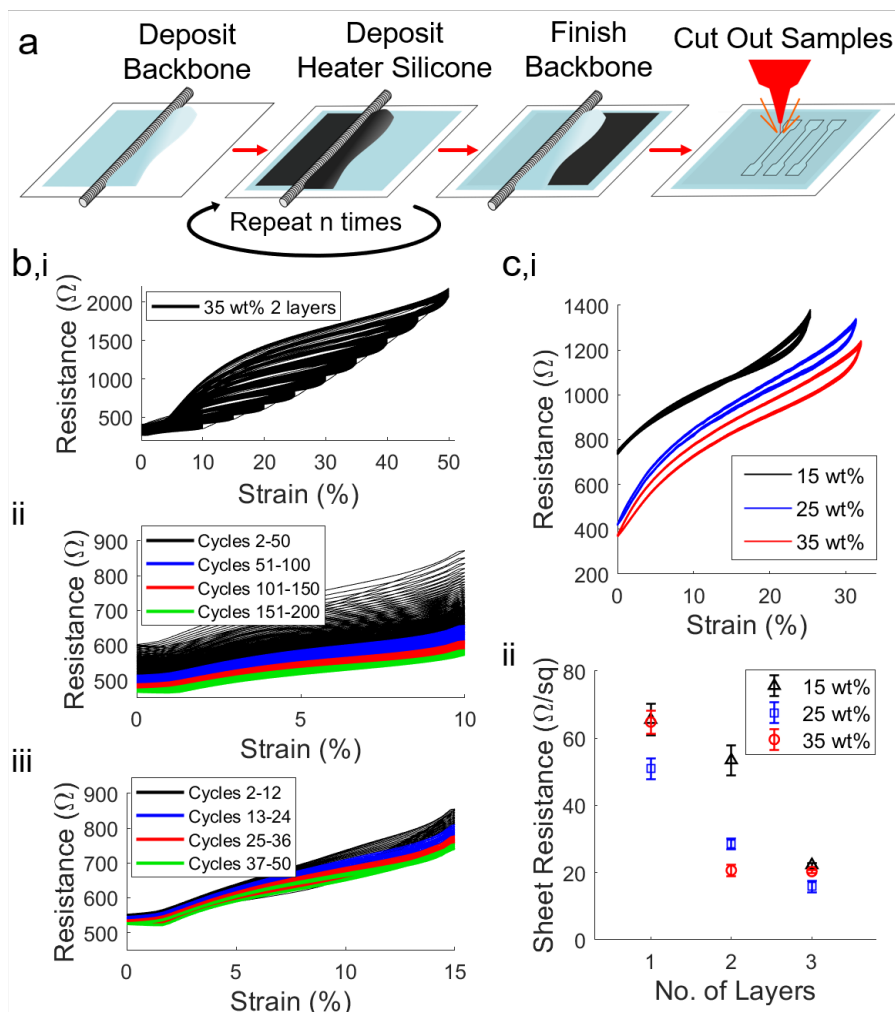


Figure 6.1. Manufacturing steps and electrical characterization data from the strain tests performed on high aspect ratio samples of the heater silicone. a) Multiple layers of EIG composite silicone are deposited onto a neat silicone backbone to create the heater silicone sheet, and samples are cut out of the sheet with a laser cutter for electrical testing. b,i) An example of a cyclic test dataset (sample design parameters: 10 cm x 1 cm, 35 wt% EIG, $n = 2$ layers). b,ii-b,iii) cyclic tests focusing on 10% and 15% strain (10 cm x 1 cm, 15 wt% EIG, $n = 2$ layers) with the same y-scale and color distinguishing test cycles (1st cycle always omitted). c,i) Representative resistance-strain curves from heater silicone samples (10 cm x 1 cm, $n = 3$ layers) with different concentrations of EIG. Curves show the final 10 repetitions of a 50-cycle test (steady-state response). c,ii) Sheet resistance of unstrained heater silicone with different concentrations of filler and increasing numbers of layers.

to incrementally higher strain values (5% strain increase per increment, making the test 15%, 20%, 25%, etc.). The reason for the decrease in cycle count at higher strains is based on the material more rapidly reaching a steady-state strain response after the 200 cycle ‘break-in’. Initially, at 10% strain, the samples would undergo a lengthy settling response (see Figure 6.1b,ii) and so we cycled the sample to ensure that the sample’s resistance had settled before testing at higher strains. After that initial break-in, each sample settled after about 40 cycles (see Figure 6.1b,iii), and so all comparisons of sample performance were based on the resistances measured in the last set of 10 cycles (cycles 41-50) at each strain value. We note that the overall decrease in resistance during cycling is an interesting characteristic of the composite material. We suspect that the decrease is due to a combination of the porosity of the material, slow alignment of the disk-like EIG particles during a (relatively) slow strain of the material, and viscoelastic effects of the silicone undergoing a constant strain cycling.

The last 10 cycles of three samples are plotted in Figure 6.1c,i. Each sample shown was manufactured with the same number of conductive layers but, by increasing the loading, the initial (unstrained) resistance of the samples decreased, as did the resistivity of the sample over the entire strain-curve. We also observed that the backbone allowed us to repeatedly strain samples over 25% while maintaining a good electrical resistance for Joule heating (for additional information, see Supporting Information S1). Although the lowest weight percent (155 wt% EIG) showed a significantly higher resistance (at lower strains), this did not make it ineligible for use as a Joule-heating material. Instead, we altered subsequent sample geometries to take into account the higher initial resistance. Figure 6.1c,ii that, all other parameters held constant, increasing the number of layers resulted in a decrease in the overall ‘sheet resistance’ of the material. This holds logically, since sheet resistance does not consider the thickness of the conductive layer, whereas overall resistance is a volumetric property, and therefore effected by material thickness. The material characterization performed here enabled us to select which manufacturing and design parameters to use, based

on the desired geometry or stretchability goals, while performing the subsequent experiments.

6.2.2 Liquid Metal Interfacing and Localized Heating

To create stretchable electrodes that can connect to the heater silicone, we embedded soft wiring directly into the supporting backbone using a eutectic gallium-indium-tin alloy (galinstan) as conductive (conductivity = $3.4 \times 10^4 \text{ S cm}^{-1}$) [166] stretchable wiring. Galinstan is liquid at room temperature allowing it to bend and stretch with the surrounding silicone [9, 166]. Additionally, the liquid alloy is stable at the elevated temperatures used in our heater, preventing electrode burnout problems.

While experimenting with stretchable liquid metal wiring, we qualitatively noticed that liquid metals interfaced better with the heater silicone as compared to copper wire, *i.e.*, the system had a reduced overall resistance. To confirm our observations, we performed a simple test to measure the difference in resistance for a sample of material with a copper wire electrode and a liquid metal electrode of the same geometry, as demonstrated in Supplemental Figure S2. The liquid metal electrode dropped the contact resistance by over $10 \text{ } \Omega$, when compared to the uncompressed wire connection (see Supporting Information S2 for more details). The numeric value of this improvement depends heavily on the geometry of the heater silicone sample and the electrode connection, but in the subsequent examples we present throughout this work, the reduction of contact resistance greatly improved our ability to evenly heat the planar silicone sheets.

To improve the functionality of the heating silicone, we wanted to be able to do more than just heat the whole system from end-to-end, but also at select locations in the body. We used direct filament casting to embed conductive wiring throughout the heater silicone so that we could create soft, localized contacts and therefore heat targeted areas of the conductive silicone sheet. Li, *et al.* demonstrated a direct filament casting method to create high-resolution liquid-metal circuits in parallel, in

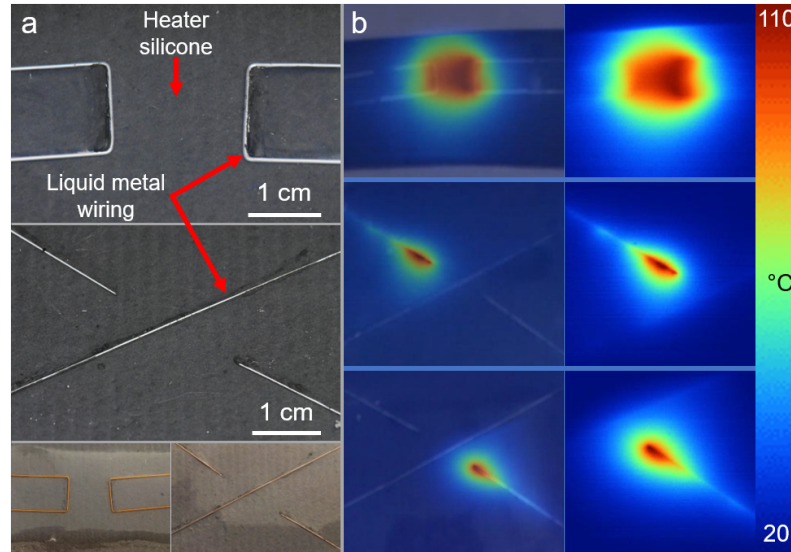


Figure 6.2. Two different liquid metal channels cast into the heating silicone, and their corresponding effect on the way the material heats up. a) Top: Two parallel line electrodes create a heat ‘patch’ over an area. Middle: Liquid metal channels ending at point create a point of heat. Bottom: photographs showing the copper wires cast into the silicone to create the channels. b) The left column has a semi-transparent IR image overlaid on a visible light image of the heater silicone/liquid metal line pattern. The right column is a zoomed in view of the IR image.

an additive-based manufacturing processes [167]. By placing a filament during the silicone casting process where a liquid-metal channel is desired, hollow channels are created in the cured silicone once the filaments are removed which can then be filled with liquid metal. We implemented this method using copper wire as our filament (28-30 AWG, 0.25-0.3 mm dia) and embedded the liquid metal channels directly into the heater silicone backbone.

In Figure 6.2 we show the results of casting two types of liquid-metal channels during the heater manufacture. Since we used a wire as the mold for the electrode traces, the electrodes could be shaped into nearly any 2D shape we desired (so long as the wire can be removed after casting). For this work, we used U-shaped and straight-line electrodes to apply an electric field in the heater silicone between two

parallel lines and two points, respectively, which allows for us to change the type of heat addressability between heating a swath of silicone, to focusing the heat on a single spot (see Figure 6.2). The spot-heat sample in Figure 6.2 was designed with the liquid metal line embedded into the conductive composite; therefore, the tear-drop shape is due to Joule heating along the entire liquid metal line. This inspired us to move the liquid metal lines to be fully embedded in the backbone (except at the spot-heat location) to reduce the electrical contact between electrode and heater.

6.2.3 Stretchable Heating

To corroborate the results of the electrical characterization, we performed cyclic strain tests on samples of the heater silicone while Joule heating them to over 100°C. We chose to test shorter samples than in our electrical tests (with a 3:1 aspect ratio), and so we were able to use the 15 wt% EIG loading to improve the uniformity of the heating at high strains. We designed a custom straining device that allowed us to use liquid metal contacts to Joule heat only the portion of the heater silicone experiencing a uniform strain field. This removed any effects of clamping on the sample’s electrical performance, so we could focus on the effects of linear strain on the sample’s ability to Joule heat. Preliminary pull-to-failure tests revealed that the heater silicone could robustly support 40% strains while continuing to uniformly heat up to over 100°C. We then performed cyclic tests on fresh samples, cycling them to 40% strain, while continuously Joule heating them to over 100°C. Supporting Information S3 has more details on our strain setup, as well as the preliminary pull-to-failure tests.

Figure 6.3 shows the results of the cyclic tests for three samples, as well as IR images of one of the samples tested. Both the normalized, average resistance and the average power consumed by the samples are shown over the 1000 cycles. The sample resistance was calculated from the voltage and current draw (as measured by the programmable power supply) and, unsurprisingly, increased while the samples were strained and decreased while the strain was being released. The average resistance of

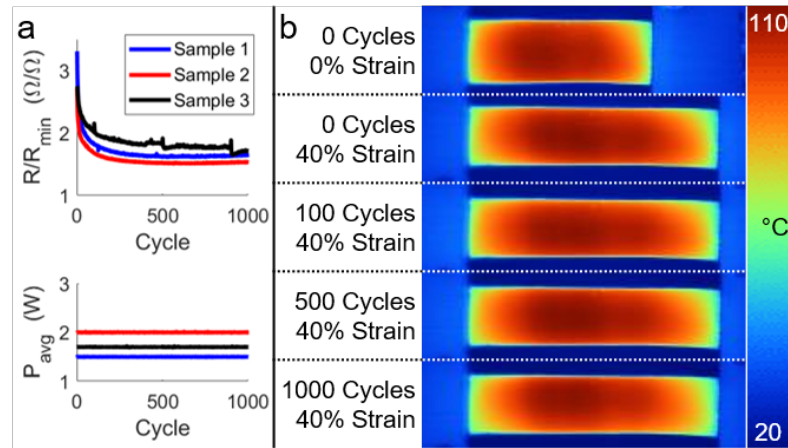


Figure 6.3. Results from cyclic strain tests while Joule heating samples of heater silicone. a) The normalized, average resistance of the sample in each cycle, as well as the average power required to Joule heat the sample, presented against the cycle number. The plateau in the resistance curve and the flat power consumption indicate good sample health throughout the tests. b) IR images of one of the samples tested, at 0% strain and then at the maximum strain (40% strain) over the 1000 cycle period, showing little-to-no degradation in the sample's ability to evenly heat. Sample heating area is approximately 3 cm x 1 cm at 0% strain.

each cycle is presented in Figure 6.3a, normalized by the lowest resistance value of the final cycle. As expected from the electrical tests, (see Figure 6.1), the samples each show a steady decrease in their resistances until they plateau after 100-200 cycles for the remainder of the 1000 cycles. Uniform power-consumption of the samples (Figure 6.3a), paired with the sample maintaining the same temperature, (Figure 6.3b) acts as a good initial indicator of the health of each sample throughout all 1000 cycles (see Supporting Information S3 for more details). Occasional spikes and drops in the calculated power (due to the power supply) were smoothed out by taking the average power consumed within each cycle. Figure 6.3b shows the IR image from one of the samples that, after 1000 cycles, shows no difference in its heating pattern when compared to its initial first cycle. Additionally, a quantitative analysis of the centerline temperature of the sample is plotted in Supplemental Figure S6 for the IR images in Figure 6.3b, showing the sample’s consistent temperature profile throughout the entire cycling process. From this test, we concluded that, when properly manufactured, the heater silicone functions well over 1000 cycles. Additional details are discussed further in Supporting Information S3.

6.3 Implementation in Silicone-based Material Devices

The utility of our heater silicone arises from its stretchability and addressability, allowing it to be seamlessly embedded into “all-soft” systems. We demonstrate these attributes by integrating thermally-responsive silicones with the heater silicone platform to create both stretch-and-hold operations and color changing functionality.

6.3.1 Stretch-and-Hold Operations

To demonstrate the utility of a repeatably stretchable, silicone-based heater, we performed some basic stretch-and-hold experiments using a silicone-based, variable elasticity “wax silicone” (see Figure 6.4). The wax silicone is a composite of paraffin wax microparticles embedded into a silicone matrix. At room temperature, the wax is

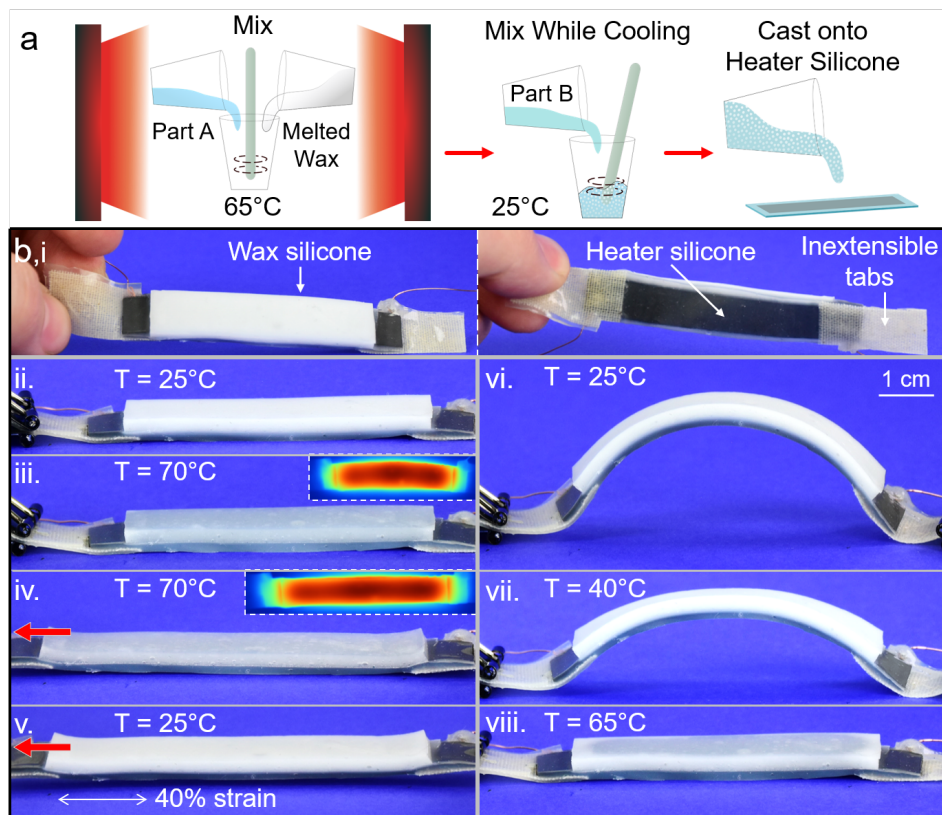


Figure 6.4. ‘Stretch and hold’ shape change. a) Manufacture of the temperature-sensitive wax-silicone composite which leverages the low temperature phase change of wax to hold a new length when cooled while stretched. b,i) a sample of heater silicone bonded to wax silicone used for this demonstration, with inextensible tabs to allow for an even straining of the heater silicone while reinforcing the liquid metal electrical contacts. b,ii-viii) the sequential steps as the system starts from cooled state, is heated to melt the wax silicone, stretched, cooled to solidify the wax silicone, allowed to relax (with the wax silicone holding its extension), and then reheated to re-melt the wax silicone and restore it to its unstrained state.

solid and increases the silicone’s elastic modulus. When the wax melts, the silicone is ‘softened’ and can stretch like any other closed-cell silicone foam. If the wax is cooled (and solidified) while the silicone matrix is stretched, the solidified wax inclusions hold an elongated shape, preventing the silicone matrix from relaxing back to its original length. After this, when the wax is re-melted, the silicone’s restoring elastic force allows the system to return to its original, unstrained length.

We cast the wax silicone onto our heater silicone to create a material system capable of stretch-and-hold operations. In Figure 6.4a, we demonstrate the basic process used to make this stretch-and-hold composite. We mixed melted wax by hand into a heated Part A of the two-part silicone pre-cure at a high enough temperature to keep the wax melted. The mixture was then cooled by mixing in a room-temperature Part B, creating solid wax particulates, and cast onto the heater silicone. Once again, the backbone of our heater silicone provides an additional advantage as it bonds very well to the wax silicone’s matrix. Figure 6.4 shows both the final sample used (with inextensible tabs to pull from and liquid metal electrodes (not visible)) as well as a fully reversible stretch-and-hold cycle, described as follows. The heater silicone melts the wax (resulting in a translucent color change in the wax silicone), and the composite system is stretched while cooling the wax silicone. Once cooled and released, the system pops up out-of-plane to obtain a minimum energy state between the heater silicone’s restoring elastic compressive energy, and the wax silicone’s elongation. To restore the original state of the system, we simply reheat the heater silicone to melt the wax. At this point, the stretch-and-hold cycle can begin anew. We repeated this cycle several times, achieving a pop-up structure each time with no observable degradation in the heater silicone between cycles. One cycle is demonstrated in Supplemental Video 1.

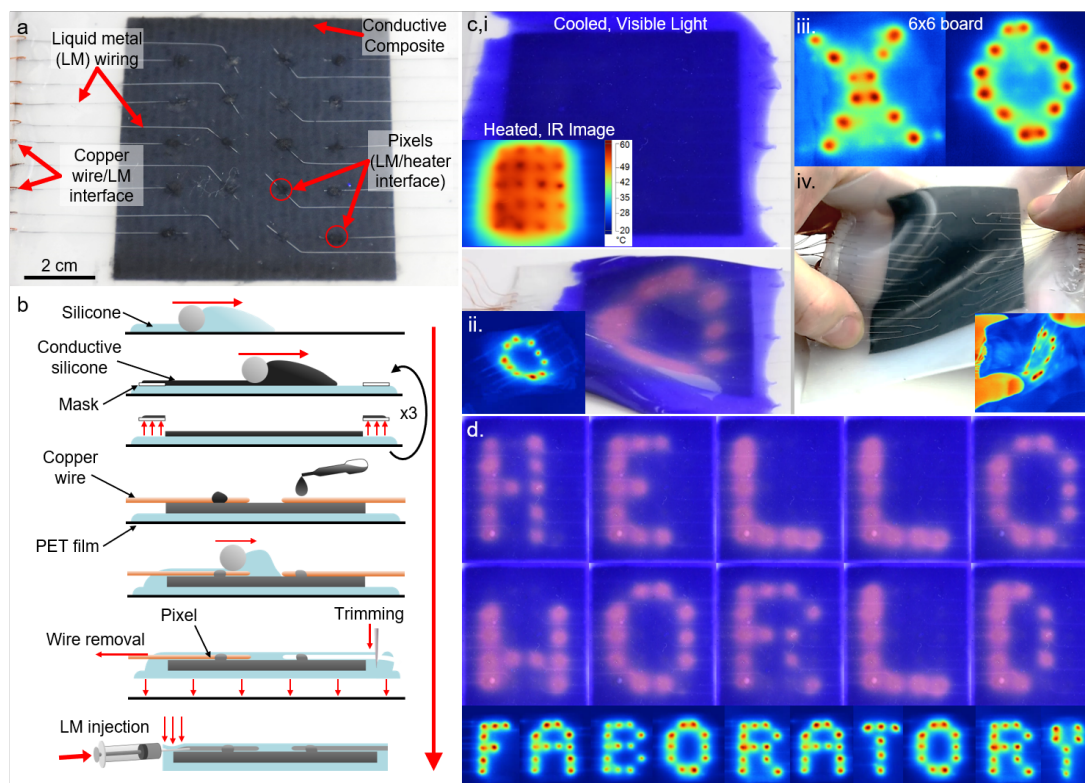


Figure 6.5. a) A visible light image of our fully soft 2D addressable heater composed of a heater silicone square with liquid metal electrodes. b) Manufacturing the 2D addressable heater pixel interfaces by adding a droplet of heater silicone at the location of interest on the wire molds. The liquid silicone seeps under the wire separating the rest of the liquid metal channel from the conductive composite. c,i) The 2D addressable heater with a temperature-responsive silicone laid on top (visible and IR images). c,ii) The addressable heater functions even when warped/flexed during operation (visible and IR images). c,iii) a higher-density board with 36 pixels (6x6) in the same form-factor as the 4x5 board, showing several letters. c,iv) The 6x6 board remains active while experiencing a large deformation stress. d) Visible light images of the automated system printing out the letters “HELLOWORLD” consecutively, and IR images of other letters captured, and organized to spell “FABORATORY”.

6.3.2 Robust, Addressed Spot Heating

Having successfully demonstrated both the stretchability and the addressability of our heater silicone sheets, we then created a 2D addressed heater with rectangular arrays of spot heating “pixels” (shown in Figure 6.5a). Each pixel in the array was capable of heating locally to above 100°C, and the system could be stretched and manipulated during operation. To get this 2D array of localized contact points, the liquid metal wires had to overlap the active area of the heater silicone. Fortuitously, the bottom-up heater silicone sheet manufacturing allowed us to lift the liquid metal wiring out-of-plane from the conductive composite silicone (see Figure 6.5b). After the conductive composite cured, copper wires were gently placed on top and droplets of the composite were deposited at each pixel, connecting the copper wire at these locations to the bulk heater underneath. As the silicone backbone was cast on top to finish the heater silicone sheet, liquid silicone seeped under the wires, separating the rest of the electrode’s channel from the conductive silicone with a thin, non-conductive barrier. Once the wires were removed and the channels filled with liquid metal, the only connection between the liquid metal traces and the planar heater was at the individual points. To control the activation of each pixel, we designed a high current PCB which could switch each channel between a high-voltage state, ground state, or a neutral (‘floating’) state (see Supporting Information S4).

To demonstrate one application of this heating array, we created a mechanically robust digital thermal display. To elicit a response in the visible-light spectrum from the display, a layer of silicone loaded with thermochromic pigment was added on top of the heater patterned with a 4x5 pixel array in a 2 in x 1.5 in rectangle (5.1 cm x 3.8 cm) (see Figure 6.5c). We activated groups of pixels and showed that we could both heat the whole area or cause various letters of the alphabet to appear (see Figure 6.5d and Supplemental Video 2). Since the whole system was made of silicone composites, we were able to change the orientation and folding direction of the display while it was changing letters. Additionally, to test an increased density of heating

pixels, we manufactured a higher density pixel array with 6x6 pixels in the same active rectangular region as the 4x5 pixel display. This increased the pixel density from 1 to 1.9 pixels/cm². We used this higher-density array to demonstrate the robustness of the system to external perturbations, by both crumpling and stretching the display, while it continued to display different letters (see Figure 6.5c,vi and Supplemental Video 3). Though a thermally responsive, color changing display may seem limited in utility, we see additional applications for digitally controllable, stretchable, color changing silicones in situations similar to those presented by Morin *et al.* , who added visible light camouflage to their soft actuators by actively changing the color of the silicone by injecting colored fluids into their actuator [168].

6.4 On-Demand Shape Change

After demonstrating the robustness of the heater silicone and its addressable heating functionality while undergoing deformations, we desired to implement the platform in reversible shape changing structures. To do this, we used the heater silicone to soften a variable stiffness material (PLA) and demonstrated several shape-change modes in the variable stiffness sheet. Additionally, we integrated the addressable heating to selectively soften regions for on-demand shaping and folding.

6.4.1 Reversible Shape Change

To create reversible shape change (and shape holding), we bonded the heater silicone to the PLA using a robust epoxy bond, resulting in a composite heater/variable stiffness material (see Figure 6.6a, and Supporting Information S5 and S6 for more details) [62,65]. Since the bonded heater silicone can both stretch and compress without loss of bond integrity or functionality, the system could maintain elevated temperatures for reshaping and then be cooled to hold the new shape (see Figure 6.6b,i). It also allowed us to reheat the shaped PLA to reverse the shape change. Though the heater silicone could heat the PLA sheet to 150°C, when the PLA's temperature

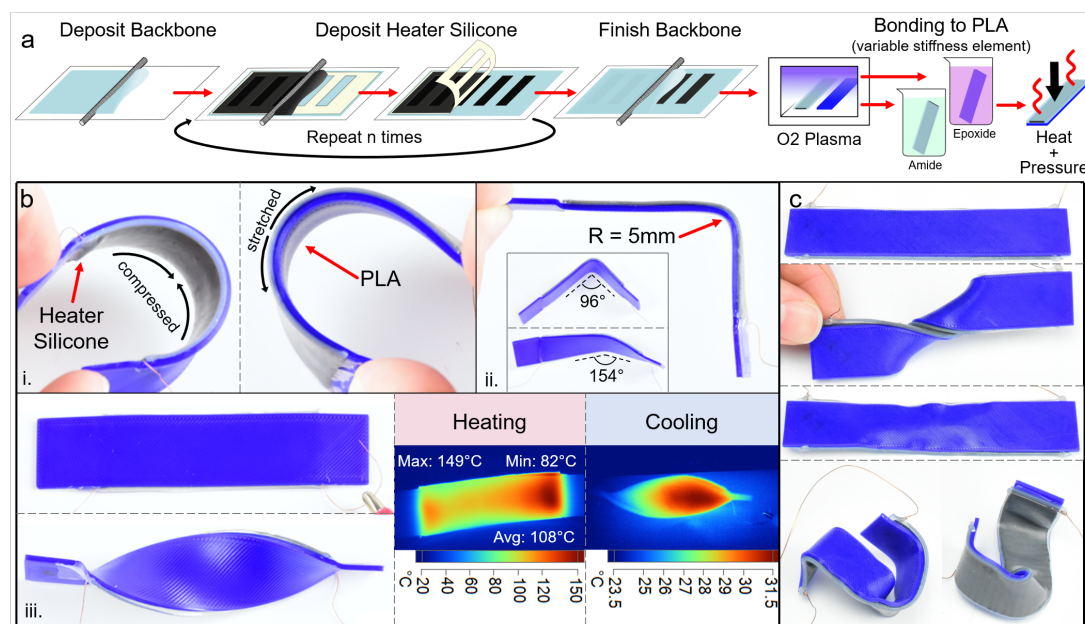


Figure 6.6. Reversible shape change. a) Manufacturing the heater silicone sheets with bonded variable stiffness elements (PLA). b) Heater silicone bonded to PLA is Joule heated enabling shape changing and holding operations in the PLA. b,i) The bond keeps the silicone connected to the PLA even when compressed and stretched. b,ii) A 90° fold in the variable stiffness sheet. Inset shows the shape-memory recovery of the material when Joule heated again. b,iii) The bonded system is given a permanent twist, with IR images of the sample as it is heated and cooled into the twisted shape. c) A second sample of the material undergoing a much tighter twist & hold (360°). After reheating, the PLA showed permanent warping. The heated system was then crumpled to produce additional folds, twists, and bends, demonstrating the continued functionality of the heater silicone.

increased above 65°C we could begin to reshape the sheet (see also Supporting Information S7). Various shapes were imparted onto the sheet including smooth curves (Figure 6.6b,i), 90° angles (Figure 6.6b,ii), and, permanent twists (Figure 6.6b,iii). This last demonstration goes beyond traditional origami folding, showing that this variable stiffness material is capable of twist-and-hold as well as bend-and-hold operations (see also Supplemental Video 4). We made several of these samples to test the ability of the material system to undergo several different shape changes, like tighter twists and being crumpled by hand (Figure 6.6c). Though these shape-changes could be reversed, the 3D printed PLA did not prove to be a very good variable-stiffness material in this regard as it remained permanently deformed from where it was forced to stretch. Taylor, *et al.* recently demonstrated a simple chemical platform that enables the bonding of many types of commercial polymers (with glass transition temperatures $< 150^{\circ}\text{C}$) to pure silicone [169].

In Figure 6.6b,ii we also show that, due to both the elasticity of the silicone and the shape memory effect in the PLA variable stiffness sheet [170,171], the material is able to recover some of the set shape when reheated after shape fixing. The $\sim 90^{\circ}$ bend flattened itself, recovering 69% of its bend, and the twisted 180° sample was able to recover 66% of its twist (see also Supplemental Video 4). Though this effect is relatively weak, it is valuable to note that the bonded heater silicone can instigate this self-reversing shape change.

6.4.2 Reversible Hinges

To create reversible on-demand hinges in a stiff sheet, we combined the heater silicone, liquid metal wiring, and silicone-PLA bonding into a one-dimensional, addressable, heating array with 5 liquid metal channels bonded to a variable stiffness sheet, creating 4 addressed variable stiffness “pixels” in a straight line (see Figure 6.7a,c). Each 1D pixel heating area in the heater silicone can be activated (*i.e.*, the temperature raised to above 65°C) independently or concurrently with other active pixels

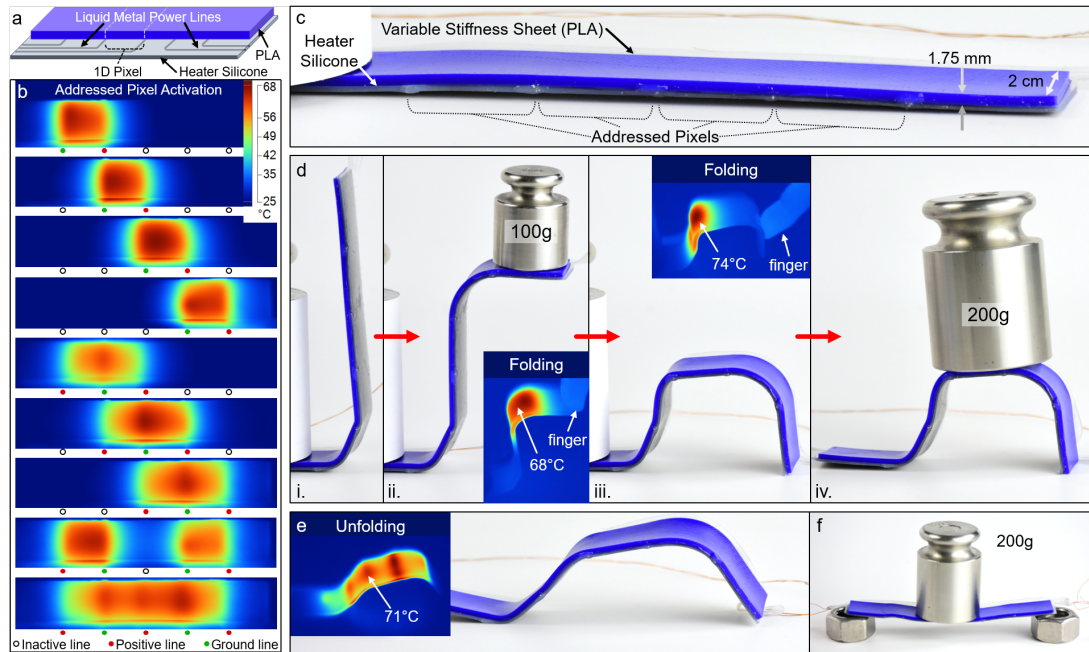


Figure 6.7. 1D pixelized addressable variable stiffness system. a) Schematic of the system demonstrating the various components allowing for addressable variable stiffness. b) IR images of the PLA side of the functional system with each pixel heated above the glass transition temperature ($\sim 62^{\circ}\text{C}$), showing the capability of a digitally controlled system to heat various pixels simultaneously. c) Visible light photo of the addressable system. d) The system undergoing shape-changes into two load-bearing forms (see ii. and iv.) through heating of individual pixels. Insets in ii. and iii. show that the addressed pixel is the only heated point, allowing the system to be folded by a single finger. e) All pixels activated allowing the system to relax and be flattened into its original shape. f) The system, once cool, is again load bearing.

(see Figure 6.7b). This capability enables folds-on-demand in high-modulus thermoplastics. In Figure 6.7d, we show that by selectively engaging an individual pixel, we can bend the system on-demand at targeted locations while contacting the system at only a single point (*i.e.*, a single fingertip). Since the rest of the system is rigid, only the targeted location bends under the input force (see inset to Figure 6.7d,ii-iii).

To demonstrate the versatility of a pixelized variable stiffness system, we formed several functional structures. We first formed the planar sheet into a load-bearing, raised cantilever (Figure 6.7d,ii). We then improved the load bearing design by adding another bend, turning the whole sheet into a raised table (see Figure 6.7d,ii and also Supplemental Video 5). Finally, we demonstrated that the reversibility of the pixels, as enabled by bonding the heater silicone to the variable stiffness sheet, allows the whole system to revert to its original shape. We did this by activating all the pixels simultaneously, and then manually flattening the system back into a straight plank (Figure 6.7e). It should be noted that the PLA sheet does not return to a pristine condition, as the heating and folding process naturally causes some warping in the re-flattened sheet, but regardless of this, the re-flattened plank could still support a mass (Figure 6.7f). This demonstration shows the possibilities for addressed fold-on-demand systems, as none of the load-bearing structures were preprogrammed into the material but formed by selectively heating one (or more) of four pixels. This concept can be further extended to joints-on-demand which has ramifications for controlling the active workspace of continuum manipulators.

6.4.3 2D On-Demand Hinges

Finally, returning to our initial motivation of ‘blank-slate’ fold-on-demand, shape-changing structures, we used our 2D heating arrays to create some origami-like folding structures both adjacent to and bonded to the heating arrays (see Figure 6.8). In our first demonstration, we used the 4x5 addressable heater to fold a 2D sheet of PLA into a 3D “paper” airplane (see both Figure 6.8a-b and Supplemental Video 6).

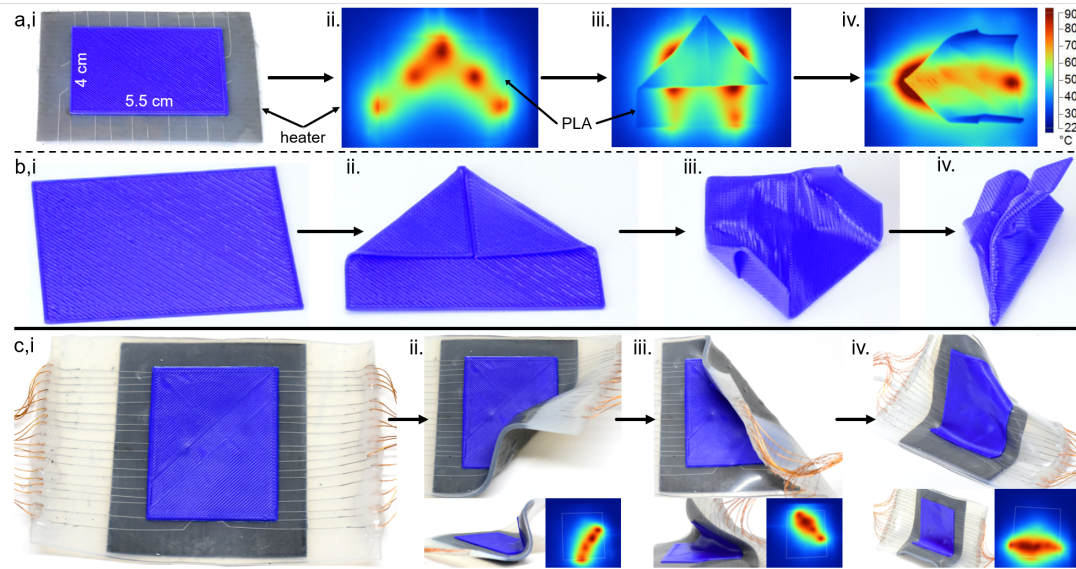


Figure 6.8. a-b) An unprogrammed variable stiffness sheet is heated using the 4x5 pixel heater to create artificial folds. a,i) The sheet laying on the heater. a,ii-iv) Top-down IR images showing the heated folds on the sheet. b) Images of the sheet in i) its initial state, ii-iii) intermediate states, and iv) final airplane-like shape after being cooled. c,i) PLA sheet bonded to a 6x6 pixel heater silicone sheet. c,ii-iv) The PLA sheet is bent (and flattened) along lines not previously defined in the polymer block, simply by heating a selection of pixels that make up a line with the heater silicone sheet. In both ii) and iii) the top view and a side-profile view of two successive bends are presented, along with an IR photo just before the bend occurred with the PLA sheet outlined. iv) An isometric view showing multiple bends in the same sheet, as well as an isometric view of the initial straight-line bend on the bottom (with its associated IR image). All IR images show temperatures up to 90°C. All PLA sheets are 4 cm x 5.5 cm.

This was made possible by selectively heating both straight and diagonal lines using individual pixels in the heater, while the PLA sheet was placed on top of the silicone. We did not bond the array to the variable stiffness sheet, simply to allow for sharper folds in the variable stiffness sheet.

To further illustrate the possibilities of a system that allows for folds-on-demand, with reversible folds, we bonded a sheet of PLA to the 6x6 addressable heater. This allowed us to use the 2D pixel array to create localized folding lines in the PLA sheet in multiple directions, as demonstrated in Figure 6.8c. As visible in the IR images in Figure 6.8c,ii, we observe that the pixels heated ($\sim 62^{\circ}\text{C}$) a spot with diameter 0.87 ± 0.11 cm. The spot size variation was due to the open-loop nature of the heating controller used. The center-to-center distance between diagonally adjacent pixels was 1.27 cm. Though the pixel density can be modulated, for our purposes the density of our 6x6 pixel array provided a good balance between the temperature required to heat each spot and the overlap between each pixel creating a continuous heated (softened) region. We demonstrate adding folds to the planar, stiff sheet, removing them to add additional folds, bi-directionality of the folds (a fold able to bend in both directions) and adding multiple folds at a time to a single sheet. For the sake of visibility, we held each fold partially open rather than having them completely flattened as in Figure 6.8b. These are just two demonstrations from the myriad possibilities of fold-on-demand sheet shaping via selective Joule heating.

6.5 Conclusion

We have developed a materials-based tool to fill the need of a stretchable, addressable heater useful for controlling thermally responsive soft materials. We demonstrated a conductive heater silicone composite sheet that can heat an adjacent material to 150°C and can be cyclically strained 1000 times at 40% strain while heating, due to reinforcement of the conductive silicone composite with an all-silicone backbone. This backbone became the key to successful implementation of localized, addressed

heating within the heater silicone sheets, as well as both extend-and-hold demonstrations and fold-on-demand (shape changing) structures. The backbone was critical to successful implementation of addressed heating pixels as it carries stretchable liquid metal electrode channels out-of-plane, until the electrode is ready for interfacing at specific locations in the heater silicone. We demonstrated a 6x6 array of heating pixels with a density of 1.9 pixels/cm², with each pixel able to (via open-loop control) heat up and soften an approximately 0.87 cm diameter spot in adjacent PLA sheets. By introducing closed-loop control on the power being passed through each addressable pixel (rather than the current open-loop state) we envision future work in which the local temperature can be far more precisely controlled, enabling uniform, gradient, or targeted heating. Although the backbone underpins the stretchability of the heater silicone, manufacturing of the composite layer also had a large impact on the uniformity of the heating and the stretchability of the sample. In future work, we aim to improve the thermal conductivity of the system so that the heater silicone is able to self-regulate the heat and distribute it more evenly around each point and swath.

The silicone backbone also allows for strong bonding to both a wax silicone composite and variable-stiffness polymer sheets to create composite material sheets which can change their stiffness on-demand. With the wax silicone, we were able to illustrate the potential of an all-silicone, bulk material, planar heater by performing stretch-and-hold operations which can potentially open a whole new frontier of planar material reconfiguration in which parts of the plane can be made stretchable. Future work in this area will involve balancing the force the wax-silicone exerts when in its extended-and-held state with the heater silicone's restoring force, so the system can remain both elongated and flat. We envision the methods presented here used to create ready-to-use slates that can be stretched, folded, twisted, and formed into complex 3D structures using pixel-controlled soft 'origami' folding in an otherwise blank material.

6.6 Experimental Section

Materials: Dragonskin 10(r) (Smooth-On Inc.) was used as the silicone for all experiments. Variable stiffness sheets were FDM 3D printed polylactic acid (PLA) sheets. This allowed for control over all three dimensions (length, width, and height) in the variable stiffness sheets for the various applications and demonstrations. Paraffin wax (melting temperature 60-65°C) was used as the stiffness changing filler in the stretch-and-hold silicone examples. It was mixed into the silicone matrix in a 1:2 ratio (33.3% wax by weight).

Expanded intercalated graphite composite was prepared by first exfoliating graphene sheets from graphite flakes and second, mixing it into the composite via a solvent carrier. 10g of dry expandable graphite (Sigma-Aldrich) was heated in an oven at 800°C, causing the exfoliation of the graphene flakes into noodle-like, ultra-low-density structures in approximately 20 seconds. These noodles were soaked in cyclohexane (BDH1111, VWR) and sonicated for 4 hours (Q700 sonicator fitted with 1/2" tip, QSonica, 20kHz, 36 μm (30% setting) amplitude) creating a slurry of solvent and individual EIG particles. The slurry was allowed to settle, and excess solvent was decanted off until the solution had a ratio between 3-5 wt% EIG, giving it a paste-like consistency. To finish the composite, equal parts A and B of the silicone elastomer were pre-mixed and chilled to prevent premature crosslinking. A few grams of this mixture were added to the EIG, according to the final desired mix ratio and volume of composite, and the whole solution was mixed thoroughly. The composite was then rod-coated into sheets, allowing the remaining cyclohexane solvent to evaporate away. Subsequent layers were rod-coated after the previous layer had fully cured.

Thermally responsive color-changing silicone (for Figure 6.3c) was made by adding a thermochromatic additive powder (Hali Industrial Co., Ltd.) to the silicone. The material begins to exhibit a visible color change at approximately 30°C, though higher temperatures cause a more distinct change.

Strain testing: A heater silicone specimen was cyclically strained in an Instron 3345 materials tester while measuring the resistance across the sample. The active (stretched) area of samples tested was 10 cm long, 1 cm wide, with a conductive layer $< 300 \mu\text{m}$ thick. The strain test procedure was as follows: samples were cyclically strained to 10% strain 200 times at 200mm/minute. The samples were then strained at incrementally higher strain values for 50 cycles per increment (5% strain increase per increment, making the test 15%, 20%, 25%, etc.) for 50 cycles at each strain value up to 50% strain.

Cyclic Heat Testing: Heater silicone was cyclically strained in a custom test apparatus, while maintaining an elevated, Joule heated temperature. The electrically active area (between two liquid metal electrodes) was 3 cm x 1 cm, and was strained at a strain rate of 35mm/min.

7. UNIFORM CONDUCTIVITY IN STRETCHABLE SILICONES VIA MULTIPHASE INCLUSIONS

The following chapter is based on work previously published as [172] R. A. Bilodeau*, A. Mohammadi Nasab*, D. S. Shah, and R. Kramer-Bottiglio, “Uniform Conductivity in Stretchable Silicones via Multiphase Inclusions,” *Soft Matter*, 2020.

* indicates co-first-authorship

Contributions: This chapter was worked on primarily by two individuals: myself and Dr. Amir Nasab. Original inception of the composite’s components came from me, whereas Amir studied and determined the exact composition required to ensure a very high success rate. Amir performed most of the materials characterizations while I continued to refine the manufacturing techniques such that we could make the composite in a variety of sizes and shapes (including reducing the thickness to sub 250 μm , and still connect to it electrically. I developed, manufactured, and implemented all of the applications, but credit for testing the sensors and capturing the sensing data goes to Dylan Shah.

7.1 Introduction

Soft robotic technologies have achieved increasing success in a wide range of actuation domains including robotic grippers [3,173], wearable assistive devices [174–176], and robot arms [177]. Simultaneously, stretchable electronics have shown success in a variety of use cases, including as biocompatible devices [178,179], wearable technologies [176,180], and, of course, soft robotic electronics [181,182]. Though there are many ways to create mechanically compliant stretchable electronics (patterning, printing, etc.) [183,184], within the context of soft robots it is often architecturally simpler to embed conductivity into a bulk stretchable material that matches the material compliance of the other soft robot components [185]. Recently, researchers have integrated stretchable, electrically conductive materials into soft robots to add

sensing [123], heating [149, 186], or signal and power lines [127], while reducing manufacturing complexity of the overall system [28].

To create high-strain, bulk conductive composites, many groups have embedded rigid conductive inclusions into stretchable materials. Only a few of these types of composites can handle linear strains of up to 100% [185, 187], and those composites often require specialized composite filler materials with complex manufacturing techniques [188, 189] or require specialized rubbers [190]. Even so, conductive composites can be used for electrical signaling and sensing, but when their conductivity is not spatially uniform under strain, they experience uneven energy dissipation while Joule heating, creating “hot spots” in the material. This non-uniform conductivity prevents them from being an embedded heat source for thermally triggered soft robotic components, such as volumetrically expanding silicones [133, 137], stiffness-varying stretchable silicones [122], and liquid crystal elastomer actuators [191]. In a recent work, we showed that adding expanded intercalated graphite (EIG) [59] into a silicone matrix in high enough concentrations (> 7 vol%) creates a composite with uniform electrical conductivity capable of Joule heating up to 150°C [128]. However, due to the high quantity of stiff EIG inclusions, the composite could not be stretched higher than 40% strain without cracking internally, creating thermal hot spots for Joule heating (although the material retained its electrical conductivity).

To improve material performance beyond the current limits of rigid inclusions, we draw on principles from a new class of liquid metal embedded elastomers (LMEEs). LMEEs are made by mechanically mixing a room temperature liquid metal (eutectic gallium-indium, or eGaIn) into uncured silicone at high volumetric ratios ($> 30\%$), which creates a highly-stretchable thermally-conductive composite that maintains the elastomer’s mechanical properties, while often improving other characteristics, such as dielectric strength and thermal conductivity [192–194]. Although non-conductive as cast, LMEEs easily integrate with other elastomers to improve current soft robotic actuator technologies [195, 196].

LMEEs can be activated using mechanical “sintering” techniques which cause the liquid metal inclusions to flow together and create channels with high electrical conductivity [127]. Sintering has been achieved by applying localized pressure on the composite [127, 191] and freezing the system to simultaneously activate the entire composite [197]. Hybrid composites exist in which liquid metal and a solid conductor are blended in the same silicone to create a composite that is conductive as-cast [198–200]. So far this has been primarily to use the liquid metal to enhance the functionality of the solid conductive filler, as evidenced by low volume fractions of liquid metal. Wang *et al.*, recently reported a high strain elastomer composite ($> 700\%$) using rigid particles and liquid metal inclusions [201], but the composite requires over 1000 cycles to stabilize its resistance, and exhibited relatively low conductivity compared with other liquid metal-silicone composites [26, 202].

In this paper, we show that the addition of a small amount of rigid EIG filler enables highly stretchable LMEEs to self-activate, becoming highly conductive and Joule heating-capable composites. This novel multiphase composite (MPC) self-activates under high linear strains ($> 200\%$), which drops its electrical resistivity by up to five orders of magnitude to $4 \times 10^{-5} \Omega\cdot\text{m}$. The MPC maintains a uniform, low resistivity while undergoing 200% linear strain, even when cycled 10,000 times. MPC silicone can be used in a wide range of applications, including Joule heating (Figure 7.1) and strain sensing. We show that, because of its high deformation capability, MPC silicone is highly compatible with other new soft robotic silicone composites and enables the creation of solid-state soft actuators that are robust to damage, and multifunctional thin film pneumatic bladders that can dynamically change their trajectory while providing sensory feedback. With its high conductivity and high strain capacity, MPC silicone is a step towards versatile soft robotic components which can change their shape and sense their deformations, using the same material.

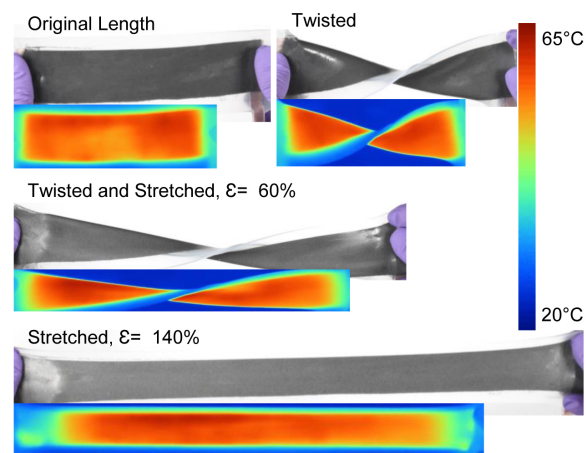


Figure 7.1. An activated 4×16 cm sample of MPC being simultaneously twisted and stretched, while maintaining a consistent, uniform Joule heating profile. The sample is fully encapsulated in silicone.

7.2 Principles of Operation

MPC silicone has three main components: eGaIn as the liquid metal (LM) alloy; EIG as the rigid conductive filler; and silicone elastomer (SE) as the composite matrix. In brief, it is manufactured by shear mixing 60% LM with 40% SE by volume, and then adding 1% vol EIG filler to the mixture (Additional details in Materials and Methods). As cast, the EIG fillers bridge the LM particles in the silicone matrix, and the material is electrically conductive, and stretchable up to $\sim 100\%$ strain, but it has a high electrical resistivity ($1.28 \pm 0.57 \, \Omega \cdot \text{m}$).

To activate the composite and increase its electrical conductivity, the material is strained to such a degree that the silicone matrix tears locally, allowing the LM inclusions to flow and coalesce into a low resistance network percolating throughout the composite (see Supplemental Videos 1 and 2). This strain-based activation requires the MPC to be supported by an extensible backing layer that adheres to the MPC to prevent catastrophic failure, by absorbing some of the energy released when the matrix tears. The supportive backing layer can be another silicone layer or even a stretchable adhesive tape (3M VHB tape) which is removable after activation (Figure S1). Most of the samples in this paper use some form of silicone backing layer, to improve mechanical robustness and facilitate the addition of electrodes.

Thrasher *et al.*, recently demonstrated a similar strain-activated mechanism in so-called “polymerized liquid metal networks” [203]. Acrylate ligands were bound to the surface of liquid metal particles, then cast and polymerized together, forming a 99% LM particle film on a substrate. Similar to the mechanism shown here, strain caused the initially isolated LM particles to rupture, allowing the liquid metal cores to flow and coalesce into a percolating conductive network. Our work differs from this in that we use a lower concentration of liquid metal, and our silicone matrix is typically more compatible with other traditional materials used in soft robots [23].

To demonstrate MPC silicone’s activation mechanism, we compared the activation (*i.e.*, first-strain behavior) of a LM-SE-EIG composite with that of LM-SE and SE-

Figure 7.2. Principles of operation of the MPC. a) Schematic compares pre- and post-stretch structures of three composite materials of LM-SE [192, 204], SE-EIG [128], and LM-SE-EIG (left to right). In the left column, although some microcracks appear on the surface of the LM-SE composite while being stretched, a conductive pathway through the whole structure does not form. In the middle column, the majority of conductive pathways in the SE-EIG composite are lost due to macroscopic cracks forming in the material. In the right column, the EIG facilitates microcracks in the LM-SE-EIG composite during stretching, which creates conductive pathways throughout the structure (activation). b) mm- and μm -scale images show the surface features of the three composites as cast, while stretched, and relaxed post-stretch. Light reflections from the microscope are visible on the LM beads expelled from the LM-SE-EIG surface. c) Optical and thermal images of samples of the three aforementioned composites Joule heated with electrical current at rest and stretched states, after a one-time ‘activation’ event. Temperature variance is used to view the resistance uniformity, as higher resistance areas generate more heat when a current is passed through the system.

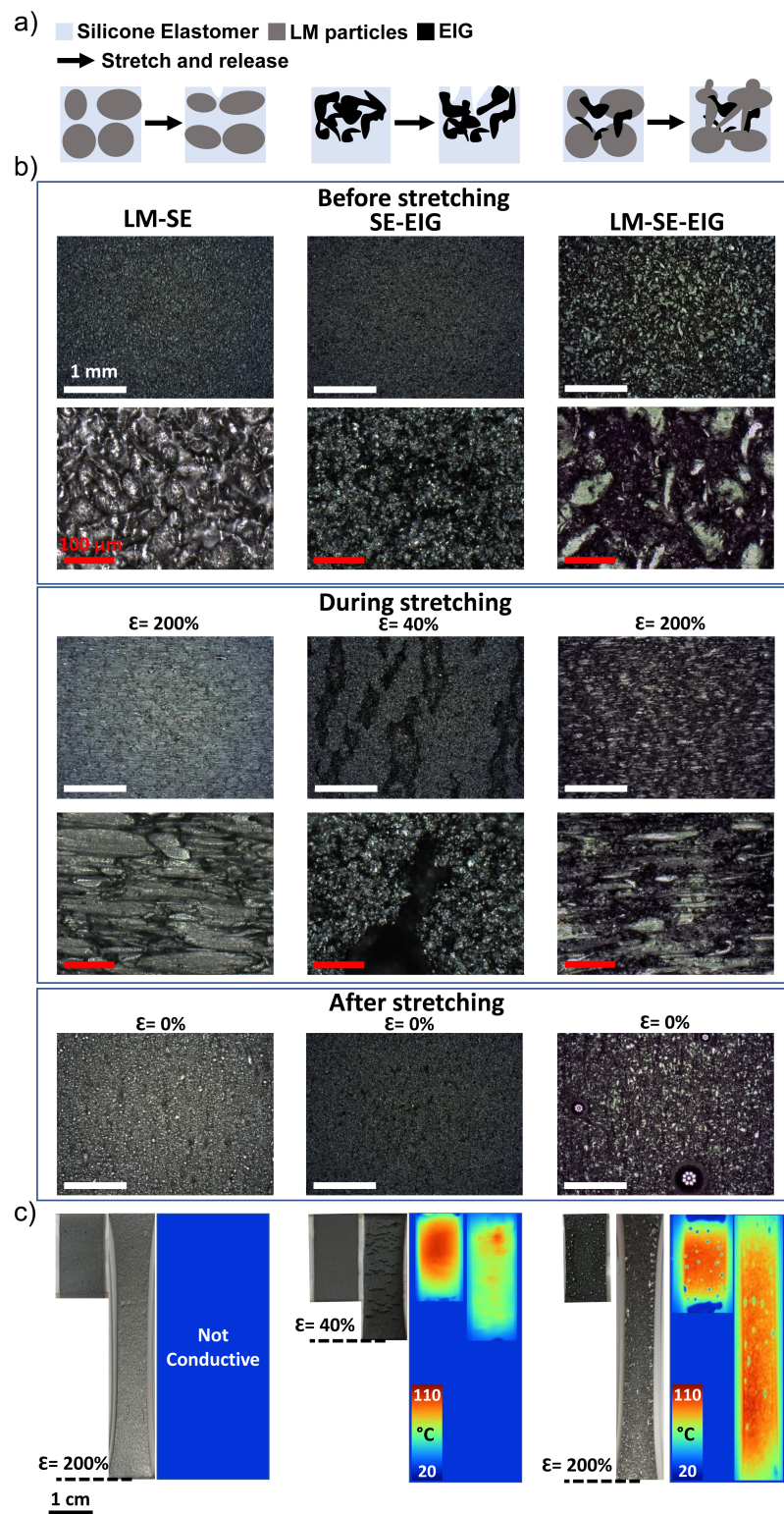


Figure 7.2.

EIG composites (Figure 7.2). When 60% LM and 40% SE by volume are shear-mixed and cured (Figure 7.2a-c, left column), the material is neither electrically conductive as cast, nor after being stretched, even with the high volume fraction of conductive LM. With no internal stress concentrators (*i.e.*, rigid particles) to incite microscopic failures in the silicone matrix, the liquid metal cannot coalesce into a conductive network. When 90% SE is mixed with 10% EIG by volume (Figure 7.2a-c, middle column), the material is electrically conductive as cast, but also comparatively brittle (failure at 40% strain) due to the rigid inclusions. When the two composites are combined to create LM-SE-EIG composite, the MPC silicone develops a uniform distribution of microcracks both internally and visibly on the surface after stretch (Figure 7.2a-c, right column). The LM particles coalesce through these pathways creating a continuous conductive network (seen as reflective pools forming at the microcrack sites, visible in Supporting Video 2), uniformly lowering the resistivity by several orders of magnitude. Additional evidence of a continuous internal liquid metal network is presented in Figure S2, where liquid metal drains out the bottom of a vertically-oriented MPC sample over a period of 40 minutes.

Figure 7.2b presents optical images of the surface of the three composite structures pre- and post-stretch. In the LM-SE composite (left column), LM particles maintain their boundaries, even at 200% strain. Some minor microcracks form on the surface of the LM-SE composite, but these are insufficient to create a conductive pathway through the whole structure (Figure 7.2c, left). This same microscale robustness holds when the LM-SE composite is compressed, a technique used in other works to create conductive pathways using silicones with lower yield strains [127]. In contrast, the SE-EIG composite exhibits brittle behavior from macrocracks on the surface when stretched to only 40% strain (Figure 7.2b, middle column). These cracks cause a rapid rise in the electrical resistance of the structure and a non-uniform electrical conductivity (Figure 7.2c, middle). Neither of these composite mixtures generate the desired high stretchability with uniform conductivity that is shown in our final MPC mixture.

Combining the fillers for the two non-functioning composites, microcracks are formed in the LM-SE-EIG silicone matrix when stretched (Figure 7.2, right column), resulting in a low, uniform electrical resistivity (Figure 7.2c, right). When released, some LM inclusions are displaced from inside the system and LM beads form on the surface of the MPC (Supplemental Video 2), a phenomenon previously observed in other strain-activated liquid metal composites [203]. We hypothesize that the displaced LM is due to the plastic deformation of the MPC (see Figure S1) relative to the elastic deformation of its backing layer during strain, which induces buckles and wrinkles throughout the MPC when relaxed [33]. Such wrinkling is visible in Figure 7.2b and Supplemental Video 2, and explains the displaced volume of LM during strain activation. To aid in transporting or attaching the MPC to another material system, we simply remove the excess LM beads by gently wiping the surface of the material with a cloth infused with Simple Green (Sunshine Makers, Inc) or another acidic or basic cleaning agent.

Figure 7.2c shows 10×20 mm samples of three composites at rest and in stretched states while they were Joule heated. MPC silicone shows a uniform temperature distribution on its surface as an indication of uniform electrical conductivity. Note that cool spots on the thermal image are not actually lower in temperature. They are the LM surface beads causing the IR camera to misreport their temperature as cooler, since LM has a lower emissivity than silicone.

7.3 Material Characterization

As previously noted, the primary MPC mixture we use is initially mixed to 60% LM and 40% SE by volume, with subsequent addition of 1% EIG by volume (suspended in cyclohexane as a carrier solvent). Although this makes a composite that is 59.4%-39.6%-1%, we use a shorthand convention to simplify notation, as 60-40-1. This notation is used for all other mix ratios tested.

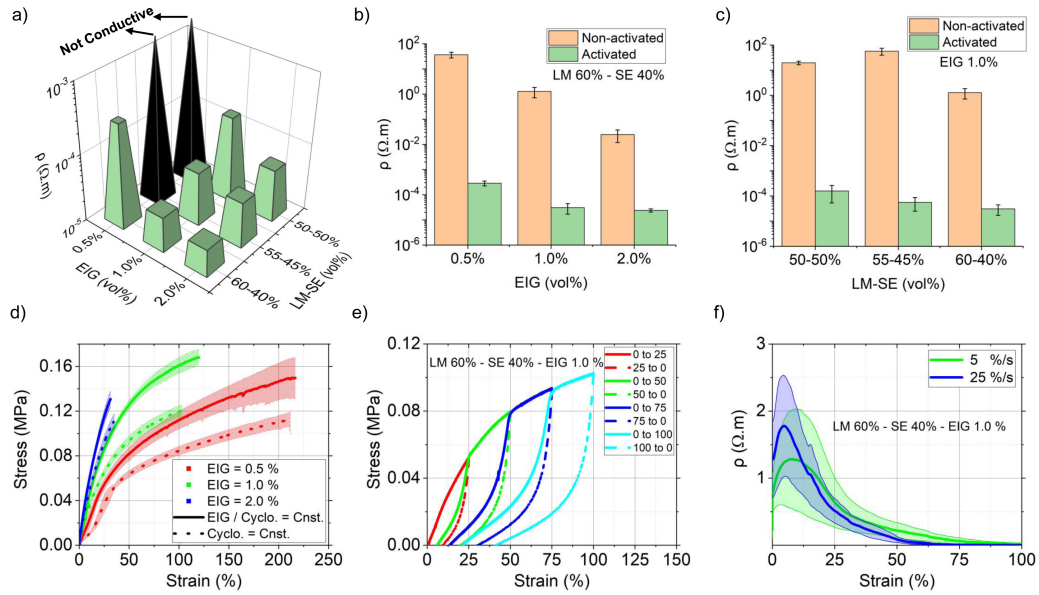


Figure 7.3. Electrical and mechanical characterization of MPC silicone. a) Electrical resistivity of the MPC after stretch as a function of LM and EIG volume fractions. Truncated pyramids show the compositions with electrical conductivity and full pyramids show the non-conductive compositions. b-c) Electrical resistivity of MPC silicone pre- and post-activation. b) LM 60%-SE 40% composition, varying the EIG volume fraction. c) EIG 1% composition, varying the LM-SE volume fraction. d) Mechanical testing of unactivated MPC (LM 60%-SE 40%, no backing layer), with 0.5%, 1.0%, and 2.0% volume fractions of EIG showing the elongation at break. e) Cyclic loading of MPC silicone (LM 60%-SE 40%) with 1.0% volume fraction of EIG. The material displays a Mullins effect at the first loading cycle at each strain. The stress is significantly smaller in the next cycles at the same strain level. f) Activation process of the MPC at two strain rates of 5%/s and 25.0%/s. Five samples at each speed are stretched up to 250% strain for the first time and the resistivity change is recorded. The material begins activating at lower strains when stretched with a higher strain rate. A representative plot of resistance drop for a sample is shown in Figure S3. Error bars in b and c, and shaded regions in d and f represent ± 1 standard deviation.

7.3.1 Electrical and Mechanical Properties

Volume fractions of LM and EIG were varied in the MPC compositions to investigate their role in the electrical conductivity of MPC silicone (Figure 7.3). For the tests evaluating the electrical resistivity, the MPC samples were supported with a pure silicone backing layer. Figure 7.3a shows the electrical resistivity of the activated (post-stretch) samples of MPC silicone for various volume fraction of LM and EIG. The electrical resistivity ρ , was calculated by measuring the electrical resistance R , thickness t , length l , and width w of MPC silicone samples using $\rho = R(tw)/l$.

As volume fractions of LM or EIG increased, the electrical resistivity of the MPC decreased. We found that there is a lower-limit to filler concentrations that, if the combination of LM and EIG is too low, the material does not activate (black pyramids in Figure 7.3a). If the material is filled with 60% LM volume fraction, even adding just 0.5% EIG will make the MPC electrically conductive. This concentration is close to the theoretical upper limit based on the maximum packing fraction in a randomly dispersed 3D mixture for fillers with aspect ratio close to one (about 64% [205]). Since the LM does not have an aspect ratio of exactly one, it might be possible to increase the concentration beyond 60% LM, but we discovered that any more LM made the materials very difficult to mix together uniformly.

Figure 7.3a shows that for compositions with LM volume fraction of 50%, increasing the EIG content from 1% to 2% decreased the electrical resistivity of the MPC after activation by 66%. However, for MPC compositions with LM volume fraction of 60%, that same increase in EIG content only decreased the electrical resistivity of the MPC by 22%. This indicates that the EIG, as a conductive filler, contributes relatively little to the material's activated conductivity for compositions with a high ($> 50\%$) LM volume fraction.

Figure 7.3b-c is a before and after comparison of the electrical resistivity of MPC silicone for various material compositions. Varying the volume fraction of EIG in the MPC, the resistance drop after activating the material is 5, 4, and 3 orders of mag-

nitude for 60-40-0.5, 60-40-1, and 60-40-2 compositions, respectively (Figure 7.3b). Notably, the electrical resistivity of the activated 60-40-1 composition is about one order of magnitude lower than that of the activated 60-40-0.5 composition. This notable drop in electrical resistivity is likely due to an increase of microcrack nucleation sites in the composite matrix from the increased EIG content (rather than a direct result of the EIG being conductive) enabling an improved LM network in the final, activated composite. The pre- and post-activation electrical resistivity of different MPC compositions with varying LM concentrations and 1% EIG is shown in Figure 7.3c, with a more gradual downward trend in the resistivity as LM concentration increases.

It has been shown that solvents trapped in silicones can influence mechanical properties [206]. Cyclohexane is a relatively volatile solvent and it evaporates during the process of mixing the material and casting it into thin sheets. However, a small amount of solvent still evaporates after the MPC is cured leaving some voids behind in the structure of the composite. To investigate the effect of the EIG carrier solvent (cyclohexane) volume fraction on the mechanical properties of the MPCs, evaluations were performed for two mixture ‘recipes’: 1) the ratio of EIG to cyclohexane kept constant while the EIG content is varied in the mixture, and 2) the volume fraction of cyclohexane kept constant in the mixture disregarding variations in the EIG content, which resulted in a higher fraction of cyclohexane to silicone in the uncured mixture. Figure 7.3d shows the tensile mechanical behavior of unactivated MPC silicone samples (with no backing layer) for compositions 60-40-0.5, 60-40-1, and 60-40-2 as samples were stretched to failure. Increasing the EIG volume fraction in the composition increases the elastic modulus and decreases elongation at break. In the first recipe, MPC silicone with 0.5%, 1.0%, and 2.0% EIG volume fractions break at 216%, 120%, and 31% strain, respectively. For the second recipe, the elongation at break is only slightly lower at each composition, although the elastic modulus is reduced, as expected [206]. These observations support our hypothesis that elongation at break is strongly dependent on EIG content after curing and only weakly dependent on the

solvent content during mixing. Additionally, the ultimate strains recorded here provide minimum strains required to begin activation of each material composition such that there will be internal microcracking, and demonstrate the need for the backing layer (so the system can stretch to 250%) during activation.

MPC silicone displays a Mullins effect at the first loading cycle to an elevated strain value (Figure 7.3e). The stress is significantly smaller in the next cycles at the same strain level. This response to the initial loading is expected in liquid-composite elastomers [192], as it is observed in most elastomers. If the MPC is stretched to the same strain after the first loading, the Mullins effect disappears, but returns if the MPC is stretched more than its previous maximum strain.

MPC silicone also exhibits viscoelastic properties (*i.e.*, strain rate dependencies), as would be expected by a silicone elastomer system. This viscoelasticity results in higher stresses in the composite when the material is strained at higher rates, triggering the nucleation of microcracks at lower strain levels. Therefore the MPC activates at a lower strain level when stretched at a higher strain rate, as shown in Figure 7.3f. Figure S3 shows the representative resistance-strain activation curve for a single sample strained up to 250% strain.

Among all the compositions evaluated in Figure 7.3, 60-40-1 and 60-40-2 MPC silicone compositions always result in uniform electrical conductivity when strained to 250% strain. We suspect the reason to be that the increased volume fraction of LM increases the statistical uniformity of the distribution of LM inclusions, as well as their local proximity to each other. This uniform distribution of inclusions, combined with slightly elevated quantities of EIG, likely ensures that there is simultaneous microcracking throughout the composite during activation. We note that other factors influence the uniform conductivity of the MPC as well. Such factors include constant sample thickness, activation strain value (mature vs premature activation), and uniformity of the activation strain field, as shown in Figure S4. We chose a 60-40-1 MPC silicone composition for the applications shown in the paper, to keep uniform electrical conductivity after activation.

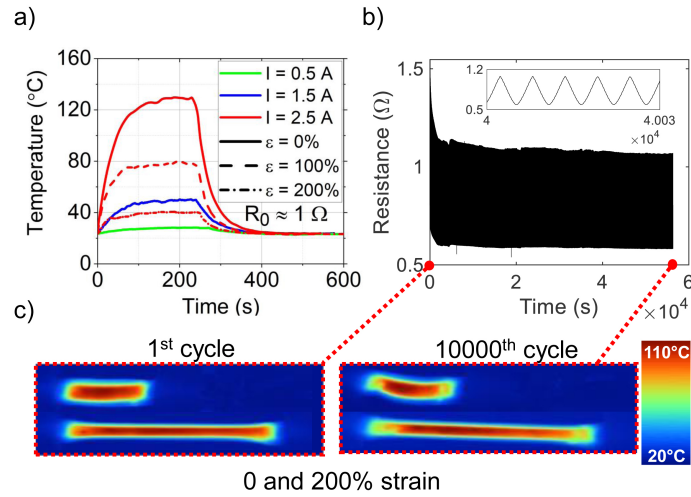


Figure 7.4. Thermal characteristics and cyclic robustness. a) Temperature of a $40 \times 10 \times 0.4$ mm activated MPC silicone sample supported with a 1 mm thick backing layer while being Joule heated with 0.5 A, 1.5 A, and 2.5 A for four minutes at 0% strain. The sample was then allowed to cool for six minutes at room temperature. Additionally overlaid is the same sample heated with 2.5 A at 100% and 200% strain. b) Resistance change of a MPC silicone sample ($30 \times 10 \times 0.4$ mm) cycled 10,000 times to 200% strain. Inset shows 30 s of cycling. c) IR images of the sample heating up with electrical current of 2.2 A before and after the cyclic test, showing no visible decrease in uniformity inside the main body.

7.3.2 Thermal Characteristics and Cyclic Robustness

Conductive silicone composites have been previously used as Joule heaters, trading off between high temperature-change capabilities [207] or improved stretchability [128, 142, 149, 186]. In order to be easily integrated into soft robots, desired properties include high temperature change capability, stretchability, and uniform resistivity (leading to uniform heating capabilities). Here we aim to quantify the suitability of the MPC as a heater material, while identifying potential limitations and advantages of our material.

Specifically, we used 60-40-1 MPC silicone as a heater, and evaluated its thermal response to different electrical inputs. Figure 7.4a shows the surface temperature of a $40 \times 10 \times 0.4$ mm MPC sample supported with a 1 mm thick silicone backing layer. The initial resistance of the sample at 0% strain was 1Ω . The sample was stretched to 100 and 200% strain and still demonstrated a uniform heat distribution over its surface, though the resistance increase caused the maximum achievable temperature at a fixed electrical current input (2.5 A) to decrease. Reducing the thickness of the backing layer allows the material to heat up faster, since there is less mass to absorb the thermal energy. An example is shown in Figure S5, in which an activated MPC silicone and its silicone backing layer have a total thickness of less than 250 μm .

To further characterize MPC silicone’s robustness as a heater, we coated neat silicone on both sides of $30 \times 10 \times 0.4$ mm MPC samples and cycled them 10,000 times to 200% strain. In Figure 7.4b we show electrical resistance over the whole test on one sample, with an initial settling in the resistance for 300 cycles followed by a plateau in the sample’s resistance. Mechanical strength after 10,000 cycles was observed to be similar to the original material, consistent with prior work in which robust cyclic mechanical testings have been performed on similar materials [59, 195]. IR images of the sample Joule heated at 0 and 200% strain with 2.2 A electrical current is displayed in Figure 7.4c, showing negligible difference in heating performance of the sample before and after the cyclic test.

We performed additional cyclic tests on samples that were coated with only a single backing layer of neat silicone (*i.e.*, ‘one-sided’ backings). These samples could only achieve 10,000 cycles if the strain was reduced to 150% (Figure S6). If they were strained cyclically to 200%, the one-sided samples would fail between 3000 and 5000 cycles. We therefore conclude that the highest cyclic performance is enabled by coating neat silicone on both sides of the MPC, which agrees with more detailed investigations done in prior work [128].

7.4 Applications

In the previous experiments, we have shown that MPC silicone can be used to make planar, skin-like sheets with high stretchability and uniform conductivity. We now use the material as a key component in three distinct systems, achieving multiple functions while reducing system complexity. The first application leverages the high conductivity of the MPC to enable high-strain sensory feedback with low noise. We then apply the MPC as a “skin” around a solid silicone composite that increases in volume when heated, producing a solid-state, all-soft actuator. Finally, we integrate it into the walls of a pneumatically inflating bladder with thermally controlled stretchability, allowing a single-bladder pneumatic actuator to attain multiple motion trajectories via electrical stimulus, all while using the MPC to simultaneously measure the actuator’s state.

7.4.1 High Deformation Sensing

We used activated 60-40-1 MPC silicone to create capacitive strain sensors which exhibit a repeatable linear response over strains as high as 200%. Capacitive strain sensors have been deployed in numerous applications ranging from measuring human body motion [208, 209], reconfigurable robotic skins [210], robot grippers [28], and numerous other applications [211, 212]. The classic 3-layer design (used in this work) has stretchable planar electrodes on the top and bottom of a stretchable dielectric

material. Capacitive sensors provide a more consistent response than resistive sensors, where comparisons between the capacitance and resistance of sensors of the same material are available [59, 208]. Measuring the capacitance of such sensors (typically on the order of 1-100 pF) is a challenging task however, and several methods have been employed [213]. Each proposed method has benefits and drawbacks, but generally low electrode resistance and high capacitance are desirable, giving our new MPC silicone an opportunity to improve current sensor systems.

One drawback to capacitive sensing methods is that they are relatively susceptible to external noise. Noise can come from many sources, including an unstable ground or supply line. Additionally, the sensor will pick up external electromagnetic noise in the form of an unstable electrode voltage and correspondingly noisy capacitance measurements. Filtering can be used to mitigate the effects of such noise, for example using analog low-pass filters [52], or using digital signal processing methods (as is done on the MPR121, manufactured by NXP Semiconductor). Here, we found that our sensor paired with the MPR121 results in a stable system, with resting noise standard deviation σ of only $\sim 0.05\%$ of the full scale range of the sensors' response over 200% strain, or $\sigma = 0.1\%$ (further analysis presented in Supplemental Materials as Table S1).

To investigate the advantages and disadvantages of various combinations of sensors and sensing circuits, we compared the MPC sensors to SE-EIG sensors [59] (*i.e.*, sensors made from the conductive graphite composite without the added liquid inclusions) using two sensing methods: a commercial charge integration circuit (MPR121), and an in-house designed charge integration circuit described in prior works [52] (Figure 7.5). This second circuit was designed to work well with the relatively high resistance of the graphite sensors ($\sim 1\text{-}10\text{ k}\Omega$ initially, and increasing to $\sim 100\text{-}1000\text{ k}\Omega$ at 200% strain). The low resistance of MPC silicone was predicted to result in more stable sensor response, which was confirmed experimentally in Figure 7.5a and Figure S7. The low, stable resistance over large strains results in stable capacitance readings when MPC is used as the electrode material (Figure 7.5). In

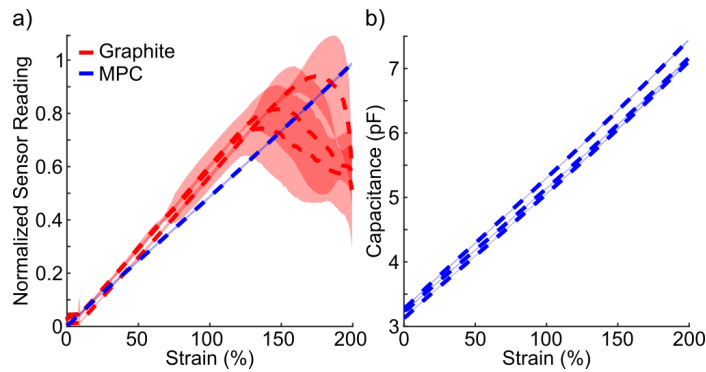


Figure 7.5. Response of MPC strain sensors. a) Comparison to SE-EIG capacitive sensors [59], as measured using our charge-integration capacitance measuring circuit over 10 cycles. Normalized response is highly stable across all eight MPC sensors, while each of the three graphite sensors behaved similar over strains lower than $\sim 60\%$ but had large inter- and intra- specimen variation at high strains. b) MPC sensors stretched to 200% for 1000 cycles. Three sensors are plotted individually, showing high linearity and that they mainly differ in their intercept and slope. Dashed lines represent the mean over 10 cycles. Shaded regions in both plots represent ± 1 standard deviation.

contrast, the graphite sensors experience cracking of their electrodes after around 60% strain, making them difficult to use as a strain sensor. MPC sensor readings S were normalized as $\bar{S} = \frac{S-S_0}{S_{max}-S_{min}}$, where S_{max} and S_{min} are the maximum and minimum reading over 10 cycles, respectively. Once this is done, the data from all eight MPC sensors that we tested collapsed into a single, linear response curve. Graphite sensors were normalized as $\bar{S} = \frac{S-S_0}{10000}$, and plotted individually due to the high inter-sensor and intra-sensor variability at strains greater than $\approx 60\%$. Raw data for each sensor are plotted individually in Figure S7.

In addition to yielding stable readings, low electrode resistance makes it possible to utilize commercial off-the-shelf components. Here we used the commercial MPR121 circuit to measure capacitance over 1000 cycles to 200% strain, for three sensors separately (Figure 7.5b). The relatively high resistance of the graphite sensors made them impossible to reliably read using the MPR121, giving an essentially flat curve after an inconsistent initial increase (Figure S7).

7.4.2 Solid State, Damage Resilient Actuation

Recent developments in solid-state soft actuators have been boosted by the development of other liquid-inclusion silicone composites, such as the ethanol silicone blend developed by Miriyev *et al.* [133,214]. This composite operates on a simple principle: heating the ethanol above its boiling temperature causes expansion via the liquid-gas transition. This in turn causes the silicone to increase in volume, up to 900% [133]. It is possible to harness this volumetric expansion inside of a McKibben-like mesh sleeve to control the direction of motion and the output forces, resulting in similar behavior to pneumatic actuators. The authors of the original work note that although the system can be rejuvenated by soaking in an ethanol bath for a period of time [215], Joule heating the system with a Nichrome wire often results in localized burning of the silicone and eventual degradation of the silicone system beyond recovery.

Joule heating ethanol silicone with a soft, stretchable heater is difficult due to the large expansion of the system. One work has embedded kirigami-cut conductive fabrics inside of the ethanol silicone to distribute heat throughout the core [216]. We previously used our conductive SE-EIG composite as a Joule heating core inside these solid-state actuators to generate high contraction forces (> 200 N) [137], but due to the low strain capacity of the initial heating composite (Figure 7.2), we could only show contraction actuation.

Because the ethanol silicone composite is a closed-cell foam-like composite with millimeter sized ethanol capsules [133], it is relatively agnostic to damage. If the silicone is sliced or pierced, the material will continue to expand so long as it has a heat source. This adds an additional layer of complexity to heating the system: finding a heat source that is both compatible with the large expansion and also agnostic to damage received while operating.

Since the MPC is a bulk composite material, it can be damaged and continue to function. Figure 7.6a shows an activated 4×16 cm strip of 60-40-1 MPC silicone (on a silicone backing layer) Joule heating before and after being cut with a blade. As long as the electrodes are reinstalled, the system continues to perform as it did prior to being damaged, with each segment showing uniform Joule heating.

As shown in Figure 7.6b-d (and Supplemental Video 3), we created a directional-controlled, damage resilient expansion actuator by wrapping an ethanol silicone core in a fiber-reinforced silicone composite and then our MPC silicone. The fiber-reinforced silicone is similar to the material found here [217], and prevents radial expansion of the ethanol-silicone tube. Figure S8 shows that this can enable both extension and rotation actuation, although we focused on the high-strain extension actuation case, activated by the MPC layer wrapped around the outside.

Since the system is solid state (*i.e.*, actuating with no parts moving relative to each other), and MPC silicone is robust to damage, we added electrodes by simply piercing the tube with pins (see Figure 7.6b,c insets). The pins provided a mechanical anchor for electrical clips, such that there was no concern of the clips losing connection

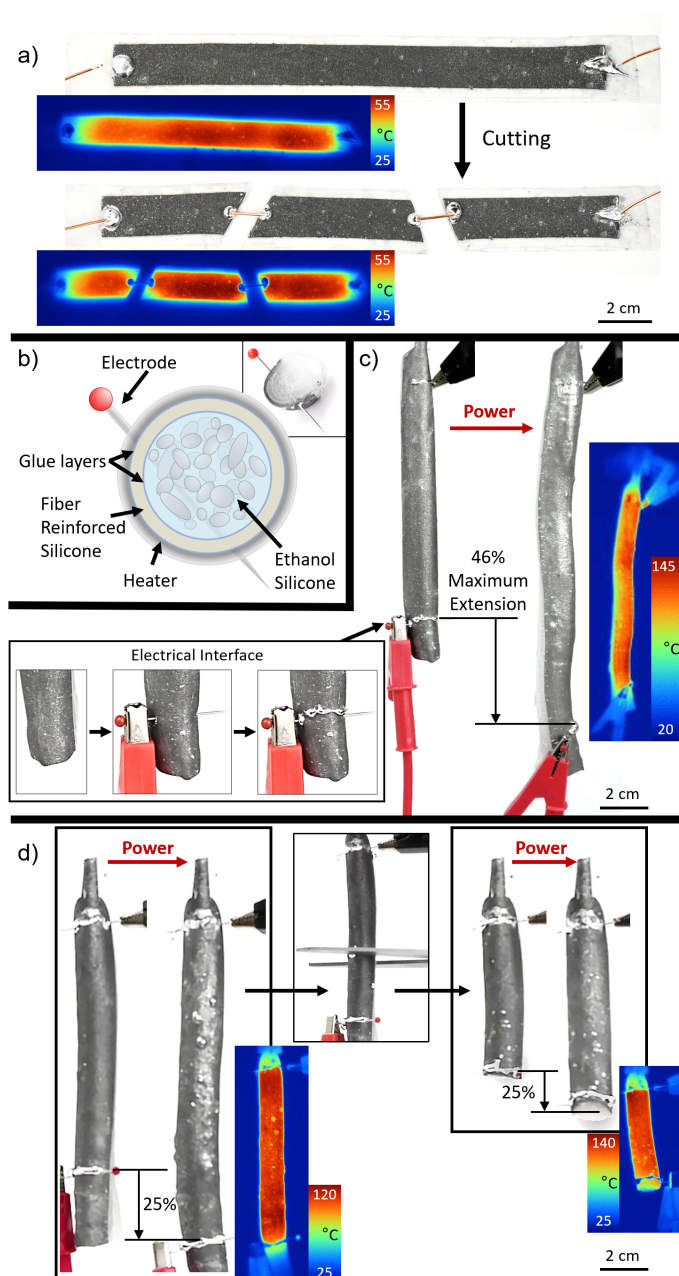


Figure 7.6. MPC silicone damage resilience. a) MPC silicone shown to be conductive before and after being cut into pieces. b) Cross-sectional diagram of the actuator system, with photograph inset of the same. c) Joule heating the MPC boils the ethanol trapped in the silicone core. The resulting expansion is controlled by the fiber reinforced silicone wrap, resulting in a 46% maximum elongation of the actuator. (Inset) The solid-state nature of the system allows for easy electrode creation by piercing the system with a pin. d) Both the actuator and the MPC silicone heater are agnostic to being cut in half, and, once the electrodes are restored, the system can continue to produce a 25% elongation.

to the heater during operation. After applying extra liquid metal to reduce contact resistance between the pins and MPC silicone [128], we Joule heated the external MPC could to over 140°C, causing the actuator to extend over 45% in length.

We demonstrated additional damage resilience by cutting the actuator in half and reactivating it (Figure 7.6d). Since both the heater and the actuator were made of bulk materials, trimming them down with scissors only resulted in a shorter actuator. Adding new electrodes near the cut re-established electrical conductivity and the system could resume extension actuation via Joule heating.

Electrically interfacing with a highly deformable soft material is usually difficult (See Materials and Methods for more discussion). Being able to run a pin through the entire system is a simple solution to a traditionally complex interfacing problem [137]. The pin becomes a robust connection point for rigid electronics that bring the power to the actuator (*i.e.*, copper wires or cables). Even though the system is undergoing large strains, the pins remain firmly lodged in the actuator. In this way, we gain the benefits demonstrated in our prior work [137], with improved ability to interface with the electrical heater and an actuator that can extend instead of just contract.

7.4.3 Multi-directional single-channel pneumatic soft actuators

In addition to functioning as the heat source for a liquid-to-gas phase change (driving the silicone actuator), MPC silicone can also induce solid-to-liquid phase changes, resulting in silicones with a variable material modulus. For example, it has been shown that when Field’s metal is added as a composite filler into a thin film of silicone, and attached to a pneumatic bladder, selectively heating the walls allows for a trajectory change as the pneumatic bladder inflates [122, 218]. This Field’s metal silicone composite (FMSi) experiences a change in its stretchability when the Field’s metal is melted ($T_m = 62^\circ\text{C}$). Additionally, it has been shown that this phase transition allows the FMSi to experience a type of “shape locking”. If the silicone is

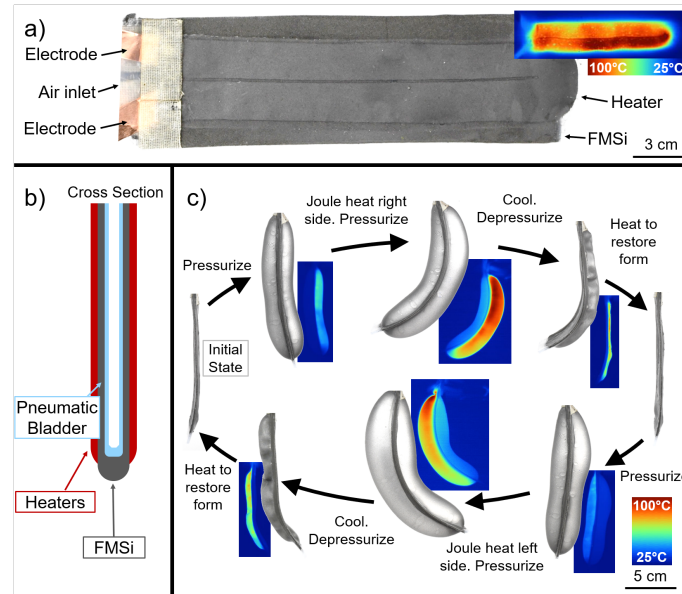


Figure 7.7. MPC silicone applied as a heater on a stretchability-changing pneumatic bladder. a) Front view of the pneumatic bladder, along with an IR image showing the MPC increasing the temperature sufficiently to melt the metal particles inside the Field's metal silicone (FMSi) bladder wall. b) Cross-sectional diagram of the actuator. c) Still frames (both IR and visible light) of the trajectory-changing pneumatic bladder cycling through different trajectories enabled by selectively heating the bladder's walls.

cooled while stretched, the inclusions will freeze and attempt to hold their deformed shape. In both prior examples though, an external heat source was needed.

To create a self-activating trajectory changing actuator, we prepared a demonstration similar to that shown by Buckner *et al.* [122], with an additional layer of pre-activated 60-40-1 MPC silicone on the outside in order to allow for on-demand Joule heating of the FMSi walls. Figure 7.7a shows a front view of the bladder, with one of the MPC heaters clearly visible in a U-shape on top of the FMSi. We chose this shape to allow for heating of the whole surface while also enabling us to access both ends of the heater from the top of the pneumatic bladder. We attached heaters to both sides of the bladder so that we could independently control the stretchability of each side (Figure 7.7b). Stiffness control is derived from thermally controlling the phase of the Field’s metal particles (solid particles below T_m , liquid inclusions above T_m): melted particles increase the composite’s ability to stretch.

By patterning material stiffness on the surface of an inflatable actuator, the trajectory of inflation can be changed on-demand. Figure 7.7c shows that selectively softening one side of the bladder (by applying current to the co-located stretchable Joule heater MPC sheet) influences actuator bending in the stiff-material direction. Selectively softening the opposite side of the bladder influences bending in the opposite direction. This demonstration shows that it is possible to achieve at least three different actuation trajectories in a pneumatic bladder (straight, bending left, and bending right) using only a single air input. The high-strain, highly electrically uniform MPC silicone on the outside of the bladder enabled Joule heating of the bladder’s walls, yielding a way to electrically control the actuator’s inflation trajectory..

7.4.4 Pneumatic bladder trajectory change with sensor feedback

Embedding sensors into pneumatic actuators is difficult due to the noise generated by the pneumatic inflation against the sensor. Often, researchers resort to using flexible (but not stretchable) sensors [28, 48, 219]. Stretchable sensors added to the

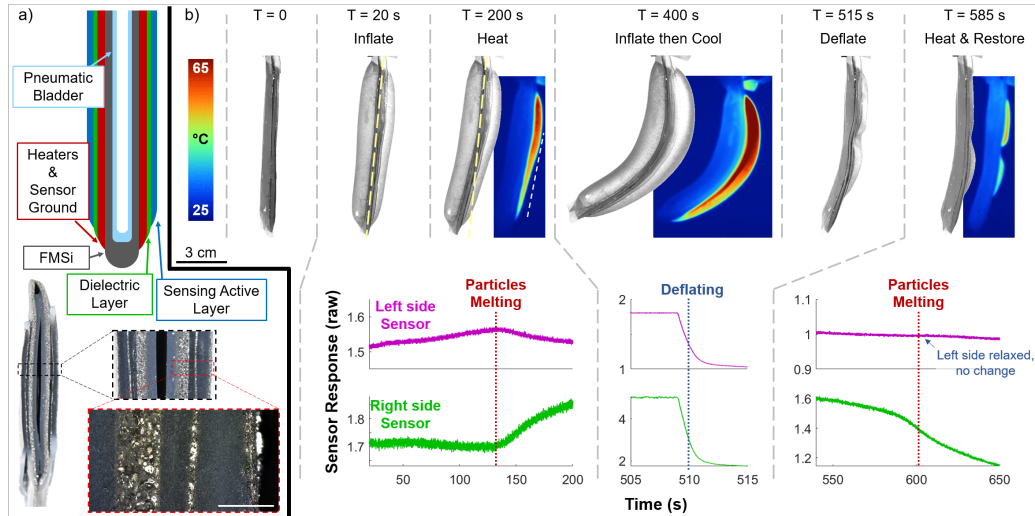


Figure 7.8. MPC silicone applied as a heater and a sensor on a stiffness-changing pneumatic bladder. a) Schematics and photographs of the cross section of the pneumatic bladder. Inset scalebar is 1 mm. Silicone glue layers are not shown in the schematic unless they serve an additional functional purpose b) Visible light and IR photographs of the sensorized bladder at various times, along with graphs of the raw sensor response as the system undergoes both temperature and pressure changes.

system require careful planning of sensor location so as to reduce the noise generated by the pneumatic inflation on the sensor's response to the curvature in the actuator [1]. In this work, our MPC silicone is capable of withstanding high strains and, when used as a capacitive strain sensor, provides a low-noise signal. In Figure 7.7, we show that the synergy between heating and strain capabilities allowed the variable-trajectory actuator to sense its motion. Specifically, we added a second layer of MPC onto the outside of the bladder (see diagram and cross-sections in Figure 7.8a), and observed the sensor response as the system underwent inflation, trajectory change, and shape recovery (Figure 7.8b, and Supplemental Video 4).

To minimize system complexity, we used the heater MPC silicone layer as the ground plane of the capacitive sensor (Figure 7.8a). This allowed us to reduce the thickness to approximately 3.25 mm per wall. Each layer of MPC silicone on each wall

is relatively thin (120 μm each, for a total of $\sim 240 \mu\text{m}$), while the remaining thickness came from the glue layer between the MPC silicone and the FMSi, in addition to the dielectric layer. For this reason, we used a stiffer silicone for the FMSi, so that the glue layer's thickness would not dominate the wall's stretchability (see the **Materials and Methods** section for more details). Note that the FMSi is not conductive, and so it could not be used as part of the sensor.

Figure 7.8b shows the data, as well as the experimental steps used to test the sensor response. First, the system was inflated partially, to engage the sensors. Then, we heated up the right wall (from the perspective shown throughout Figure 7.8), using the MPC heater. As the Field's Metal particles melted, the system subtly shifted the direction it was pointing and both sensors on the bladder responded to the positional shift in the expected manner: As the right wall heated up and softened, the whole wall expanded from the constant air pressure in the bladder. This caused the corresponding sensor to increase its capacitance. Furthermore, the sensor on the left (the cold wall) dropped its capacitance as the wall was able to contract slightly from its initial stretched state as the softer right wall expanded further.

After initiating trajectory change, we followed a similar method to that of the demonstration in Figure 7.7c. First, we inflated the actuator the rest of the way, observing that the sensor on the heated wall experienced a much greater change in capacitance. Then, we cooled the wall down and deflated the actuator, noting that the sensors detected the pressure change. Once the bladder was deflated, the right wall was holding an "expanded" shape, and so the sensor did not return to its original value. We used the MPC silicone heater to re-melt the Field's Metal particles in that wall and the sensor values dropped back to their relaxed states. Since the pressure in the bladder was in equilibrium with atmosphere, the left hand sensor did not respond to the heating and restoration of the original shape, as the left wall was already relaxed. This sequence showed that it is possible to use MPC silicone to create a thin, sensorized, trajectory changing, single-air-input pneumatic bladder.

7.5 Conclusions

We have presented a liquid-composite silicone with a high, spatially uniform conductivity (as demonstrated by Joule heating), which is robust to high deformations (200% strain) at high cycles of use (over 10,000 cycles), and has only a $2\times$ increase in resistance at 200% strain. All these properties together in a thin film enable many applications, some of which we demonstrated, including a stretchable Joule heater and a capacitive sensor responsive to strains up to 200%. We also showed both the heater and sensor being applied to drive high-strain linear actuation and stretchability change in high-deformation, shape-locking silicone composites. Furthermore, we showed that this material is robust to damage—if the system is cut, one must simply add a new electrode and it will continue to function as normal—a potentially impactful trait for a new soft robotic material.

In the future, we hope to continue to explore new activation methods, as well as new rigid filler materials. We do this with the goal of slightly increasing the overall material resistivity while maintaining the current manufacturing reliability and uniform conductivity. A higher resistivity would help us to scale-up the system to larger areas (geometrically reducing the resistance), so that we can Joule heat the MPC silicone using higher voltages and lower currents. By choosing a different activation stimulus (such as freeze activating [197]) or non-conductive rigid fillers, it may be possible to reduce the volume fraction of liquid metal in the MPC silicone so that the system could have both a lower mass and a higher resistance, while still maintaining a highly reliable activation mechanism.

7.6 Addendum about Generalizability

The material system that we made is potentially more generalizable for broader use than the specific formula presented herein, since it is the activation technique that enables the material functionality and applications. The holistic overview of the material is three basic components: a stretchable matrix with two composite fillers,

one a solid and the other a liquid. The solid induces stresses in the matrix, so that the matrix experiences localized failures as it is strained higher than 100%. These failure points are then filled in by the liquid, creating a continuous path of liquid throughout the body of the material, essentially converting a closed-cell stretchable foam into an open-cell foam, already fully saturated with the liquid. This materially-enabled activation technique could allow for a new class of materials, where one (or more) chemically or electrically responsive fluids could be contained in a stretch-to-activate silicone matrix (*e.g.*, stretchable glow-sticks, but as a patch that you stretch to activate then can wrap around an object of interest).

Exploring the idea of generalizability, each of the three elements of the material need specific traits for the system to work. The matrix needs to be highly stretchable or it will not be able to withstand strains up 200% (even after activation-induced wrinkling provides some geometric stretchability). This general property can apply to many different material classes, including silicones, stretchable acrylamides, or even thermoplastic elastomers. The liquid needs to be able to flow freely, likely with a low viscosity: since that the stretchable matrix is only 40% of the total volume of material and the system needs to reliably stretch to 200% strain without failure after activation, a low viscosity fluid facilitates the high-stretchability of the system as it flows more easily while experiencing high shear strains. Finally, and most importantly, the solid particle additives need to be a size and shape whereby they can generate a large quantity of stress concentrators, without needing to occupy a significant volume in the matrix. I suspect that the properties of the solid filler are more of geometry and material rigidity, rather than a specific chemical makeup (except that they should not react with the liquid), though this hypothesis would require additional modeling or investigation to validate. To create stretchable Joule heaters, we need to add one more requirement: the liquid must be conductive.

Generalizability aside, the materials used in the work presented herein have some useful secondary properties that enhance the material performance for the desired task (highly stretchable, uniform electrical activation). The silicone is compatible with

many existing soft robotic systems, while still being highly stretchable and enabling direct integration of the filler materials via mechanical mixing before curing. The compatibility and ease of manufacture allows for the material to be made relatively quickly, and is what enabled the enhanced-system demonstrations at the end of the chapter. The liquid metal is very conductive compared to most other conductive fluids (ionic liquids), and it can carry both alternating current (AC) and direct current (DC), whereas ionic liquids can only carry AC continuously. The gallium oxide layer that forms nearly instantly around the liquid metal also stabilizes the material during activation. When beads form on the MPC surface, the solid oxide layer prevents the beads from running off the material. It also prevents leakage when the material is moved and manipulated post activation. The EIG is a great solid additive as it is inexpensive and relatively easy to make in bulk. Additionally, it has a very high aspect ratio, disk-like shape (the diameter of EIG flakes is on the order of microns, with a thickness in the 10s of nanometers), making it an ideal stress concentrator (its extremely sharp edges encourage internal crack formation). Another, less important property is that the EIG is conductive, making the as-cast MPC conductive as well. This doesn't have much impact on the final conductivity, but it did prove useful in enabling electrical observation of the real-time activation (via the strain-resistance curves, as discussed in the chapter).

7.7 Materials and Methods

7.7.1 Materials and Material Preparation

Silicone.

Ecoflex 50 (Smooth-On Inc.) was used as the primary silicone elastomer for all experiments, as both matrix for the liquid inclusions and the reinforcing backing layer. Dragonskin 10 (Smooth-On Inc.) was used as the matrix silicone for the Field's metal

silicone (FMSi), to ensure that the stiffness of the FMSi sheets dominated the effects of the glue layers in the composite system.

Composite fillers.

Expanded intercalated graphite (EIG) was prepared using the techniques detailed in previous works [59, 128]. Expandable graphite (Sigma-Aldrich) was roasted at 800°C, added to a carrier solvent (cyclohexane, BDH1111, VWR), then sonicated to break the graphite into microscopic, graphene-like particles. Once the excess solvent was decanted, the solution was weighed and mixed into silicone precursors.

Eutectic gallium-indium (eGaIn) was prepared in-house by mixing 1 kg of indium (99.9% pure, RotoMetals) with 3 kg of gallium (99.99% pure, RotoMetals) in a beaker heated to 150°C overnight on a hot plate. Once mixed, any residual solids were scraped off the top of the liquid alloy, then the alloy was allowed to cool back down to room temperature. Once cooled, the eutectic components were decanted off from the remaining residual solids and stored for later use.

Field's metal alloy (Roto144F Low Melt Fusible Ingot Alloy, RotoMetals) was reduced into microscopic filler particles (size range 100 - 375 μm) using the same techniques detailed in previous works [122]. The alloy was melted in a beaker of hot water (80°C), mixed with a homogenizer for 2.5 min to break the liquid alloy into particles. When the cycle finished, cold water was immediately added to reduce the ambient temperature around the particles to less than 62°C, solidifying the particles and preventing them from fusing. The particles then sink to the bottom and are sieved out of the water, dried, and stored for later use.

Composites preparation.

LM-SE-EIG multiphase composite (MPC) silicone was manufactured in the following steps: 1) both parts of a two-part silicone elastomer were premixed, ensuring a proper 1-to-1 ratio of the two components. 2) LM was carefully shear-mixed with sili-

cone elastomer manually for several minutes, until no visible droplets of LM remained. 3) The EIG/cyclohexane solution was added to the LM-SE mixture in sufficient quantity so that the amount of EIG remaining in the system after the cyclohexane evaporated would be the desired volumetric ratio. 4) Once all parts were mixed together, if the system's viscosity was higher than desired, additional cyclohexane was added. A mask was cut out of 20 μm thick paper, and placed on a flat acrylic sheet. The final composite mixture was poured at one end of the mask and coated over the whole mask using custom made drawbars of 300 μm , 500 μm , and 1 mm thickness. After the mask was removed, the composite was left at room temperature to dry and then cure. At this point, the composite could be lifted and removed from the acrylic, or the first silicone elastomer reinforcing backing layer could be draw-coated over the top, depending on the sample being made.

LM-SE, and SE-EIG were manufactured using the same steps as the MPC silicone, withholding only the material that needed to be omitted.

Ethanol Silicone was prepared using the same techniques detailed in previous works [137]. Parts A and B of a two part silicone and pure ethanol were mixed in a 2-2-1 ratio (by volume) resulting in a final composite of 20% vol ethanol. The silicone was mixed slowly at first by hand to trap the ethanol in small bubbles internal to the system (approximately 1 minute of mixing). Once all the liquid ethanol on top of the silicone was mixed in, the composite was mixed at 2000 RPM in a planetary centrifugal mixer machine (Thinky Mixer, Thinky USA) for an additional minute in order to reduce the size of the ethanol bubbles. Then, the silicone was cast into its desired shape (a tube), and sealed to prevent the ethanol from escaping during the curing process.

The fiber reinforced silicone was manufactured using methods similar to those recorded in previous works [217]. A 0.3 mm diameter polyester fiber (sewing thread) was wound around a large drum (6 in [15.24 cm] diameter) with a spacing of approximately 0.8 mm between fiber centers. Then, while the drum continued to rotate, uncured silicone was coated over the fibers using a flat surface to ensure an even

coating of silicone over all the fibers. Finally, the drum was allowed to spin gently for several hours as the silicone cured to ensure a uniform thickness of silicone. Once cured, the sheet was removed from the drum. This resulted in a thin sheet of fiber reinforced silicone (0.75 mm thick).

The directional controlled solid-state actuators were made by cutting the fiber reinforced silicone into appropriate sizes, wrapping it twice around the ethanol silicone tubes, and gluing it together with additional uncured silicone.

Field's metal silicone was manufactured by mixing 30% Field's Metal particles by volume into Part A and B of Dragonskin 10 (SMooth-On Inc.). The uncured composite paste was then coated on a flat acrylic sheet with a 1 mm drawbar. After curing for 4 hours, appropriate sized sheets were cut and glued to each side of the silicone pneumatic bladder using an additional thin layer of silicone.

7.7.2 Mechanical and Electrical Characterization

Elongation at break and cyclic loading of LM-SE-EIG rectangular specimens (40 mm gauge length by 10 mm width and between 0.2 to 0.4 mm thickness) were evaluated in Instron 3345 testing machine equipped with a 50 N load cell (Figure 7.3d and e). Electrical characterization specimens included active dimensions of 20 mm \times 10 mm \times 0.2-0.4 mm thickness, and were supported by an additional backbone layer of pure silicone to prevent premature failure. Resistance change in the activation process of MPC silicones (Figure 7.3f) was evaluated by measuring the voltage across the specimens while simultaneously straining them in the Instron testing machine. We also measured the resistance of two samples (1-sided and 2-sided backbone) with 50-50-2 composition over a period of 90 days (Figure S9). After an initially sharp rise in resistance over the first 7 days, both samples settled into a very gradual increase for the remaining time.

7.7.3 Electrodes and Interfaces

For the simplest demonstrations, a bead of LM was placed on the surface of the MPC silicone and copper wires gently connected to the beads. The bead of LM reduced contact resistance between the copper wires and the MPC [128], enabling the demonstration of uniform conductivity through the MPC itself.

For the more detailed demonstrations (including the activation testing done in a vertical testing apparatus (Figure 7.3), as well as the cyclic testing (Figure 7.4)), a low-resistance, high stretchable electrode is a technical challenge. Often, the biggest challenge is the interface between the soft, high-deformation material and inextensible copper wires [220]. To create most of the electrical interfaces in this paper, we followed a similar tactic used in our previous works [128] where a bead of LM was placed directly on the MPC, and a copper wire (or film) was interfaced into that bead. Then, the electrode was sealed with silicone and an inextensible layer (porous muslin fabric tabs) that significantly reduced the strains in the joint between the liquid metal and the copper. This method is also supported by recent literature [221].

The only deviance from these two methods was in the solid-state actuator demonstration, where a pin was simply driven through the actuator, and a small layer of LM wrapped around the MPC to create an electrode with uniform conductivity along the entire circumference of the heating skin.

7.7.4 Capacitive Strain Sensors

Two types of three-layer sensors (electrode, dielectric, electrode) were manufactured using a conductive SE-EIG composite made with 10 wt.% EIG [59], and the new MPC as electrodes materials. The active region of both types was 10 cm by 1 cm.

Two capacitance measuring devices were used: MPR121 (by NXP Semiconductor, used as a component in a breakout board sold by Adafruit, Inc.), and a customized charge-integration circuit developed by our lab (described in [59], theory elaborated

in [52]). This custom circuit charged the sensors' top electrode for a constant time, then measured the time it took to discharge through a $10\text{ M}\Omega$ resistor to a known voltage reference. Importantly, the MPR121 is designed for capacitors with low electrode resistance, while the custom circuit was designed to be used with capacitive sensors with a wide range of resistances. Three test protocols were considered: 1) the sensors at resting length ($\epsilon = 0\%$) with no noise intentionally injected; 2) the sensors at resting length with a DC motor placed 3 cm away and ran at 12 V (resulting in ~ 100 RPM; item number 2826 from Pololu); 3) the sensors with no noise intentionally injected, pulled (using an Instron 3345) at 200 mm/min until 200 mm ($\epsilon = 200\%$) for 10 cycles. Data were collected for all combinations of sensor type, measuring device, and these three test protocols. Finally (test protocol 4), three MPC sensors were tested with the MPR121 and pulled at 200 mm/min until 200 mm for 1000 cycles. Key findings were presented in the main text, while noise characterization and complete raw data are presented in the supplementary materials.

8. SUMMARY

In order for soft robots to achieve their true potential as feature-complete robotic devices, they are going to need to continue pulling in multifunctional material components that both reduce design complexity and enhance performance. While traditional, rigid robots often rely on computer controls to enable self-adaptability, environmental conformability, as well as ‘softness,’ soft robots instead aim to produce material composites with these features designed directly into the material. This dissertation presents a few such multifunctional material systems that show the capacity to actuate, adapt, and even provide state feedback, with each of these systems designed to work in tandem with each other.

In chapter 2, I present a fluidically functionalized soft-bodied robot that integrates both sensing and actuation. Rather than combining these functions as an afterthought, I designed sensors and actuators into the robot at the onset, both reducing fabrication complexity and optimizing component interactions. I utilized liquid metal strain sensors and pneumatic actuators embedded into a silicone robotic gripper. I show that the liquid metal strain gauges provide a repeatable resistance response during robotic actuation. Building on this in chapter 3, I designed sensor-controlled antagonistic pneumatic actuators (SCAPAs) that integrate soft robotic actuators and sensors into a simplified, controllable design. The antagonistic actuators together compose a bidirectional bending actuator with embedded capacitive strain sensors. By designing the SCAPAs from the ground up for closed-loop control, I was able to minimize both the number of constituent components and the types of materials used, and further streamline the manufacturing processes. These improvements are embodied in the multipurpose use of a single conductive fabric sheet for both actuation and sensing, integrated into an otherwise all-silicone device. I

demonstrated that this design enables the use of simple control strategies to achieve closed-loop position control over the actuator.

In chapter 4, I introduced active variable stiffness fibers made from shape memory alloy and thermally responsive polymers carefully coated around each other, layer-by-layer. This combines the actuation of shape memory alloy with the variable stiffness of a thermoplastic using electric current as the stimulus. The multifunctional fibers can move to a new position and stiffen to hold it without requiring additional power. I integrated the active variable stiffness fibers into a fabric to demonstrate multifunctional robotic fabrics that can control the motion of soft, compliant bodies from their surface. Building on this work, in chapter 5, I showed increased functionality in active fabrics with improved actuator wires, stiffening fibers, and substrate-embedded sensors. Improved actuators allowed for pure-curvature bending motions to be developed in the fabric. Low-melting-point metallic alloy inclusions enhanced the stiffness change of the stiffening fibers enabling the fabric to hold additional force once cooled. Finally the fabric-embedded sensors allowed for closed-loop control over antagonistically paired actuation fibers sewn into the fabric substrate.

In chapter 6, I presented stretchable, addressable heating silicone sheets that can control soft, thermally responsive materials. The sheets are created using layer-by-layer deposition of a bulk conductive elastomer that can be Joule heated, with embedded liquid-metal microchannels used as electrodes. This combination allows the bulk, addressed material to be stretched and twisted while in operation. I demonstrated the utility of these sheets to become a thermal control platform in many situations. In chapter 7, I improved the overall functionality of the conductive silicone, enabling it to maintain a uniform conductivity while experiencing 200% linear strains. I showed how this material opens up possibilities for electrically controllable shape changing soft robotic actuators, as well as all-silicone actuation systems powered only by electrical stimulus. Additionally, I show that this stretchable composite can be used as an electrode material in other applications than those of chapter 6, including a strain sensor which attains a linear response up to 200% strain with near-zero signal noise.

Chapter 5 is the first of two ‘capstone’ works in this dissertation. A capstone work is one that integrates the intellectual contributions from a number of prior projects and demonstrates their broad-range applicability. This chapter was the cumulative result of the work, tools, and experience gained from prior chapters, although perhaps less-so than chapter 7. First is the obvious reliance on previous experience with fiber-based actuation and stiffness control in chapter 4. Next, the realization of bidirectional tracking of an actuator using sensors that are near-to the neutral axis is a key concept explored in chapter 3, and then brought over to the work in chapter 5. Additionally, critical tools were developed for the work in chapter 3 to enable closed loop control of an antagonistically actuated fabric system, and although the actuators were different, in both chapters I show that it is possible to achieve feedback control over a fabric-centered device.

Chapter 7, the final chapter of this dissertation, is the second of the capstone works. Not only does the work in chapter 7 directly build on ideas presented in chapter 6, but it also pulls from the materials, experience, and knowledge gained (directly or indirectly) from most of the other preceding chapters. Specifically, it culminates the experience in handling liquid metal in chapters 2 and Appendix A, the experience with inflatable pneumatic devices from chapters 2 and 3, and the ability to integrate Joule heating silicones with an active silicone in Appendix B. Finally, chapter 7 also pulls inspiration from the multifunctional planar robotic fabric systems, with sensor feedback and closed loop control, found in chapters 4 and 5. As such, this chapter demonstrates the applicability of the scientific discoveries and intellectual contributions presented in the previous chapters.

In conclusion, this dissertation presents both the materials and design concepts required to craft multifunctional soft robotic components. It has shown that it is possible to integrate sensing, actuation, structure, and electrical pathways into soft robotic systems. It has introduced design guidelines to ensure that the integration of these parts does not negatively impact the performance of the individual components, or of the overall system. Additionally it has presented a novel composite material

along with tools that enable the integration of this material into bulk, multifunctional composites. This work paves the way for the future design of fully realized soft robots, where much of the robot's adaptive, reactive, and communicative functionality is integrated directly into its body.

REFERENCES

- [1] R. A. Bilodeau, E. L. White, and R. K. Kramer, "Monolithic fabrication of sensors and actuators in a soft robotic gripper," in *2015 IEEE/RSJ International Conference on Intelligent Robots and Systems (IROS)*, Sep. 2015, pp. 2324–2329.
- [2] R. F. Shepherd, F. Ilievski, W. Choi, S. A. Morin, A. A. Stokes, A. D. Mazzeo, X. Chen, M. Wang, and G. M. Whitesides, "Multigait soft robot," *Proceedings of the National Academy of Sciences*, vol. 108, no. 51, pp. 20 400–20 403, Dec. 2011.
- [3] F. Ilievski, A. D. Mazzeo, R. F. Shepherd, X. Chen, and G. M. Whitesides, "Soft Robotics for Chemists," *Angewandte Chemie International Edition*, vol. 50, no. 8, pp. 1890–1895, Feb. 2011.
- [4] M. T. Tolley, R. F. Shepherd, B. Mosadegh, K. C. Galloway, M. Wehner, M. Karpelson, R. J. Wood, and G. M. Whitesides, "A Resilient, Untethered Soft Robot," *Soft Robotics*, vol. 1, no. 3, pp. 213–223, Sep. 2014.
- [5] C. D. Onal, X. Chen, G. M. Whitesides, and D. Rus, "Soft mobile robots with on-board chemical pressure generation," in *International Symposium on Robotics Research*, 2011, pp. 1–16.
- [6] S. Seok, C. Onal, R. Wood, D. Rus, and S. Kim, "Peristaltic locomotion with antagonistic actuators in soft robotics," in *2010 IEEE International Conference on Robotics and Automation (ICRA)*, 2010, pp. 1228–1233.
- [7] C. D. Onal and D. Rus, "Autonomous undulatory serpentine locomotion utilizing body dynamics of a fluidic soft robot," vol. 8, no. 2, p. 026003, Jun. 2013.
- [8] J. A. Rogers, T. Someya, and Y. Huang, "Materials and Mechanics for Stretchable Electronics," vol. 327, no. 5973, pp. 1603–1607, Mar. 2010.
- [9] M. D. Dickey, "Emerging Applications of Liquid Metals Featuring Surface Oxides," *ACS Applied Materials & Interfaces*, vol. 6, no. 21, pp. 18 369–18 379, Nov. 2014.
- [10] M. Yuen, A. Cherian, J. C. Case, J. Seipel, and R. K. Kramer, "Conformable actuation and sensing with robotic fabric," in *Intelligent Robots and Systems (IROS 2014), 2014 IEEE/RSJ International Conference on*. IEEE, 2014, pp. 580–586.
- [11] B. Mosadegh, P. Polygerinos, C. Keplinger, S. Wennstedt, R. F. Shepherd, U. Gupta, J. Shim, K. Bertoldi, C. J. Walsh, and G. M. Whitesides, "Pneumatic Networks for Soft Robotics that Actuate Rapidly," *Advanced Functional Materials*, vol. 24, no. 15, pp. 2163–2170, Apr. 2014.

- [12] A. A. Stokes, R. F. Shepherd, S. A. Morin, F. Ilievski, and G. M. Whitesides, "A Hybrid Combining Hard and Soft Robots," *Soft Robotics*, vol. 1, no. 1, pp. 70–74, Jul. 2013.
- [13] M. D. Dickey, R. C. Chiechi, R. J. Larsen, E. A. Weiss, D. A. Weitz, and G. M. Whitesides, "Eutectic Gallium-Indium (EGaIn): A Liquid Metal Alloy for the Formation of Stable Structures in Microchannels at Room Temperature," *Advanced Functional Materials*, vol. 18, no. 7, pp. 1097–1104, Apr. 2008.
- [14] R. C. Chiechi, E. A. Weiss, M. D. Dickey, and G. M. Whitesides, "Eutectic Gallium-Indium (EGaIn): A Moldable Liquid Metal for Electrical Characterization of Self-Assembled Monolayers," vol. 120, no. 1, pp. 148–150, 2008.
- [15] Y.-L. Park, D. Tepayotl-Ramirez, R. J. Wood, and C. Majidi, "Influence of cross-sectional geometry on the sensitivity and hysteresis of liquid-phase electronic pressure sensors," vol. 101, no. 19, p. 191904, Nov. 2012.
- [16] C. Majidi, R. Kramer, and R. J. Wood, "A non-differential elastomer curvature sensor for softer-than-skin electronics," vol. 20, no. 10, p. 105017, Oct. 2011.
- [17] R. K. Kramer, C. Majidi, R. Sahai, and R. J. Wood, "Soft curvature sensors for joint angle proprioception," in *2011 IEEE/RSJ International Conference on Intelligent Robots and Systems (IROS)*, 2011, pp. 1919–1926.
- [18] Y.-L. Park and R. Wood, "Smart pneumatic artificial muscle actuator with embedded microfluidic sensing," in *2013 IEEE Sensors*, Nov. 2013, pp. 1–4.
- [19] Y.-L. Park, B.-R. Chen, and R. J. Wood, "Design and Fabrication of Soft Artificial Skin Using Embedded Microchannels and Liquid Conductors," vol. 12, no. 8, pp. 2711–2718, 2012.
- [20] J.-B. Chossat, Y.-L. Park, R. Wood, and V. Duchaine, "A Soft Strain Sensor Based on Ionic and Metal Liquids," *IEEE Sensors Journal*, vol. 13, no. 9, pp. 3405–3414, Sep. 2013.
- [21] J. W. Boley, E. L. White, G. T.-C. Chiu, and R. K. Kramer, "Direct Writing of Gallium-Indium Alloy for Stretchable Electronics," *Advanced Functional Materials*, vol. 24, no. 23, pp. 3501–3507, Jun. 2014.
- [22] B. Finio, R. Shepherd, and H. Lipson, "Air-powered soft robots for K-12 classrooms," in *Proceedings of the IEEE Integrated STEM Education Conf.(ISEC)*, 2013, pp. 1–6.
- [23] J. C. Case, E. L. White, and R. K. Kramer, "Soft Material Characterization for Robotic Applications," *Soft Robotics*, vol. 2, no. 2, pp. 80–87, Jun. 2015.
- [24] D. Zrnic and D. S. Swatik, "On the resistivity and surface tension of the eutectic alloy of gallium and indium," vol. 18, no. 1, pp. 67–68, May 1969.
- [25] H.-J. Kim, T. Maleki, P. Wei, and B. Ziaie, "A Biaxial Stretchable Interconnect With Liquid-Alloy-Covered Joints on Elastomeric Substrate," *Journal of Microelectromechanical Systems*, vol. 18, no. 1, pp. 138–146, Feb. 2009.

- [26] S. Zhu, J.-H. So, R. Mays, S. Desai, W. R. Barnes, B. Pourdeyhimi, and M. D. Dickey, "Ultrastretchable Fibers with Metallic Conductivity Using a Liquid Metal Alloy Core," *Advanced Functional Materials*, vol. 23, no. 18, pp. 2308–2314, May 2013.
- [27] J. T. B. Overvelde, Y. Mengüç, P. Polygerinos, Y. Wang, Z. Wang, C. J. Walsh, R. J. Wood, and K. Bertoldi, "Numerical mechanical and electrical analysis of soft liquid-embedded deformation sensors," *Extreme Mechanics Letters*, 2014.
- [28] R. A. Bilodeau, M. C. Yuen, J. C. Case, T. L. Buckner, and R. Kramer-Bottiglio, "Design for Control of a Soft Bidirectional Bending Actuator," in *2018 IEEE/RSJ International Conference on Intelligent Robots and Systems (IROS)*, Oct. 2018, pp. 1–8.
- [29] P. Polygerinos, N. Correll, S. A. Morin, B. Mosadegh, C. D. Onal, K. Petersen, M. Cianchetti, M. T. Tolley, and R. F. Shepherd, "Soft Robotics: Review of Fluid-Driven Intrinsically Soft Devices; Manufacturing, Sensing, Control, and Applications in Human-Robot Interaction," *Advanced Engineering Materials*, vol. 19, no. 12, p. 1700016, Dec. 2017.
- [30] H. Zhao, K. O'Brien, S. Li, and R. F. Shepherd, "Optoelectronically innervated soft prosthetic hand via stretchable optical waveguides," *Science Robotics*, vol. 1, no. 1, p. 10, Dec. 2016.
- [31] N. Farrow and N. Correll, "A soft pneumatic actuator that can sense grasp and touch," in *2015 IEEE/RSJ International Conference on Intelligent Robots and Systems (IROS)*, Sep. 2015, pp. 2317–2323.
- [32] C. M. Best, J. P. Wilson, and M. D. Killpack, "Control of a pneumatically actuated, fully inflatable, fabric-based, humanoid robot," in *2015 IEEE-RAS 15th International Conference on Humanoid Robots (Humanoids)*, Nov. 2015, pp. 1133–1140.
- [33] D. Yang, B. Mosadegh, A. Ainla, B. Lee, F. Khashai, Z. Suo, K. Bertoldi, and G. M. Whitesides, "Buckling of Elastomeric Beams Enables Actuation of Soft Machines," *Advanced Materials*, vol. 27, no. 41, pp. 6323–6327, Nov. 2015.
- [34] M. A. Robertson and J. Paik, "New soft robots really suck: Vacuum-powered systems empower diverse capabilities," *Science Robotics*, vol. 2, no. 9, p. eaan6357, Aug. 2017.
- [35] B. Trimmer, "Soft Robot Control Systems: A New Grand Challenge?" *Soft Robotics*, vol. 1, no. 4, pp. 231–232, Dec. 2014.
- [36] D. Rus and M. T. Tolley, "Design, fabrication and control of soft robots," *Nature*, vol. 521, no. 7553, pp. 467–475, May 2015.
- [37] E. H. Skorina, M. Luo, S. Ozel, F. Chen, W. Tao, and C. D. Onal, "Feedforward augmented sliding mode motion control of antagonistic soft pneumatic actuators," in *2015 IEEE International Conference on Robotics and Automation (ICRA)*, May 2015, pp. 2544–2549.
- [38] C. M. Best, M. T. Gillespie, P. Hyatt, M. D. Killpack, L. Rupert, and V. Sherrod, "Model predictive control for pneumatically actuated soft robots," *Robotics and Automation Magazine. IEEE*, 2015.

- [39] M. T. Gillespie, C. M. Best, and M. D. Killpack, "Simultaneous position and stiffness control for an inflatable soft robot," in *2016 IEEE International Conference on Robotics and Automation (ICRA)*, May 2016, pp. 1095–1101.
- [40] E. H. Skorina, W. Tao, F. Chen, M. Luo, and C. D. Onal, "Motion control of a soft-actuated modular manipulator," in *2016 IEEE International Conference on Robotics and Automation (ICRA)*, May 2016, pp. 4997–5002.
- [41] S. I. Rich, R. J. Wood, and C. Majidi, "Untethered soft robotics," *Nature Electronics*, vol. 1, no. 2, pp. 102–112, Feb. 2018.
- [42] A. D. Marchese, K. Komorowski, C. D. Onal, and D. Rus, "Design and control of a soft and continuously deformable 2D robotic manipulation system," in *2014 IEEE International Conference on Robotics and Automation (ICRA)*, May 2014, pp. 2189–2196.
- [43] P. Polygerinos, Z. Wang, K. C. Galloway, R. J. Wood, and C. J. Walsh, "Soft robotic glove for combined assistance and at-home rehabilitation," *Robotics and Autonomous Systems*, vol. 73, no. Supplement C, pp. 135–143, Nov. 2015.
- [44] R. V. Martinez, J. L. Branch, C. R. Fish, L. Jin, R. F. Shepherd, R. M. D. Nunes, Z. Suo, and G. M. Whitesides, "Robotic Tentacles with Three-Dimensional Mobility Based on Flexible Elastomers," *Advanced Materials*, vol. 25, no. 2, pp. 205–212, Jan. 2013.
- [45] P. Moseley, J. M. Florez, H. A. Sonar, G. Agarwal, W. Curtin, and J. Paik, "Modeling, Design, and Development of Soft Pneumatic Actuators with Finite Element Method: Modeling, Design, and Development of SPAs with FEM . . .," *Advanced Engineering Materials*, vol. 18, no. 6, pp. 978–988, Jun. 2016.
- [46] G. Agarwal, M. A. Robertson, H. Sonar, and J. Paik, "Design and Computational Modeling of a Modular, Compliant Robotic Assembly for Human Lumbar Unit and Spinal Cord Assistance," *Scientific Reports*, vol. 7, no. 1, Dec. 2017.
- [47] B. S. Homberg, R. K. Katzschnann, M. R. Dogar, and D. Rus, "Haptic identification of objects using a modular soft robotic gripper," in *2015 IEEE/RSJ International Conference on Intelligent Robots and Systems (IROS)*, Sep. 2015, pp. 1698–1705.
- [48] S. Ozel, E. H. Skorina, M. Luo, W. Tao, F. Chen, Y. Pan, and C. D. Onal, "A composite soft bending actuation module with integrated curvature sensing," in *2016 IEEE International Conference on Robotics and Automation (ICRA)*, May 2016, pp. 4963–4968.
- [49] K. Elgeneidy, N. Lohse, and M. Jackson, "Bending angle prediction and control of soft pneumatic actuators with embedded flex sensors – A data-driven approach," *Mechatronics*, Oct. 2017.
- [50] H.-J. Kim, C. Son, and B. Ziaie, "A multiaxial stretchable interconnect using liquid-alloy-filled elastomeric microchannels," *Applied Physics Letters*, vol. 92, no. 1, p. 011904, Jan. 2008.
- [51] J. C. Case, E. L. White, and R. K. Kramer, "Sensor enabled closed-loop bending control of soft beams," *Smart Materials and Structures*, vol. 25, no. 4, p. 045018, 2016.

- [52] E. L. White, J. C. Case, and R. Kramer-Bottiglio, "A Soft Parallel Kinematic Mechanism," *Soft robotics*, vol. 5, no. 1, pp. 36–53, 2018.
- [53] E. L. White, M. C. Yuen, and R. K. Kramer, "Distributed sensing in capacitive conductive composites," in *2017 IEEE SENSORS*, Oct. 2017, pp. 1–3.
- [54] T. Giffney, E. Bejanin, A. S. Kurian, J. Travas-Sejdic, and K. Aw, "Highly stretchable printed strain sensors using multi-walled carbon nanotube/silicone rubber composites," *Sensors and Actuators A: Physical*, vol. 259, pp. 44–49, Jun. 2017.
- [55] M. C.-S. Yuen, T. R. Lear, H. Tonoyan, M. Telleria, and R. Kramer-Bottiglio, "Toward Closed-Loop Control of Pneumatic Grippers During Pack-and-Deploy Operations," *IEEE Robotics and Automation Letters*, vol. 3, no. 3, pp. 1402–1409, Jul. 2018.
- [56] J. C. Case, J. Booth, D. S. Shah, M. C. Yuen, and R. Kramer-Bottiglio, "State and stiffness estimation using robotic fabrics," in *2018 IEEE International Conference on Soft Robotics (RoboSoft)*. IEEE, Apr. 2018, pp. 522–527.
- [57] Y. Yang and Y. Chen, "Innovative Design of Embedded Pressure and Position Sensors for Soft Actuators," *IEEE Robotics and Automation Letters*, vol. 3, no. 2, pp. 656–663, Apr. 2018.
- [58] H. Zhao, R. Huang, and R. F. Shepherd, "Curvature control of soft orthotics via low cost solid-state optics," in *2016 IEEE International Conference on Robotics and Automation (ICRA)*, May 2016, pp. 4008–4013.
- [59] E. L. White, M. C. Yuen, J. C. Case, and R. K. Kramer, "Low-Cost, Facile, and Scalable Manufacturing of Capacitive Sensors for Soft Systems," *Advanced Materials Technologies*, vol. 2, no. 9, p. 1700072, Sep. 2017.
- [60] N. Farrow, L. McIntire, and N. Correll, "Functionalized textiles for interactive soft robotics," in *2017 IEEE International Conference on Robotics and Automation (ICRA)*, May 2017, pp. 5525–5531.
- [61] J. W. Booth, J. C. Case, E. L. White, D. S. Shah, and R. Kramer-Bottiglio, "An Addressable Pneumatic Regulator for Distributed Control of Soft Robots," in *2018 IEEE International Conference on Soft Robotics (RoboSoft)*. IEEE, Apr. 2018, pp. 25–30.
- [62] M. C. Yuen, R. A. Bilodeau, and R. K. Kramer, "Active Variable Stiffness Fibers for Multifunctional Robotic Fabrics," *IEEE Robotics and Automation Letters*, vol. 1, no. 2, pp. 708–715, Jul. 2016.
- [63] J. Berzowska and M. Coelho, "Kukkia and Vilkas: Kinetic Electronic Garments," in *Ninth IEEE International Symposium on Wearable Computers (ISWC'05)*. Osaka, Japan: IEEE, Oct. 2005, pp. 82–85.
- [64] B. Holschuh and D. Newman, "Two-spring model for active compression textiles with integrated NiTi coil actuators," *Smart Mater. Struct.*, vol. 24, no. 3, p. 035011, Mar. 2015.

- [65] T. P. Chenal, J. C. Case, J. Paik, and R. K. Kramer, "Variable stiffness fabrics with embedded shape memory materials for wearable applications," in *2014 IEEE/RSJ International Conference on Intelligent Robots and Systems*. Chicago, IL, USA: IEEE, Sep. 2014, pp. 2827–2831.
- [66] B. Vanderborght, A. Albu-Schaeffer, A. Bicchi, E. Burdet, D. G. Caldwell, R. Carloni, M. Catalano, O. Eiberger, W. Friedl, G. Ganesh, M. Garabini, M. Grebenstein, G. Grioli, S. Haddadin, H. Hoppner, A. Jafari, M. Laf-franchi, D. Lefeber, F. Petit, S. Stramigioli, N. Tsagarakis, M. Van Damme, R. Van Ham, L. C. Visser, and S. Wolf, "Variable impedance actuators: A review," *Robotics and Autonomous Systems*, vol. 61, no. 12, pp. 1601–1614, Dec. 2013.
- [67] A. Bicchi, G. Tonietti, M. Bavaro, and M. Piccigallo, "Variable Stiffness Actuators for Fast and Safe Motion Control," in *Robotics Research. The Eleventh International Symposium*, ser. Springer Tracts in Advanced Robotics, P. Dario and R. Chatila, Eds. Springer Berlin Heidelberg, 2005, no. 15, pp. 527–536.
- [68] B.-S. Kim and J.-B. Song, "Hybrid dual actuator unit: A design of a variable stiffness actuator based on an adjustable moment arm mechanism," in *2010 IEEE International Conference on Robotics and Automation (ICRA)*, May 2010, pp. 1655–1660.
- [69] S. Wolf and G. Hirzinger, "A new variable stiffness design: Matching requirements of the next robot generation," in *IEEE International Conference on Robotics and Automation, 2008. ICRA 2008*, May 2008, pp. 1741–1746.
- [70] C. E. English and D. Russell, "Mechanics and stiffness limitations of a variable stiffness actuator for use in prosthetic limbs," *Mechanism and Machine Theory*, vol. 34, no. 1, pp. 7–25, Jan. 1999.
- [71] G. Tonietti, R. Schiavi, and A. Bicchi, "Design and Control of a Variable Stiffness Actuator for Safe and Fast Physical Human/Robot Interaction," in *Proceedings of the 2005 IEEE International Conference on Robotics and Automation, 2005. ICRA 2005*, Apr. 2005, pp. 526–531.
- [72] L. Visser, R. Carloni, and S. Stramigioli, "Energy-Efficient Variable Stiffness Actuators," *IEEE Transactions on Robotics*, vol. 27, no. 5, pp. 865–875, Oct. 2011.
- [73] C.-P. Chou and B. Hannaford, "Static and dynamic characteristics of McKibben pneumatic artificial muscles," in *Robotics and Automation, 1994. Proceedings., 1994 IEEE International Conference on*. IEEE, 1994, pp. 281–286.
- [74] Y. Shan, M. Philen, A. Lotfi, S. Li, C. E. Bakis, C. D. Rahn, and K. W. Wang, "Variable Stiffness Structures Utilizing Fluidic Flexible Matrix Composites," *Journal of Intelligent Material Systems and Structures*, vol. 20, no. 4, pp. 443–456, Mar. 2009.
- [75] C. Santulli, S. I. Patel, G. Jeronimidis, F. J. Davis, and G. R. Mitchell, "Development of smart variable stiffness actuators using polymer hydrogels," *Smart Mater. Struct.*, vol. 14, no. 2, p. 434, Apr. 2005.

- [76] W. Wang, H. Rodrigue, and S.-H. Ahn, "Smart soft composite actuator with shape retention capability using embedded fusible alloy structures," *Composites Part B: Engineering*, vol. 78, pp. 507–514, Sep. 2015.
- [77] M. D. Lima, N. Li, M. J. d. Andrade, S. Fang, J. Oh, G. M. Spinks, M. E. Kozlov, C. S. Haines, D. Suh, J. Foroughi, S. J. Kim, Y. Chen, T. Ware, M. K. Shin, L. D. Machado, A. F. Fonseca, J. D. W. Madden, W. E. Voit, D. S. Galvão, and R. H. Baughman, "Electrically, Chemically, and Photonically Powered Torsional and Tensile Actuation of Hybrid Carbon Nanotube Yarn Muscles," *Science*, vol. 338, no. 6109, pp. 928–932, Nov. 2012.
- [78] T. Mirfakhrai, J. Oh, M. Kozlov, E. C. W. Fok, M. Zhang, S. Fang, R. H. Baughman, and J. D. W. Madden, "Electrochemical actuation of carbon nanotube yarns," *Smart Mater. Struct.*, vol. 16, no. 2, p. S243, Apr. 2007.
- [79] J. Foroughi, G. M. Spinks, G. G. Wallace, J. Oh, M. E. Kozlov, S. Fang, T. Mirfakhrai, J. D. W. Madden, M. K. Shin, S. J. Kim, and R. H. Baughman, "Torsional Carbon Nanotube Artificial Muscles," *Science*, vol. 334, no. 6055, pp. 494–497, Oct. 2011.
- [80] C. S. Haines, M. D. Lima, N. Li, G. M. Spinks, J. Foroughi, J. D. W. Madden, S. H. Kim, S. Fang, M. Jung de Andrade, F. Goktepe, O. Goktepe, S. M. Mirvakili, S. Naficy, X. Lepro, J. Oh, M. E. Kozlov, S. J. Kim, X. Xu, B. J. Swedlove, G. G. Wallace, and R. H. Baughman, "Artificial Muscles from Fishing Line and Sewing Thread," *Science*, vol. 343, no. 6173, pp. 868–872, Feb. 2014.
- [81] G. K. Stylios and Taoyu Wan, "Shape memory training for smart fabrics," *Transactions of the Institute of Measurement & Control*, vol. 29, no. 3/4, pp. 321–336, Aug. 2007.
- [82] S.-I. Vasile, K. E. Grabowska, I. L. Ciesielska-Wrobel, and J. Ghitaiga, "Analysis of hybrid woven fabrics with shape memory alloys wires embedded," *FIBRES & TEXTILES IN EASTERN EUROPE*, vol. 18, no. 1, pp. 64–69, 2010.
- [83] Y. Y. F. C. Vili, "Investigating Smart Textiles Based on Shape Memory Materials," *Textile Research Journal*, vol. 77, no. 5, pp. 290–300, May 2007.
- [84] J. Hu, *Adaptive and functional polymers, textiles and their applications*. World Scientific, 2010.
- [85] S. Seok, C. D. Onal, K.-J. Cho, R. J. Wood, D. Rus, and S. Kim, "Meshworm: A Peristaltic Soft Robot With Antagonistic Nickel Titanium Coil Actuators," *IEEE/ASME Transactions on Mechatronics*, vol. 18, no. 5, pp. 1485–1497, Oct. 2013.
- [86] N. G. McCrum, C. P. Buckley, and C. B. Bucknall, *Principles of Polymer Engineering*. Oxford University Press, Jan. 1997.
- [87] M. Stoppa and A. Chiolerio, "Wearable Electronics and Smart Textiles: A Critical Review," *Sensors*, vol. 14, no. 7, pp. 11 957–11 992, Jul. 2014.
- [88] S. Coyle, Y. Wu, K.-T. Lau, D. D. Rossi, G. Wallace, and D. Diamond, "Smart Nanotextiles: A Review of Materials and Applications," *MRS Bulletin*, vol. 32, no. 5, pp. 434–442, May 2007.

- [89] J. Cheng, B. Zhou, P. Lukowicz, F. Seoane, M. Varga, A. Mehmman, P. Chabreck, W. Gaschler, K. Goenner, H. Horter, S. Schneegass, M. Hassib, A. Schmidt, M. Freund, R. Zhang, and O. Amft, "Textile Building Blocks: Toward Simple, Modularized, and Standardized Smart Textile," in *Smart Textiles*, ser. Human-Computer Interaction Series. Springer, Cham, 2017, pp. 303–331.
- [90] J. K. Paik, R. K. Kramer, and R. J. Wood, "Stretchable Circuits and Sensors for Robotic Origami," in *2011 IEEE/RSJ International Conference on Intelligent Robots and Systems*. San Francisco, CA: IEEE, Sep. 2011, pp. 414–420.
- [91] R.-h. Kim, D.-h. Kim, J. Xiao, B. H. Kim, S.-i. Park, B. Panilaitis, R. Ghafari, J. Yao, M. Li, Z. Liu, V. Malyarchuk, D. G. Kim, A.-p. Le, R. G. Nuzzo, D. L. Kaplan, F. G. Omenetto, Y. Huang, Z. Kang, and J. A. Rogers, "Waterproof AlInGaP optoelectronics on stretchable substrates with applications in biomedicine and robotics," *Nature Materials; London*, vol. 9, no. 11, pp. 929–37, Nov. 2010.
- [92] R. K. Kramer, C. Majidi, and R. J. Wood, "Wearable tactile keypad with stretchable artificial skin," in *2011 IEEE International Conference on Robotics and Automation*. Shanghai, China: IEEE, May 2011, pp. 1103–1107.
- [93] S. Biswas, A. Schöberl, M. Mozafari, J. Pezoldt, T. Stauden, and H. O. Jacobs, "Deformable printed circuit boards that enable metamorphic electronics," *NPG Asia Materials*, vol. 8, no. 12, p. e336, Dec. 2016.
- [94] S. Biswas, J. Reiprich, T. Cohrs, D. T. Arboleda, A. Schoeberl, M. Mozafari, L. Schlag, T. Stauden, J. Pezoldt, and H. O. Jacobs, "3D Metamorphic Stretchable Microphone Arrays," *Advanced Materials Technologies*, vol. 2, no. 10, p. 1700131, Oct. 2017.
- [95] L. M. Castano and A. B. Flatau, "Smart fabric sensors and e-textile technologies: a review," *Smart Materials and Structures*, vol. 23, no. 5, p. 053001, May 2014.
- [96] S. Bauer, S. Bauer-Gogonea, I. Graz, M. Kaltenbrunner, C. Keplinger, and R. Schwödiauer, "25th Anniversary Article: A Soft Future: From Robots and Sensor Skin to Energy Harvesters," *Advanced Materials*, vol. 26, no. 1, pp. 149–162, Jan. 2014.
- [97] K. Jost, G. Dion, and Y. Gogotsi, "Textile energy storage in perspective," *Journal of Materials Chemistry A*, vol. 2, no. 28, pp. 10 776–10 787, 2014.
- [98] L. Bao and X. Li, "Towards Textile Energy Storage from Cotton T-Shirts," *Advanced Materials*, vol. 24, no. 24, pp. 3246–3252, Jun. 2012.
- [99] S. Zhai, H. E. Karahan, L. Wei, Q. Qian, A. T. Harris, A. I. Minett, S. Ramakrishna, A. K. Ng, and Y. Chen, "Textile energy storage: Structural design concepts, material selection and future perspectives," *Energy Storage Materials*, vol. 3, pp. 123–139, Apr. 2016.
- [100] J. McCann and D. Bryson, *Textile-led Design for the Active Ageing Population*, ser. Woodhead publishing series in textiles. Amsterdam: Elsevier, Aug. 2014, no. 142.

- [101] L. Stirling, C.-H. Yu, J. Miller, E. Hawkes, R. Wood, E. Goldfield, and R. Nagpal, "Applicability of Shape Memory Alloy Wire for an Active, Soft Orthotic," *Journal of Materials Engineering and Performance*, vol. 20, no. 4-5, pp. 658–662, Jul. 2011.
- [102] R. Granberry, J. Abel, and B. Holschuh, "Active Knit Compression Stockings for the Treatment of Orthostatic Hypotension," in *Proceedings of the 2017 ACM International Symposium on Wearable Computers - ISWC '17*, ser. ISWC '17. Maui, Hawaii: ACM Press, 2017, pp. 186–191.
- [103] T. L. Buckner and R. Kramer-Bottiglio, "Functional fibers for robotic fabrics," *Multifunctional Materials*, vol. 1, no. 1, p. 012001, Aug. 2018.
- [104] J. D. W. Madden, N. A. Vandesteeg, P. A. Anquetil, P. G. A. Madden, A. Takshi, R. Z. Pytel, S. R. Lafontaine, P. A. Wieringa, and I. W. Hunter, "Artificial muscle technology: physical principles and naval prospects," *IEEE Journal of Oceanic Engineering*, vol. 29, no. 3, pp. 706–728, Jul. 2004.
- [105] Y. Meng, J. Jiang, and M. Anthamatten, "Body temperature triggered shape-memory polymers with high elastic energy storage capacity," *Journal of Polymer Science Part B: Polymer Physics*, vol. 54, no. 14, pp. 1397–1404, Jul. 2016.
- [106] S. Kim, E. Hawkes, K. Choy, M. Joldaz, J. Foley, and R. Wood, "Micro artificial muscle fiber using NiTi spring for soft robotics," in *2009 IEEE/RSJ International Conference on Intelligent Robots and Systems*. St. Louis, MO, USA: IEEE, Oct. 2009, pp. 2228–2234.
- [107] P. Chen, S. He, Y. Xu, X. Sun, and H. Peng, "Electromechanical Actuator Ribbons Driven by Electrically Conducting Spring-Like Fibers," *Advanced Materials*, vol. 27, no. 34, pp. 4982–4988, Sep. 2015.
- [108] C. S. Haines, N. Li, G. M. Spinks, A. E. Aliev, J. Di, and R. H. Baughman, "New twist on artificial muscles," *Proceedings of the National Academy of Sciences*, vol. 113, no. 42, pp. 11 709–11 716, Oct. 2016.
- [109] H. J. Lee and J. J. Lee, "Evaluation of the characteristics of a shape memory alloy spring actuator," *Smart Materials and Structures*, vol. 9, no. 6, pp. 817–823, Dec. 2000.
- [110] J. Abel, J. Luntz, and D. Brei, "Hierarchical architecture of active knits," *Smart Materials and Structures*, vol. 22, no. 12, p. 125001, 2013.
- [111] J. K. Paik, E. Hawkes, and R. J. Wood, "A novel low-profile shape memory alloy torsional actuator," *Smart Materials and Structures*, vol. 19, no. 12, p. 125014, Nov. 2010.
- [112] J. K. Paik and R. J. Wood, "A bidirectional shape memory alloy folding actuator," *Smart Materials and Structures*, vol. 21, no. 6, p. 065013, May 2012.
- [113] S. Gupta, A. R. Pelton, J. D. Weaver, X.-Y. Gong, and S. Nagaraja, "High compressive pre-strains reduce the bending fatigue life of nitinol wire," *Journal of the mechanical behavior of biomedical materials*, vol. 44, pp. 96–108, Apr. 2015.

- [114] E. Alarcon, L. Heller, S. A. Chirani, P. Šittner, J. Kopeček, L. Saint-Sulpice, and S. Calloch, "Fatigue performance of superelastic NiTi near stress-induced martensitic transformation," *International Journal of Fatigue*, vol. 95, pp. 76–89, Feb. 2017.
- [115] M. Manti, V. Cacucciolo, and M. Cianchetti, "Stiffening in Soft Robotics: A Review of the State of the Art," *IEEE Robotics Automation Magazine*, vol. 23, no. 3, pp. 93–106, Sep. 2016.
- [116] L. Wang, Y. Yang, Y. Chen, C. Majidi, F. Iida, E. Askounis, and Q. Pei, "Controllable and reversible tuning of material rigidity for robot applications," *Materials Today*, vol. 21, no. 5, pp. 563–576, Jun. 2018.
- [117] A. Tonazzini, S. Mintchev, B. Schubert, B. Mazzolai, J. Shintake, and D. Floreano, "Variable Stiffness Fiber with Self-Healing Capability," *Advanced Materials*, vol. 28, no. 46, pp. 10 142–10 148, Dec. 2016.
- [118] R. Zhao, Y. Yao, and Y. Luo, "Development of a Variable Stiffness Over Tube Based on Low-Melting-Point-Alloy for Endoscopic Surgery," *Journal of Medical Devices*, vol. 10, no. 2, p. 021002, May 2016.
- [119] Y. J. Kim, S. Cheng, S. Kim, and K. Iagnemma, "A Stiffness-Adjustable Hyperredundant Manipulator Using a Variable Neutral-Line Mechanism for Minimally Invasive Surgery," *IEEE Transactions on Robotics*, vol. 30, no. 2, pp. 382–395, Apr. 2014.
- [120] T. M. Huh, Y.-J. Park, and K.-J. Cho, "Design and analysis of a stiffness adjustable structure using an endoskeleton," *International Journal of Precision Engineering and Manufacturing*, vol. 13, no. 7, pp. 1255–1258, Jul. 2012.
- [121] T. L. Buckner, E. L. White, M. C. Yuen, R. A. Bilodeau, and R. K. Kramer, "A move-and-hold pneumatic actuator enabled by self-softening variable stiffness materials," in *2017 IEEE/RSJ International Conference on Intelligent Robots and Systems (IROS)*, Sep. 2017, pp. 3728–3733.
- [122] T. L. Buckner, M. C. Yuen, S. Y. Kim, and R. Kramer-Bottiglio, "Enhanced Variable Stiffness and Variable Stretchability Enabled by Phase-Changing Particulate Additives," *Advanced Functional Materials*, vol. 29, no. 50, p. 1903368, Dec. 2019.
- [123] S. Y. Kim, Y. Choo, R. A. Bilodeau, M. C. Yuen, G. Kaufman, D. S. Shah, C. O. Osuji, and R. Kramer-Bottiglio, "Sustainable manufacturing of sensors onto soft systems using self-coagulating conductive Pickering emulsions," *Science Robotics*, vol. 5, no. 39, p. eaay3604, Feb. 2020.
- [124] H. E. Smeenk, M. Koster, R. A. Faaij, D. B. d. Geer, and M. E. Hamaker, "Compression therapy in patients with orthostatic hypotension: a systematic review." *The Netherlands journal of medicine*, vol. 72, no. 2, pp. 80–5, 2014.
- [125] N. C. Tejwani, I. Immerman, P. Achan, K. A. Egol, and T. McLaurin, "Tourniquet Cuff Pressure: The Gulf Between Science and Practice:," *The Journal of Trauma: Injury, Infection, and Critical Care*, vol. 61, no. 6, pp. 1415–1418, Dec. 2006.

- [126] S. Felton, M. Tolley, E. Demaine, D. Rus, and R. Wood, "A method for building self-folding machines," *Science*, vol. 345, no. 6197, pp. 644–646, Aug. 2014.
- [127] E. J. Markvicka, M. D. Bartlett, X. Huang, and C. Majidi, "An autonomously electrically self-healing liquid metal–elastomer composite for robust soft-matter robotics and electronics," *Nature Materials*, vol. 17, no. 7, p. 618, Jul. 2018.
- [128] R. A. Bilodeau, M. C. Yuen, and R. Kramer-Bottiglio, "Addressable, Stretchable Heating Silicone Sheets," *Advanced Materials Technologies*, vol. 4, no. 9, p. 1900276, Sep. 2019.
- [129] M. Calisti, G. Picardi, and C. Laschi, "Fundamentals of soft robot locomotion," *Journal of The Royal Society Interface*, vol. 14, no. 130, p. 20170101, 2017.
- [130] E. W. Hawkes, L. H. Blumenschein, J. D. Greer, and A. M. Okamura, "A soft robot that navigates its environment through growth," *Science Robotics*, vol. 2, no. 8, p. eaan3028, 2017.
- [131] D. Drotman, S. Jadhav, M. Karimi, P. deZonia, and M. T. Tolley, "3D printed soft actuators for a legged robot capable of navigating unstructured terrain," in *2017 IEEE International Conference on Robotics and Automation (ICRA)*. 2017 IEEE International Conference on Robotics and Automation (ICRA), 2017, pp. 5532–5538.
- [132] J. Hughes, U. Culha, F. Giardina, F. Guenther, A. Rosendo, and F. Iida, "Soft Manipulators and Grippers: A Review," *Frontiers in Robotics and AI*, vol. 3, p. 69, 2016.
- [133] A. Miriyev, K. Stack, and H. Lipson, "Soft material for soft actuators," *Nature Communications*, vol. 8, no. 1, p. 596, 2017.
- [134] L. Blanc, A. Delchambre, and P. Lambert, "Flexible Medical Devices: Review of Controllable Stiffness Solutions," *Actuators*, vol. 6, no. 3, p. 23, 2017.
- [135] M. Taghavi, T. Helps, B. Huang, and J. Rossiter, "3D-Printed Ready-To-Use Variable-Stiffness Structures," *IEEE Robotics and Automation Letters*, vol. 3, no. 3, pp. 2402–2407, 2018.
- [136] S. Rich, S.-H. Jang, Y.-L. Park, and C. Majidi, "Liquid Metal-Conductive Thermoplastic Elastomer Integration for Low-Voltage Stiffness Tuning," *Advanced Materials Technologies*, p. 1700179, 2017.
- [137] R. A. Bilodeau, A. Miriyev, H. Lipson, and R. Kramer-Bottiglio, "All-soft material system for strong soft actuators," in *2018 IEEE International Conference on Soft Robotics (RoboSoft)*. Livorno, Italy: IEEE, Apr. 2018, pp. 288–294.
- [138] E.-S. Park, L. Wook Jang, and J.-S. Yoon, "Resistivity and thermal reproducibility of carbon black and metallic powder filled silicone rubber heaters," *Journal of Applied Polymer Science*, vol. 95, no. 5, pp. 1122–1128, 2005.
- [139] J. Kang, H. Kim, K. S. Kim, S.-K. Lee, S. Bae, J.-H. Ahn, Y.-J. Kim, J.-B. Choi, and B. H. Hong, "High-Performance Graphene-Based Transparent Flexible Heaters," *Nano Letters*, vol. 11, no. 12, pp. 5154–5158, 2011.

- [140] D. Sui, Y. Huang, L. Huang, J. Liang, Y. Ma, and Y. Chen, "Flexible and Transparent Electrothermal Film Heaters Based on Graphene Materials," *Small*, vol. 7, no. 22, pp. 3186–3192, 2011.
- [141] B. W. An, E.-J. Gwak, K. Kim, Y.-C. Kim, J. Jang, J.-Y. Kim, and J.-U. Park, "Stretchable, Transparent Electrodes as Wearable Heaters Using Nanotrough Networks of Metallic Glasses with Superior Mechanical Properties and Thermal Stability," *Nano Letters*, vol. 16, no. 1, pp. 471–478, 2016.
- [142] J. Jang, B. G. Hyun, S. Ji, E. Cho, B. W. An, W. H. Cheong, and J.-U. Park, "Rapid production of large-area, transparent and stretchable electrodes using metal nanofibers as wirelessly operated wearable heaters," *NPG Asia Materials*, vol. 9, no. 9, p. e432, Sep. 2017.
- [143] N. Lazarus and B. Hanrahan, "Thermotherapy Platform Based on a Highly Stretchable Wireless Heater," *Advanced Materials Technologies*, vol. 1, no. 8, p. 1600130, 2016.
- [144] Y. Li, Z. Zhang, X. Li, J. Zhang, H. Lou, X. Shi, X. Cheng, and H. Peng, "A smart, stretchable resistive heater textile," *Journal of Materials Chemistry C*, vol. 5, no. 1, pp. 41–46, 2017.
- [145] R. C. Webb, A. P. Bonifas, A. Behnaz, Y. Zhang, K. J. Yu, H. Cheng, M. Shi, Z. Bian, Z. Liu, Y.-S. Kim, W.-H. Yeo, J. S. Park, J. Song, Y. Li, Y. Huang, A. M. Gorbach, and J. A. Rogers, "Ultrathin conformal devices for precise and continuous thermal characterization of human skin," *Nature Materials*, vol. 12, no. 10, pp. 938–944, 2013.
- [146] J. A. Fan, W.-H. Yeo, Y. Su, Y. Hattori, W. Lee, S.-Y. Jung, Y. Zhang, Z. Liu, H. Cheng, L. Falgout, M. Bajema, T. Coleman, D. Gregoire, R. J. Larsen, Y. Huang, and J. A. Rogers, "Fractal design concepts for stretchable electronics," *Nature Communications*, vol. 5, no. 1, p. 3266, 2014.
- [147] L. Zhang, M. Baima, and T. L. Andrew, "Transforming Commercial Textiles and Threads into Sewable and Weavable Electric Heaters," *ACS Applied Materials & Interfaces*, vol. 9, no. 37, pp. 32 299–32 307, 2017.
- [148] S. Choi, J. Park, W. Hyun, J. Kim, J. Kim, Y. B. Lee, C. Song, H. J. Hwang, J. H. Kim, T. Hyeon, and D.-H. Kim, "Stretchable Heater Using Ligand-Exchanged Silver Nanowire Nanocomposite for Wearable Articular Thermotherapy," *ACS Nano*, vol. 9, no. 6, pp. 6626–6633, 2015.
- [149] S. Hong, H. Lee, J. Lee, J. Kwon, S. Han, Y. D. Suh, H. Cho, J. Shin, J. Yeo, and S. H. Ko, "Highly Stretchable and Transparent Metal Nanowire Heater for Wearable Electronics Applications," *Advanced Materials*, vol. 27, no. 32, pp. 4744–4751, Aug. 2015.
- [150] Y. Wang, Z. Yu, G. Mao, Y. Liu, G. Liu, J. Shang, S. Qu, Q. Chen, and R.-W. Li, "Printable Liquid-Metal@PDMS Stretchable Heater with High Stretchability and Dynamic Stability for Wearable Thermotherapy," *Advanced Materials Technologies*, vol. 4, no. 2, p. 1800435, Feb. 2019.
- [151] D. Kim, L. Zhu, D.-J. Jeong, K. Chun, Y.-Y. Bang, S.-R. Kim, J.-H. Kim, and S.-K. Oh, "Transparent flexible heater based on hybrid of carbon nanotubes and silver nanowires," *Carbon*, vol. 63, pp. 530–536, 2013.

- [152] A. C. Siegel, S. T. Phillips, B. J. Wiley, and G. M. Whitesides, "Thin, lightweight, foldable thermochromic displays on paper," *Lab on a Chip*, vol. 9, no. 19, p. 2775, 2009.
- [153] P. Liu, L. Liu, K. Jiang, and S. Fan, "Carbon-Nanotube-Film Microheater on a Polyethylene Terephthalate Substrate and Its Application in Thermochromic Displays," *Small*, vol. 7, no. 6, pp. 732–736, 2011.
- [154] H. Kim, H. Lee, I. Ha, J. Jung, P. Won, H. Cho, J. Yeo, S. Hong, S. Han, J. Kwon, K.-J. Cho, and S. H. Ko, "Biomimetic Color Changing Anisotropic Soft Actuators with Integrated Metal Nanowire Percolation Network Transparent Heaters for Soft Robotics," *Advanced Functional Materials*, vol. 28, no. 32, p. 1801847, 2018.
- [155] E. A. Allen and J. P. Swensen, "Directional Stiffness Control Through Geometric Patterning and Localized Heating of Field's Metal Lattice Embedded in Silicone," *Actuators*, vol. 7, no. 4, p. 80, 2018.
- [156] D. McCoul, S. Rosset, N. Besse, and H. Shea, "Multifunctional shape memory electrodes for dielectric elastomer actuators enabling high holding force and low-voltage multisegment addressing," *Smart Materials and Structures*, vol. 26, no. 2, p. 025015, 2017.
- [157] S. Puce, T. Dattoma, F. Rizzi, M. Emara, A. Qualtieri, and M. De Vittorio, "A thermo-activated tactile micro-actuator for displays," *Microelectronic Engineering*, vol. 205, pp. 6–13, 2019.
- [158] M. A. McEvoy and N. Correll, "Thermoplastic variable stiffness composites with embedded, networked sensing, actuation, and control," *Journal of Composite Materials*, vol. 49, no. 15, pp. 1799–1808, 2015.
- [159] N. Besse, S. Rosset, J. J. Zarate, and H. Shea, "Flexible Active Skin: Large Reconfigurable Arrays of Individually Addressed Shape Memory Polymer Actuators," *Advanced Materials Technologies*, vol. 2, no. 10, p. 1700102, 2017.
- [160] M. Cai, D. Thorpe, D. H. Adamson, and H. C. Schniepp, "Methods of graphite exfoliation," *Journal of Materials Chemistry*, vol. 22, no. 48, pp. 24 992–25 002, 2012.
- [161] D. D. L. Chung, "A review of exfoliated graphite," *Journal of Materials Science*, vol. 51, no. 1, pp. 554–568, 2015.
- [162] W. Zhang, A. A. Dehghani-Sani, and R. S. Blackburn, "Carbon based conductive polymer composites," *Journal of Materials Science*, vol. 42, no. 10, pp. 3408–3418, 2007.
- [163] R. Verdejo, M. M. Bernal, L. J. Romasanta, and M. A. Lopez-Manchado, "Graphene filled polymer nanocomposites," *Journal of Materials Chemistry*, vol. 21, no. 10, pp. 3301–3310, 2011.
- [164] M. Kujawski, J. D. Pearce, and E. Smela, "Elastomers filled with exfoliated graphite as compliant electrodes," *Carbon*, vol. 48, no. 9, pp. 2409–2417, 2010.
- [165] K. K. Sadasivuni, D. Ponnammam, S. Thomas, and Y. Grohens, "Evolution from graphite to graphene elastomer composites," *Progress in Polymer Science*, vol. 39, no. 4, pp. 749–780, 2014.

- [166] M. D. Dickey, "Stretchable and Soft Electronics using Liquid Metals," *Advanced Materials*, vol. 29, no. 27, p. 1606425, 2017.
- [167] B. Li, Y. Gao, A. Fontecchio, and Y. Visell, "Soft capacitive tactile sensing arrays fabricated via direct filament casting," *Smart Materials and Structures*, vol. 25, no. 7, p. 075009, 2016.
- [168] S. A. Morin, R. F. Shepherd, S. W. Kwok, A. A. Stokes, A. Nemiroski, and G. M. Whitesides, "Camouflage and Display for Soft Machines," *Science*, vol. 337, no. 6096, pp. 828–832, 2012.
- [169] J. M. Taylor, K. Perez-Toralla, R. Aispuro, and S. A. Morin, "Covalent Bonding of Thermoplastics to Rubbers for Printable, Reel-to-Reel Processing in Soft Robotics and Microfluidics," *Advanced Materials*, vol. 30, no. 7, p. 1705333, 2018.
- [170] F. S. Senatov, K. V. Niaza, M. Y. Zadorozhnyy, A. V. Maksimkin, S. D. Kaloshkin, and Y. Z. Estrin, "Mechanical properties and shape memory effect of 3D-printed PLA-based porous scaffolds," *Journal of the Mechanical Behavior of Biomedical Materials*, vol. 57, no. Supplement C, pp. 139–148, 2016.
- [171] S. K. Leist, D. Gao, R. Chiou, and J. Zhou, "Investigating the shape memory properties of 4D printed polylactic acid (PLA) and the concept of 4D printing onto nylon fabrics for the creation of smart textiles," *Virtual and Physical Prototyping*, vol. 12, no. 4, pp. 290–300, 2017.
- [172] R. A. Bilodeau, A. Mohammadi Nasab, D. S. Shah, and R. Kramer-Bottiglio, "Uniform conductivity in stretchable silicones via multiphase inclusions," *Soft Matter*, 2020.
- [173] E. Brown, N. Rodenberg, J. Amend, A. Mozeika, E. Steltz, M. R. Zakin, H. Lipson, and H. M. Jaeger, "Universal robotic gripper based on the jamming of granular material," *Proceedings of the National Academy of Sciences*, vol. 107, no. 44, pp. 18 809–18 814, 2010, publisher: National Academy of Sciences.
- [174] F. Connolly, D. A. Wagner, C. J. Walsh, and K. Bertoldi, "Sew-free anisotropic textile composites for rapid design and manufacturing of soft wearable robots," *Extreme Mechanics Letters*, vol. 27, pp. 52–58, Feb. 2019. [Online]. Available: <http://www.sciencedirect.com/science/article/pii/S2352431618302141>
- [175] C. Walsh, "Human-in-the-loop development of soft wearable robots," *Nature Reviews Materials*, vol. 3, no. 6, pp. 78–80, Jun. 2018.
- [176] Q. Shi, J. Sun, C. Hou, Y. Li, Q. Zhang, and H. Wang, "Advanced Functional Fiber and Smart Textile," *Advanced Fiber Materials*, vol. 1, no. 1, pp. 3–31, Sep. 2019.
- [177] T. G. Thuruthel, E. Falotico, M. Manti, and C. Laschi, "Stable Open Loop Control of Soft Robotic Manipulators," *IEEE Robotics and Automation Letters*, pp. 1–1, 2018.
- [178] Y. Gao, L. Yu, J. C. Yeo, and C. T. Lim, "Flexible Hybrid Sensors for Health Monitoring: Materials and Mechanisms to Render Wearability," *Advanced Materials*, vol. 32, no. 15, p. 1902133, Apr. 2020.

- [179] I. D. Joshipura, M. Finn, S. T. M. Tan, M. D. Dickey, and D. J. Lipomi, "Stretchable bioelectronics—Current and future," *MRS Bulletin*, vol. 42, no. 12, pp. 960–967, Dec. 2017. [Online]. Available: <https://www.cambridge.org/core/journals/mrs-bulletin/article/stretchable-bioelectronicscurrent-and-future/E701163AE09FE145F8AB781AC371A2CC>
- [180] D. Kim, J. Kwon, S. Han, Y.-L. Park, and S. Jo, "Deep Full-Body Motion Network for a Soft Wearable Motion Sensing Suit," *IEEE/ASME Transactions on Mechatronics*, vol. 24, no. 1, pp. 56–66, Feb. 2019.
- [181] D. Hughes, C. Heckman, and N. Correll, "Materials that make robots smart," *The International Journal of Robotics Research*, vol. 38, no. 12-13, pp. 1338–1351, Oct. 2019.
- [182] Y. Zhao, A. Kim, G. Wan, and B. C. K. Tee, "Design and applications of stretchable and self-healable conductors for soft electronics," *Nano Convergence*, vol. 6, no. 1, p. 25, Aug. 2019.
- [183] N. Matsuhisa, X. Chen, Z. Bao, and T. Someya, "Materials and structural designs of stretchable conductors," *Chemical Society Reviews*, vol. 48, no. 11, pp. 2946–2966, Jun. 2019.
- [184] D. F. Fernandes, C. Majidi, and M. Tavakoli, "Digitally printed stretchable electronics: a review," *Journal of Materials Chemistry C*, vol. 7, no. 45, pp. 14 035–14 068, Nov. 2019.
- [185] D. C. Kim, H. J. Shim, W. Lee, J. H. Koo, and D. Kim, "Material-Based Approaches for the Fabrication of Stretchable Electronics," *Advanced Materials*, vol. 32, no. 15, p. 1902743, Apr. 2020.
- [186] Y. Hu, T. Zhao, P. Zhu, Y. Zhu, X. Shuai, X. Liang, R. Sun, D. D. Lu, and C.-P. Wong, "Low cost and highly conductive elastic composites for flexible and printable electronics," *Journal of Materials Chemistry C*, vol. 4, no. 24, pp. 5839–5848, Jun. 2016.
- [187] S. Choi, S. I. Han, D. Kim, T. Hyeon, and D.-H. Kim, "High-performance stretchable conductive nanocomposites: materials, processes, and device applications," *Chemical Society Reviews*, vol. 48, no. 6, pp. 1566–1595, Mar. 2019.
- [188] S. Choi, S. I. Han, D. Jung, H. J. Hwang, C. Lim, S. Bae, O. K. Park, C. M. Tschabrunn, M. Lee, S. Y. Bae, J. W. Yu, J. H. Ryu, S.-W. Lee, K. Park, P. M. Kang, W. B. Lee, R. Nezafat, T. Hyeon, and D.-H. Kim, "Highly conductive, stretchable and biocompatible Ag–Au core–sheath nanowire composite for wearable and implantable bioelectronics," *Nature Nanotechnology*, vol. 13, no. 11, pp. 1048–1056, Nov. 2018.
- [189] C. Pan, Y. Ohm, J. Wang, M. J. Ford, K. Kumar, S. Kumar, and C. Majidi, "Silver-Coated Poly(dimethylsiloxane) Beads for Soft, Stretchable, and Thermally Stable Conductive Elastomer Composites," *ACS Applied Materials & Interfaces*, vol. 11, no. 45, pp. 42 561–42 570, Nov. 2019.
- [190] N. Matsuhisa, M. Kaltenbrunner, T. Yokota, H. Jinno, K. Kuribara, T. Sekitani, and T. Someya, "Printable elastic conductors with a high conductivity for electronic textile applications," *Nature Communications*, vol. 6, no. 1, pp. 1–11, Jun. 2015.

- [191] M. J. Ford, C. P. Ambulo, T. A. Kent, E. J. Markvicka, C. Pan, J. Malen, T. H. Ware, and C. Majidi, "A multifunctional shape-morphing elastomer with liquid metal inclusions," *Proceedings of the National Academy of Sciences*, vol. 116, no. 43, pp. 21 438–21 444, Oct. 2019.
- [192] M. D. Bartlett, A. Fassler, N. Kazem, E. J. Markvicka, P. Mandal, and C. Majidi, "Stretchable, High-k Dielectric Elastomers through Liquid-Metal Inclusions," *Advanced Materials*, vol. 28, no. 19, pp. 3726–3731, Mar. 2016. [Online]. Available: <http://onlinelibrary.wiley.com/doi/10.1002/adma.201506243/abstract>
- [193] M. D. Bartlett, N. Kazem, M. J. Powell-Palm, X. Huang, W. Sun, J. A. Malen, and C. Majidi, "High thermal conductivity in soft elastomers with elongated liquid metal inclusions," *Proceedings of the National Academy of Sciences*, vol. 114, no. 9, pp. 2143–2148, Feb. 2017.
- [194] H. Wang, Y. Yao, X. Wang, L. Sheng, X.-H. Yang, Y. Cui, P. Zhang, W. Rao, R. Guo, S. Liang, W. Wu, J. Liu, and Z.-Z. He, "Large-Magnitude Transformable Liquid-Metal Composites," *ACS Omega*, vol. 4, no. 1, pp. 2311–2319, Jan. 2019. [Online]. Available: <https://doi.org/10.1021/acsomega.8b03466>
- [195] C. Pan, E. J. Markvicka, M. H. Malakooti, J. Yan, L. Hu, K. Matyjaszewski, and C. Majidi, "A Liquid-Metal–Elastomer Nanocomposite for Stretchable Dielectric Materials," *Advanced Materials*, vol. 31, no. 23, p. 1900663, 2019.
- [196] Y. Wang, G. Sun, J. Yang, L. Zhang, and J. Zhou, "A soft sandwich structure enables voltage-induced actuation of liquid metal embedded elastomers," *AIP Advances*, vol. 10, no. 1, p. 015016, Jan. 2020.
- [197] L. Zhou, J. Fu, Q. Gao, P. Zhao, and Y. He, "All-Printed Flexible and Stretchable Electronics with Pressing or Freezing Activatable Liquid-Metal–Silicone Inks," *Advanced Functional Materials*, vol. 30, no. 3, p. 1906683, Jan. 2020.
- [198] R. Tutika, S. H. Zhou, R. E. Napolitano, and M. D. Bartlett, "Mechanical and Functional Tradeoffs in Multiphase Liquid Metal, Solid Particle Soft Composites," *Advanced Functional Materials*, vol. 28, no. 45, p. 1804336, Nov. 2018.
- [199] M. Tavakoli, M. H. Malakooti, H. Paisana, Y. Ohm, D. Green Marques, P. Alhais Lopes, A. P. Piedade, A. T. de Almeida, and C. Majidi, "EGaIn-Assisted Room-Temperature Sintering of Silver Nanoparticles for Stretchable, Inkjet-Printed, Thin-Film Electronics," *Advanced Materials*, vol. 30, no. 29, p. 1801852, Jul. 2018.
- [200] H. Sun, Z. Han, and N. Willenbacher, "Ultrastretchable Conductive Elastomers with a Low Percolation Threshold for Printed Soft Electronics," *ACS Applied Materials & Interfaces*, vol. 11, no. 41, pp. 38 092–38 102, Oct. 2019.
- [201] J. Wang, G. Cai, S. Li, D. Gao, J. Xiong, and P. S. Lee, "Printable Superelastic Conductors with Extreme Stretchability and Robust Cycling Endurance Enabled by Liquid-Metal Particles," *Advanced Materials*, vol. 30, no. 16, p. 1706157, Apr. 2018.
- [202] J. Park, S. Wang, M. Li, C. Ahn, J. K. Hyun, D. S. Kim, D. K. Kim, J. A. Rogers, Y. Huang, and S. Jeon, "Three-dimensional nanonetworks for giant stretchability in dielectrics and conductors," *Nature Communications*, vol. 3, no. 1, pp. 1–8, Jun. 2012.

- [203] C. J. Thrasher, Z. J. Farrell, N. J. Morris, C. L. Willey, and C. E. Tabor, “Mechanoresponsive Polymerized Liquid Metal Networks,” *Advanced Materials*, vol. 31, no. 40, p. 1903864, Oct. 2019.
- [204] N. Kazem, T. Hellebrekers, and C. Majidi, “Soft Multifunctional Composites and Emulsions with Liquid Metals,” *Advanced Materials*, vol. 29, no. 27, p. 1605985, Apr. 2017. [Online]. Available: <http://onlinelibrary.wiley.com.ezproxy.lib.purdue.edu/doi/10.1002/adma.201605985/abstract>
- [205] D. M. Bigg, “The effect of compounding on the conductive properties of EMI shielding compounds,” *Advances in Polymer Technology*, vol. 4, no. 3-4, pp. 255–266, 1984, iSBN: 1098-2329.
- [206] D. Sritharan and E. Smela, “Fabrication of a Miniature Paper-Based Electroosmotic Actuator,” *Polymers*, vol. 8, no. 11, p. 400, Nov. 2016. [Online]. Available: <http://www.mdpi.com/2073-4360/8/11/400>
- [207] K. Chu, S.-C. Lee, S. Lee, D. Kim, C. Moon, and S.-H. Park, “Smart conducting polymer composites having zero temperature coefficient of resistance,” *Nanoscale*, vol. 7, no. 2, pp. 471–478, Dec. 2014.
- [208] A. Tairych and I. A. Anderson, “Capacitive Stretch Sensing for Robotic Skins,” *Soft Robotics*, vol. 6, no. 3, pp. 389–398, Jun. 2019.
- [209] Q. Gao, J. Zhang, Z. Xie, O. Omisore, J. Zhang, L. Wang, and H. Li, “Highly stretchable sensors for wearable biomedical applications,” *Journal of Materials Science*, vol. 54, no. 7, pp. 5187–5223, Apr. 2019.
- [210] J. W. Booth, D. Shah, J. C. Case, E. L. White, M. C. Yuen, O. Cyr-Choiniere, and R. Kramer-Bottiglio, “OmniSkins: Robotic skins that turn inanimate objects into multifunctional robots,” *Science Robotics*, vol. 3, no. 22, pp. 1–10, 2018.
- [211] M. Amjadi, K.-U. Kyung, I. Park, and M. Sitti, “Stretchable, Skin-Mountable, and Wearable Strain Sensors and Their Potential Applications: A Review,” *Advanced Functional Materials*, vol. 26, no. 11, pp. 1678–1698, Mar. 2016. [Online]. Available: <http://onlinelibrary.wiley.com/doi/10.1002/adfm.201504755/abstract>
- [212] K. Sim, Z. Rao, F. Ershad, and C. Yu, “Rubbery Electronics Fully Made of Stretchable Elastomeric Electronic Materials,” *Advanced Materials*, vol. 32, no. 15, p. 1902417, Apr. 2020.
- [213] B. O’Brien, T. Gisby, and I. A. Anderson, “Stretch sensors for human body motion,” in *Proc. SPIE 9056, Electroactive Polymer Actuators and Devices (EAPAD)*, Y. Bar-Cohen, Ed., San Diego, California, USA, Mar. 2014, p. 905618.
- [214] A. Miriyev, G. Caires, and H. Lipson, “Functional properties of silicone/ethanol soft-actuator composites,” *Materials & Design*, vol. 145, pp. 232–242, May 2018.
- [215] A. Miriyev, C. Trujillo, G. Caires, and H. Lipson, “Rejuvenation of soft material–actuator,” *MRS Communications*, vol. 8, no. 02, pp. 556–561, Jun. 2018.
- [216] M. Cartolano, B. Xia, A. Miriyev, and H. Lipson, “Conductive Fabric Heaters for Heat-Activated Soft Actuators,” *Actuators*, vol. 8, no. 1, p. 9, Jan. 2019.

- [217] S. Y. Kim, R. Baines, J. Booth, N. Vasios, K. Bertoldi, and R. Kramer-Bottiglio, "Reconfigurable soft body trajectories using unidirectionally stretchable composite laminae," *Nature Communications*, vol. 10, no. 1, pp. 1–8, Aug. 2019.
- [218] A. M. Nasab, A. Sabzehzar, M. Tatari, C. Majidi, and W. Shan, "A Soft Gripper with Rigidity Tunable Elastomer Strips as Ligaments," *Soft Robotics*, vol. 4, no. 4, pp. 411–420, 2017, iISBN: 0340995491 Publisher: Mary Ann Liebert, Inc. 140 Huguenot Street, 3rd Floor New Rochelle, NY 10801 USA.
- [219] K. Elgeneidy, G. Neumann, M. Jackson, and N. Lohse, "Directly Printable Flexible Strain Sensors for Bending and Contact Feedback of Soft Actuators," *Frontiers in Robotics and AI*, vol. 5, p. 2, Feb. 2018.
- [220] O. D. Yirmibesoglu and Y. Menguc, "Hybrid soft sensor with embedded IMUs to measure motion," in *2016 IEEE International Conference on Automation Science and Engineering (CASE)*, Aug. 2016, pp. 798–804.
- [221] M. Li, Y. Wu, L. Zhang, H. Wo, S. Huang, W. Li, X. Zeng, Q. Ye, T. Xu, J. Luo, S. Dong, Y. Li, H. Jin, and X. Wang, "Liquid metal-based electrical interconnects and interfaces with excellent stability and reliability for flexible electronics," *Nanoscale*, vol. 11, no. 12, pp. 5441–5449, 2019.
- [222] R. A. Bilodeau, D. Y. Zemlyanov, and R. K. Kramer, "Liquid Metal Switches for Environmentally Responsive Electronics," *Advanced Materials Interfaces*, vol. 4, no. 5, Mar. 2017.
- [223] R. J. Whitney, "The measurement of volume changes in human limbs," *The Journal of physiology*, vol. 121, no. 1, pp. 1–27, 1953.
- [224] R. K. Kramer, "Soft electronics for soft robotics," in *Micro- and Nanotechnology Sensors, Systems, and Applications VII*, vol. 9467, 2015, pp. 946 707–946 707–9.
- [225] J. Tersoff, D. E. Jesson, and W. X. Tang, "Running Droplets of Gallium from Evaporation of Gallium Arsenide," *Science*, vol. 324, no. 5924, pp. 236–238, Apr. 2009.
- [226] W. X. Tang, C. X. Zheng, Z. Y. Zhou, D. E. Jesson, and J. Tersoff, "Ga droplet surface dynamics during Langmuir evaporation of GaAs," *IBM Journal of Research and Development*, vol. 55, no. 4, pp. 10:1–10:7, Jul. 2011.
- [227] J. Wu, Z. M. Wang, A. Z. Li, M. Benamara, S. Li, and G. J. Salamo, "Nanoscale Footprints of Self-Running Gallium Droplets on GaAs Surface," *PLOS ONE*, vol. 6, no. 6, p. e20765, Jun. 2011.
- [228] S. Kanjanachuchai and C. Euaruksakul, "Self-Running Ga Droplets on GaAs (111)A and (111)B Surfaces," *ACS Applied Materials & Interfaces*, vol. 5, no. 16, pp. 7709–7713, Aug. 2013.
- [229] E. Hilner, A. A. Zakharov, K. Schulte, P. Kratzer, J. N. Andersen, E. Lundgren, and A. Mikkelsen, "Ordering of the Nanoscale Step Morphology As a Mechanism for Droplet Self-Propulsion," *Nano Letters*, vol. 9, no. 7, pp. 2710–2714, Jul. 2009.
- [230] E. Palleau, S. Reece, S. C. Desai, M. E. Smith, and M. D. Dickey, "Self-Healing Stretchable Wires for Reconfigurable Circuit Wiring and 3D Microfluidics," *Advanced Materials*, vol. 25, no. 11, pp. 1589–1592, Mar. 2013.

- [231] M. R. Khan, G. J. Hayes, J.-H. So, G. Lazzi, and M. D. Dickey, "A frequency shifting liquid metal antenna with pressure responsiveness," *Applied Physics Letters*, vol. 99, no. 1, p. 013501, Jul. 2011.
- [232] Y.-L. Park, C. Majidi, R. Kramer, P. Bérard, and R. J. Wood, "Hyperelastic pressure sensing with a liquid-embedded elastomer," *Journal of Micromechanics and Microengineering*, vol. 20, no. 12, p. 125029, Dec. 2010.
- [233] V. Sivan, S.-Y. Tang, A. P. O'Mullane, P. Petersen, N. Eshtiaghi, K. Kalantar-zadeh, and A. Mitchell, "Liquid Metal Marbles," *Advanced Functional Materials*, vol. 23, no. 2, pp. 144–152, Jan. 2013.
- [234] W. Zhang, J. Z. Ou, S.-Y. Tang, V. Sivan, D. D. Yao, K. Latham, K. Khoshmanesh, A. Mitchell, A. P. O'Mullane, and K. Kalantar-zadeh, "Liquid Metal/Metal Oxide Frameworks," *Advanced Functional Materials*, vol. 24, no. 24, pp. 3799–3807, Jun. 2014.
- [235] X. Tang, S.-Y. Tang, V. Sivan, W. Zhang, A. Mitchell, K. Kalantar-zadeh, and K. Khoshmanesh, "Photochemically induced motion of liquid metal marbles," *Applied Physics Letters*, vol. 103, no. 17, p. 174104, Oct. 2013.
- [236] V. Kocourek, C. Karcher, M. Conrath, and D. Schulze, "Stability of liquid metal drops affected by a high-frequency magnetic field," *Physical Review E*, vol. 74, no. 2, p. 026303, Aug. 2006.
- [237] J. Zhang, Y. Yao, L. Sheng, and J. Liu, "Self-Fueled Biomimetic Liquid Metal Mollusk," *Advanced Materials*, vol. 27, no. 16, pp. 2648–2655, Apr. 2015.
- [238] J. Zhang, R. Guo, and J. Liu, "Self-propelled liquid metal motors steered by a magnetic or electrical field for drug delivery," *Journal of Materials Chemistry B*, vol. 4, no. 32, pp. 5349–5357, Aug. 2016.
- [239] S.-Y. Tang, V. Sivan, K. Khoshmanesh, A. P. O'Mullane, X. Tang, B. Gol, N. Eshtiaghi, F. Lieder, P. Petersen, A. Mitchell, and K. Kalantar-zadeh, "Electrochemically induced actuation of liquid metal marbles," *Nanoscale*, vol. 5, no. 13, pp. 5949–5957, Jun. 2013.
- [240] M. R. Khan, C. B. Eaker, E. F. Bowden, and M. D. Dickey, "Giant and switchable surface activity of liquid metal via surface oxidation," *Proceedings of the National Academy of Sciences*, vol. 111, no. 39, pp. 14047–14051, Sep. 2014.
- [241] L. Sheng, J. Zhang, and J. Liu, "Diverse Transformations of Liquid Metals Between Different Morphologies," *Advanced Materials*, vol. 26, no. 34, pp. 6036–6042, Sep. 2014.
- [242] S.-Y. Tang, K. Khoshmanesh, V. Sivan, P. Petersen, A. P. O'Mullane, D. Abbott, A. Mitchell, and K. Kalantar-zadeh, "Liquid metal enabled pump," *Proceedings of the National Academy of Sciences*, vol. 111, no. 9, pp. 3304–3309, Mar. 2014.
- [243] J. Y. Zhu, S.-Y. Tang, K. Khoshmanesh, and K. Ghorbani, "An Integrated Liquid Cooling System Based on Galinstan Liquid Metal Droplets," *ACS Applied Materials & Interfaces*, vol. 8, no. 3, pp. 2173–2180, Jan. 2016.

- [244] M. Mohammed, R. Sundaresan, and M. D. Dickey, "Self-Running Liquid Metal Drops that Delaminate Metal Films at Record Velocities," *ACS Applied Materials & Interfaces*, vol. 7, no. 41, pp. 23 163–23 171, Oct. 2015.
- [245] Y. y. Yao and J. Liu, "Liquid metal wheeled small vehicle for cargo delivery," *RSC Advances*, vol. 6, no. 61, pp. 56 482–56 488, Jun. 2016.
- [246] T. Liu, P. Sen, and C. J. Kim, "Characterization of Nontoxic Liquid-Metal Alloy Galinstan for Applications in Microdevices," *Journal of Microelectromechanical Systems*, vol. 21, no. 2, pp. 443–450, Apr. 2012.
- [247] Q. Xu, N. Oudalov, Q. Guo, H. M. Jaeger, and E. Brown, "Effect of oxidation on the mechanical properties of liquid gallium and eutectic gallium-indium," *Physics of Fluids*, vol. 24, no. 6, p. 063101, 2012.
- [248] K. Doudrick, S. Liu, E. M. Mutunga, K. L. Klein, V. Damle, K. K. Varanasi, and K. Rykaczewski, "Different Shades of Oxide: From Nanoscale Wetting Mechanisms to Contact Printing of Gallium-Based Liquid Metals," *Langmuir*, vol. 30, no. 23, pp. 6867–6877, Jun. 2014.
- [249] Q. Xu, E. Brown, and H. M. Jaeger, "Impact dynamics of oxidized liquid metal drops," *Physical Review E*, vol. 87, no. 4, Apr. 2013.
- [250] I. D. Joshipura, H. R. Ayers, C. Majidi, and M. D. Dickey, "Methods to pattern liquid metals," *Journal of Materials Chemistry C*, vol. 3, no. 16, pp. 3834–3841, Apr. 2015.
- [251] W. Irshad and D. Peroulis, "A silicon-based galinstan magnetohydrodynamic pump," in *Proceedings of the 9th International Workshop on Micro and Nanotechnology for Power Generation and Energy Conversion Applications (PowerMEMS)*, 2009, pp. 127–129.
- [252] G. Li, M. Parmar, D. Kim, J.-B. J. Lee, and D.-W. Lee, "PDMS based coplanar microfluidic channels for the surface reduction of oxidized Galinstan," *Lab on a Chip*, vol. 14, no. 1, pp. 200–209, Nov. 2013.
- [253] D. Kim, P. Thissen, G. Viner, D.-W. Lee, W. Choi, Y. J. Chabal, and J.-B. J. Lee, "Recovery of Nonwetting Characteristics by Surface Modification of Gallium-Based Liquid Metal Droplets Using Hydrochloric Acid Vapor," *ACS Applied Materials & Interfaces*, vol. 5, no. 1, pp. 179–185, Jan. 2013.
- [254] D. Kim, Y. Lee, D.-W. Lee, W. Choi, K. Yoo, and J.-B. J. Lee, "Hydrochloric acid-impregnated paper for gallium-based liquid metal microfluidics," *Sensors and Actuators B: Chemical*, vol. 207, Part A, pp. 199–205, Feb. 2015.
- [255] G. Li, X. Wu, and D.-W. Lee, "A galinstan-based inkjet printing system for highly stretchable electronics with self-healing capability," *Lab on a Chip*, vol. 16, no. 8, pp. 1366–1373, Apr. 2016.
- [256] N. Ilyas, D. P. Butcher, M. F. Durstock, and C. E. Tabor, "Ion Exchange Membranes as an Interfacial Medium to Facilitate Gallium Liquid Metal Alloy Mobility," *Advanced Materials Interfaces*, vol. 3, no. 9, pp. n/a–n/a, May 2016.
- [257] M. Hoorfar and A. W. Neumann, "Recent progress in Axisymmetric Drop Shape Analysis (ADSA)," *Advances in Colloid and Interface Science*, vol. 121, no. 1–3, pp. 25–49, Sep. 2006.

- [258] J. D. Berry, M. J. Neeson, R. R. Dagastine, D. Y. C. Chan, and R. F. Tabor, "Measurement of surface and interfacial tension using pendant drop tensiometry," *Journal of Colloid and Interface Science*, vol. 454, pp. 226–237, Sep. 2015.
- [259] M. R. Khan, C. Trlica, J.-H. So, M. Valeri, and M. D. Dickey, "Influence of Water on the Interfacial Behavior of Gallium Liquid Metal Alloys," *ACS Applied Materials & Interfaces*, vol. 6, no. 24, pp. 22 467–22 473, Dec. 2014.
- [260] H. P. Wampler, D. Y. Zemlyanov, K. Lee, D. B. Janes, and A. Ivanisevic, "Mixed Adlayer of Alkanethiol and Peptide on GaAs(100): Quantitative Characterization by X-ray Photoelectron Spectroscopy," *Langmuir*, vol. 24, no. 7, pp. 3164–3170, Apr. 2008.
- [261] M. S. Makowski, D. Y. Zemlyanov, J. A. Lindsey, J. C. Bernhard, E. M. Hagen, B. K. Chan, A. A. Petersohn, M. R. Medow, L. E. Wendel, D. Chen, J. M. Canter, and A. Ivanisevic, "Covalent attachment of a peptide to the surface of gallium nitride," *Surface Science*, vol. 605, no. 15–16, pp. 1466–1475, Aug. 2011.
- [262] R. Paul, R. G. Reifengerger, T. S. Fisher, and D. Y. Zemlyanov, "Atomic Layer Deposition of FeO on Pt(111) by Ferrocene Adsorption and Oxidation," *Chemistry of Materials*, vol. 27, no. 17, pp. 5915–5924, Sep. 2015.
- [263] A. Gharachorlou, M. D. Detwiler, X.-K. Gu, L. Mayr, B. Klötzer, J. Greeley, R. G. Reifengerger, W. N. Delgass, F. H. Ribeiro, and D. Y. Zemlyanov, "Trimethylaluminum and Oxygen Atomic Layer Deposition on Hydroxyl-Free Cu(111)," *ACS Applied Materials & Interfaces*, vol. 7, no. 30, pp. 16 428–16 439, Aug. 2015.
- [264] J. Čechal, T. Matlocha, J. Polčák, M. Kolíbal, O. Tomanec, R. Kalousek, P. Dub, and T. Šikola, "Characterization of oxidized gallium droplets on silicon surface: An ellipsoidal droplet shape model for angle resolved X-ray photoelectron spectroscopy analysis," *Thin Solid Films*, vol. 517, no. 6, pp. 1928–1934, Jan. 2009.
- [265] C. V. Ramana, E. J. Rubio, C. D. Barraza, A. M. Gallardo, S. McPeak, S. Kotru, and J. T. Grant, "Chemical bonding, optical constants, and electrical resistivity of sputter-deposited gallium oxide thin films," *Journal of Applied Physics*, vol. 115, no. 4, p. 043508, Jan. 2014.
- [266] B. Mosadegh, D. J. Fitzgerald, G. M. Whitesides, J. A. Lewis, M. Wehner, R. J. Wood, and R. L. Truby, "An integrated design and fabrication strategy for entirely soft, autonomous robots," *Nature*, vol. 536, no. 7617, p. 451, Aug. 2016.
- [267] S. Kim, C. Laschi, and B. Trimmer, "Soft robotics: a bioinspired evolution in robotics," *Trends in Biotechnology*, vol. 31, no. 5, pp. 287–294, May 2013.
- [268] S. Sridar, C. J. Majeika, P. Schaffer, M. Bowers, S. Ueda, A. J. Barth, J. L. Sorrells, J. T. Wu, T. R. Hunt, and M. Popovic, "Hydro Muscle -a novel soft fluidic actuator," in *2016 IEEE International Conference on Robotics and Automation (ICRA)*, May 2016, pp. 4014–4021.

- [269] A. D. Marchese, R. K. Katzschmann, and D. Rus, "A Recipe for Soft Fluidic Elastomer Robots," *Soft Robotics*, vol. 2, no. 1, pp. 7–25, Mar. 2015.
- [270] A. De Greef, P. Lambert, and A. Delchambre, "Towards flexible medical instruments: Review of flexible fluidic actuators," *Precision Engineering*, vol. 33, no. 4, pp. 311–321, Oct. 2009.
- [271] C.-P. Chou and B. Hannaford, "Measurement and modeling of McKibben pneumatic artificial muscles," *IEEE Transactions on Robotics and Automation*, vol. 12, no. 1, pp. 90–102, Feb. 1996.
- [272] Y. Sun, Y. S. Song, and J. Paik, "Characterization of silicone rubber based soft pneumatic actuators," in *2013 IEEE/RSJ International Conference on Intelligent Robots and Systems*, Nov. 2013, pp. 4446–4453.
- [273] B. Audergon, G. Agarwal, J. Paik, and N. Besuchet, "Stretchable Materials for Robust Soft Actuators towards Assistive Wearable Devices," *Scientific Reports*, vol. 6, p. 34224, Sep. 2016.
- [274] Y. Bar-Cohen, K. J. Kim, H. R. Choi, and J. D. W. Madden, "Electroactive polymer materials," *Smart Mater. Struct.*, vol. 16, no. 2, Apr. 2007.
- [275] F. Carpi, Ed., *Electromechanically Active Polymers*. Cham: Springer International Publishing, 2016.
- [276] A. O'Halloran, F. O'Malley, and P. McHugh, "A review on dielectric elastomer actuators, technology, applications, and challenges," *Journal of Applied Physics*, vol. 104, no. 7, p. 071101, Oct. 2008.
- [277] P. Brochu and Q. Pei, "Advances in Dielectric Elastomers for Actuators and Artificial Muscles," *Macromolecular Rapid Communications*, vol. 31, no. 1, pp. 10–36, Jan. 2010.
- [278] F. B. Madsen, A. E. Daugaard, S. Hvilsted, and A. L. Skov, "The Current State of Silicone-Based Dielectric Elastomer Transducers," *Macromolecular Rapid Communications*, vol. 37, no. 5, pp. 378–413, Mar. 2016.
- [279] K. J. Kim and M. Shahinpoor, "A novel method of manufacturing three-dimensional ionic polymer-metal composites (IPMCs) biomimetic sensors, actuators and artificial muscles," *Polymer*, vol. 43, no. 3, pp. 797–802, Feb. 2002.
- [280] M. Shahinpoor and K. J. Kim, "Ionic polymer-metal composites: I. Fundamentals," *Smart Materials and Structures*, vol. 10, no. 4, p. 819, 2001.
- [281] W. Huang, "On the selection of shape memory alloys for actuators," *Materials & Design*, vol. 23, no. 1, pp. 11–19, Feb. 2002.
- [282] D. Ratna and J. Karger-Kocsis, "Recent advances in shape memory polymers and composites: a review," *Journal of Materials Science*, vol. 43, no. 1, pp. 254–269, Jan. 2008.
- [283] S. Pourazadi, A. Shagerdmootaab, H. Chan, M. Moallem, and C. Menon, "On the electrical safety of dielectric elastomer actuators in proximity to the human body," *Smart Materials and Structures*, vol. 26, no. 11, p. 115007, 2017.

- [284] F. Schiedeck and S. Mojrzisch, “Design of a robust control strategy for the heating power of shape memory alloy actuators at full contraction based on electric resistance feedback,” *Smart Materials and Structures*, vol. 20, no. 4, p. 045002, Apr. 2011.
- [285] N. W. Bartlett, M. T. Tolley, J. T. B. Overvelde, J. C. Weaver, B. Mosadegh, K. Bertoldi, G. M. Whitesides, and R. J. Wood, “A 3D-printed, functionally graded soft robot powered by combustion,” *Science*, vol. 349, no. 6244, pp. 161–165, Jul. 2015.
- [286] M. Wehner, M. T. Tolley, Y. Mengüç, Y.-L. Park, A. Mozeika, Y. Ding, C. Onal, R. F. Shepherd, G. M. Whitesides, and R. J. Wood, “Pneumatic Energy Sources for Autonomous and Wearable Soft Robotics,” *Soft Robotics*, vol. 1, no. 4, pp. 263–274, Oct. 2014.
- [287] J. I. Lipton, S. Angle, R. E. Banai, E. Peretz, and H. Lipson, “Electrically Actuated Hydraulic Solids,” *Advanced Engineering Materials*, vol. 18, no. 10, pp. 1710–1715, Oct. 2016.

VITA

Education

- **Purdue University** Doctor of Philosophy, May 2020
- **Purdue University** Master of Science in Mechanical Engineering, May 2017
- **Brigham Young University, Provo** Bachelor of Science in Mechanical Engineering, Aug. 2014

Research Experience

- **Faboratory** Purdue University and Yale University, Prof. Rebecca Kramer-Bottiglio, Aug. 2014 - May. 2020
- **Composite Materials with Negative Piezoresistivity** Brigham Young University, Provo. Prof. David T. Fullwood, Jan. 2013 - Aug. 2014

Journal Publications

- **R. A. Bilodeau***, A. Mohammadi Nasab*, D. S. Shah, and R. Kramer-Bottiglio, “Uniform Conductivity in Stretchable Silicones via Multiphase Inclusions,” *Soft Matter*, 2020.
- S. Y. Kim, Y. Choo, **R. A. Bilodeau**, M. C. Yuen, G. Kaufman, D. S. Shah, C. O. Osuji, R. Kramer-Bottiglio, “Sustainable manufacturing of sensors onto soft systems using self-coagulating conductive Pickering emulsions,” *Science Robotics*, vol. 5, no. 39, (2020).

- **R. A. Bilodeau**, M. C. Yuen, and R. Kramer-Bottiglio, “Addressable, Stretchable Heating Silicone Sheets,” *Advanced Materials Technologies*, vol. 4, no. 9, (2019)
- **R. A. Bilodeau** and R. K. Kramer, “Self-Healing and Damage Resilience for Soft Robotics: A Review,” *Frontiers in Robotics and AI*, vol. 4, (2017).
- **R. A. Bilodeau**, Zemlyanov, D. Y., and R. K. Kramer. “Liquid Metal Switches for Environmentally Responsive Electronics.” *Advanced Materials Interfaces*, vol. 4, no. 5, (2017).
- **R. A. Bilodeau***, M. C. S. Yuen*, and R. Kramer, “Active Variable Stiffness Fibers for Multifunctional Robotic Fabrics,” *IEEE Robotics and Automation Letters*, vol. 1, no. 2, pp. 708-715, 2016.

Under Review:

- T. L. Buckner, **R. A. Bilodeau**, S. Y. Kim, R. Kramer-Bottiglio, “A method for Roboticizing Fabric by Integrating Functional Fibers,” manuscript under review.

Conference Publications

- **R. A. Bilodeau***, M. C.-S. Yuen*, J. Case, T. Buckner, and R. Kramer-Bottiglio, “Design for Control of a Soft Bidirectional Bending Actuator,” in *Intelligent Robots and Systems (IROS)*, 2018 IEEE/RSJ International Conference on, 2018, pp. 5936-5943.
- **R. A. Bilodeau**, A. Miriyev, H. Lipson, and R. Kramer-Bottiglio, “All-soft material system for strong soft actuators,” in *2018 IEEE International Conference on Soft Robotics (RoboSoft)*, 2018, pp. 288–294.[†]
- **R. A. Bilodeau**, E. L. White, and R. K. Kramer, “Monolithic Fabrication of Sensors and Actuators in a Soft Robotic Gripper.” In *2015 IEEE/RSJ International Conference on Intelligent Robots and Systems (IROS)* (2015).

- T.L. Buckner, E.L. White, M.C. Yuen, **R.A. Bilodeau**, and R.K. Kramer, “A move-and-hold pneumatic actuator enabled by self-softening variable stiffness materials,” in 2017 IEEE/RSJ International Conference on Intelligent Robots and Systems (IROS), Vancouver, BC, 2018, pp. 3728-3733.

* indicates co-first-authorship

† awarded ‘Best Student Paper’.

A. LIQUID METAL SWITCHES FOR ENVIRONMENTALLY RESPONSIVE ELECTRONICS

This appendix is based on work previously published as [222] R. A. Bilodeau, D. Y. Zemlyanov, and R. K. Kramer, “Liquid Metal Switches for Environmentally Responsive Electronics,” *Advanced Materials Interfaces*, vol. 4, no. 5, Mar. 2017. Copyright ©2017, John Wiley and Sons, reproduced with permission.

A.1 Introduction

More than six decades ago, liquid mercury was used to demonstrate the potential of room-temperature liquid metals as soft circuit elements. [223] This sparked an exploration into using liquid metals to conduct both heat and electricity in systems that are either physically compliant or reconfigurable. General use of mercury is impeded by its toxicity, so in the past decade gallium-based room-temperature liquid metals have begun to replace mercury for use in conductive circuitry applications. The value of flexible and adaptable liquid-metal conductors is probably best exemplified in recent soft robotics design, development, and control applications. [1, 31, 51, 224] In order to harness the full potential of liquid metal circuitry, more investigation is necessary into the fundamental principles governing liquid metals’ behavior, as well as possible applications for these liquid metals.

Gallium-based alloys can be found in a liquid form at both room and elevated temperatures. At high temperatures ($>600^{\circ}\text{C}$), researchers have controlled the motion of liquid gallium arsenide via chemical decomposition of the alloy, controlling the direction of motion via surface crystallinity of the substrate. [225–228] Other high-temperature gallium alloys have been controlled and directed by surface roughness. [229] This previous work demonstrates the feasibility of metallic droplet manipu-

lation, but the high temperatures involved make it impractical for common, everyday use.

Gallium-indium based room-temperature liquid metal alloys (usually eGaIn, a eutectic gallium-indium alloy, or galinstan, a gallium-indium-tin alloy) have become even more commonplace as researchers develop reconfigurable and soft electronic devices. These gallium alloys have appeared in a number of soft electronics [9] including self-healing electronics, [230] tunable electronics, [231] and stretchable sensors. [232] In these examples, the liquid metal is manipulated through encapsulation inside of a flexible polymer, enabling mechanical shape-giving and shape-changing of soft electronics.

There is also a growing interest in the ability to manipulate the geometry and electric path of the liquid metal via non-mechanical techniques. By powder coating small droplets, researchers created microscopic marbles, [233] [234] which Tang et al. moved by shining a light on the powder-coated surface. [235] High frequency magnetic fields can drive galinstan droplet motion, [236] providing a second system for non-mechanical liquid metal manipulation. Zhang et al. fed aluminum chips to a galinstan droplet as fuel for self-propulsion, [237] and have since developed non-contacting magnetic controls for the droplet. [238] Finally, a large category of recent research has used electricity to create relative motion and shape change in liquid metals, [239–241] enabling non-contacting pumps for microfluidic flow [242] and cooling, [243] self-destructive circuitry (path-destructive liquid metal droplet motion), [244] and most recently as a source for rigid-body locomotion. [245]

It is well known that gallium oxidizes rapidly in normal atmospheric conditions, or in any environment with oxygen levels above 1ppm, [9,13,246] forming a gallium-oxide that has been studied in detail. [247–249] This oxide is solid at room temperature and forms a nanoscale stabilizing shell around liquid gallium-indium alloys, enabling the liquid metal to be patterned onto, and subsequently adhere to, many different material surfaces (via a plethora of techniques). [250] If the oxide is removed, the liquid metal loses its adhesion to the substrate and will reflow under the influence of gravity

(or other forces), enabling a fixed liquid-metal pattern to change. In other words, oxide removal enables real-time, non-mechanical manipulation of liquid metals. This has typically been done either in nitrogen boxes (via passive oxide prevention) or in chemical etchant baths (via active oxide removal). [236, 237, 239, 242–244] Unfortunately, these methods require enclosed (air-tight or water-proof) chambers that limit the practical applications for manipulation of liquid metal circuits on the fly, as the circuits must remain inside the chamber.

The two main etchants used in aqueous oxide removal are hydrochloric acid (HCl, a low-pH acid) [233, 236, 239, 247, 248, 251] and sodium hydroxide (NaOH, a high-pH base). [237, 239, 240, 242–244] Both of these etchants mix readily with water and can be contained safely at high concentrations. A non-aqueous alternative for oxide removal comes though exposing the liquid metals to concentrated HCl vapor, [252–256] but practical applications of this are generally limited to environments that can withstand the presence of a highly corrosive gas.

In this work, we demonstrate control over the surface oxide of liquid metal droplets, which in turn controls the wetting and adhesion of those drops on a substrate, using purely environmental stimuli. We compare HCl and NaOH (in solution) for use in completely removing liquid metal droplets from substrates onto which they have adhered, showing that NaOH performs this task faster than HCl. We then provide evidence for the use of ordinary water as a means to regrow the surface oxide and increase the thickness of the gallium-oxide layer, demonstrating the ability to adhere the droplets back to the substrate after having been freed. Finally, we apply this depinning and repinning technique, demonstrating its viability for creating both reconfigurable and reversible circuitry. These methods enable the use of simpler aqueous techniques for liquid metal manipulation, while subsequently permitting the final liquid-metal morphology to be removed from the aqueous medium.

Table A.1. Contact angles of galinstan droplets on various substrates, immersed in either 1M HCl or 1M NaOH. \pm value is one standard deviation.

Etchant	Substrate	Contact Angle (Degrees)
HCl (1M)	Glass	164 ± 1.6
	Silicon	161 ± 1.3
	PDMS	159 ± 4.6
NaOH (1M)	Glass	165 ± 0.8
	Silicon	162 ± 0.5
	PDMS	164 ± 2.1

A.2 Experimental

A.2.1 Depinning Droplets through Oxide Removal

Oxide Removal Rate Measured by Contact Angles

Since both HCl and NaOH have been used to remove the gallium oxide layer surrounding liquid metal droplets, we begin by comparing the influence of the two chemical etchants. We measured the contact angle of galinstan droplets on the surface of various substrates while submerged in both HCl and NaOH solutions at room temperature (see Methods and Materials section for details). Our results are presented in Table A.1. All equilibrium contact angles were roughly the same (approximately 160° in 1M HCL and NaOH, which is lower than previously reported values. [247]) For glass and silicon substrates, data variance was low; but with PDMS as the substrate, the droplets had a noticeable variation in their final contact angles (with one droplet never getting higher than 153°). We suspect that this is due to chemical interaction between the etchant and the PDMS, combined with batch variations inherent to PDMS molding. [23] We also note that droplet buoyancy plays a role in contact angle when measured in aqueous solutions. Therefore, the contact angles measured are higher than reported contact angles of liquid metal droplets with the oxide removed via HCl vapor treatment. [253]

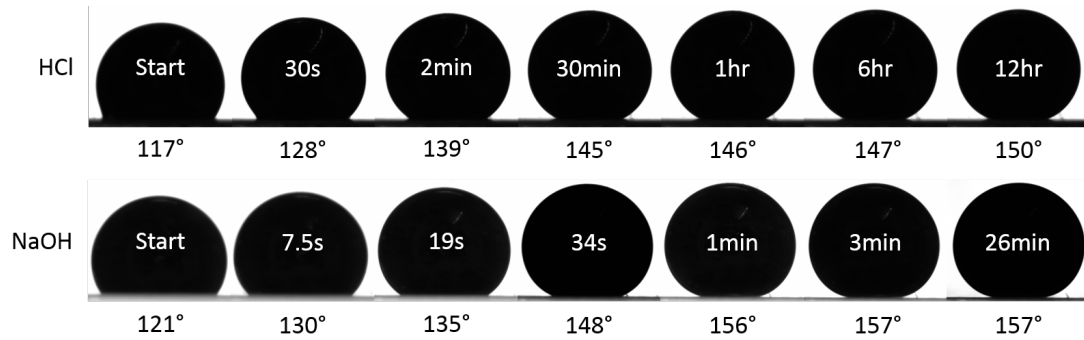


Figure A.1. The evolution of the contact angle and droplet profile for a galinstan droplet placed on a flat PDMS in either a 1M HCl or a 1M NaOH bath. It should be noted that the last frame of the NaOH shows the droplet completely depinned (it has begun rolling).

Comparing time stamps for each profile photograph, we got an approximation of the time-scale required to develop the maximum equilibrium contact angle for each droplet. At the same concentrations (1M), HCl took much longer than NaOH to develop the maximum contact angle, even though the treatment method was the same. The time difference was largest on a PDMS substrate (see Figure A.1), likely due to the softer and more porous nature of the substrate. When placed in an HCl bath on PDMS, galinstan droplets consistently took several hours to develop their maximum contact angle (like the droplet shown in HCl in Figure A.1). When placed in NaOH, the droplets would achieve a maximum contact angle in a very short amount of time (on the order of minutes).

In the context of reconfigurable electronics, this has immediate ramifications on the configuration rate. The choice of chemical etchant seems to have a large degree of influence on the speed at which an adhered droplet can be released from a substrate. Since oxide removal is the key to releasing a droplet, we further investigated the speed at which the surface oxide is removed by HCl and NaOH from a liquid metal droplet.

Oxide Removal Rate Measured Optically

To the authors' knowledge, there have been no studies on the chemical kinetics of gallium oxide reacting with HCl and NaOH. To measure the time it takes to remove the oxide by chemical etchants we developed a simple reflectance experiment, as shown in Figure A.2. We coated small, chemically inert platforms with PDMS (for adhesion) and then, using a syringe, we placed very large galinstan droplets (diameter $\approx 8\text{mm}$) onto the PDMS. The droplets sat for 24 hours to encourage oxide adhesion. We then removed the liquid metal from inside of the droplet with a syringe, leaving the encapsulating oxide behind. As the surface area of the droplet decreased from its original spherical area to an area approximately the size of the droplet's circular profile, the solid oxide skin buckled and wrinkled, developing a dull gray hue. The buckled oxide scatters light instead of reflecting it as a fresh oxide layer or the pure liquid metal does. Once the droplets are submerged in either NaOH or HCl baths, the buckled oxide is chemically removed and a reflective surface is restored to the droplet. Filming the process allowed us to record the time it takes to change the droplets surface. This optical test confirmed the difference between the speed at which HCl and NaOH remove the gallium oxide layer as observed when studying contact angles.

We set up all of the droplets onto platforms simultaneously, and randomly selected droplets for submersion in either a 1M HCl or 1M NaOH solution. Each bath was prepared fresh and used only once, and the droplets were submerged with chemically inert tweezers to prevent any interaction of the tweezers with the acid/base. Examples of the droplets are displayed in Figure A.2, and a video of the tests is available in the Supporting Information. The droplets submerged in HCl took between 9 and 13 seconds for their oxide layers to be removed (average $11.35\text{s} \pm 1.7\text{s}$ standard deviation). The galinstan droplets immersed in NaOH, however, had their oxide skins removed in 0.58s (average) with a 0.045s deviation - most of the deviation and

error being caused by the frame rate of the camera used to film the submersion instead of the actual chemical reaction.

This test provides further evidence for a comparative advantage of using NaOH over HCl in removing the gallium-oxide layer from gallium-based room-temperature liquid-metals. With the initial success of comparing the 1M concentrations using this technique, we then expanded our tests to include various concentrations of HCl and NaOH. Since 1M NaOH was already very fast at processing, we proceeded to test 0.1M, 0.01M and 0.001M. Since 1M HCl was already acting slowly, we performed the test on a range of molarities between 2M (to speed the process up) and 0.1M.

The final results of our optical tests are displayed in the log-log graphs of Figure A.2. Each data point is an average and the error bars represent a 95% confidence interval on the mean time. We fit a simple power-law curve to the data ($y = bx^m$), where the constant b represents the speed of oxide removal at 1M concentration and the constant m correlates the change of the etchant concentration and the time required to remove the oxide. The HCl fitted parameter m is -1.417, indicating a large change in oxide removal time for small changes in concentration. For NaOH this parameter was found to be -0.268, an order of magnitude smaller than the HCl, indicating minimal change in oxide removal times at even very low concentrations. Although the trend lines do not contact all of the confidence intervals, it is important to note that the plotted confidence intervals are representative of deviation in the measured time only. They do not take into account any uncertainty in the molarity of the chemical etchant baths.

To validate our procedure, we compared our data to the work performed by Xu et al. [247] who used parallel-plate rheometry to characterize the influence of various concentrations of HCl on gallium oxide. By actively removing the oxide with HCl during the parallel-plate test, they were able to observe a change in the mechanical properties of the oxide over time, until they observed complete mechanical breakdown, suggesting oxide removal. Their results do not have the timescale resolution as our simple setup does, but we interpreted their data to develop an oxide removal time

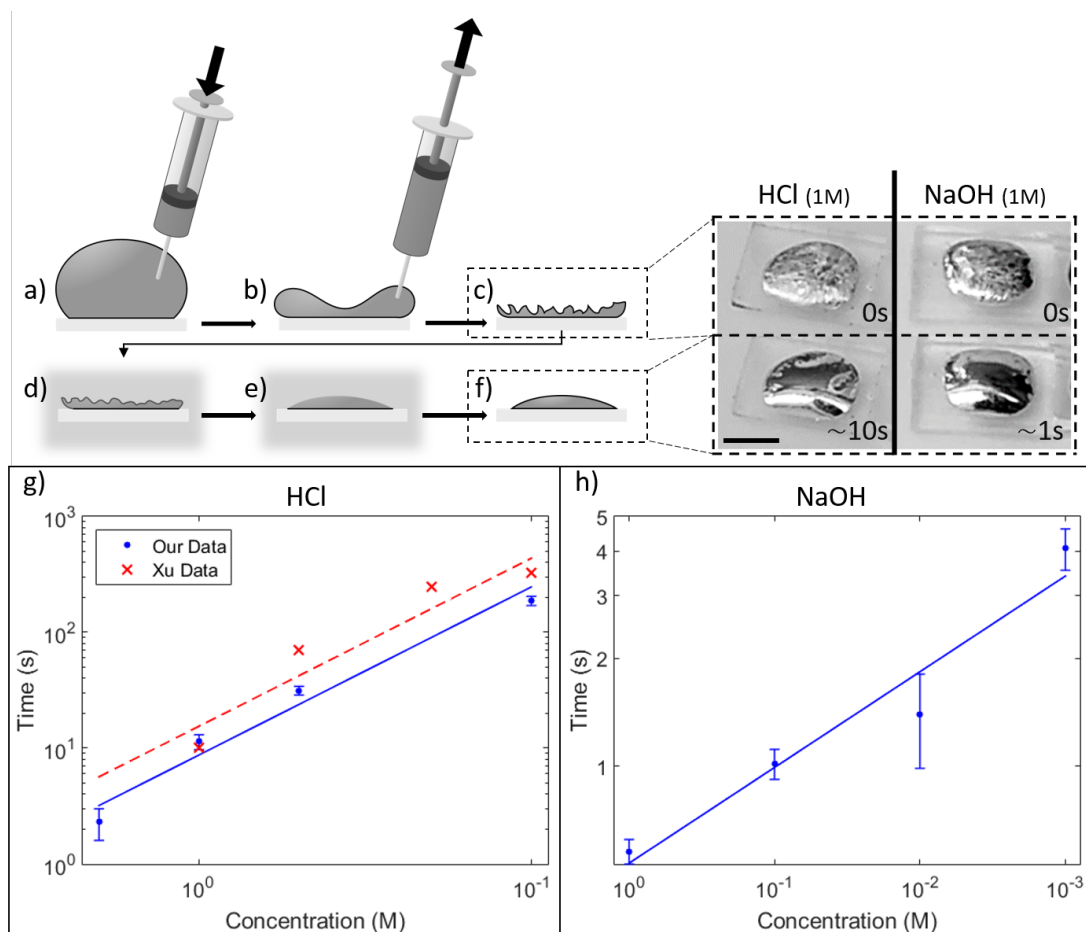


Figure A.2. Experimental method for comparing galinstan oxide removal rates by HCl and NaOH. Large droplets of galinstan are placed on a PDMS substrate (a), and allowed to sit for 24 hours. The liquid metal inside of the droplet is then removed (b), causing the solid oxide layer to develop a visible texture (c). When the textured oxide is immersed into a chemical etchant bath (d), the exterior of the oxide begins to dissolve until the original, reflective surface is restored (e-f). The time it takes to move from (d) to (e) depends on the chemical etchant used, and the insets for (c) and (f) show examples of textured droplets treated by either HCl or NaOH, along with the time required to remove the visible oxide. We tested the removal rate of the oxide at several concentrations, and present the data in logarithmically scaled plots (g-h). The data gathered by Xu et al. using rheometry (in HCl) [247] is presented alongside ours, as validation of our method. Scale bar is 4mm.

vs concentration curve, and plotted their data against ours. Via curve-fitting the b and m constants of the power-law equation, we found that their data set and our HCl-treated data set had nearly identical slopes (ours with $m = -1.417$ compared to theirs of $m = -1.501$), with an offset on the b value likely because their setup provided greater information about the complete oxide removal.

Combining this quantitative test with the qualitative work shown in Figure A.1, we can conclude that, at the same concentration, NaOH will release a droplet of pinned galinstan much more rapidly than HCl will by dissolving away the gallium oxide faster. It is not until the concentration of HCl is increased to 2M that the oxide is removed at a rate similar to very low concentration NaOH (0.005M).

Oxide Removal Rate Measured by Surface Tension

Surface tension is a key part of both liquid-substrate adhesion (in the contact angles developed by a liquid) and droplet mobility. To compare galinstan droplets' surface tension in either HCl or NaOH baths, we performed simple goniometry measurements, and our results can be found in Table A.2. We started by measuring the surface tension of galinstan droplets suspended in oxygen-rich air. The surface tension we measured was 593 ± 46 mN/m (95% confidence), exhibiting a large variation, but always greater than 500mN/m, as expected. [9]

Unlike in our contact angle tests, we were not able to have both the HCl and the NaOH at 1M concentrations. When we extruded a galinstan droplet into a 1M NaOH solution, the chemical reaction between the galinstan and the etchant was so vigorous that the droplet would disconnect from the extrusion needle before we could begin measurements. Decreasing the concentration to 0.1M enabled rapid oxide removal and droplet stabilization, while permitting measurements to be made. This required change in concentration for our goniometry tests provides a third demonstrable difference between HCl and NaOH in chemically treating galinstan.

Table A.2. Surface tension on galinstan droplets in various environments. \pm value is 95% confidence on mean.

Environment		Surface Tension (mN/m)	Time to equilibrium
Air		593 ± 46	85min
HCL	(1M)	470 ± 12	1.5hr
NaOH	(0.1M)	486 ± 6	0s
H ₂ O		230 - 350	6hr

The final surface tension of galinstan in both the HCl and NaOH baths was $470 \pm 12 \text{ mN/m}$ and $486 \pm 6 \text{ mN/m}$ (95% confidence), respectively. Though the averages are slightly different, the confidence intervals overlap sufficiently to negate any distinction between the two. We attribute the uncertainties of the values in Table 2 to the highly spherical nature of the droplets and therefore low bond numbers¹ (≈ 0.1). Although bond numbers < 1 are desired when using drop shape analysis to determine surface tension, [257] extremely low bond numbers (< 0.1) cause errors in the fitting parameters when digital systems are in use. [258] Our droplets were close to this range, causing a slightly larger variance in the measured values than we would have desired. Regardless, we conclude that the surface tension measured in both etchants is close enough to be equivalent.

A.2.2 Repinning Droplets through Oxide Regrowth

Oxide Regrowth and Transformation Measured by Surface Tension

Since a 1M solution of either HCl or NaOH has a significant water component, we wanted to determine the influence of clean water on the surface tension of liquid metals. This would help us determine if the chemistry of water was having a significant impact on the surface tension of the liquid metal droplets, or if the dissolved acid (or base) was driving the measured surface tension values. Following the same experimental procedure, we used for HCl and NaOH, we measured the surface tension of galinstan droplets in both distilled and deionized water. In both types of water, the droplets registered an initial surface tension profile at well over 500 mN/m , but over the period of hours it would drop between 40-60%, sinking to range anywhere from 230 mN/m to 350 mN/m (see Table A.2). This surface tension range is nearly half the value of the other mediums.

¹The bond number is the non-dimensional parameter used to characterize the influence of surface forces (surface tension) vs body forces (gravity) on a droplet. Bond numbers closer to zero indicate spherical droplets, with surface tension dominating over the influence of gravitational forces.

In goniometry, the time to achieve equilibrium surface tension depends primarily on the chemistry between the droplet and the surrounding environment. [258] Droplets extruded into 1M HCl took around 1.5 hours to come to an equilibrium whereas droplets extruded in the 0.1M NaOH bath achieved an equilibrium surface tension nearly instantaneously. In water, however, the droplets often took over 6 hours to come to an equilibrium state. The extreme drop in surface tension over such a long time can only be attributed to a slow chemical change of the surface properties of liquid metal by the surrounding water. This finding is supported by the work of Khan et al. who performed X-ray photoelectron spectroscopy (XPS) studies on the oxide layer and noted the generation of a gallium-hydroxide alongside the normal gallium oxide when the droplet had been exposed to water. [259] Using rheometry, they demonstrated that the hydroxide layer has a much lower modulus of elasticity than gallium oxide. This helps us to understand the results of our goniometry. When we initially extruded a droplet of liquid metal into water, the liquid metal likely used the dissolved oxygen in the water to create the characteristic thin gallium-oxide layer. Over time, however, the water reacted with the surface of the droplet, changing the surface into the softer hydroxide. Since the stiff, stabilizing oxide had been chemically changed to a weak hydroxide, the droplet distends under its own weight (see Supporting Information Figure 1). This explains both the long time required to develop the final equilibrium surface tension and the large change in surface tension. The long time was because of the slow chemical kinetics of the water reacting with the gallium oxide (having to diffuse through the whole layer of gallium oxide), and the large change in surface tension is due to the newly formed, weaker, hydroxide exterior.

Previous studies into the effects of water on eGaIn-surface interactions have mostly focused on the short-term effects of a thin ‘slip-layer’ of water. [241,259] Khan et al. observed that oxidized eGaIn could slide across a surface that it would normally stick to, when there is a layer of water present. [259] They also showed that as the substrate dries, the oxide sticks to it again. During our experiments, we observed

similar slipping of liquid metal droplets, but only on short time scales. Given longer time scales, we observed that a droplet of gallium-based liquid metal will adhere to a surface, regardless of the presence of water.

Oxide Regrowth and Transformation Measured by XPS analysis

We performed an XPS analysis to characterize the chemical effect of various surface treatments on galinstan. We tested four different conditions: droplet submersion in HCl followed by a quick rinse in water or a 24 hour immersion in water, and droplet submersion in NaOH followed by a quick rinse in water or a 24 hour immersion in water. Rinsed droplets were dipped in a clean bath for two seconds, and afterwards were immediately dried. Soaked droplets were immersed for 24 hours to compare the XPS results to the rinsed droplets and determine which surface properties were caused by the chemical etchant and which results stem from the water baths. A list of all the spectra analyzed for these results is contained in the Methods and Materials section.

Figure A.3 shows the XPS results of the four different conditions over the In 4d/Ga 3d/Sn 4d region. With the rinsed droplets, we anticipated observing an effect similar to that reported by Kim et al., [253] who demonstrated that eGaIn droplets treated with HCl vapor grow a gallium-chloride and indium-chloride shell in place of the gallium oxide. However, we did not find any trace these chloride shells. Instead, it appeared that almost all of the influences of either chemical etchant (HCl or NaOH) were completely removed when the droplets were rinsed in H₂O, making the XPS results nearly identical. We suspect that any alternative shells grown around the galinstan droplets by either the NaOH or the HCl were completely removed during the rinsing process. Notably, the surface concentration of gallium was slightly enriched after the rinsing (85 atomic % vs 78 atomic % for ideal galinstan), and there was a significant amount of oxygen present in the spectrum (not shown in the figure). Using the ratio between the metal and oxide components in Ga 2p and 3d, we calculated the

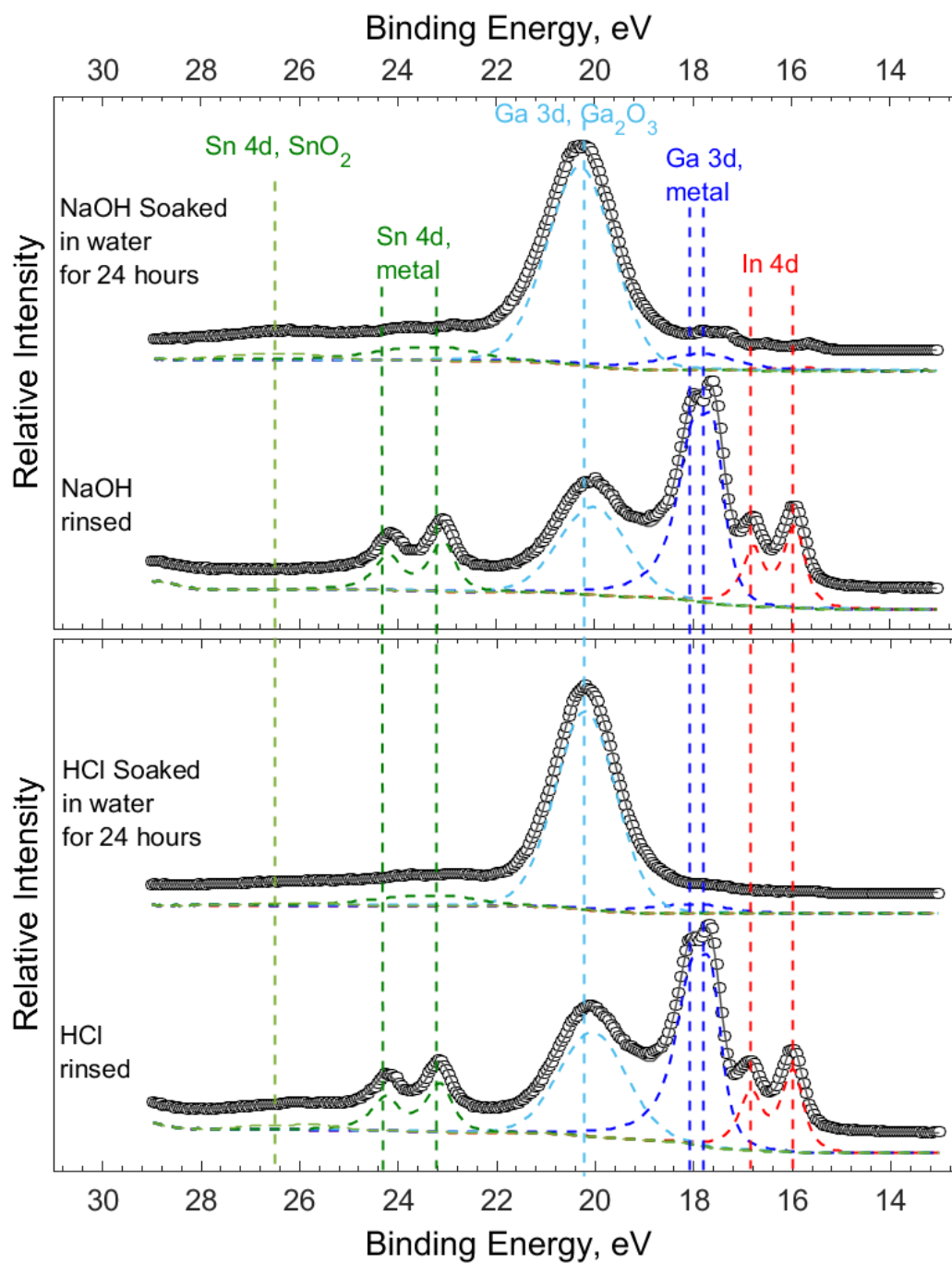


Figure A.3. In 4d/Ga 3d/Sn 4d XPS spectra obtained from the two samples that were treated with NaOH (top panel) and HCL (bottom panel). Two spectra in each panel obtained following short rinsing (bottom spectrum) and soaking for 24 hours (top spectrum).

thickness of the regrown gallium-oxide at about 3nm. The details of such calculations can be found elsewhere. [260–263]

As seen in Figure A.3, both rinsed samples showed the Sn 4d (metal) peaks, but the soaking treatment resulted in disappearance of tin from the surface of the droplet: the Sn 4d (metal) peaks are barely visible. Indium concentration follows the same trend: the amount of indium visible from the surface greatly decreased following soaking in H_2O . Inversely, there was an increase of covalently bonded gallium (shown as a shift of the Ga 2p and 3d peaks from the pure-metal energy level), indicating more oxide had grown on the surface. From this data, we estimated a new oxidized gallium layer thickness at 7 nm. This doubling of the exterior shells' thickness explains the disappearance of the tin and indium, as they were no longer visible from the surface of the droplet. Though the chemical composition of gallium oxide is mainly Ga_2O_3 , [9] the soaked sample showed much higher amount of OH groups as evidenced from the O 1s spectra (not shown), confirming a chemical shift towards gallium hydroxide on the surface of the droplet, as expected. [259, 264, 265]

From our XPS results, it is clear that gallium oxide thickness correlates with water treatment: rinsing resulted in 40-44% of gallium on the surface in the form of oxide, whereas soaking resulted in 90-93%. Furthermore, this shows evidence that the droplets' oxide layers, which had been chemically removed by the HCl or NaOH, were completely restored by simply rinsing the droplets in water. This happened for both the HCl and NaOH treated droplets, so we can easily conclude that the original method of chemically treating the galinstan is unimportant when oxide restoration is performed by rinsing with water. Finally, there is a time element involved in exposing liquid metals to water: further exposure to water (beyond rinsing) results in the oxide layer growing in thickness while changing partially into a hydroxide layer.

Oxide Regrowth and Transformation Measured by Contact Area

Since water removes the surface effects of HCl and NaOH, we could use it as a method to reattach droplets that had been removed via the chemical etchants. We tested this on a droplet through a simple experiment: we soaked a galinstan droplet in NaOH to remove its oxide, and then placed it onto a glass substrate immersed in distilled water. We tracked the profile of the droplet over a four hour period, and recorded the radius of the droplet's contact area on the substrate. From this information, we calculated the contact area as it changed with time and present our findings in Figure A.4. Although the droplet began to adhere on the order of minutes, the increasing contact area improved the adhesion over the period of the test.

The contact angle did not change much during the test, but the contact area of the droplet increased significantly with increasing time submerged in H₂O. As is visible in the inset images in Figure A.4, the original circular droplet shape collapsed down into a flattened ellipsoid, maintaining a high contact angle as the droplet spread outward and enabling a large contact area on the substrate.

As with the surface tension work reported previously, we hypothesize that the changing contact area (and adhesion to the substrate) is due to the rapid triple-effect during the initial submersion of the droplet. First, the water removed any influence of the NaOH. Second, the dissolved oxygen grew a gallium-oxide shell. Third, the water quickly changed the outer surface of the shell to a hydroxide, leaving the rest of the oxide untouched. While continuing to soak in the bath, the hydroxide slowly diffused through the whole thickness of the shell, weakening the droplet walls and causing the spherical droplet to collapse under its own weight. This process resulted in a pulsing/shape changing effect on the droplet, as evidenced from Figure A.4 between minutes 50-150, and can be seen in Supporting Video 2 between timestamps 0:50 and 1:00.

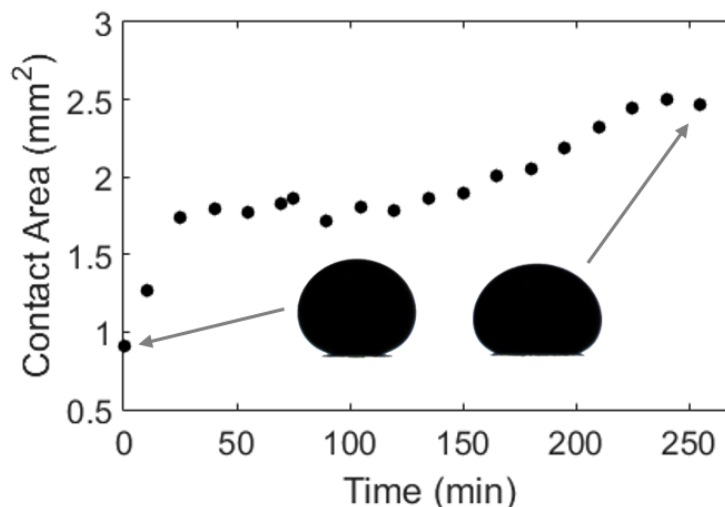


Figure A.4. Changing contact area between a galinstan droplet and a glass substrate in water. The droplet was initially removed from the substrate using a 1M NaOH solution. The NaOH was replaced with clean water, and the droplet collapse was observed for 4 hours. The inset shows the droplet's initial and final states in the water.

We note that after the water was removed, the droplet had fully adhered to the substrate. We tested other techniques (details in Supporting Information) to repin the droplet, but they were not as successful as this method.

A.2.3 Applications

Liquid Metal Droplet Mobility

With droplet adhesion driven by the gallium-oxide layer on the liquid metal, we can free the droplet by removing the oxide layer with either HCl or NaOH, causing the droplet to roll freely on the substrate. Afterwards, we can repin the droplet to the substrate by rinsing it with water, encouraging regrowth of either a gallium-oxide or a gallium-hydroxide layer on the surface of the droplet. These two chemical tools are all that is required to remove galinstan droplets from a substrate and then fix them

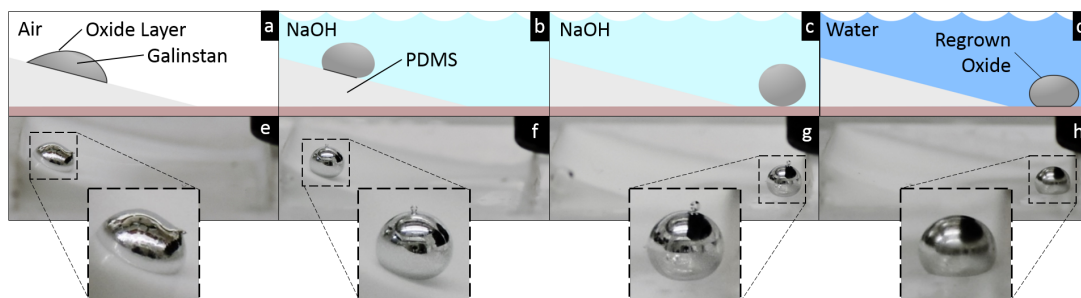


Figure A.5. Controlling the location and fixity of a liquid metal droplet. a) The droplet is pinned to the substrate in air. b) Submerging the droplet in 1M NaOH causes the droplet to depin. c) The depinned droplet moves under gravitational force. d) The droplet is repinned to the substrate through an H_2O bath. e-h) shows photographs of the active test, matching the diagrams in a-d). Inset boxes are approximately 3mm x 3mm.

in a desired location, and we now demonstrate the potential for this to be applied in manipulating liquid-metal based electronics.

Figure A.5 shows our results being applied for environmentally stimulated liquid metal droplet mobility. We depinned a droplet from one location, enabling it to roll to a new location, and then pinned the drop back to the substrate. Figure A.5(a) shows the droplet of galinstan that has been adhered to a substrate in an initial position. The droplet is then exposed to a 1M NaOH bath (Figure A.5(b)), which causes the droplet to depin from the substrate and change location (Figure A.5(c)) by gravitational forces. Finally, by replacing the NaOH bath with water, the droplet is able to reattach to the substrate in the final position (Figure A.5(d)). The high contact-angle on the droplet enables extremely rapid droplet motion once the droplet has been depinned. Furthermore, this droplet mobility is controlled by the environment alone, with gravity being the only source of force. We see future opportunities to combine this process with environmentally controllable surface morphology, which would in turn enable control over droplet locomotion direction, as well as applications in connecting/disconnecting circuitry for reconfigurable logic.

Liquid Metal Switch

Using environmental stimuli, we also demonstrate the ability to repeatedly disconnect and reconnect a conductive pathway, as shown in Figure A.6. We connected an LED and a droplet of galinstan in series in a circuit (visible in Figure A.6(e)). The galinstan droplet was in a special environmental chamber with two conductive tungsten leads emerging from the chamber walls for the droplet to rest on. We alternately tested the resistance across the galinstan droplet and applied a power-source to the whole circuit (Korad KA3005D DC power supply, set to provide either a max of 3.3V or 10mA) to see if the LED would illuminate. For each test, we cycled the fluid in the environmental chamber, starting with air and then filling the chamber with a 1M NaOH bath, continuing on to distilled water, and then drying all the water out of the chamber with air again. Figure A.6(a-d) is a schematic representation of the cycle, showing a profile view of the droplet and how it contacts the electrodes based on the chemical bath in the chamber. A video of the droplet profile during a cycle is available in the Supporting Information.

We were able to disconnect and reconnect the LED using the NaOH bath to lift the droplet up, disconnecting the electrodes, and the water bath to collapse the droplet back down, reconnecting the electrodes. Figure A.6(f-g) describe the current stage of the cycle and the resistance measured across the liquid metal droplet, while (h-i) are a series of simultaneous photographs of the LED and the galinstan droplet during each stage of the cycle. It is important to note that although the NaOH bath disconnected the liquid metal droplet from the circuit, the NaOH itself was able to conduct electricity via electrochemical means. This is why although the resistance is very high with both the NaOH and the water baths, the LED illuminates (partially) when power is applied during the NaOH portion of the cycle. Furthermore, the electrochemical interaction is what causes the gas bubbles visible around the galinstan droplet in Figure A.6(i) during this portion of the cycle (also visible in the video). Once we rinsed the NaOH away with distilled water, the water no longer connected

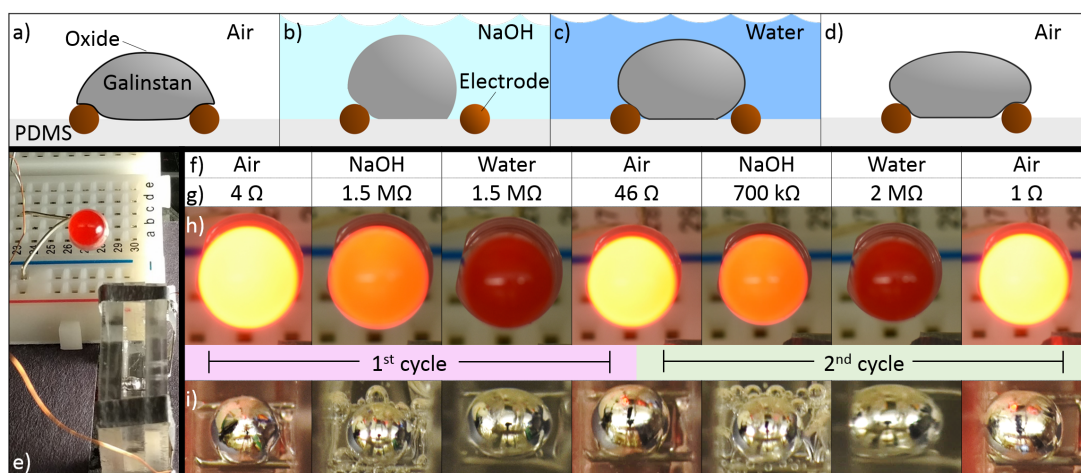


Figure A.6. Opening and closing a circuit via chemical manipulation of a liquid metal droplet. a-d) Schematic representation of the side profile of the droplet during one Air-NaOH-Water-Air treatment cycle: a) initial state, b) submersion in 1M NaOH disconnecting the circuit, c) replacing the NaOH with water encourages the droplet to collapse, d) the droplet is dried reconnecting the circuit. e) A photograph of the environmental chamber and LED used for this test (for scale, the LED is 3mm dia). h) A series of photographs of the LED with power supplied to the circuit during two consecutive cycles. i) Close up views of the droplets in the chamber when power was supplied, along with f) the chamber environment and g) a measurement of the resistance across the chamber's leads, during the two consecutive cycles. A video of the droplet profile during a third cycle is available in the Supporting Information.

the electrodes and the LED ceased to illuminate. We also note that, although not shown in the figure, if we rinse out the NaOH from the chamber and then rapidly dry the water from the chamber (with a small fan) the droplet holds its new shape, keeping the circuit open. The circuit can then be closed at any time by soaking the droplet in water.

Having successfully developed a system where we were able to completely disconnect and reconnect the circuit via environmental stimulation, we cycled the circuit to ensure repeatability. In Figure A.6 we show two consecutive disconnect and reconnect cycles, without changing the liquid metal droplet or any other part of the circuit. We cycled it a third time, while recording the video found in the Supporting Information. In the video we demonstrate the mobility of the chamber after the droplet had dried, proving that liquid metals can be manipulated, reconfiguration, and then pinned in place so that circuits built from these liquid metals can be removed from environmental control chambers.

A.3 Conclusion

In this paper, we have quantified the influence of acidic (HCl), alkaline (NaOH) and neutral (water) aqueous environments on liquid metal droplets prone to surface oxidation. Our results demonstrate the use of environmental stimuli to control the removal, formation and transformation of surface oxide on liquid metal droplets, thereby controlling the adhesion of the droplets on various surfaces. While previous studies have shown liquid metal oxide removal in HCl and NaOH baths, our results indicate the time scales for these removals differ by orders of magnitude at similar concentrations, with NaOH emerging as the more aggressive etchant. Furthermore, we have shown that rinsing the liquid metal droplet in water reverses the effects of HCl and NaOH, allowing formation of a surface oxide at short time scales and surface hydroxide at long time scales, which differ in mechanical properties but both encourage liquid metal adhesion to the substrate. Finally, we have employed our

findings to demonstrate liquid metal droplet mobility on-demand and environmentally responsive liquid metal switches.

A.4 Methods & Materials

The three types of substrates primarily used were P-type silicon (Wafer World), microscope slide glass (Home Science Tools) and Sylgard 184 as PDMS (Dow Corning). These substrates were used as they are representative of substrates typically utilized for liquid metal patterning since galinstan readily adheres to them. Galinstan (68.5% Ga, 21.5% In, 10% Sn by weight) was obtained from Sigma Aldrich, and used as-received from the manufacturer. HCl (Fisher Chemical) and NaOH (Macron Fine Chemicals) were obtained in either concentrated or dried forms and mixed with water to get the desired concentrations.

A.4.1 Contact Angles

To measure contact angles, galinstan droplets were set on a cleaned substrate for 3-5 minutes, covered. This setting time allowed the droplets to adhere to the surface, so that the droplet could be placed in the bath without dislodging it. The substrates and droplets were then placed in a 1M bath of either NaOH or HCl. Photographs of the droplet profile were taken regularly while the etchant slowly lifted the edges of the droplet and the contact angle maximized. At least 3 different droplets of different sizes were profiled and the results returned were an average of the different droplets. HCl and NaOH were used in both 1 molar concentrations for the bath, and each was tested on the following substrate types: glass, silicon and PDMS. To ensure that the PDMS substrate was flat, uncured PDMS was spin coated onto small glass slides (SCS G3-8 Spin Coater) at 2000RPM for 2 minutes, before curing them at 60°C for 2 hours. Each substrate was used only once for a single galinstan droplet, to prevent any acid/base etching of the surface from effecting subsequent results. All tests were performed at room temperature (approximately 25°C).

A.4.2 Goniometry

Pendent drop shapes were recorded and measured in a goniometer (Ramé-Hart Instrument co.) capable of performing oscillating pendent drop measurements (though this feature was not enabled). Each test was performed in a similar manner, using a non-air gap technique in which the water inside of the pipette tip directly contacts the liquid metal. This removed any viscoelastic effects of a compressible air pocket while extruding the liquid metal droplets. 5-8 μL droplets of liquid metal were extruded directly into the medium being used for the analysis (air, water, HCl or NaOH) and briefly allowed to stabilize for up to 30 seconds, to enable vibrations from the extrusion process to die off. At this point, the surface tension and volume of the droplet were recorded at intervals between 10-30 seconds (depending on the total length of the test) to allow the droplet to achieve equilibrium surface tension. The surface tension was then recorded as an average of the equilibrium tail of the data. Initial droplet volumes varied, but had a negligible impact on the recorded results.

Droplets extruded in both air and 1M HCl were allowed at least 2 hours to establish an equilibrium tail, although liquid metal droplets extruded into air often did not require as long of a time as those in HCl. Droplets extruded into 0.1M NaOH were allowed to come to an equilibrium for at least 40 minutes, and upwards of two hours, although this length of time was not necessary as the droplet had established its equilibrium surface tension before the analysis even began. Liquid metal droplet extruded into water were allowed at least 10 hours to come to an equilibrium, though many were able to establish an equilibrium before this time, the additional hours enabled a proper determination of equilibrium status.

A.4.3 XPS and Sample Preparation

X-ray Photoelectron Spectroscopy (XPS) measurements were performed using a Kratos Axis Ultra DLD spectrometer with monochromatic Al $K\alpha$ radiation ($h\nu=1486.6$ eV). The high-resolution Ga $2p_{3/2}$, O $1s$, Sn $3d$, In $3d$, C $1s$, Cl $2p$ and Ga

3d/Sn 4d/In 4d spectra were collected at constant pass energy (PE) with a PE of 20 eV. A built-in commercial Kratos charge neutralizer was used to achieve better resolution. Binding energy (BE) values refer to the Fermi edge and the energy scale was calibrated using Au 4f_{7/2} at 84.0 eV and Cu 2p_{3/2} at 932.67 eV. The photoemission peak positions were charge corrected to the adventitious carbon signal of C 1s at 284.8 eV. Spectra were analyzed using the CasaXPS software program, version 2.3.16 PR 1.6 (Casa Software Ltd.). A Shirley background was subtracted from each region before curve fitting; metal components were fitted with asymmetric Gaussian-Lorentzian peaks with tail dampening (CasaXPS Lineshapes \approx LF(1,1.4,20,50)) and oxide components – with Gaussian-Lorentzian peaks (CasaXPS Lineshapes \approx SGL(10)). Since the Ga 3d/Sn 4d/In 4d region contains the contribution of all three metal of interest, we focused qualitative/quantitative analysis on this region. Spin-orbit coupling doublets of the Sn 4d (4d_{5/2} and 4d_{3/2}), Ga 3d (3d_{5/2} and 3d_{3/2}) and In 4d (4d_{5/2} and 4d_{3/2}) electron levels were subject to spacing constraints of 1.10, 0.45 and 0.85 eV, respectively. The intensity ratio of the spin orbit coupling doublets for the d levels (d_{5/2} and d_{3/2}) was fixed to be 3:2. The atomic concentrations of the chemical elements on the near-surface region were estimated after the subtraction of a Shirley type background, taking into account the corresponding Scofield atomic sensitivity factors and inelastic mean free path (IMFP) of photoelectrons using standard procedures in the CasaXPS software.

The following protocol was used to prepare samples for the XPS measurements. (a) Glass substrates were exposed to oxygen plasma to encourage the Galinstan droplets to adhere to the surface (see Surface Treatments for more info). (b) Droplets of galinstan were immediately placed on the substrates, and were allowed to sit for 2 days to maximize adhesion between the droplet and the substrate (so the droplets do not move during treatment and testing). (c) Samples were then briefly rinsed in a chemical etchant bath of 1M NaOH or 1M HCl to alter the droplet's surface chemistry for 20 and 45 seconds, respectively. This is longer than is needed to create a visible change of the droplets surface chemistry, but the extra time was to ensure that all

oxide had been removed. (d) The two samples that were rinsed in water were quickly dried first by wicking away the majority of the remaining water (via absorption), with the remaining water forcibly evaporated by passing dry-nitrogen across the substrate and droplet. As-prepared samples were loaded to the XPS spectrometer through a load-lock.

B. ALL-SOFT MATERIAL SYSTEM FOR STRONG SOFT ACTUATORS

The following chapter is based on work previously published as [137]R. A. Bilodeau*, A. Miriyev*, H. Lipson, and R. Kramer-Bottiglio, “All-soft material system for strong soft actuators,” in 2018 IEEE International Conference on Soft Robotics (RoboSoft), Livorno, Italy, 2018, pp. 288–294. Copyright ©2018 IEEE, reproduced with permission. * indicates co-first-authorship

Contributions: This chapter was worked on primarily by two individuals: myself and Dr. Aslan Miriyev. Aslan provided experience and expertise in the novel silicone actuator material that he had only just recently developed. I provided the stretchable, solid-state heating silicone that could make his actuator work without requiring an external heat source. Much of the design and manufacturing of the final composite actuators was my work, including changing the shape of the internal heater core to facilitate the systems’ activation.

B.1 Introduction

Soft-material robotics aims to provide robots with the compliance and large strains necessary for performing natural and delicate tasks [36, 266]. Rigid robotic systems have consistently had the advantage of high-speed, high-precision, and high-output force actuation that allows them to carry both their own power supplies and control circuits while performing autonomous (untethered) tasks. Developing all-soft actuators for replication and amplification of natural muscle functionality so that soft robots can compete with their rigid counterparts is an ongoing challenge for the soft robotics research community [267].

Recently Miriyev et al. reported a self-contained, stimulus-responsive composite material by simply mixing silicone rubber and ethanol [133]. This new soft, robust composite can be used as a high-stress actuator at very low voltages (as low as 8 V), with output linear strains of up to 140%. However, lacking a soft, robust Joule heater, actuation of this material was demonstrated using an embedded, nickel-chromium (Ni-

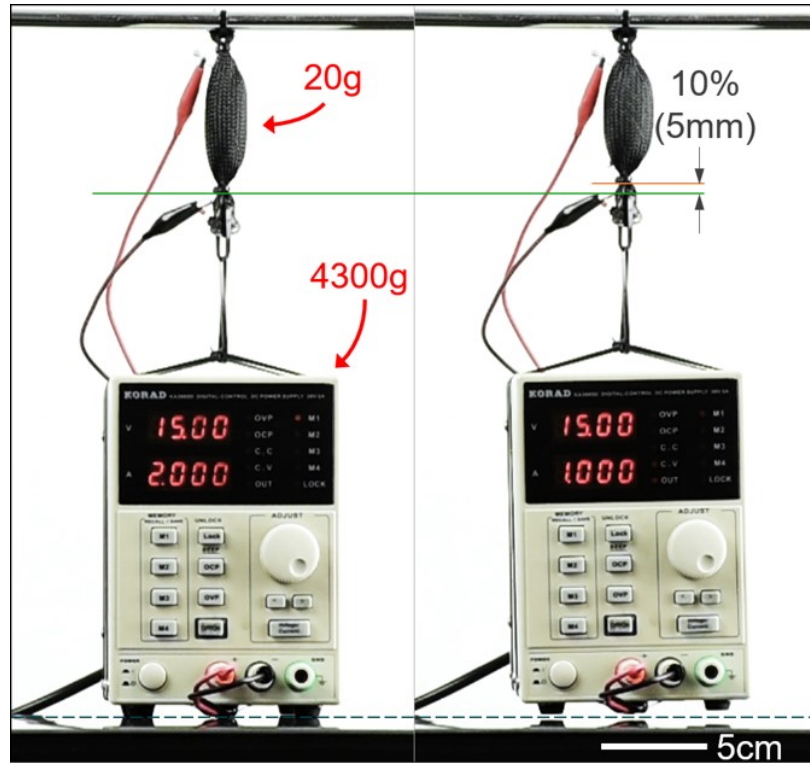


Figure B.1. All-soft heater/actuator being used as a McKibben-like muscle. The actuator is lifting its DC power supply, whose mass is greater than 200x that of the actuator.

Cr) spiral-shaped wire. Using a wire limited the ability to geometrically design an internal heater and the ability to simultaneously 3D-print the entire heater/actuator system [133]. A recent development of an electrically-conductive elastomer composite for stretchable sensors [59] possesses a promising opportunity to address the need for a soft, bulk-material Joule heater. The low-cost conductive composite, a silicone elastomer matrix with an expanded intercalated graphite (EIG) conductive additive, retains its performance even at large strains of up to 250%.

In this work, we fabricate an EIG-silicone conductive composite for use as a Joule heater and encase it within the thermally responsive ethanol-silicone composite to form an all-soft actuator. We demonstrate that at 15 wt% conductive filler, the heater core is capable of stretching with the encasing actuator and has the low resis-

tances required for Joule heating at low voltages. We characterize the heater core’s capabilities with various geometries and demonstrate its application as a Joule heater in a fully-soft artificial McKibben-like muscle that compares in force output to the original variant with a Ni-Cr wire heater. Finally, as demonstrated in Figure B.1, we show that this all-soft actuator can lift its own power supply (200x heavier than the actuator itself).

B.2 Background

Many forms of soft actuators have emerged in recent years as partial solutions to the need for high-force, high-deflection actuators, using a wide range of activation methods. These include fluidic elastomer actuators (FEA) [2,4,43,268–270] and pneumatic artificial muscles (PAM) [271–273] which operate off of pressurized fluids, as well as electrically active (and Joule-heated) solutions such as electroactive polymers (EAP) (including dielectric elastomer actuators (DEA)) [274–278], ionic polymer-metal composites (IPMC) [279,280], and shape-memory alloys (SMA) [281,282]. Each of these actuator techniques has an advantage-disadvantage trade-off, making them only partial solutions to the development of autonomous soft robotic systems.

Actuation methods combining high actuation stress along with high actuation strain include FEAs, PAMs and DEAs [133]. FEAs and PAMs require compressors and pressure regulating equipment to inflate and deflate elastomer bladders or chambers. The required external equipment accompanying these types of soft actuators is usually rigid, bulky and heavy, negating their high force output [266]. DEAs operate at >1 kV to create electromechanical response of an elastomeric membrane between two electrodes, requiring a high voltage converter and complicating the safety of human-interaction with these devices [283]. Though SMA actuators can achieve high strains through Joule heating at low voltages when properly programmed, even small amounts of overheating causes a rapid degradation of the SMA programming [284]. Alternatively, monopropellant decomposition (and even combustion-based actuation)

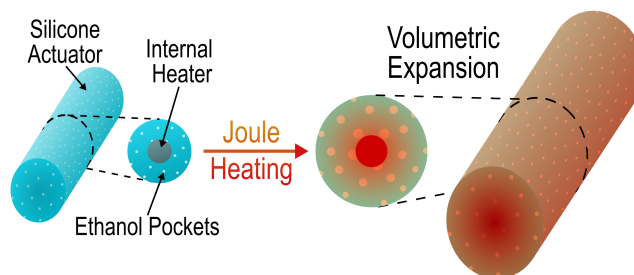


Figure B.2. All-soft actuator operation. Heating the core causes the external silicone to expand as the ethanol droplets trapped inside boil.

has been reported as a light-weight fluid pressure source for completely soft pneumatic robots [266,285]. Designing a soft robot with fuel-decomposition-based actuators has resulted in moderate output forces and complex design challenges, since noise, high temperature and toxic by-products need to be taken into account [286]. Furthermore, despite the high actuation impact of a combustion-propelled robot, controlling such actuators has been a challenge. Finally, actuation methods which show limited strain but sufficient actuation stress include paraffin-based solid-liquid phase transition actuators (only 3% strain) [287] and piezo-polymers (less than 1% actuation strain). These strain values are insufficient for most soft robotic applications, and therefore do not meet current needs.

The silicone-ethanol actuator reproduced in this work has been shown to function on a basic principle: By mixing the two materials together, the ethanol is distributed throughout the silicone matrix in micron-scale pockets that are suspended in place after curing. Upon heating to 78.4°C , ethanol boils inside the micro-pockets, leading to tremendous increase in volume of the entire composite (see Figure B.2). Ethanol was chosen for its low toxicity, its good ability to mix with silicone, and its moderate boiling temperature [133]. Previous work has succeeded in producing volumetric strains of up to 900% and exerting a force sufficient to lift a weight over 1000 times larger than the composite material.

Prior work with the EIG material has shown that it is possible to increase the amount of additive in a silicone matrix, without losing stretchability [59]. The EIG

material has also already been demonstrated as a conductive filler enabling internal heating in a rigid epoxy composite [121]. It enabled the Joule heating of the epoxy, causing the composite to soften and change its basic shape. This previous success motivated us to increase the concentration of EIG in the silicone composite and use it as a soft heater.

B.3 Manufacturing

We note that, for clarity, the silicone-ethanol actuator mixture will be referred to as the actuator composite, and the EIG-silicone mixture will be referred to as the heater composite. The manufactured silicone composite with a heater core will be referred to as the silicone actuator. Finally, when referencing the whole system (the silicone actuator in a mesh sleeve like a McKibben actuator), the system is referred to as a muscle.

B.3.1 Silicone Actuator Manufacturing

We used Ecoflex 00-50 (Smooth-On) for both the actuator composite and the heater composite. It is received from the manufacturer in two parts (part A and B) and we used it a 1:1 ratio. To create the actuator composite, we cast the silicone ethanol mixture into a 20 mm dia. cylindrical mold, 50 mm tall with a central shaft (see Figure B.3a and B.5a). We mixed both part A and B with ethanol (20 vol% ethanol) by hand for 1 min and then in a planetary centrifugal mixer machine (Thinky Mixer, Thinky USA) for 1 min. Once the silicone cured, the 3-part mold was removed, leaving an internal hollow core for later insertion of the heater composite.

For the heater composite, expandable graphite was purchased in a pre-prepared, dry state from Sigma-Aldrich. It was expanded and sonicated into EIG through a high-temperature oven roasting process (800°C) previously detailed by White et al. [59], with one key difference being the use of ethanol as the sonication solvent. We made this change (from cyclohexane used previously) to improve compatibility with

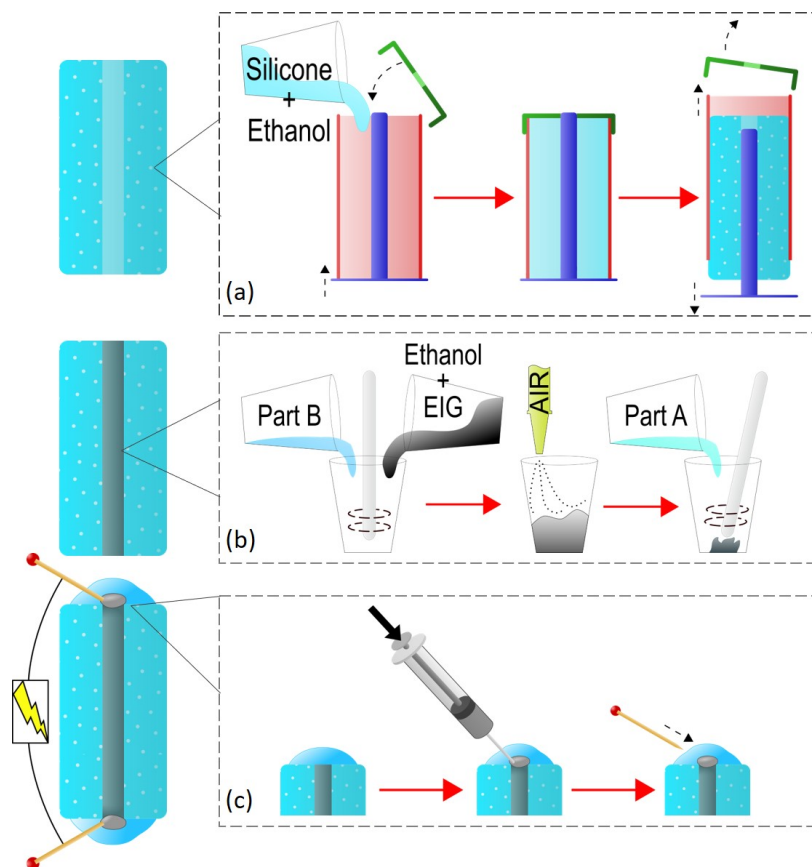


Figure B.3. Manufacturing the all-soft silicone based actuator. (a) A silicone-ethanol mixture is poured into a mold to cure, creating a cylindrical actuator with a hollow core. (b) To make the heater core, part B is mixed with an EIG-ethanol mixture, set under an airflow until nearly dry, and then part A is mixed in. Before it cures, the silicone-EIG composite is injected into the hollow core of the actuator. (c) The ends of the actuator are sealed with silicone and liquid metal is injected into the joint at the end of the heater composite. Finally, a pin (or copper wire) is inserted into the liquid metal bead to create an electrical connection to the heater core.

the actuator, with no noticeable degradation of the conductivity of the final silicone composite. After preparation of the EIG-ethanol mixture (through sonication and drying), the mixture is still mostly ethanol (only ~ 4 wt% graphite). Part B of the silicone was mixed with the EIG composite, and then air was blown across the composite to force the evaporation of the ethanol (see Figure B.3b). This dries the mixture down while still enabling dispersion of the EIG in the silicone. Once the composite was dried to only 50 wt% ethanol, Part A was added and the entire composite was mixed thoroughly to create a ratio of 15 wt% EIG-silicone. The heater composite was then injected into the hollow core of the actuator composite using a syringe, and allowed to cure.

B.3.2 Muscle Assembly and Electrode Contacts

We used eutectic gallium-indium-tin (galinstan, Sigma Aldrich), a room-temperature liquid metal, to create a simple interface connecting the soft core heating composite with rigid wires and electrical components (Figure B.3c). We sealed each end of the silicone actuator with additional (stronger) silicone (Dragonskin Fast, Smooth-on) and then injected galinstan into the ends of the actuator using a 25 gauge syringe needle. On removing the syringe, we sealed the hole with additional silicone and assembled the muscle by placing the silicone actuator into a mesh sleeve (Polyurethane terephthalate mono-filament yarn, Techflex) and tying it off.

In order to electrically connect to the core, we punctured a needle through the mesh and into the liquid metal bead, allowing us to connect the heater to a power source. In the case of experiments where free-expansion (or heating) was required, the mesh sleeve was omitted. We note here that while these electrodes provided an ideal electrical interface, they were susceptible to leakage under high pressures, which manifested as electrical noise.

B.4 Characterization

B.4.1 Manufacturing Implementation

Heating Core Resistance

The resistance in the heater silicone cores varied between 15-65 Ω , comparable to the 15 Ω in the original Ni-Cr wires [133]. Two key factors in our design and manufacturing allowed for such a low, uniform resistance in the composite material: the use of the liquid metal electrodes and prevention of the ethanol from drying out of the composite material during preparation. The liquid metal contacts decrease the contact resistance between copper wire electrodes and the soft heater composite. Without the liquid metal, the resistance in the heater core increases by 20-40 Ω , often doubling the sample resistance and causing uneven Joule heating due to the additional resistance concentrated at ends of the actuator. This is why the liquid metal was used even though it leaked during actuation.

Preventing the ethanol from fully drying out of the heater composite before it cures is the second key to maintaining low resistance. If the heater composite dries completely before mixing in Part A (during the manufacturing, as previously explained) the resultant resistance of the core jumps 1-2 orders of magnitude (from 25-65 Ω to 800-2500 Ω , measured on cores with a diameter of 5 mm and 7 mm). It is still possible to mix in Part A and inject the material, but the high resistance makes the core unusable as a heater. We suspect that when the composite dries prematurely the EIG flakes clump, resulting in poor dispersion throughout the composite. If the silicone cures in the 50% ethanol mixture, the EIG flakes remain suspended in the unmoving polymer after the ethanol dries off.

Heater Microstructure

We placed a silicone actuator into a scanning electron microscope (SEM) in order to determine the quality of the heater composite mixture and to visually observe the joint

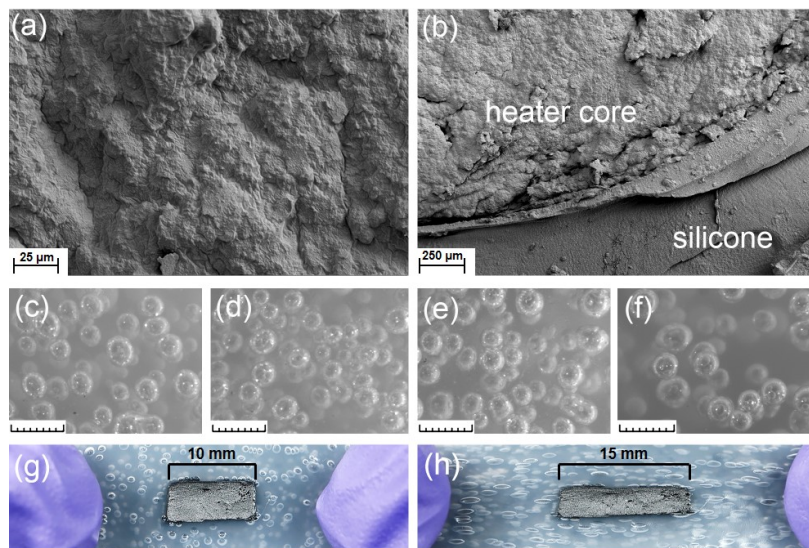


Figure B.4. Macro- and microstructure images of the all-soft material system for actuators. (a) SEM image of the soft heater composite. (b) SEM image of a silicone/heater interface cross-section. (c)-(f) macrostructure of actuator composites after preparation with different mixing modes and rates: (c) hand mixing for 4 min, (d) mixer machine mixing for 0.5 min, (e) mixer machine mixing for 1 min, (f) mixer machine mixing for 3 min (scale bars are 500 μm). All-soft actuator composite before (g) and during (h) hand-stretching, showing 50% linear strain extension in the core.

between the actuator composite and the heater composite. Figure B.4a,b are images taken of both the pure heater composite and the heater composite interfacing with a pure silicone exterior. We also prepared a sample without ethanol in the actuator (to remove incompatibility with the high-vacuum SEM), and cut it with a knife to expose an inner cross-section for imaging. The heater composite has a textured microstructure topography on a scale from single microns to tens of microns, caused by the conductive EIG additive (Figure B.4a). Although individual EIG flakes are too small to be seen at this scale, no EIG clumps are observable, indicating a good mixture of the EIG into the silicone. The interface between the heater composite and pure silicone rubber is characterized by multiple micro-cracks, and a noticeable difference in topography between the two materials (Figure B.4b).

Actuator Macrostructure

To ensure that the ethanol was distributed evenly throughout the actuator composite when machine mixed, we tested the effect of mixing the actuator composite by hand or in a mixer machine on the bubble density of the composite. Four samples of silicone-ethanol composite were inspected under a microscope to observe the density of air-pockets (or ethanol droplets) in the mixed composite. Each sample was prepared with different mixing time/method. The first sample was mixed by hand for four minutes. The other three were mixed by hand for one minute (to fold the low-viscosity ethanol into the high-viscosity silicone) and then mixed in the mixer machine for 0.5 min, 1 min, and 3 min respectively. All samples were then cast into sheets 5 mm thick to allow the microscope to capture the images of the bubbles through the sample. Figure B.4c-f shows that the largest amount of air bubbles was achieved after 30 s of mixing in the mixer machine, whereas mixing for three minutes resulted in the lowest density of air bubbles. This validates our mixing for 1 min, as the actuator composite has a comparable macrostructure to the hand-mixing method used in previous work [133].

Heater Stretchability and Interfacing

Although the interface in the all-soft material system was shown to have micro-cracks (Figure B.4b), we still achieved a high bond between the heater composite and the actuator composite. To demonstrate this, we cast a large, flat sample of the actuator composite, with a small, 10 mm wide rectangular core, and filled the core with the heater silicone composite (Figure B.4g). This enabled us to stretch the external silicone and observe the reactionary stretching of the internal heater. As Figure B.4g-h demonstrates, we could achieve both good adhesion between the disparate composites and a 50% linear expansion of the heater composite. The ability to both adhere the bulk composites together and for both to have high strain capacities is vital for the success of these all-soft actuators.

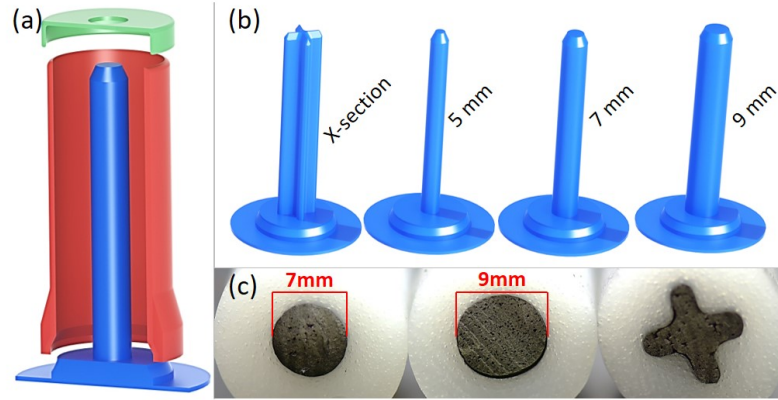


Figure B.5. CAD diagrams and photographs of the various heater core geometries. (a) A cut-away of the CAD rendering of the three-part mold. (b) Models of the four different cores used in the mold. (c) Cross-sectional photographs of three of the resultant heater core/actuator combinations.

B.4.2 Heating and Energy Distribution

Core Design

We used four different types of internal shafts in order to compare differences in heater performance based on the geometry of the core (Figure B.5). Three actuators had circular cores with diameters varying between 5 mm, 7 mm and 9 mm. We also created a fourth core in the shape of an X, with the same cross-sectional area as the 7 mm circle (38.38 mm^2 , see Figure B.5c). This shape has the same volume of heater composite as the 7 mm core, but a larger contact area with the actuator composite. Ni-Cr wire (Remington Industries) heaters were coiled in a double-spiral and cast directly into the actuator composite in order to compare the current all-soft system to the original work employing this silicone-ethanol actuator technology [133].

Core Performance

We used a thermal camera (Fluke TiX580, Fluke) to characterize the ability of the heater composite to heat the surrounding actuator composite up to (78.4°C), the boiling temperature of ethanol. We started by heating a simple, pure elastomer sheath around the heater core (to remove the effects of the expanding ethanol). All four varieties of heater composite cores (5, 7, 9 mm, X-shape) and a Ni-Cr wire heater were encased in the silicone rubber and Joule heated with 9 W of power (only two of which are shown in Figure B.6a,b).

After two minutes of heating, the X-shaped heater composite shows better heat distribution than any other composite (Figure B.6a). The X-shaped heater also heated the entire outer surface to 78°C two minutes faster than the other setups, taking only 5.5 min. The X-shaped heater core proved to be the best Joule heater design when power was controlled as it can heat the required volume both quickly and evenly. Though it has a higher resistance than the 9 mm heater composite rod and Ni-Cr wire spiral (also shown in Figure B.6a,b), those two suffered from localized overheating near the heaters and/or peripheral under-heating. The higher contact area of the X-shaped core with the actuator composite is more efficient as it nearly eliminates localized overheating. Note that the slight expansion of the specimen with the X-shaped heater composite core is caused by a small amount of ethanol trapped in the heater core during the filling process.

The spiral-shaped Ni-Cr wire has the smallest volume of the heating cores, and, though rigid, it causes significant expansion and shape deformation of the silicone actuator due to the high flexibility of the wire spiral and local overheating (Figure B.6c). When heated, the X-shaped heater composite showed a smaller but more even expansion of the surrounding silicone actuator (Figure B.6d). This difference, however, does not prevent the X-shaped heater from producing large output forces when constrained in a mesh (see next section).

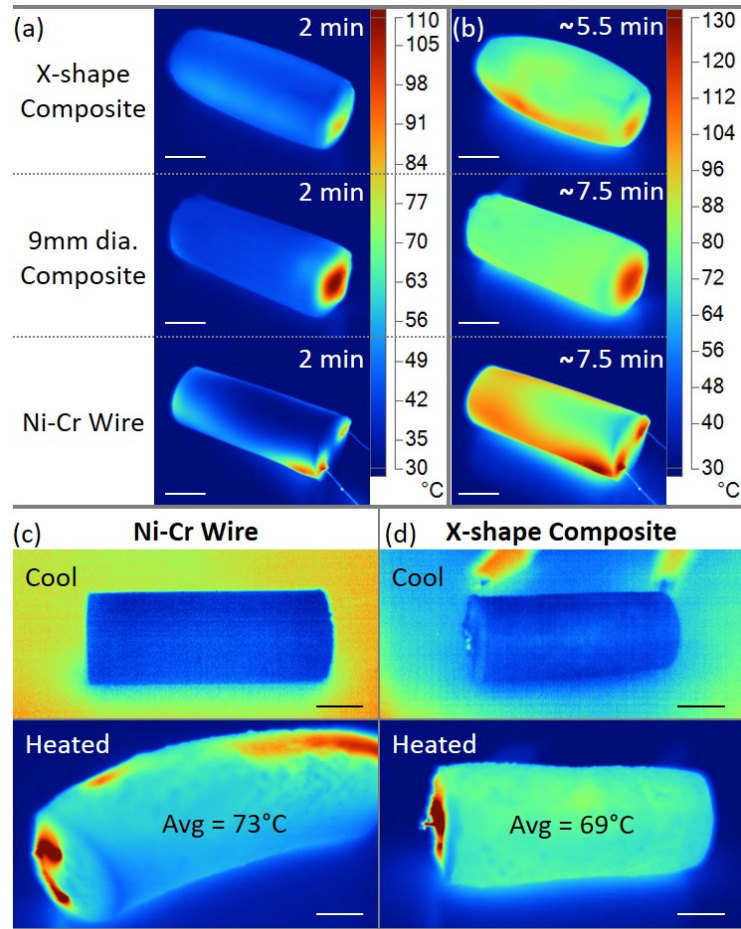


Figure B.6. IR images of several Joule heating experiments using 9 W of input power. (a)-(b) Two silicone heater composite cores are compared with a Ni-Cr wire heater via encapsulation in pure silicone. (a) At 2 min, the X-shaped core is distributing its heat better to the exterior of the silicone, when compared to the other two systems. (b) The same cross section achieves an external temperature of $\sim 78^{\circ}\text{C}$ two minutes faster than the other systems. (c) The Ni-Cr wire heater compared with (d) the X-shape core, encapsulated in the actuator composite in their initial (cool) and final (heated) states. Scale bars are 1 cm.

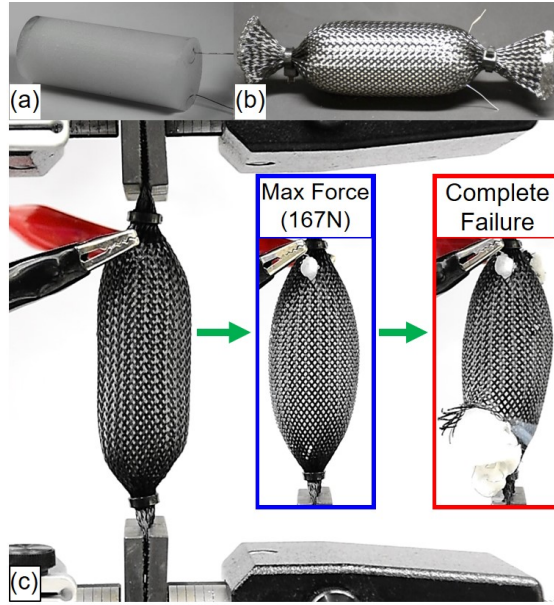


Figure B.7. Blocked force setup and test. (a) A Ni-Cr wire heated actuator. (b) The same actuator inside a mesh sleeve for use as a McKibben-like muscle. (c) The actuator installed in a blocked force test. Insets show the Joule heated actuator at its maximum force and then after complete failure (due to melting the external mesh).

B.4.3 Force Output

In Figure B.7 and B.8, we show the potential of our all-soft material system to be the actuator in a fully soft McKibben-like artificial muscle. When encased in a braided mesh sleeve (Figure B.7a,b), the silicone actuator is capable of radial expansion in the net, leading to axial contraction of the entire muscle. The muscle is activated by supplying electrical power to the internal Joule heater. For comparison, the original work, which also demonstrated the actuator as a McKibben-like muscle [133], was also recreated (Figure B.7).

To determine the maximum pulling force of these muscles, we performed a series of blocked force tests. We clamped a new artificial muscle in an Instron 3345 using pneumatic grips (Figure B.7c) and Joule heated the actuator with 30 V and unregulated DC current. We measured the force output of the statically-held muscle until

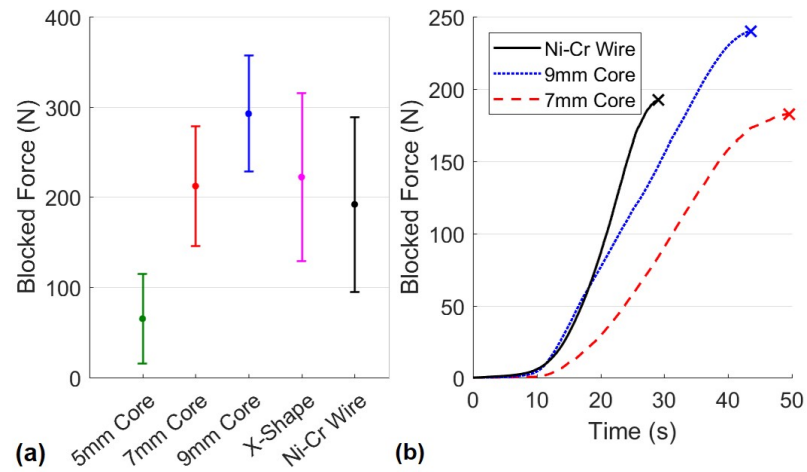


Figure B.8. Blocked force test results for the McKibben-like muscles. (a) The measured results of the force output of several all-soft muscle designs, compared with a Ni-Cr wire heater. Error bars represent 95% confidence. (b) Characteristic curves from the build up of force in the actuator muscle over time for three examples of different heater types. The 9 mm core and Ni-Cr wire, with nearly identical resistances, heat up at nearly the same rate, whereas the 7 mm core (with a higher resistance) takes longer to heat up.

it either failed mechanically (Figure B.7c) or electrically. As the current fluctuated while heating the actuators with heater composite cores, we were not able to record a steady value and were therefore unable to calculate power consumption.

We tested all four configurations of the all-soft muscles and the original Ni-Cr spiral-heated version in order to compare their maximum blocked force. The results, shown in Figure B.8a, show that most variations of the all-soft muscles can consistently exert more than 200 N of force, corresponding to more than 1000x the weight of the entire artificial muscle (<0.2 N), as can the Ni-Cr heated version. On average, the 9 mm heater composite performed best, exerting a blocked force of nearly 300 N, significantly higher than that produced by the 5 mm cores (barely 60 N).

Both the 9 mm cores and Ni-Cr wire actuators failed mechanically. The pressure of the expanding silicone actuator exceeded the strength of the mesh, typically resulting in sudden and complete failure and force loss (see Figure B.8c inset). Though the mesh failed for both types of actuators, the Ni-Cr averaged significantly less pulling force before failing (nearly 100 N less). The Ni-Cr wires would consistently draw 1.5 A of current, with the 9 mm cores drawing between 1-2 A during their testing. Although they both were drawing similar power, the 9 mm cores isolated the incoming energy as heat in the central core of the actuator, causing only an expansion of the ethanol. In contrast, the Ni-Cr wire created localized hot-spots at the exterior of the actuator (see Figure B.6) weakening the mesh, and causing them to fail prematurely. This was especially true at the ends of the actuator, where the Ni-Cr wire leads entered the mesh and where the wire turns around. Input power regulation (and therefore temperature regulation of the Ni-Cr wire) might enable the Ni-Cr wire actuators to produce higher forces by preventing overheating of these ends.

In contrast, the 5 mm dia., 7 mm dia., and X-section heater cores all failed electrically, losing connection between the two electrodes. This reduced the power input to near-zero, though only temporarily for the 7 mm dia. and X-section cores. After cooling briefly, both types would typically regain conductivity. For the 5 mm diameter cores, however, this loss-of connection was permanent, probably due to the small

contact area in the thin cores and the heater material burning around the electrodes. Between their high initial resistance and the permanent heater-core death, muscles with these cores performed poorly.

Figure B.8b shows three typical curves of blocked force as a function of time. The 9 mm heater composite and the Ni-Cr wire heat almost at the same rate, while the 7 mm core heats up slower. This may be attributed to the similar initial electrical resistance of the Ni-Cr wire and the 9 mm core used to gather these datasets (approximately $15\ \Omega$ each), compared to the higher resistance of the 7 mm core (at about $25\ \Omega$).

B.5 Results and Discussion

To demonstrate the potential of these light-weight, all-soft actuator muscles, we used one to lift its own power supply (Figure B.1). The actuator had a 7 mm dia. internal silicone heater core, and was strong enough to lift the power supply 5 mm (10% the length of the actuator) straight up, even though the supply is over 200x the mass of the actuator (see also Supplemental Video 1). Operating on a 15 V input, the actuator lifted the power supply to its maximum height in 22 s, and held it suspended for well over 1 min before being shut off.

The novel material combination of a silicone-EIG heater core with the silicone-ethanol actuator opens up many new design parameters for exploration. Apart from the entire system system being composed of elastomer composites (enabling bulk stretchability), a bulk heating material gives way to numerous possibilities in geometric design choices for the heater, beyond the few presented here. This can improve the way in which the heat from the heater core is distributed throughout the actuator (as demonstrated with the X-shaped core), potentially preventing over-heating of the ethanol and burning of the silicone immediately surrounding the actuator. By adding larger volumes of the bulk-heater, it is possible to both speed up the force generation (as demonstrated by the 9 mm cores), and increase the maximum blocked force pro-

duced by the muscles. With this bulk system, it will be possible to optimize both the size and shape of the heater core in order to improve the speed and efficiency of the all-soft muscles.

There are other advantages of this all-soft system when compared to its predecessor using the Ni-Cr wire. Although the Ni-Cr wire can have more coils looped through the actuator to facilitate heating, the system short-circuits and will not heat if any of the coils touch, a non-issue with a bulk silicone resistor. Furthermore, by limiting the heater core to a system exclusively internal to the actuator, it is less likely that an external mesh sleeve (or other materials) will heat up and weaken. Finally, because we successfully removed the Ni-Cr wire from the actuator, both the actuator and the heater are malleable in their uncured state, allowing for continued improvement to the design and manufacturing of the system.

B.6 Conclusion and Future Work

In this paper, we have demonstrated that we can integrate a new, soft, stretchable, central core material that removes the need for a Joule heating wire used in the original system. We show that actuators powered with this soft composite heater are capable of producing comparable blocked forces, while also being able to improve the heat distribution by geometric design. Finally, we demonstrate that a single one of these light-weight, all-soft muscles is strong enough to lift over 200x its own weight. This is a big step forward for the soft robotics field, as the ability for a soft robotic actuator to carry weight (such as batteries and control units) is crucial towards the development of autonomous soft robotic systems.

This all-soft system is a significant advancement from the original work, as both the soft actuator material and the soft heater may potentially be patterned using 3D-printing. This would allow automated fabrication and endless varieties of actuator (and heater) shapes, while retaining the actuator expanding performance. 3D-printing

of the silicone actuator material was shown in the original work [133], while 3D-printing of the heater composite will be explored as a part of a future work.

The accelerated Joule heating of the actuators came with a cost, reducing them to one-time use, though the muscles have been shown to be repeatably actuated at slower heating rates [133, 214]. We desire to improve both driving speed and durability by continuing to improve the mix ratios of the composite materials in the core, optimizing for stretchability, robustness, and printability. We will look to improve the interfacing of the material systems, focusing on both the interface between the heater composite and the actuator composite and the interface between the heater and any electrical leads used for power supply. Furthermore, with different bubble densities caused by different mixing times, and by using 3D printing technologies, it might be possible to combine actuator composites with different mixing times to create asymmetrically expanding actuators.